THE STABILITY OF CLIMATE ON VENUS

by

MARK ALAN BULLOCK

B.S., Harvey Mudd College, 1978

M.S., San Jose State University, 1991

A thesis submitted to the
Faculty of the Graduate School of the
University of Colorado in partial fulfillment
of the requirements for the degree of
Doctor of Philosophy
Department of Astrophysical, Planetary and Atmospheric Sciences
1997

This thesis for the Doctor of Philosophy degree by

Mark Alan Bullock

has been approved for the

Department of Astrophysical, Planetary and Atmospheric Sciences

by

____

Dr. David H. Grinspoon

____

Dr. Bruce M. Jakosky

____

Dr. Larry W. Esposito

____

Dr. Gary Thomas

____

Dr. O. Brian Toon

Date__________________

Bullock, Mark A. (Ph.D., Astrophysical, Planetary and Atmospheric Sciences)
The Stability of Climate on Venus
Thesis directed by Professor David H. Grinspoon

Abstract

The present climate of Venus is controlled by an efficient carbon dioxide-water greenhouse effect and by the radiative properties of its global cloud cover. Both the greenhouse effect and clouds are sensitive to perturbations in the abundance of atmospheric water vapor and sulfur gases. Planetary-scale processes involving the transport and sequestering of volatiles affect these abundances over time, driving changes in climate.

I have developed a numerical model of the climate evolution of Venus. Atmospheric temperatures are calculated using a one-dimensional two stream radiative-convective model that treats the transport of thermal infrared radiation in the atmosphere and clouds. These radiative transfer calculations are the first to utilize high temperature, high resolution spectral databases for the calculation of infrared absorption and scattering in Venus' atmosphere. I use a chemical/microphysical model of Venus' clouds to calculate changes in cloud structure that result from variations in atmospheric water and sulfur dioxide. Atmospheric abundances of water, sulfur dioxide, and carbon dioxide change under the influence of the exospheric escape of hydrogen, outgassing from the interior, and heterogeneous reactions with surface minerals.

Radar images from the Magellan mission show that the surface of Venus has been geologically active on a global scale, yet its sparse impact cratering record is almost pristine. This geological record on Venus is consistent with an epoch of rapid plains emplacement 600-1100 million years ago. My models show that intense volcanic outgassing of sulfur dioxide and water during this time would have resulted in the formation of massive sulfuric acid/water clouds and the cooling of the surface for about 300 million years. The thick clouds would have subsequently given way to high, thin water clouds as atmospheric sulfur dioxide was lost to reactions with the surface. Surface temperatures approaching 900 K would have been reached about 500 million years after the onset of volcanic resurfacing. Evolution to current conditions would have proceeded due to loss of atmospheric water at the top of the atmosphere and the reappearance of sulfuric acid/water clouds.

Current temperatures are maintained within a narrow range by the competing effects of cloud albedo and greenhouse warming. The present climate of Venus would be unstable if atmospheric carbon dioxide can react with surface minerals. Venus may be undergoing rapid climate change due to carbon dioxide reactions with the surface, but it is more likely stable because most of the surface is devoid of carbonate. Abundant atmospheric sulfur dioxide is maintained by the action of volcanic sources within the last 20 million years.

Even if atmospheric carbon dioxide does not today react with the surface, volcanic outgassing sufficient to increase sulfur dioxide abundance 3-10 times the present value would cool the surface enough to engage carbon dioxide-mineral reactions. This would precipitate a climate runaway to a cooler, lower pressure state at 400 K and 43 bars within 60 million years. This may be the eventual fate of Venus anyway, as sulfur dioxide equilibrates with surface minerals in the absence of outgassing. The climate may oscillate between warm, cloudy conditions and a cooler, cloud-free regime before it runs away to the cooler stable state.

Dedication

for Sean and Brian

Acknowledgments

Life in graduate school would have been dramatically different without my inimitable mentor, advisor, and friend, Dr. David Grinspoon. His prodigiously creative ideas have inspired all of my Venus research. I have further benefited from his incisive intuition for getting to the heart of problems in planetary science. More importantly, David has approached our work with a generous and compassionate spirit, showing me how science can be fun, relevant, and honest.

Dr. Bruce Jakosky was my other mentor. He cheerfully and wisely taught me how to navigate through the scientific process, dealing with issues of writing, publication and scientific ethics. Defending my ideas as he quickly saw into the physical problems we discussed was never easy and always illuminating. For these lessons, and the anticipation of continued valuable interactions, I am very grateful.

Each one of my other committee members, Dr. Larry Esposito, Dr. Gary Thomas, and Dr. Brian Toon have been interested and involved in my research. I am very grateful to them for their encouragement in pursuing the scientific ideas of this project.

The graduate student environment at LASP encourages an intense intellectual exchange of ideas, both among the students and between students and faculty. The vital ability to compare hypotheses, verify the facts, and explore the nature of the universe together is amply provided. I thank all my officemates, the other students at LASP, and Mike Mellon for remarkable and enjoyable discussions.

Bob Frodeman, a friend and true philosopher-king, has guided me along an intellectual path long forgotten. He has reminded me with beautifully crafted arguments that scientific research is meaningless without connection to the political, ethical and human fabric in which it exists.

Graduate school for me has been a team effort. The rest of the team provided support in the deepest possible way -- by the unwavering belief that becoming a scientist was the only path I should take. The rest of the team was Nancy, my wife, and my two incredible children, Sean and Brian.

I entered graduate school after spending 10 years in the U.S semiconductor and electronics industries. Although commerce drives our economy and funds public science, I have found that scientific research is a wholly different enterprise. I believe that it is a mistake to justify fundamental science on the basis that its products may eventually enhance economic well-being. However, science ultimately must be in the service of the public that funds it. If the scientific exploration of our solar system is to thrive, our culture must appreciate why it is valuable. Exploring new worlds speaks to our curiosity, imagination, and vision. It is these that are necessary for an enlightened perspective on where the human race is headed.

There is something special about a society that honors curiosity and the legitimate search for truth. I have discovered that part of our work as scientists should be to teach what Aristotle did, that “All philosophy is born in wonder”.

CONTENTS

TABLES

FIGURES

CHAPTER 1

INTRODUCTION

The Climate of Venus

Emerging together from the pre-solar cauldron, Earth and Venus today reveal widely divergent paths of planetary evolution. Almost the same size, their bulk compositions and heat producing radioactive elements are probably similar [*Turcotte*, 1995]. Volatile endowments are less certain, but current theories on the late scattering of icy planetesimals into the inner solar system suggest that initial abundances were likely close [*Ip and Fernandez*, 1988]. However, Venus receives twice the energy from the Sun than does the Earth, a major difference that is probably ultimately responsible for their incongruent evolution [*Kasting*, 1988].

Presently, the surface of Venus is about 735 K, with a 92 bar carbon dioxide-nitrogen atmosphere. An efficient greenhouse effect prevails, sustained by an atmosphere whose major constituent is a powerful (and on Earth, troublesome) infrared absorber. Liquid water is nonexistent, although its vapor exists in feeble amounts in the atmosphere. A menagerie of gaseous sulfur species, along with what water there is, provide fodder for the globally encircling sulfuric acid cloud decks [*Esposito et al.*, 1983]. The remarkably alien and hostile conditions of the atmosphere are maintained by a special relationship between the physical properties of its constituents. Water, to a large extent, absorbs infrared radiation at wavelengths that carbon dioxide doesn't [*Sagan*, 1960]. Similarly, sulfur dioxide and other sulfur gases absorb preferentially in carbon dioxide-water infrared windows [*Pollack et al.*, 1980]. These same radiatively active species, in their trace amounts, are exhaled by volcanoes, sustain the clouds, escape to space, and are most likely involved in reactions with surface rocks. All these processes are temperature and concentration-dependent, and it is very likely that complex interactions among them influence the climate of Venus [*Bullock and Grinspoon*, 1996].

This thesis has been motivated by the following questions: Was Venus hotter at sometime in the past than it is today? Or, alternatively, could Venus have been cooler, inhabiting a stable climate regime significantly different from what we see presently? How stable is the current Venus climate, and how might perturbations such as volatile outgassing, exospheric escape, and surface/atmosphere interactions alter it? The pristine impact cratering record, superposed on a surface of extensive volcanism, suggests that the atmosphere may have been injected with large quantities of radiatively active volatiles during an epoch of rapid plains emplacement. The steady decline of water vapor on short timescales due to exospheric escape of hydrogen [*Donahue and Hodges*, 1992] implies that Venus may have had 100 times as much atmospheric water 800 million years ago than it does today. Heterogeneous reactions with the surface, in seeking equilibrium, may have supplied or taken up large quantities of volatiles over timescales on the order of 100 million years.

As an example, the steady loss of atmospheric water on geologically short timescales (80 - 300 million years) can readily influence the efficiency of the Venus greenhouse. Water abundance at the cloud tops, however, influences cloud production through the hydrolysis of sulfur dioxide to form sulfuric acid aerosols. Less atmospheric water may tend to decrease the greenhouse effect and hence surface temperatures, but it may also result in thinner clouds. Thinner clouds mean a lower planetary albedo, more solar flux delivered to the atmosphere and surface, and therefore higher surface temperatures. Atmospheric radiative-convective equilibrium and cloud albedo are coupled in a complex way on Venus. Atmospheric regimes, defined by the abundances of water and sulfur dioxide, probably exist where there is a negative feedback between radiative-convective equilibrium and cloud albedo, providing stability to the climate. This may be the case for present Venus. However, there are probably values for these parameters for which a positive feedback exists, causing Venus' climate to undergo dramatic change.

Other feedbacks must also exist for Venus' climate as a result of processes that either supply volatiles to the atmosphere or remove them. Outgassing of radiatively important volatiles by volcanoes provides the means to alter atmospheric water and sulfur dioxide, and the potential to shift atmospheric temperatures into new regimes of radiative-convective/cloud albedo feedback. Because the Venus greenhouse is particularly sensitive to changes in absorbers that are active in carbon dioxide thermal infrared windows, wide excursions in temperature and cloud structure are possible, especially with a rapid, globally extensive epoch of volcanic activity.

Communication of volatiles between the surface and atmosphere on Venus may also occur due to kinetically favored heterogeneous reactions at high surface temperatures and pressures. Atmospheric sulfur dioxide reacts quickly with carbonates under current conditions. As with the Clausius-Clapeyron equation for water phase changes on the Earth, equilibrium abundances in the Venus atmosphere due to reactions with minerals are an exponential function of temperature. Again, the greenhouse effect and the clouds are influenced by sulfur dioxide abundance, which in turn depends on them via the surface temperatures they force.

Perhaps the most fascinating possibility for climate change on Venus is the role that atmospheric carbon dioxide may play in achieving equilibrium with surface minerals [*Urey*, 1952]. The amount of carbon dioxide in Venus' atmosphere is, to within experimental uncertainty, equal to the value required for its equilibrium with surface minerals [*Fegley and Treiman*, 1992]. This may be one of Nature's cosmic coincidences, or it may say something profound about the evolution and stability of climate on Venus. Perturbations to the greenhouse effect, due to the loss of atmospheric water, sulfur dioxide and water outgassing from the interior, or even the occasional impact of a large comet, are inevitable. An increase an water abundance, for example, may force higher temperatures at the surface, depending on the response of the clouds. Higher surface temperatures result in a shifting of the carbon dioxide-mineral equilibrium to one of a higher carbon dioxide partial pressure. Higher carbon dioxide pressure means a broadening of absorption bands and in increase in infrared opacity and the greenhouse effect. If carbon dioxide is available from surface minerals a runaway greenhouse ensues, driven by ever-increasing decarbonation of minerals.

Aside from these theoretical considerations, there is weak evidence for past climate change on Venus. Striking surface features are observed in Magellan images that resemble fluvial landforms more than they resemble volcanic features on Earth and Mars [*Kargel et al.*, 1994]. Venusian canali, up to 7000 km long, exhibit features similar to meandering river channels and flood plains on Earth. Many are terminated by outflow channels that resemble river deltas. An example of one of these is shown in Figure 1.1. This lava delta exists at the terminus of an 800 km long canale in the northern volcanic plains of Venus. Chemical equilibrium with the atmosphere makes it likely that the upper crust contains large amounts of calcite, anhydrite, and other salts. These salts could melt at temperatures of a few tens to hundreds of Kelvins higher than Venus surface temperatures today. *Kargel et al.* [1994] hypothesize that a molten carbonatite (salt-rich) aquifer may currently exist beneath a few hundred to several kilometers of solidified salt-rich 'permafrost'. Moderately higher surface temperatures in the past could have mobilized a vast reservoir of liquid, producing the fluvial features we see today.

The origin of crustal plateaus, which contain the oldest surface features seen on Venus (the tessera), is currently a subject of intense investigation. Crustal plateaus are distinguished by small gravity anomalies and shallow apparent depths of compensation, consistent with isostatic compensation by thickened crust.

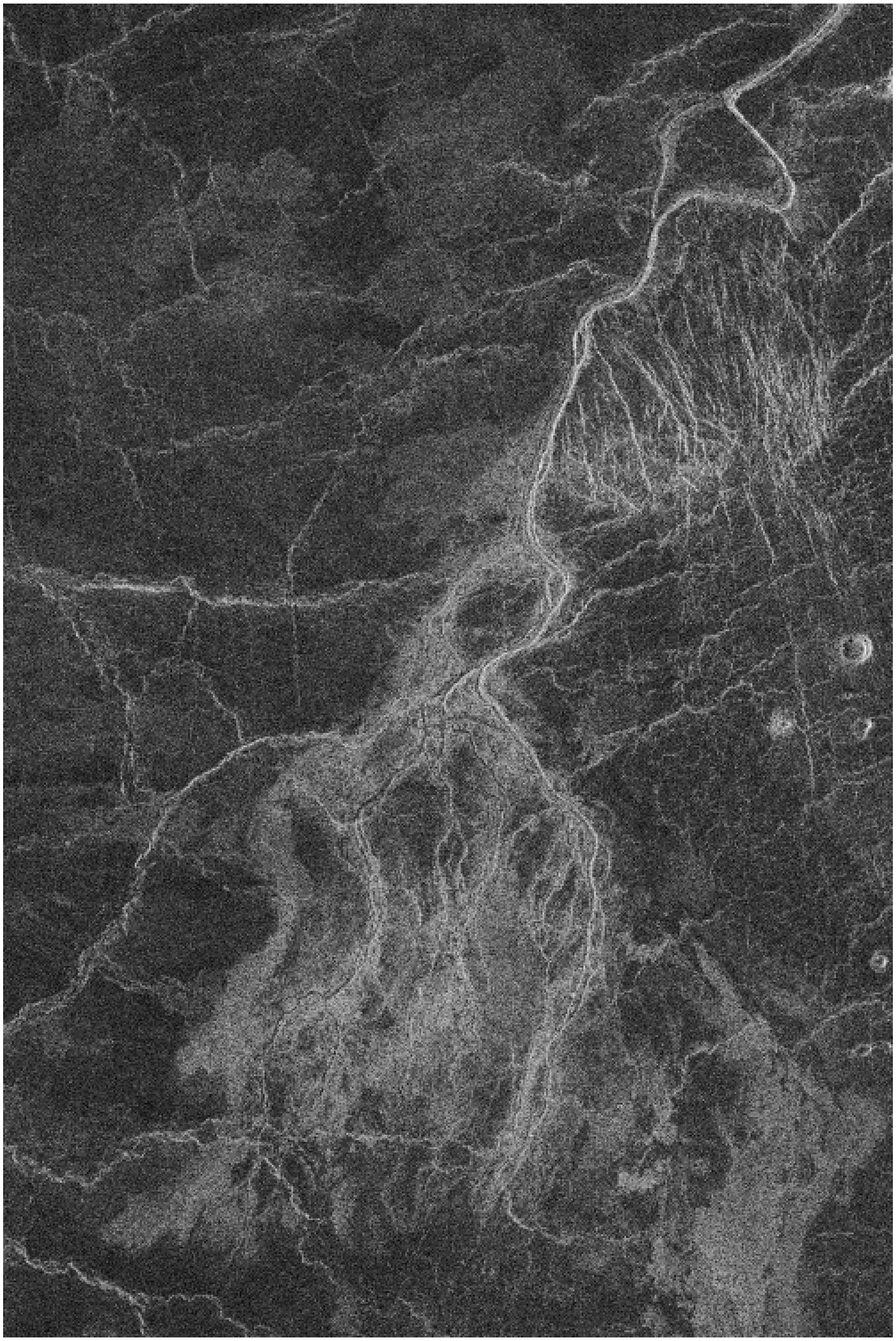

Figure 1.1 Fluvial feature on Venus attributed to carbonatite volcanism. The region shown here is approximately 67 x 90 km.

Recent analyses of the tessera indicate that crustal plateaus were formed by the extension of hot crust, indicating an uplift and stretching origin consistent with a mantle plume source [*Phillips and Hansen*, 1997]. An example of this extensional 'ribbon terrain', found on the Ovda Regio crustal plateau, is shown in Figure 1.2. Modeling of the structure of these features indicates that they could only have been produced when the lithosphere was quite thin, resulting in large fractional partial melting in the plumes and the creation of crustal plateaus by crustal thickening. Such a scenario requires a very shallow brittle-ductile transition and an exceptionally plastic crust near the surface.

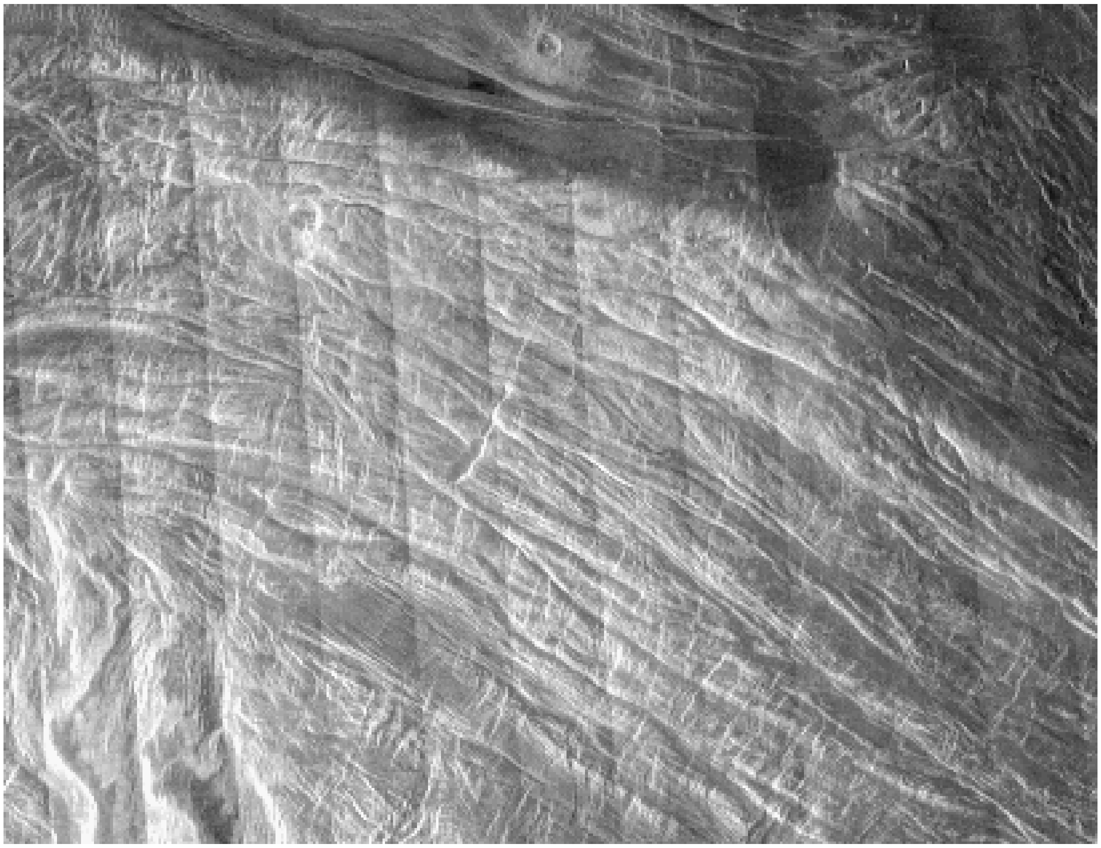

Figure 1.2 'Ribbon terrain' in the tessera of the crustal plateau Ovda Regio. This image is 180 x 140 km, and is at latitude 5^{o} N, longitude 98^{o}.

Phillips and Hansen [1997] concluded that the most likely mechanism for the production of these tectonic features was an epoch of elevated surface temperatures during their formation.

The study of climate interactions on Venus is more than an academic exercise. All natural philosophy has the potential to sharpen or illuminate our perspective as a sentient race existing in the cosmos. It is furthermore imperative for the continued existence of planetary science that this aspect of solar system exploration be deeply appreciated by our culture. In the field of climate study, this perspective is particularly poignant. We are engaged in a massive, uncontrolled experiment of the Earth's climate on a truly global scale due to the growing effluent from our technologies. While some are dogmatic with regard to how technological society may deal with the results, I believe this a techno-centric response that betrays a Ptolemaic perspective. The study of the alien climate of Venus is particularly capable of illuminating this issue. Discerning the factors that affect the stability of climate on Venus charts new territory in the study of climate and with it, new perspectives on how climate on terrestrial planets works.

In addition to assessing the prospects for anthropogenic climate change on Earth, there are other scientific issues that the study of terrestrial planetary climates address. It is becoming increasingly clear that the Earth's climate behaves as a complex dynamical system, with interactions between the oceans, crust, mantle and atmosphere driving its evolution, as well as astronomical perturbations to its orbit. The study of complex dynamical systems has led to an appreciation of their general properties, and in particular, the way they exhibit regular, quasi-periodic, and chaotic behaviors. Climate change on the Earth is written in the biota, the geologic strata, and the atmosphere. Sedimentary deposits as old as 3.8 billion years have been found in Isua, Greenland, implying conditions conducive to liquid water at that time [*Schidlowski*, 1988]. An examination of the history of Earth's surface temperature, as synthesized from a variety of these records (Figure 1.3) reveals its complexity. Climate change on the Earth occurs over a broad range of timescales. Although certain features of the record are understood, such as climate change due to Melankovich cycles, large impacts, and the carbon geochemical cycle, the global dynamical properties of climate evolution on the Earth are not.

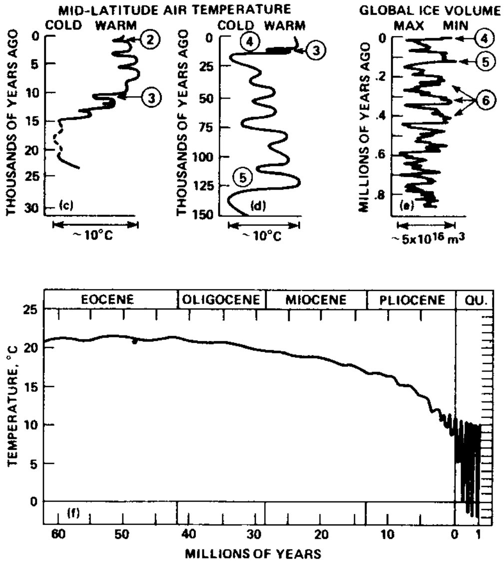

Figure 1.3 The history of surface temperatures on the Earth in the last 60 million years, from *Pollack* [1979]

An important lesson from the study of complex systems is that they may exhibit deterministic, regular patterns for a while, and suddenly bifurcate to entirely different regimes. Large changes in some parameters may leave the system relatively unchanged, due to negative feedbacks, but an infinitesimal change somewhere else can lead to widely divergent behavior. How and when can such changes in a terrestrial planet's climate occur?

Still looking at Figure 1.3, a broader question to ask is, what features of this record have been conducive to the origin and sustainment of life? Stability over some timescales, certainly, but diurnal, annual and geological variations are integrated into the network of the Earth's biosphere. Variations in temperature cause material fluxes, cyclic transport, mixing, and new opportunities for evolution. Does it take some providential mixture of cycles to resonate with life's processes, or will anything do? While no answers to these questions are forthcoming from the investigations discussed here, the study of life's early history is to some extent a study of Earth's early climate. A quest for general principles of climate variation and stability on terrestrial planets has important implications for understanding conditions that may or may not be conducive to life.

The purpose of this Ph.D. thesis is to investigate the recent evolution and stability of climate on Venus. This is achieved by quantifying the relationships between atmospheric species in the atmosphere, cloud structure, and the radiative balance of energy in the atmosphere. I have developed numerical models of the Venus greenhouse effect and cloud structure that employ the best available spacecraft and ground-based data, spectral databases and laboratory measurements. Climate on the terrestrial planets is driven by solar energy and by the evolution of atmospheric gases under the influence of global sources and sinks. Recent spacecraft and laboratory-derived data have now made it possible to model the magnitude and temporal behavior of geological sources of volatiles, possible heterogeneous reactions between the surface and atmosphere, and exospheric escape processes. I have developed numerical models for these as well, which serve as time-dependent drivers for the combined radiative transfer-cloud atmospheric model. Specifically, the theoretical work I will present has been designed to provide answers to the following questions:

1. How do variations in atmospheric water and sulfur dioxide affect cloud structure and planetary albedo? How do these, in turn, affect the temperature at the surface?

2. How does the equilibration of atmospheric sulfur dioxide with surface minerals affect cloud structure and surface temperature, and over what timescales?

3. How have changes in atmospheric water abundance due to exospheric escape of hydrogen and volcanic outgassing affected cloud structure and surface temperature, and over what timescales?

4. What was the effect on Venus' cloud structure and surface temperature of an epoch of rapid plains emplacement and consequent widespread, global volcanism?

5. What is the stability of Venus' climate (as described by its surface temperature and pressure) with respect to the equilibration of carbon dioxide with surface minerals? Over what timescales can the climate of Venus change due to this process?

Studies of Venus Climate and Evolution

Venus has been intensively studied by spacecraft in the past, receiving 24 robotic explorers from the planet Earth since the beginning of human space exploration. It was the first destination for an interplanetary craft (Mariner 2), in 1962. Soviet landers survived long enough to return fantastic pictures of its surface, but a truly comprehensive picture of the planet was not available until 1992, when the Magellan spacecraft mapped nearly its entire surface with radar to a resolution of 200 meters. A detailed description of the Venus atmosphere became available to us in the late 1970's with the return of diverse datasets transmitted to the Earth by the Pioneer Venus spacecraft. It deployed four atmospheric descent probes, providing *in situ* measurements of cloud and atmospheric characteristics which form the basis for Venus atmospheric models today.

Venus absorbs less sunlight than does the Earth, yet its surface temperature is about 735 K, due to a strong greenhouse effect [*Pollack et al.*, 1980; *Sagan*, 1960; *Wildt*, 1940]. The first indications that Venus' atmosphere had evolved to a temperature much higher than ours was from Earth-based radio observations [*Mayer et al.*, 1958]. Further confirmation of high atmospheric temperatures was provided by centimeter wavelength measurements from the Mariner 2 spacecraft [*Barath et al.*, 1963]. Using existing laboratory data, *Sagan* [1960], showed that water vapor and CO_2 absorbed in complementary parts of the thermal infrared, and together could produce a greenhouse effect sufficient to explain the high surface temperature. The first nongray greenhouse model of Venus' atmosphere was developed by *Pollack* [1969a; 1969b], in which CO_2, H_2O, and N_2 were responsible for the infrared opacity. This 1-D radiative convective model incorporated an adiabatic temperature profile in a layer beneath optically thick water clouds. Although some pressure induced bands of CO_2 were considered, the radiative properties of CO_2 at high temperatures and pressures were poorly constrained by the available data. Pollack concluded that an H_2O mixing ratio of 0.5% was needed to explain the observed temperature distribution in Venus' atmosphere. Although the model was consistent with the available spacecraft data (from the Venera 4 mission) on H_2O abundances [*Nature*, 1967], later H_2O measurements from the Venera 11 and 12 spacecraft in 1977 and from Pioneer Venus in 1980 indicated a far lower abundance of about 100 ppm [*Moroz et al.*, 1978; *Oyama et al.*, 1979; *Oyama et al.*, 1980]. *Pollack et al.* [1980] published an improved radiative transfer model, utilizing updated solar flux, gaseous composition, temperature and cloud structure measurements from Pioneer Venus. SO_2, CO, and HCl were added as sources of infrared opacity, as well as several pressure induced transitions of CO_2. They were able to reproduce the observed surface temperature and lapse rate structure of Venus' atmosphere very closely with a greenhouse model that contained water vapor abundances consistent with measurements from the Pioneer gas chromatograph and Venera spectrophotometer.

Venus’ thick cloud cover is composed mostly of sulfuric acid, in an 85% solution with water. It may be the remnant of large scale, sulfurous outgassing associated with vigorous volcanism. Using radar to peer through the clouds, the Magellan spacecraft vividly depicted for us a planet that has known volcanism in massive proportion. 80% of the planet is volcanic plains, with enormous, younger volcanic shields towering over them. Before Magellan, we could only speculate on Venus’ volcanic history. During Magellan, we were assailed by the impressions of a violent tectonic history and impressive displays of volcanic features. After Magellan, and as a result of stratigraphic analysis and crater age dating, we can attempt to reconstruct Venus’ volcanic history. The degree to which volcanism can affect climate is dependent on its strength, duration and the composition of erupted lavas. Volcanism represents the dominant source in both the terrestrial and martian CO_2 cycles, and it may be inferred that during periods of large scale volcanism, CO_2, SO_2, H_2O, and other radiatively important volatiles were injected into Venus' atmosphere. UV spectroscopic measurements [*Esposito*, 1984] showed approximately an order of magnitude decrease in cloud-top SO_2 abundances from 1978 to 1983. It was suggested then that this temporal variability could have been the result of major volcanic activity prior to the Pioneer Venus mission.

The stunning difference between the evolution of the climates of Earth and Venus led naturally to theoretical studies of their early atmospheres. Much of the theoretical work on the early climate evolution of Venus focused on the fate of its water. The atmosphere of Venus currently has about 100,000 times less water than the oceans and atmosphere of Earth. The ratio of D/H in the water within Venus cloud particles was measured *in situ* by the Pioneer Venus neutral mass spectrometer, and was found to be an astonishing 120 times the D/H of terrestrial water [*Donahue et al.*, 1982]. Massive fractionating loss by exospheric escape from a large primordial reservoir is a likely mechanism for the D/H signature seen in the Venus atmosphere today [*Donahue and Hodges*, 1992; *Kasting*, 1988; *Pepin*, 1991; *Zahnle and Kasting*, 1986].

Ingersoll [1969] first showed that for planetary atmospheres with a condensable infrared absorber in them, equilibrium between phases is impossible when the solar flux exceeds a critical value. Below this value, the condensable component may be in equilibrium with a large surface reservoir, like an ocean. Such an atmosphere can radiate only so much energy to space. If the solar flux exceeds the critical value, the heat that cannot be radiated away rapidly evaporates the condensed phase and puts it into the atmosphere. The expression Ingersoll coined was 'the runaway greenhouse effect' to describe the positive feedback between the thermodynamics of the volatile species and radiative-convective equilibrium. He used a grey Eddington model and arguments based on an analytic analysis of the thermodynamics of water and radiative-convective equilibrium. For water, at least (with its spectrally broad infrared absorption), he found that the effect was robust with respect to the details of the absorber's spectrum and the relative humidity of the atmosphere.

Conditions on the Earth are evidently subcritical with respect to water (and have been for most of its history), but present conditions on Venus lead us to suspect that a runaway greenhouse took place there at one time. *Ingersoll* [1969] demonstrated that atmospheric water during a runaway greenhouse on Venus would have resided in a tenuous stratosphere, where solar UV photons could readily dissociate it. The boiling and loss of an ocean's worth of water via rapid H escape becomes a likely scenario.

Kasting et al. [1984] developed a non-grey one-dimensional radiative-convective model to compute temperature and water vapor profiles as functions of solar flux for an Earth-like atmosphere. Neglecting cloudiness, they estimated that the critical solar flux required to initiate a runaway greenhouse of the type envisioned by Ingersoll was about 1.45 the present flux at Earth. This corresponds to the solar flux at the orbit of Venus 4 billion years ago, allowing for a 30% fainter sun at that time [*Sagan and Mullen*, 1972]. However, *Kasting et al.* [1984] also considered the possibility of a slightly subcritical Venus, with hot oceans and wet stratosphere. With a very moist troposphere resulting in no cold trapping at the tropopause, stratospheric water would have been susceptible to photodissociation by the early intense solar ultraviolet flux. Hydrodynamic escape of H was rapid enough in this case to eliminate an ocean's worth of water in 600 million years. This situation was termed the 'moist greenhouse', and has the added advantage of explaining how the D/H ratio in the atmosphere can be only 150 times terrestrial in the face of the loss of a great deal of water. Nonthermal, fractionating escape would only begin when surface water was eliminated entirely, which would have occurred when there was about 0.4 bars of it left in the atmosphere. The persistence of a hot ocean would have kept atmospheric levels of CO_2 low by dissolving it and promoting carbonate formation at the surface. Levels of CO_2 substantially below present values would have aided in the transport of H upward, providing a pathway for escape. In this scenario, CO_2 accumulates in the atmosphere through volcanic activity uncompensated by subduction and recycling of carbon rich crust.

Recent scientific developments have made it possible to refine theoretical models of the Venus climate and its recent evolution. Most importantly, the Magellan mission has given us a detailed picture of the surface geology, providing important constraints on the magnitude and timing of volatile outgassing [*Bullock et al.*, 1993; *Namiki*, 1994; *Saunders et al.*, 1992]. Laboratory experiments on the thermodynamics and kinetics of heterogeneous reactions under Venus-like conditions have yielded important insights into the role that surface/atmosphere reactions may play on a global scale [*Fegley et al.*, 1995; *Fegley and Treiman*, 1992]. Ground-based observations of the night side of Venus in near-infrared windows has allowed for the retrieval of trace species in the deep atmosphere [*Bezard et al.*, 1990; *de Bergh et al.*, 1995; *Meadows and Crisp*, 1996; *Pollack et al.*, 1993]. The Galileo spacecraft, during a swing-by of Venus on its way to Jupiter, improved our understanding of cloud characteristics and variability with high spatial resolution images of the disk in the infrared [*Carlson et al.*, 1993; *Grinspoon et al.*, 1993]. Finally, improvements in spectral databases, particularly for high temperature water and carbon dioxide have become available and permit more accurate modeling of infrared radiative transfer in the atmosphere of Venus [*Rothman et al.*, 1992; *Rothman et al.*, 1997]. This dissertation provides the first synthesis of these results into a detailed model of climate interactions on Venus.

Thesis Summary

This chapter, **Chapter 1**, (Introduction) provides the background for studying climate on Venus and the scientific motives for pursuing it. I discuss, qualitatively, the physical processes that are responsible for climate interactions. My approach to modeling the various elements of Venus' climate is briefly discussed. I summarize the scientific goals of this work as providing answers to five key questions on the evolution and stability of climate on Venus.

In **Chapter 2** (Radiative Transfer in the Atmosphere of Venus) I develop and present the results from a detailed, state-of-the-art model of infrared radiative transfer in the Venus atmosphere. Beginning with a description of the applied spectral databases, I explain how infrared opacities are calculated and how they are applied in determining infrared fluxes in the Venus atmosphere. My approach to calculating radiative-convective equilibrium is described, and the results from modeling the current Venus atmosphere are discussed. Comparisons are made with results from earlier published models in order to validate the approach and to show the advantages of the theoretical methods I have employed. The ultimate purpose of the atmospheric radiative transfer model is to include it as a flexible element in a description of Venus' climate evolution. The behavior of the atmospheric radiative transfer model is explored with respect to changes in the abundances of important gases in the atmosphere.

Chapter 3 (Atmospheric Chemistry and Clouds) describes the development of a simple chemical/microphysical model of the clouds of Venus. Results from modeling the present clouds of Venus are given, and then the effects of varying atmospheric abundances of SO_2 and H_2O are discussed. The cloud model is then incorporated into the infrared radiative transfer model of Chapter 2. The combined greenhouse/albedo effects of varying SO_2 and H_2O are of interest in understanding a fundamental aspect of climate stability. The physics of this interesting interaction are discussed, and relevant results from this coupled model are presented. In particular, I show how cloud optical depths, planetary albedo, and surface temperature are related to the abundance of atmospheric H_2O and SO_2.

Current theories and state of knowledge of the evolution of Venus' crust are described in **Chapter 4** (Geological Sources of Volatiles). The geological surface record of impact cratering and landform morphologies from Magellan SAR images is used to constrain a 3-D Monte Carlo model of impact cratering and volcanism in the recent past. Several plausible volcanic histories are derived which are consistent with the surface record. Estimates of volatile contents of erupting lavas on Venus are then used to deduce possible volatile outgassing histories. The outgassing models are provided as time-dependent inputs to the combined cloud-radiative transfer model.

Possible geochemical sources and sinks of volatile species in Venus' atmosphere are discussed in **Chapter 5** (Geochemical Processes on Venus). Laboratory data on the chemical equilibrium and kinetics of gas-mineral assemblages under Venus conditions are employed to calculate global fluxes of CO_2, SO_2 and COS into and out of the surface. To do this, I describe a reaction-diffusion formalism that can be used to scale laboratory experiments of this sort to problems of planetary climate evolution. These models of surface-atmosphere interactions are incorporated in a time-iterative fashion into the cloud-radiative transfer model. Similar to the volatile source functions provided for volatile outgassing, surface-atmosphere interactions alter atmospheric abundances and hence the radiative-convective state of the atmosphere. However, since equilibrium abundances for the gas-mineral reactions are themselves temperature and concentration dependent, evolution of climate under the influence of surface reservoirs is highly coupled to atmospheric radiative-convective equilibrium. I also discuss how a simple diffusion-limited model of H and D escape can also be applied to the climate evolution model to simulate the cloud and radiative effects of a continual loss of water.

The separate models described in Chapters 2-5 are integrated into a single Venus climate model that describes the evolution of the atmosphere over time, in **Chapter 6** (The Venus Climate Evolution Model). Abundances of radiatively active species are varied under the influence of volcanic outgassing, surface-atmosphere reactions, and exospheric escape. Cloud structure and optical properties evolve with these changing abundances, as does the radiative-convective state of the atmosphere. I describe the Venus climate evolution model in detail, and the approach taken in integrating the above models of the various planetary processes. Results for eight evolutionary scenarios designed to address the five climate evolution questions in Chapter 1 are presented in this chapter.

Chapter 7 (Summary and Conclusions) summarizes the results from the entire thesis and discusses the implications of the results from the Venus climate model. The sensitivity of the clouds to changes in atmospheric abundances from a variety of processes are first presented. The climatic implications of a steady loss of atmospheric water to exospheric escape of H are considered. I then discuss the climatic effects of a global geological resurfacing event in the past such as rapid plains emplacement. The role that surface/atmosphere interactions may have had on Venus' climate evolution and the current climate stability are discussed next. Finally, primary feedbacks in the climate system are identified, and along with them, timescales for climate change on Venus.

A final note to the reader: The essential chapters of this thesis are this one and Chapters 6 and 7. Chapters 2-5 are highly detailed descriptions of the individual models that make up the Venus climate evolution model. The important scientific results from this work are contained entirely in the final two chapters.

CHAPTER 2

RADIATIVE TRANSFER IN THE ATMOSPHERE OF VENUS

Atmospheric Structure and Composition

Temperatures at the surface of Venus range from 630 K at the mountain tops, to 750 K in the deepest lowlands. Rocks at the surface, in some places, are hot enough that the ground would glow visibly to a human observer at night. The atmosphere is mostly CO_2 (96.5%) with 3.5% N_2 and trace amounts of H_2O vapor and various sulfur gases. Atmospheric abundances of the 11 most abundant molecular species found in Venus' atmosphere are shown in Table 2.1.

Table 2.1 Major Constituents of the Atmosphere of Venus

Atmospheric Species	Molar Mixing Ratio
CO_2	0.965
N_2	0.035
SO_2	180 ppm
Ar	70 ppm
OCS	50 ppm
CO	40 ppm
H_2O	30 ppm
Ne	5 ppm
HDO	3 ppm
HCl	0.5 ppm
HF	2.5 ppb

After CO_2 and N_2, SO_2 is the next most abundant gas in Venus' atmosphere. All three of these species, as well as O_2, Ar, CO and H_2O were measured *in situ* by the Pioneer Venus gas chromatography experiment [*Oyama et al.*, 1980]. With a molar mixing ratio of 180 parts per million near the surface, the majority of atmospheric sulfur is in the form of SO_2. It is consumed in the production of the clouds, with cloud top SO_2 abundances near 20 parts per billion [*Esposito*, 1984]. Abundances in the lower atmosphere are corroborated by Earth based observations [*Bezard et al.*, 1993; *Meadows and Crisp*, 1996; *Pollack et al.*, 1993] and data from the Soviet VEGA 1 and VEGA 2 entry probes [*Bertaux et al.*, 1996].

The next most important sulfur gas in Venus' atmosphere is COS which is about 1/3 as abundant as SO_2. A more reduced sulfur species, H_2S, exists in the ppm range in roughly constant mixing ratio in Venus' atmosphere. Retrievals of minor constituent abundances from Earth-based near-IR spectroscopy have been instrumental in discovering the make-up of the deep atmosphere of Venus, especially COS, CO, H_2O, HDO, HCl and HF [*Bezard et al.*, 1990; *Crisp et al.*, 1991; *de Bergh et al.*, 1995; *Meadows and Crisp*, 1996; *Pollack et al.*, 1993]. CO, a product of dissociation of the massive CO_2 atmosphere, varies in abundance from 10 to 40 ppm. H_2O abundances are typically about 30 ppm near the surface, decreasing within the clouds as it is consumed and the hydrogen is transferred to H_2SO_4. H_2O abundances above the clouds are about 1 ppm. Deuterated H_2O, HDO, is far more abundant on Venus than on Earth, a fact that figures prominently in theories of the evolution of Venus' atmosphere. Preferential escape of atomic hydrogen over deuterium from an early large terrestrial-like reservoir is one possibility, but others have been suggested [*Donahue and Hodges*, 1992; *Kasting*, 1988]. The D/H may be in steady-state with a cometary influx, a reasonable possibility given the small amount of water presently in the Venus atmosphere [*Grinspoon*, 1993; *Grinspoon and Lewis*, 1988]. The D/H ratio in Venus' atmosphere is approximately 0.018, or about 150 times that found in H_2O on the Earth [*de Bergh et al.*, 1991]. The halogen gases HCl and HF exist in small quantities (500 ppb and 2.5 ppb respectively), but are important both chemically and radiatively for the state of Venus' atmosphere. The noble gases He, Ar, Kr and Xe are also all present, and their isotopic abundance ratios provide important clues to the origin of volatiles and competing processes of influx and escape over the history of Venus' atmosphere [*Zahnle*, 1993]. The mixing ratios of the nine most important radiatively active gases as a function of altitude in Venus' atmosphere are shown in Figure 2.1.

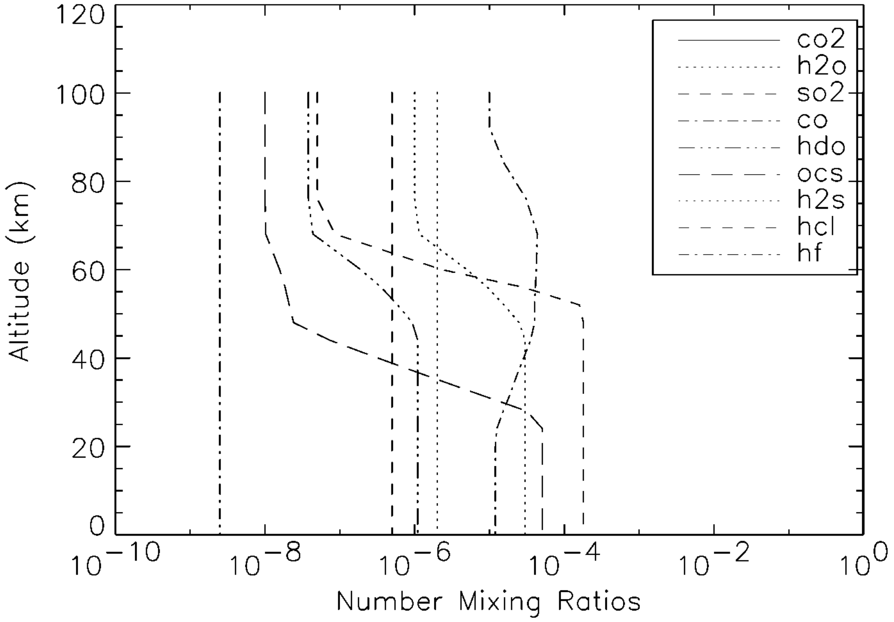

Figure 2.1 Gaseous molar mixing ratios in Venus' atmosphere. CO_2 and N2 mixing ratios are constant at 0.965 and 0.0365, respectively. Only radiatively important gases are shown (N_2 is omitted). These molar mixing ratios form an input dataset to the nominal case Venus radiative transfer model.

The atmospheric pressure at the surface is so great that many thermodynamic and optical properties of the atmosphere are better termed oceanic than atmospheric. Venus' atmosphere is one hundred times as massive as the Earth's, and one tenth as massive as the Earth's oceans. The surface temperature and pressure exceed the critical point for CO_2 (304 K, 73 bars), so that the lower scale height or so of the atmosphere is a supercritical fluid. Clouds of sulfuric acid droplets inhabit the entire atmospheric region from approximately 48 km above the surface to 70 km, forming a vast liquid reservoir of sulfur and hydrogen [*Esposito et al.*, 1983]. For the most part, they appear to globally encircle the planet. Being about the same size as the Earth and with an average distance of 0.72 AU from the Sun, Venus receives about twice as much solar energy as the Earth. However, due to the brilliant global cloud layer, the planetary albedo is about 0.78, compared with the Earth's 0.32. More than twice as much solar energy is reflected back into space by Venus. Solar energy is received over an area of πr^2, where r is the radius of the planet, and infrared energy is radiated to space over an area of $4\pi r^2$. If A is the albedo, F_S the solar flux at 1 AU, and R the distance from the sun to Venus, in AU, then the energy balance of the planet may be described by

$$\frac{\pi r^2}{R^2} F_S(1 - A) = 4\pi r^2 \sigma T_e^4 \tag{2.1}$$

where T_e is the temperature at which a blackbody would radiate to maintain thermodynamic equilibrium with the input of solar energy, and σ is the Stefan-Boltzmann constant. Simplifying and rearranging

$$T_e = \left[\frac{F_s(1 - A)}{\sigma R^2} \right]^{\frac{1}{4}} \tag{2.2}$$

The effective temperature, T_e, for Venus is 232 K, lower by 23 K than the 255 K effective radiating temperature of the Earth. That is, there is less total energy driving the climate on Venus than on the Earth. The reason for Venus' high surface temperatures is an efficient greenhouse effect, sustained by a remarkable property of its atmosphere: the major constituents are gases that are highly absorbing in the infrared [*Pollack et al.*, 1980; *Sagan*, 1960; *Wildt*, 1940]. Not only is CO_2 an efficient absorber, but it is aided by pressure-broadening of its major bands and by complementary spectral absorption by H_2O and sulfur gases such as SO_2.

Atmospheric temperature and pressure profiles from 4 probes dropped by the Pioneer Venus spacecraft into Venus' atmosphere in 1978 are shown in Figures 2.2 and 2.3.

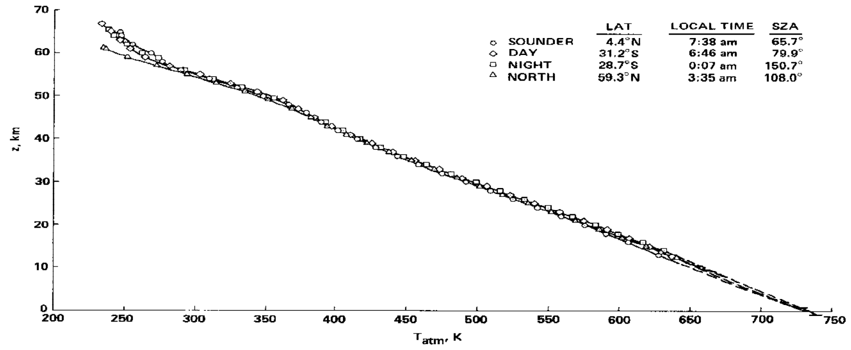

Figure 2.2

Atmospheric temperature measurements from the four Pioneer Venus atmospheric entry probes [*Seiff*, 1983]. SZA is solar zenith angle.

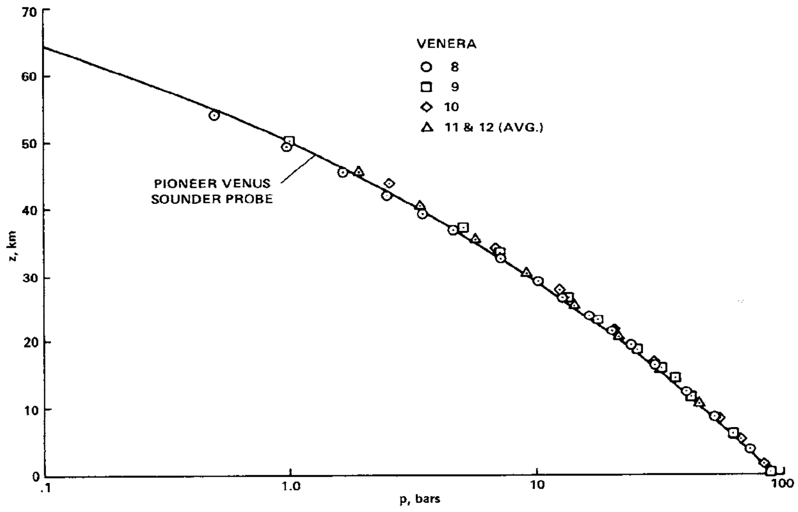

Figure 2.3 Pressure in the Venus atmosphere from Veneras 8-12 and the Pioneer Venus sounder probe [*Seiff*, 1983].

The temperature is roughly adiabatic from the surface to just beneath the clouds. Solar energy is absorbed mostly in the clouds, where longer path lengths due to scattering increase the efficiency of solar absorption. The lower cloud base is at about

1 bar and upper cloud tops are at about 40 mb. Only about 8% of the sunlight that is not reflected from the cloudtops makes its way to the surface, providing a significantly different radiative forcing for the greenhouse effect than on the Earth or Mars. The energy balance in Venus' atmosphere is therefore controlled by CO_2 as well as minor species and by the high albedo and visible wavelength absorption of its clouds.

Modeling Approach

The goal of the Venus atmospheric radiative transfer model is to accurately describe the transport and balance of energy within the atmosphere. Ultimately, the model should predict thermal infrared fluxes, temperature structure, heating rates and stability structure consistent with spacecraft and ground-based observations. In addition, the model must be flexible and fast enough to predict these quantities with respect to changes in solar flux and atmospheric composition as they may change over time. To this end, I have chosen to develop a one dimensional, two-stream model of infrared radiative transfer that employs correlated-k gaseous absorption coefficients to describe the spectral properties of the gases [*Lacis and Oinas*, 1991]. The HITRAN 1996 and HITEMP databases provided high-resolution spectral data for nine molecular species found in Venus' atmosphere: CO_2, H_2O, SO_2, CO, OCS, HDO, H_2S, HCl and HF [*Rothman et al.*, 1992; *Rothman et al.*, 1997]. Atmospheric abundances for most of these species were taken from the Venus International Reference Atmosphere (VIRA) [*Kliore et al.*, 1986], with H_2O abundances updated by more recent retrievals from Earth-based near-infrared spectroscopy [*Crisp et al.*, 1991; *de Bergh et al.*, 1995; *Meadows and Crisp*, 1996; *Pollack et al.*, 1993]. Correlated-k absorption coefficients for 68 spectral intervals in the infrared were interpolated in pressure and temperature from tabulated line-by-line calculations of the HITRAN 1996 and HITEMP databases. These cumulative absorption probabilities were convolved with atmospheric mixing ratios to calculate the gaseous absorption of the Venus atmosphere. Continuum opacity due to CO_2 pressure-induced transitions [*Moskalenko et al.*, 1979] and H_2O continuum [*Liou*, 1992] were also included, as was Rayleigh scattering by CO_2 and N_2 [*van de Hulst*, 1981]. Cloud aerosol size modes and number densities were derived from analysis of the Pioneer Venus nephelometer data [*Knollenberg and Hunten*, 1980]. Optical data for H_2SO_4/ H_2O aerosols [*Palmer and Williams*, 1975] were used in Mie calculations to determine aerosol extinction optical depths, single-scattering albedos and scattering asymmetry factors due to cloud particles [*Hansen and Travis*, 1974].

For the purpose of modeling the present Venus atmosphere, solar net fluxes from the Pioneer Venus flux radiometer were used as a constraint [*Tomasko et al.*, 1980]. Infrared flux calculations used the hemispheric mean approximation, appropriate to an emitting, highly absorbing and scattering atmosphere [*Toon et al.*, 1989]. Use of the correlated-k method involves mapping the wavenumber dependence of absorption coefficients to a smooth probability function for the absorption coefficients. Integration of the flux equations within each spectral interval, over this probability space was achieved using an 8-point Gaussian integration [*Abramowitz and Stegun*, 1965; *Arfken*, 1985]. To calculate radiative equilibrium, net infrared fluxes were determined which balanced the observed solar net flux profile, using an iterative variational method [*McKay et al.*, 1989; *Pollack et al.*, 1980]. Most calculations were done with 20 atmospheric layers, with initial values from VIRA [*Kliore et al.*, 1986]. Convection was treated by taking the radiative equilibrium temperature profile and adjusting the lapse rate to be adiabatic wherever the radiative equilibrium lapse rate exceeded the adiabat [*McKay et al.*, 1989].

Results from the model calculations were compared with the Venus International Reference Atmosphere [*Kliore et al.*, 1986]. Also found therein were general physical data for Venus and thermodynamic data for the Venus atmosphere.

Comparisons were also made with the behavior of several numerical models of Venus' atmosphere published previously [*Pollack et al.*, 1980].

All quantities in the model are expressed using the following subscript nomenclature

$$\tau_{i,j,k,l} \begin{cases} i = 0 \rightarrow N-1 & \text{Atmospheric Layer} \\ j = 0 \rightarrow M-1 & \text{Wavenumber Interval} \\ k = 0 \rightarrow Q-1 & \text{Molecular Species} \\ l = 0 \rightarrow ngauss-1 & \text{Gaussian subinterval} \end{cases} \tag{2.3}$$

The atmosphere is divided into N layers, bounded by $N+1$ levels and shown in Figure 2.4. Layer i is bounded by levels i and $i+1$, with the top layer designated as $i = 0$. Level $N+1$ is the ground, so that the bottom-most layer is layer N. Pressures and temperatures at level i are designated P_i and T_i, respectively. Atmospheric molecular mixing ratios for each level and each molecule are designated X_{ik}, so that level number densities, using the ideal gas law, are

$$n_{ik} = \frac{X_{ik} P_i}{k_B T_i} \tag{2.4}$$

where k_B is the Boltzmann constant. Level altitudes are calculated from the equation for hydrostatic equilibrium

$$dP = -g\rho dz \tag{2.5}$$

where g is gravitational acceleration and the density ρ is

$$\rho_i = \frac{n_i W_i}{N_A} \tag{2.6}$$

where n_i is the total number density and W_i the mean molecular weight of the atmosphere at level i. N_A is Avagadro's number.

z(0) ======================================= P(0), T(0), {X_j(0)}

--- * -------------- Pl(0), Tl(0), {Xl_j(0)}, ul(0), zl(0), gl(0)

z(1) ======================================= P(1), T(1), {X_j(1)}

--- * -------------- Pl(1), Tl(1), {Xl_j(1)}, ul(1), zl(1), gl(1)

z(i-1) ======================================= P(i-1), T(i-1), {X_j(i-1)}

--- * -------------- Pl(i-1), Tl(i-1), {Xl_j(i-1)}, ul(i-1), zl(i-1), gl(i-1)

z(i) ======================================= P(i), T(i), {X_j(i)}

--- * -------------- Pl(i), Tl(i), {Xl_j(i)}, ul(i), zl(i), gl(i)

z(i+1) ======================================= P(i+1), T(i+1), {X_j(i+1)}

--- * -------------- Pl(i+1), Tl(i+1), {Xl_j(i+1)}, ul(i+1), zl(i+1), gl(i+1)

z(N) ======================================= P(N), T(N), {Xj(N)}
//

Figure 2.4 Venus radiative transfer model atmospheric grid and variables. There are N layers bounded by $N+1$ levels. Pressure, temperature and mixing ratios P_i, T_i, X_{ij} are defined at the levels, and interpolated for layer-averaged quantities Pl_i, Tl_i, Xl_{ij}. Level altitudes z_i are calculated from hydrostatic equilibrium. Path lengths ul_i, layer averaged gravities gl_i, mixing ratios Xl_{ij} and altitudes zl_i are then calculated.

Pressure and altitude are then related by

$$\frac{dP}{P} = \frac{gW}{N_A k_B T} dz \tag{2.7}$$

and the altitudes are calculated from

$$z_i = z_{i+1} + \frac{1}{N_A k_B} \int_{P_i}^{P_{i+1}} \frac{gW}{T}\frac{dP}{P} \tag{2.8}$$

Specific heats at constant pressure, c_{pi}, for each level are calculated from empirical formulas for CO_2 [*Anderson*, 1989].

Layer temperatures Tl_i are calculated from a Planck-weighted mean

$$Tl_i = \left(\frac{T_i^4 + T_{i+1}^4}{2} \right)^{\frac{1}{4}} \tag{2.9}$$

The total amount of gas in a layer column, or the path length for the layer is defined as

$$ul_i = \int_{z_{i+1}}^{z_i} \rho dz = \frac{1}{N_A} \int_{z_{i+1}}^{z_i} nW dz \tag{2.10}$$

Layer pressures Pl_i are calculated so that equal amounts of gas exist in the layer above and below. Using the equation for hydrostatic equilibrium again the pressure difference across the layer is

$$\Delta P_i = -\frac{1}{N_A} \int_{z_i}^{z_{i+1}} gnW dz = gl_i ul_i \tag{2.11}$$

where gl_i are the layer-averaged gravities. Since the path length scales as $\Delta P/g$, the layer pressures are defined as

$$Pl_i = \frac{P_{i+1} - P_i}{2} \tag{2.12}$$

Each atmospheric layer has the following calculated properties

$$\tau_{ijl} = \tau_{ijl}^{gas} + \tau_{ij}^{con} + \tau_{ij}^{ray} + \tau_{ij}^{aer} \tag{2.13}$$

Where τ_{ijl} is the total optical depth in atmospheric layer *i*, wavenumber interval *j*, and Gaussian subinterval *l*. τ_{ijl}^{gas} is the optical depth due to the gaseous absorption of the mixture of gases in layer *i*, and t_{ij}^{con} is the optical depth due to continuum sources of opacity. In this model, opacity due to CO_2 pressure-induced transitions and H_2O continuum are included. τ_{ij}^{ray} is the opacity due to Rayleigh scattering by CO_2 and N_2. Aerosol extinction opacities due to H_2SO_4/ H_2O cloud particles is τ_{ij}^{aer}. In addition, single scattering albedos, ω_{0ij}, and scattering asymmetry factors, g_{ij} are also calculated for each layer and wavenumber interval.

Net solar flux at each level, integrated over the visible wavenumbers, are denoted as Fs_i. Lower and upper ends of the infrared wavenumber intervals are designated ν_{0i}, ν_{1i}, respectively. The Planck function

$$B_{ij} = \int_{\nu_{0_i}}^{\nu_{1_i}} \frac{2h\nu^3c^2}{e^{\frac{hc\nu}{k_B T_i}} - 1} d\nu \tag{2.14}$$

where h is Planck's constant, and c is the speed of light, is integrated for the level temperatures T_i over each wavenumber interval ν_{1i} - ν_{0i} to obtain the emission for each layer and wavenumber interval, B_{ij}. Upward and downward fluxes are F_up_{ijl} and F_dn_{ijl}, for each layer i, wavenumber interval j and Gaussian subinterval l.

Sources of Opacity

Vibrational-Rotational Energy Transitions in Gases

Spectral Databases

Monochromatic absorption coefficients for many atmospheric molecules over a wide range of temperatures may be derived from data tabulated in the HITRAN 1996 [*Rothman et al.*, 1992] and HITEMP [*Rothman et al.*, 1997] spectral databases. HITRAN 1996 is a compilation of high-resolution laboratory spectra for 37 major atmospheric species found in the Earth's atmosphere, supplemented by theoretical calculations. It provides line positions, strength, half-widths, and lower state energies for approximately 1 million spectral lines from millimeter wavelengths through the ultraviolet. Similar high-resolution data is available for H_2O, HDO, CO_2 and CO for temperatures up to 1000 K on the HITEMP database. Spectral parameters for these four molecules were taken from HITEMP for use in the Venus atmospheric radiative transfer model. Included in HITEMP is data on numerous CO_2 and H_2O hot bands, spectral lines due to transitions between excited states, that have not been previously available. Significant improvements in the data for CO_2 bands in the 2.3 and 1.7 μm regions, and the inclusion of hot bands associated with the 2.2 μm CO_2 transition are of prime importance for modeling the atmosphere of Venus [*Giver and Chackerian*, 1991; *Wattson and Rothman*, 1992]. The high temperature database for H_2O includes high-rotational quantum number lines, those originating from hot bands, and those from weak ground state transitions, providing a major improvement in H_2O opacity data. Data for SO_2, OCS, H_2S, HCl and HF came from HITRAN 1996. Spectral data for all these species have either been included where they were not previously available, or improved upon significantly. Table 2.2 summarizes the attributes of the spectral data used for the Venus atmospheric radiative transfer model.

Table 2.2 Spectral Data Used in the Venus Radiative Transfer Model

Molecule	Database	Number of Lines
CO_2	HITEMP	7200000
H_2O	HITEMP	1283468
SO_2	HITRAN 1996	38853
CO	HITEMP	4477
HDO	HITEMP	49444
OCS	HITRAN 1996	858
H_2S	HITRAN 1996	7151
HCl	HITRAN 1996	533
HF	HITRAN 1996	107

Monochromatic absorption coefficients for each molecule were obtained with line-by-line calculations of the HITRAN and HITEMP spectral data for all combinations of 9 pressures and 8 temperatures. Calculations on this coarse grid, P_I, T_I, were done by Richard Freedman under the direction of the late Jim Pollack at the NASA Ames Research Center, and incorporated full pressure and temperature dependence of absorption line shapes. Line wing contributions from adjacent absorption bands were also included, with calculations being truncated at 120 cm^{-1} from line centers. The coarse grid was chosen to cover a pressure and temperature parameter space appropriate to a Venus climate evolution model. Monochromatic absorption coefficients for all 9 molecules were obtained for pressures of 0.1, 0.3, 1.0, 3, 10, 30, 100, 300 and 1000 bars and temperatures of 150, 250, 400, 550, 700, 850, 1000 and 1200 K.

The Correlated-k Distribution

The probability that a photon with wavenumber ν (cm^{-1}) will survive passage through a homogeneous layer of absorbing gas is

$$T_{\upsilon}(u) = e^{-k_{\upsilon}u} \tag{2.15}$$

T_{ν} is the (unitless) transmission function, u is the molecular absorber amount in the column traversed by the photon (molecules/cm^2) and k_{ν} is the monochromatic molecular absorption cross section (cm^2/molecule) for molecules interacting with photons of wavenumber ν. The molecular cross section is henceforth termed the 'molecular absorption coefficient', and its units are consistent with the products of the line-by-line calculations described above. The physical description of radiant energy transport in a planetary atmosphere involves the calculation of the intensity field that results from the interaction of the gases and electromagnetic energy. In the infrared, rotational-vibrational energy transitions of the gaseous molecules account for most of these interactions. For a finite wavenumber interval $\Delta\nu$, the transmission function is

$$T_{\Delta\nu}(u) = \frac{1}{\Delta\nu} \int_{\Delta\nu} e^{-k_{\upsilon}u} d\nu \tag{2.16}$$

An accurate calculation of the transmission of radiation throughout the entire infrared spectrum would require on the order of 10^8 calculations due the large number of absorption lines (Table 2.2). Such an approach, while accurate, is impractical for many applications such as general circulation models and evolutionary climate models, where the radiant energy balance of the atmosphere under a variety of conditions must be calculated many times. Computational efficiency can be improved by dividing the infrared spectrum into intervals, and reordering the absorption coefficients by their strength within each interval [*Lacis and Oinas*, 1991]. Within a spectral interval, the probability of finding the absorption coefficient between the values *k* and *k* + *dk* is defined as *f(k)dk*, where

$$\int_0^{\infty} f(k)dk = 1 \tag{2.17}$$

f(k) is the normalized probability distribution for k_ν. In terms of the absorption coefficient probability distribution then, the transmission function for wavenumber interval $\Delta\nu$ is

$$T_{\Delta\nu} = \int_0^\infty e^{-k(f)u} f(k) dk \tag{2.18}$$

The cumulative probability of finding the absorption coefficient within the spectral interval to be less than *k* is

$$g(k) = \int_0^k f(k') dk' \tag{2.19}$$

in which case *dg(k) = f(k)dk*, and the spectral transmittance can be written

$$T_{\Delta\nu}(u) = \int_0^1 e^{-k(g)u} dg \tag{2.20}$$

Because *g(k)* is a smooth function of *k*, *k(g)* is also a smooth function of the cumulative probability *g*, and the integral in g-space (2.20) may be evaluated as a finite sum of exponentials with far fewer terms than are required for evaluating (2.16). The transmission integral in wavenumber space is approximated as

$$T_{\Delta\nu}(u) \cong \sum_{l=0}^{ngauss-1} e^{-k(g_l)u} \Delta g_l \tag{2.21}$$

Here, the integral is evaluated using Gaussian quadrature with *ngauss* quadrature points, with the Δg_l as the appropriate Gaussian weights [*Abramowitz and Stegun*, 1965]. This transformation from wavenumber space to g-space is illustrated in Figure 2.5. The line-by-line absorption coefficients for the 660-670 cm^{-1} region of the 15 μm CO_2 band at a pressure of 10 mbar and temperature of 240 K is shown in Figure 2.5a. The complex structure of the spectrum is apparent. The absorption coefficient probability distribution is plotted in Figure 2.5b, as *f(k)* vs. *k*. The cumulative probability function is plotted as a function of absorption coefficient in Figure 2.5c. Finally, this relationship is inverted, and the absorption coefficient as a function of cumulative probability is plotted as a smooth and monotonically increasing function in Figure 2.5d [*Lacis and Oinas*, 1991].

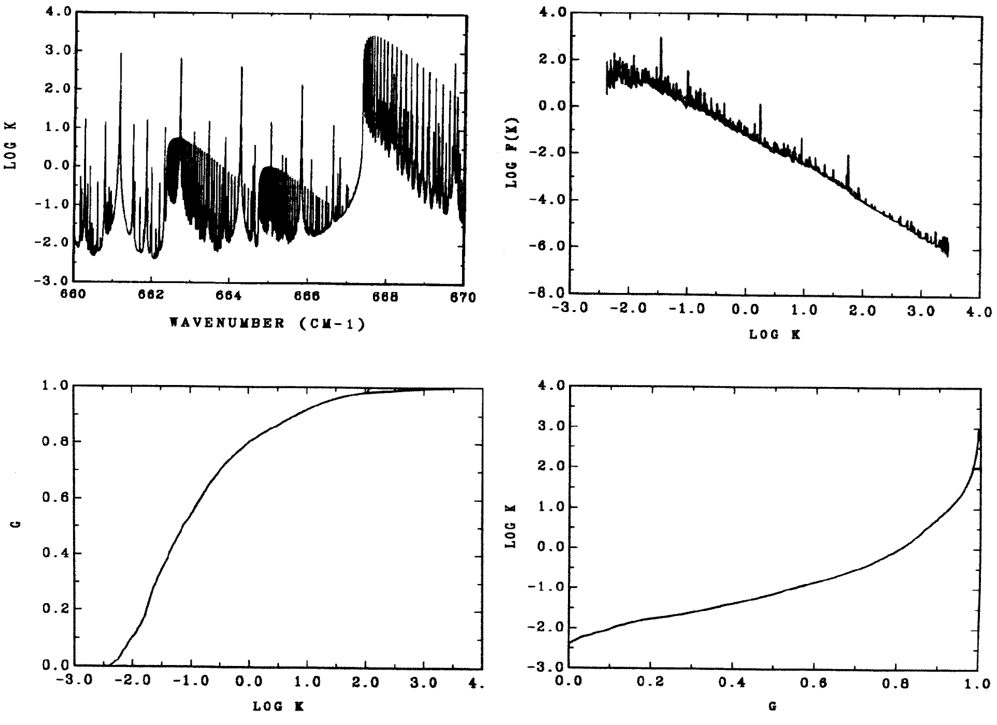

Figure 2.5 Applying the correlated-k method to the 15 μm CO_2 band [*Lacis and Oinas*, 1991]. 2.5a is the spectrum of the band in the wavenumber regime, displaying a great deal of structure. 2.5b shows the mapping to k-space via the probability function *f(k)*. Shown in 2.5c is the cumulative absorption probability *g(k)* as a function of the absorption coefficient. Fig 2.5d is the inversion of 2.5c, with absorption coefficient *k* plotted against cumulative absorption probability *g*.

Any function of the absorption coefficients may be evaluated over the spectral interval $\Delta\nu$ using the above quadrature scheme. Identifying the Gaussian weights as $w_l = \Delta g_l$, then, the flux in atmospheric layer i and wavenumber j would be

$$F_{ij} = \int_0^1 F_{ij}(g)dg \cong \sum_{l=0}^{ngauss-1} w_l F_{ijl} \tag{2.22}$$

The correlated-k method is so-called because if line positions within each wavenumber interval are assumed to be correlated from one layer to the next, quadrature points need to be calculated only once for each wavenumber interval and applied to all layers. Therefore, only *ngauss* flux calculations are necessary for each of the N atmospheric layers and M wavenumber intervals.

The cumulative probabilities for all nine molecular species, all 68 wavenumber intervals, and at all of the 72 coarse pressure, temperature grid points were calculated and tabulated from the appropriate line-by-line absorption coefficients. Line-by-line data within each spectral interval were sampled in wavenumber space at resolutions of less than a spectral line half width. The absorption coefficients were then sorted by strength, and placed into K_n (200) bins. The resulting histogram was normalized to unity. From this normalized probability distribution, the cumulative distribution was produced by simply adding bins. The absorption coefficients and their associated cumulative probabilities were designated

$$\begin{matrix} k_{IJjkl'} \\ g_{IJjkl'} \end{matrix} \left\{ \quad l' = 0 \rightarrow K_n \right. \tag{2.23}$$

where I is the coarse temperature, J is the coarse pressure, j is the wavenumber interval, k is the molecular species, and l' is the index for the relationship between tabulated values of g and k. In all cases, $g_{IJjkl'}$ was identical for all values of I, J, j and k. With total $I = 8$, $J = 9$, $M = 68$, $Q = 9$ and $K_n = 200$, the infrared spectral properties of the Venus atmosphere are described with approximately 9 million pairs of tabulated points. These tabulated values for absorption coefficients and their associated cumulative probabilities for all molecules, wavenumber intervals, and coarse temperature and pressure grid points represent the basic gaseous opacity input to the Venus atmospheric radiative transfer model.

Interpolation and Convolution

Each atmospheric layer was treated as homogeneous, with a single pressure, Pl_i and temperature Tl_i, for the ith layer. Cumulative absorption coefficients for the 4 coarse grid points bracketing Pl_i and Tl_i were used to interpolate the cumulative absorption coefficients to Pl_i, Tl_i. That is,

$$\begin{aligned} T_I < Tl_i < T_{I+1} \\ P_J < Pl_i < P_{J+1} \end{aligned} \tag{2.24}$$

Cumulative absorption coefficients for each molecule and each wavenumber interval were first interpolated logarithmically in pressure between P_J and P_{J+1}

$$\begin{aligned} k_{Iijkl'} &= A_{Iijkl'} Pl_i^{b_{Iijkl'}} \\ k_{I+1,ijkl'} &= A_{I+1,ijkl'} Pl_i^{b_{I+1,ijkl'}} \end{aligned} \tag{2.25}$$

where the coefficients $A_{Iijkl'}$, $b_{Iijkl'}$ were determined from $k_{IJjkl'}$ and $k_{IJ+1,jkl'}$, and the coefficients $A_{I+1,ijkl'}$, $b_{I+1,ijkl'}$ were determined from $k_{I+1,Jjkl'}$ and $k_{I+1,J+1,jkl'}$. These pressure-interpolated coefficients were then interpolated logarithmically in temperature between T_I and T_{I+1}.

$$k_{ijkl'} = C_{ijkl'} Tl_i^{d_{ijkl'}} \tag{2.26}$$

where the coefficients $C_{ijkl'}$ and $d_{ijkl'}$ were determined from $k_{Iijkl'}$ and $K_{I+1,ijl'}$.

Once the interpolated cumulative absorption coefficients for every molecule and wavenumber interval in a single layer were calculated, they were convolved according to their molar mixing ratios in the layer to produce a single cumulative absorption coefficient distribution [*Goody et al.*, 1989]. Cumulative absorption coefficients for each gas are converted to opacity by multiplying them by the path lengths for each molecule. That is,

$$\tau_{ijkl'}^{gas} = ul_{ik}k_{ijkl'} \tag{2.27}$$

For illustration purposes, I will consider the absorption of a 2-component gas in a single wavenumber interval, with layer opacities τ_a and τ_b. The gases are assumed to have overlapping but uncorrelated line positions in their spectra. With the correlated-k method, the probability that gas a will have an opacity between τ and $\tau + d\tau$ is $F_a(\tau)d\tau$. If gas b contributes opacity τ_b then gas a must contribute $\tau - \tau_b$, where $\tau_b < \tau$. Then the probability that gas b has an opacity between τ_b and $\tau_b + d\tau_b$ and that gas a has opacity $\tau - \tau_b$ is

$$dF_{a,b}(\tau) = F_b(\tau_b)F_a(\tau - \tau_b)d\tau_b \tag{2.28}$$

So the convolved probability that the gas mixture will have an opacity between τ and $\tau + d\tau$ is $F_{ab}(\tau)d\tau$, where

$$F_{a,b}(\tau) = \int_0^\tau F_b(\tau_b)F_a(\tau - \tau_b)d\tau_b \tag{2.29}$$

Since it is the cumulative probabilities

$$G(\tau) = \int_0^\tau F(\tau')d\tau' \tag{2.30}$$

that are tabulated, these are used for the convolutions instead. With $dG(\tau) = F(\tau)d\tau$, (2.29) becomes

$$G_{a,b}(\tau) = \int_0^\tau G_a(\tau - \tau_b)dG_b(\tau_b) \tag{2.31}$$

In the model, these convolutions are carried out repeatedly for each molecule, using the interpolated values $\tau_{ijkl'}$ for each atmospheric layer and wavenumber interval. The integrals are performed numerically, with l' as the integration indices. Thus

$$G_{ijl'}\left(\tau_{ijkl'}^{gas}\right) = \int_0^{\tau_{ijl'}} \cdots \int_0^{\tau_{ijl'} - \tau_{ijkl'} \cdots} G_{ijkl'}\left(\tau_{ijl'}^{gas} - \tau_{ijkl'}^{gas} \ldots\right) dG_{ijkl'} \ldots \qquad (2.32)$$

Since $G_{ijl'}$ is mapped to $\tau_{ijl'}{}^{gas}$, the interpolated, convolved cumulative opacities are thus acquired for each atmospheric layer and wavenumber interval.

Pressure-Induced Transitions

CO_2 Self-Broadened Continuum Opacity

The gaseous opacities above were calculated from laboratory data for vibrational-rotational energy transitions permitted by selection rules. Molecular wave function symmetry determines if a given dipole or multipole transition can occur. Thus, perturbations to the symmetry of molecular wavefunctions, caused by collisions, can allow forbidden dipole transitions to occur during the collision. Because of the high pressures encountered in Venus' atmosphere, binary collisions enabling forbidden transitions among CO_2 molecules contribute significant infrared opacity to the atmosphere. For the Venus radiative transfer model, laboratory data on the temperature dependence of CO_2-CO_2 pressure induced opacity were used [*Moskalenko et al.*, 1979]. CO_2 self-broadened continuum opacity was calculated from the tabulated data by interpolation to the model wavenumber intervals, *j,* and by applying temperature coefficients appropriate for layer temperatures, T_{li}. These absorption coefficients $k_{ijCO2}{}^{con}$ were then converted to opacities via

$$\tau_{ij,CO_2}^{con} = \left(ul_{i,CO_2}\right)^2 k_{ij,CO_2}^{con} \qquad (2.33)$$

Figure 2.6 shows a typical continuum absorption spectrum for CO_2-CO_2 pressure induced opacity, for Venus surface conditions. Strongest absorption occurs at wavenumber less than 1000 cm^{-1}, with a very rapid dropoff so that CO_2 continuum opacities are relatively unimportant above 2000 cm^{-1}.

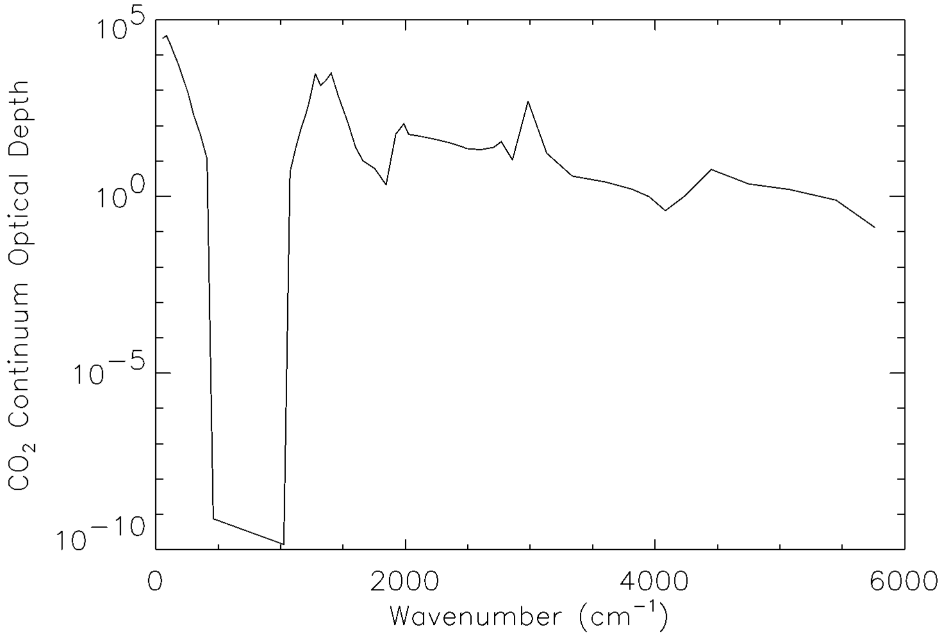

Figure 2.6 CO_2 continuum optical depth as a function of wavenumber calculated for the bottom scale height of Venus' atmosphere

H_2O Continuum Opacity

Continuum opacity in the 800 - 1200 cm^{-1} region due to H_2O vapor is observed, but its origin is not well understood. Explanations include the contributions from accumulated absorption of distant wings of H_2O vapor lines [*Clough et al.*, 1980], or continuous absorption by water dimer $(H_2O)_2$ [*Liou*, 1992]. For the Venus radiative transfer model, empirically derived H_2O continuum data are employed [*Roberts et al.*, 1976]. The absorption coefficients for H_2O continuum is expressed as the sum of self and foreign-broadened components as

$$k_{ij,H_2O} = \sigma s_{ij}\left[Xl_{i,H_2O}Pl_i + \frac{\sigma n_{ij}}{\sigma s_{ij}}\left(Pl_i - Xl_{i,H_2O}Pl_i\right)\right] \tag{2.34}$$

where σs_{ij} and σn_{ij} are the self-broadening and foreign-broadening coefficients for H_2O vapor, for temperature at layer *i*, and for wavenumber interval *j*. The temperature and wavenumber dependence of σs_{ij} are given empirically as

$$\sigma s_{ij} = e^{c\left(\frac{Tr}{Tl_i}-1\right)}\left[a + be^{-\beta\left(v1_j - \upsilon 0_j\right)}\right] \tag{2.35}$$

for the 800-1200 cm^{-1} region. T_r is a reference temperature, 296 K, and *a,b,c* and β are constants derived from laboratory experiments. For the 2000 to 3300 cm^{-1} region, (2.35) is used, but with different empirical constants. [*Kneizys et al.*, 1980]. Due to the lack of definitive empirical data, foreign-broadening coefficients for H_2O vapor are relatively unconstrained. I use a value $\sigma n_{ij} = 0.002\sigma s_{ij}$ [*Liou*, 1992] for the Venus radiative transfer model. H_2O vapor continuum absorption coefficients are then converted to optical depths via

$$\tau_{ij,H_2O}^{con} = ul_{i,H_2O}k_{ij,H_2O}^{con} \tag{2.36}$$

Figure (2.7) plots a typical water vapor continuum spectrum for the Venus atmosphere for conditions at the surface. The total optical depth due to CO_2 and H_2O continuum opacity is

$$\tau_{ij}^{con} = \tau_{ij,CO_2}^{con} + \tau_{ij,H_2O}^{con} \tag{2.37}$$

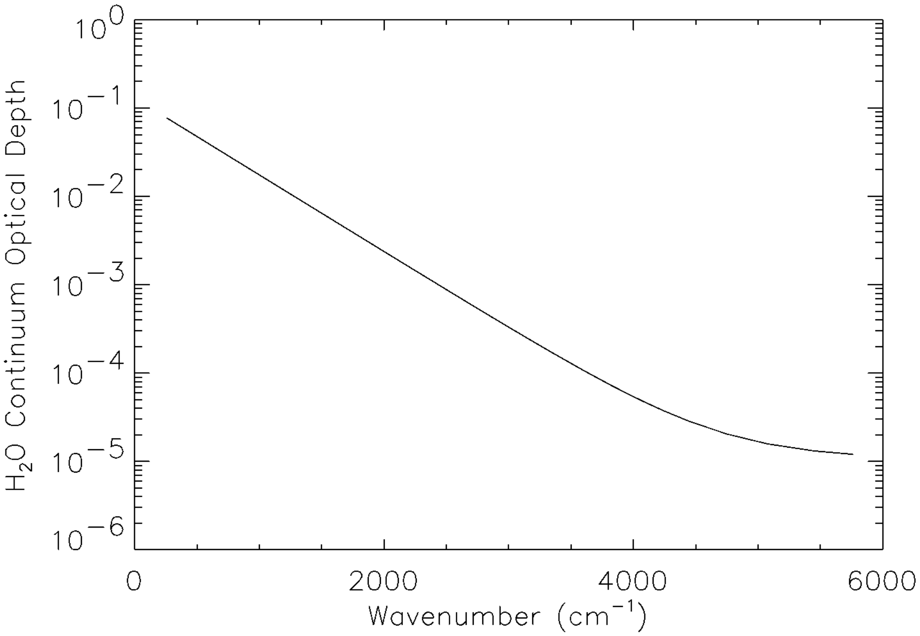

Figure 2.7 H$_2$O continuum optical depth as a function of wavenumber calculated for the bottom scale height of Venus' atmosphere

Rayleigh Scattering

Isotropic elastic scattering of electromagnetic energy by gas molecules which are much smaller than the wavelength of the radiation gives rise to Rayleigh scattering. The molecular cross section usually given in textbooks, from Rayleigh's original theory is

$$\sigma_r = \frac{8\pi^3 (n_r^2 - 1)^2}{3\lambda^4 n^2} f(\delta) \tag{2.38}$$

where n_r is the real index of refraction of the gas at standard temperature and pressure (STP), λ is the wavelength of the scattered radiation, and n is the molecular number density [*Goody and Yung*, 1989]. $f(\delta)$ is an anisotropic correction term that accounts for the lack of symmetry of molecular scatterers, where

$$f(\delta) = \frac{6 + 3\delta}{6 - 7\delta} \tag{2.39}$$

In the present model, I include the effects of Rayleigh scattering for CO_2 and N_2. For CO_2, the anisotropy factor is $\delta = 0.0805$ while for N_2 it is 0.0305. For the Earth's atmosphere, Rayleigh scattering in the infrared is usually ignored. However, in the dense Venus atmosphere, Rayleigh scattering may account for optical depths in the near infrared of 1 or more [*Crisp*, 1986; *Meadows and Crisp*, 1996]. The temperature and pressure dependence of the real index of refraction as a function of wavenumber is accounted for by empirical data from the International Critical Tables [*Washburn et al.*, 1930]. For an atmospheric level with temperature Tl_i and pressure Pl_i, the index of refraction for wavenumber j and species k is given by

$$n_{r_{ijk}} = \frac{\beta_k Pl_i}{\left[1 + \alpha_k (Tl_i - T_r)\left(\mu_k - (\nu_{1j} - \nu_{0j})^2\right)\right] + 1} \tag{2.40}$$

where α_k, β_k and μ_k are empirically derived constants, different for CO_2 and N_2, and Tr is a reference temperature (273.18 K). Converting (2.38) to the units used in the model, the molecular scattering coefficient at level i and wavenumber j for species k is then

$$\sigma_{r_{ijk}} = \frac{8\pi^3 \left(n^2_{r_{ijk}} - 1\right)^2 k_B^2 Tl_i^2 Xl_{ik}}{3\left(\nu_{1j} - \upsilon_{0j}\right)^4 Pl_i^2} \frac{(6 + 3\delta_k)}{(6 - 7\delta_k)} \tag{2.41}$$

where k_B is the Boltzmann constant. Then the total optical depth due to Rayleigh scattering by CO_2 and N_2 molecules is

$$\tau_{ij}^{ray} = \sigma_{r_{ij,CO_2}} ul_i Xl_{i,CO_2} + \sigma_{r_{ij,N_2}} ul_i Xl_{i,N_2} \tag{2.42}$$

CO_2 Rayleigh scattering optical depths for the bottom scale height of the Venus atmosphere are plotted as a function of wavelength in Figure 2.8.

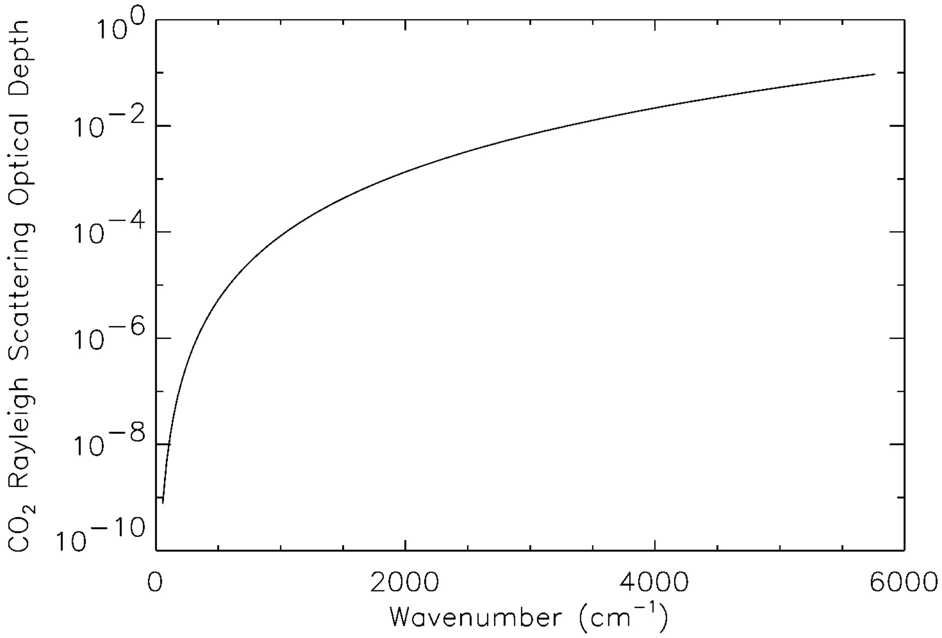

Figure 2.8 Rayleigh scattering optical depth as a function of wavenumber calculated for the bottom scale height of Venus' atmosphere

Scattering and Absorption Due to Atmospheric Aerosols

Aerosols in Venus' atmosphere exist in 3 global cloud layers between 48 and 70 km, and are constituents of hazes above and below this [*Esposito et al.*, 1983; *Grinspoon et al.*, 1993; *Knollenberg and Hunten*, 1980]. Four distinguishable size modes have been inferred from the Pioneer Venus particle size spectrometer experiments and subsequent modeling [*Crisp*, 1986; *Esposito et al.*, 1983; *Grinspoon et al.*, 1993; *Pollack et al.*, 1980]. Mode 1 (r_{ave} = 0.3 μm) particles are ubiquitous throughout the Venus clouds, and may also be representative of some of the hazes [*Esposito et al.*, 1983]. Mode 2 (r_{ave} = 1 μm) particles are constituents of the middle and lower clouds, while Mode 2' (r_{ave} = 1.4 μm) are mostly found in the upper cloud deck. Large aerosols, designated Mode 3 (r_{ave} = 3.6 μm), dominate the opacity and mass loading of the lower cloud. Small concentrations of Mode 3 particles may also exist in the upper clouds [*Crisp*, 1986]. Modeling of the polarization properties and near-infrared spectrum of radiation reflected from the cloud tops is consistent with H_2SO_4 concentrations in the cloud droplets of between 84 and 96% by mass [*Hansen and Houvenier*, 1974; *Pollack et al.*, 1978; *Young and Young*, 1973]. H_2O makes up the remainder, yielding cloud particle *p*Hs of < 0.01. On thermodynamic grounds, it is likely that the clouds become more H_2O-rich with altitude as the saturation vapor pressure of H_2SO_4 declines steeply with altitude.

The cloud particle properties and number densities used in the Venus radiative transfer model are those from the Pioneer Venus particle size experiment, modified to include the two Mode 2 distributions and additional upper haze [*Esposito et al.*, 1983; *Knollenberg and Hunten*, 1980]. The cloud model number densities and resulting mass loading are shown in Figures 2.9 and 2.10. Each of the 4 size modes are described by log-normal distributions

$$n_k(r_k) = \frac{2\pi}{r_k\, ln(\sigma_k)} e^{-\frac{1}{2}\left[\frac{ln(r_k/\bar{r}_k)}{ln(\sigma_k)}\right]^2} \tag{2.43}$$

where k is the size mode index, r_k is the modal radius, σ_k the size variance, and r_k the radius of the *k*th size mode particles. Cloud aerosol modal properties used are shown in Table 2.3.

A Mie scattering program was used with the log-normal distributions for calculating scattering and extinction optical depths $\tau_{ij}^{aer\_sca}$ and $\tau_{ij}^{aer\_ext}$ in each atmospheric layer i for each wavenumber j, as well as particle single scattering albedos ω_{0ij} and scattering asymmetry factors g_{ij} [*Hansen and Travis*, 1974].

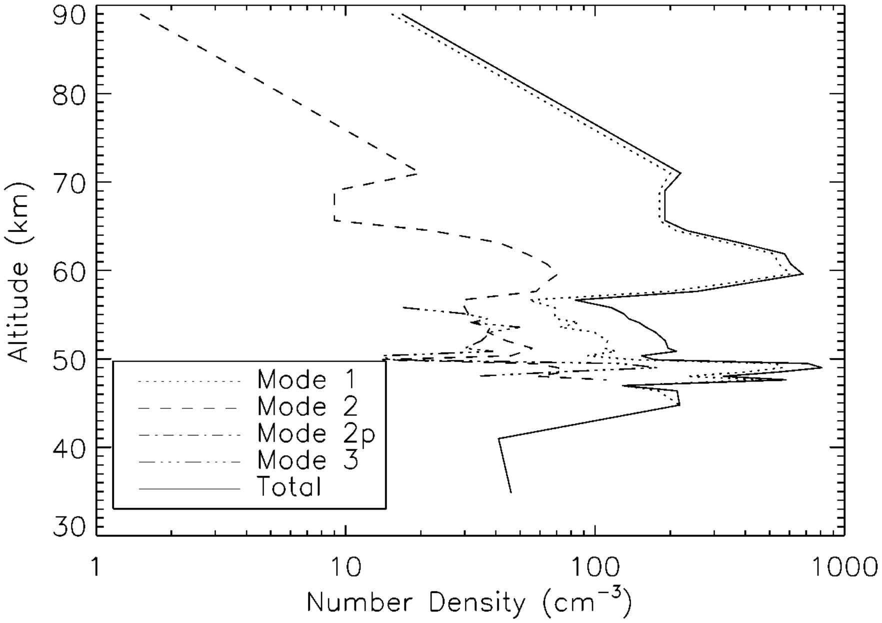

Figure 2.9 Venus cloud aerosol number densities from the Pioneer Venus particle size spectrometer experiments [*Knollenberg and Hunten*, 1980].

Table 2.3 Cloud Particle Modes and their Properties

	Mode 1	Mode 2	Mode 2'	Mode 3
r_{ave} (μm)	0.30	1.00	1.40	3.65
σ	1.56	1.29	1.23	1.28
%H_2SO_4	84.5	84.5	95.6	95.6
r_{min} (μm)	0.01	0.01	0.01	0.01
r_{max} (μm)	15.0	15.0	15.0	15.0

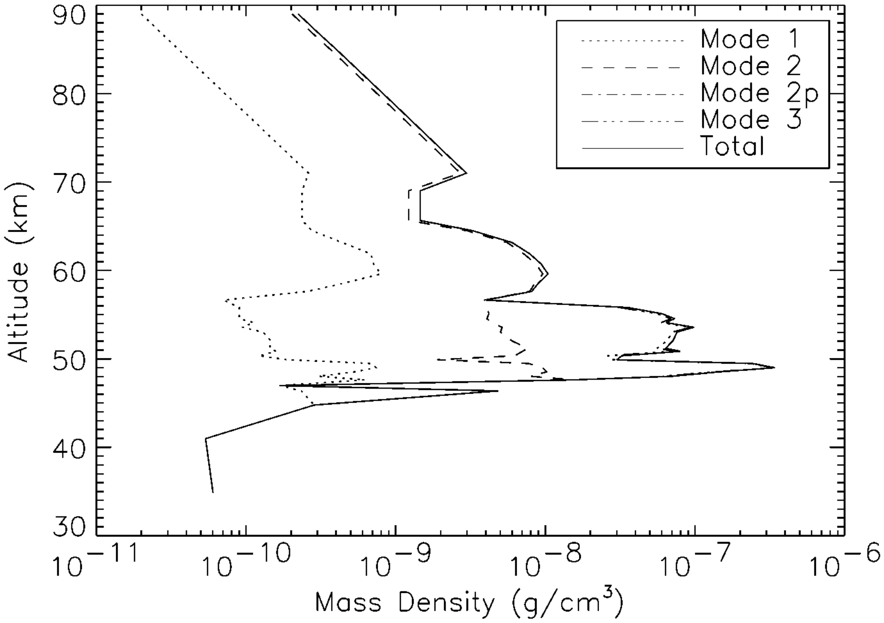

Figure 2.10 Venus cloud aerosol mass loading from the Pioneer Venus particle size spectrometer experiments.

Output from the code was in the form of optical depths per unit volume, which were then scaled by the appropriate number densities for each size mode and atmospheric layer. As input to the Mie code, laboratory-derived real and complex indices of refraction at all infrared wavenumbers were employed [*Palmer and Williams*, 1975]. The complex indices of refraction, for 84.5% sulfuric acid, are reproduced in Figure 2.11. Cloud opacities at 0.63 μm calculated for the nominal Venus cloud are shown in Figure 2.12 for an 80 layer atmospheric model. Discernible are the three distinct cloud layers at 48 km, 55 km and 60 km, with their dominant mode 3, mode 2, and mode 1 contributions, respectively. The average aerosol single scattering albedos as a function of wavenumber for a typical layer in the middle cloud are shown in Figure 2.13. For comparison, results in a slightly different form from a previous Mie scattering calculation [*Tomasko*, 1983] are shown in Figure 2.14. Here, absorption coefficients as a function of wavenumber ratioed with the extinction at 0.63 µm are plotted. Since the extinction coefficient also varies with wavenumber, this is not quite 1 - ω_0, but some of the same spectral features may be seen. The average particle scattering asymmetry factor as a function of wavenumber for a middle cloud atmospheric layer is shown in Figure 2.15.

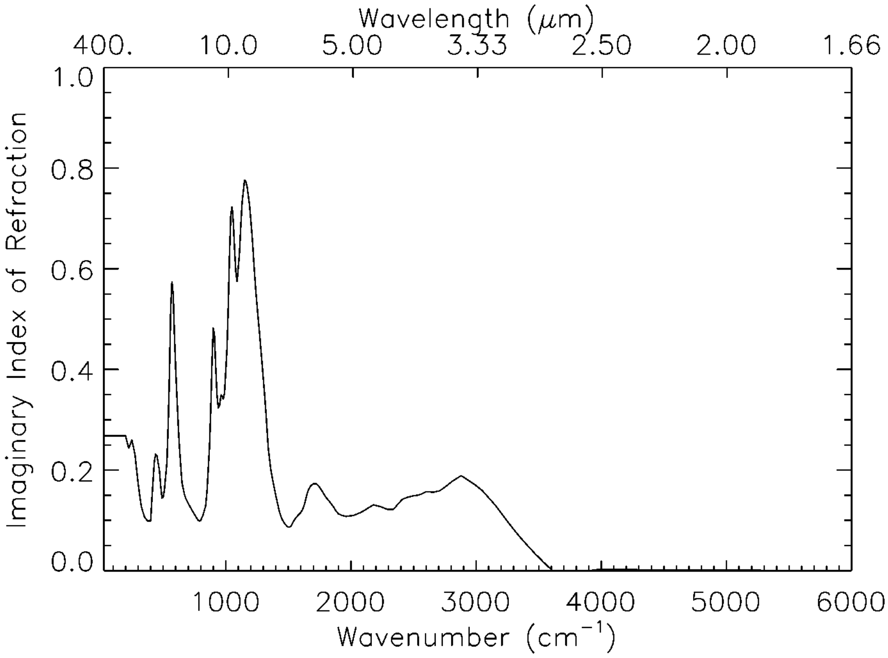

Figure 2.11 Complex index of refraction as a function of wavenumber for an 84.5% H_2SO_4/ H_2O solution [*Palmer and Williams*, 1975].

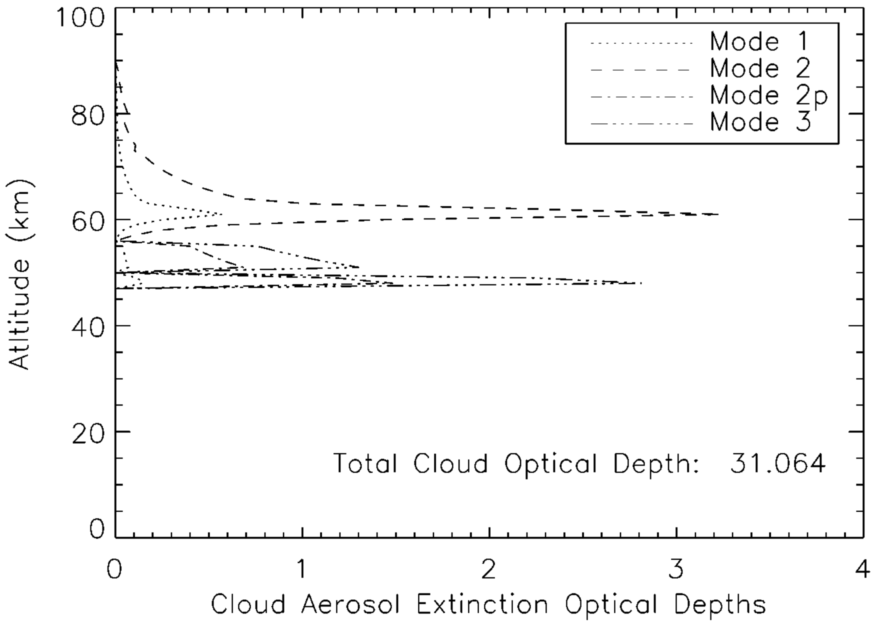

Figure 2.12 Cloud extinction optical depths at 0.63 μm from Mie calculations of the nominal Venus cloud model. Values are the optical depths for each layer of an 80 layer atmosphere.

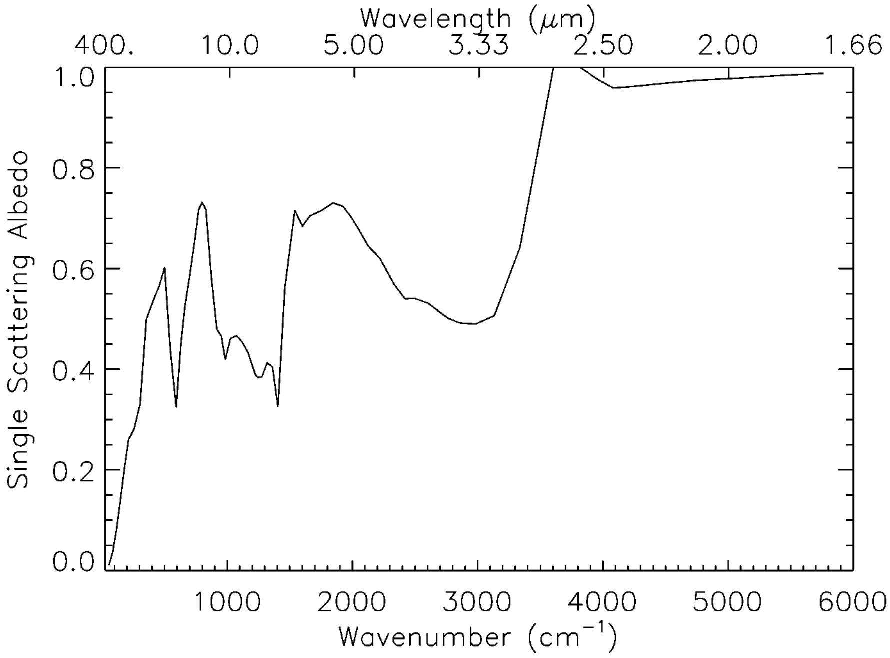

Figure 2.13 Single scattering albedos averaged over particle size modes as a function of wavenumber for an atmospheric layer within the middle cloud.

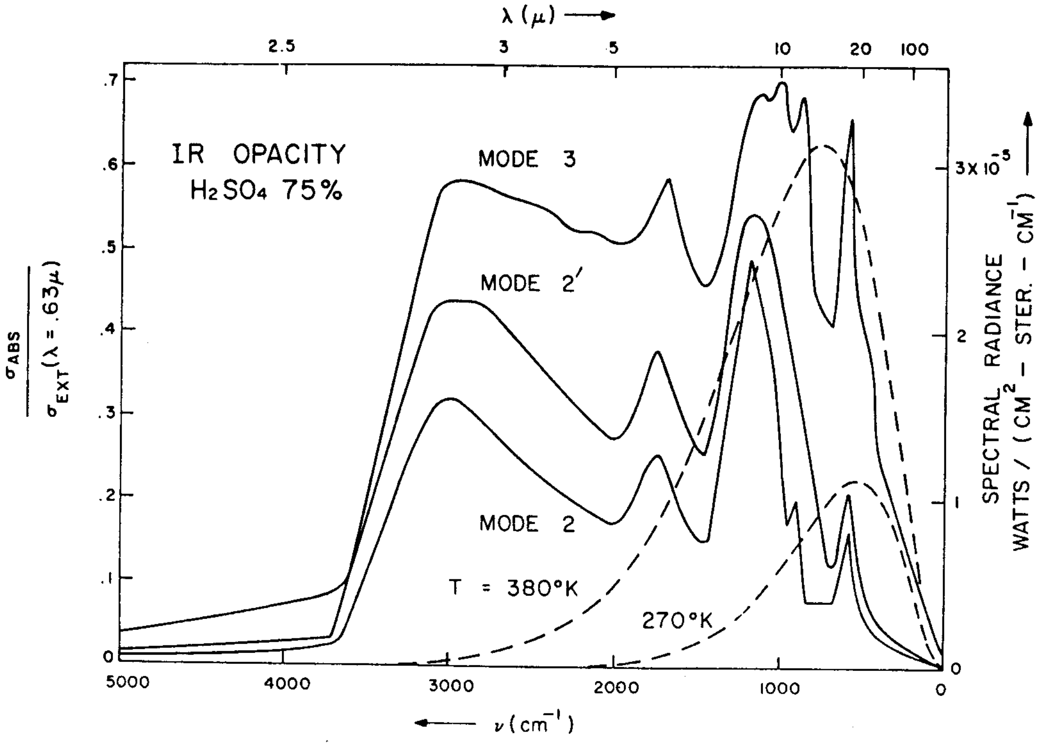

Figure 2.14 The ratio of absorption coefficient as a function of wavenumber to the extinction coefficient at 0.63 μm, for a previously published cloud opacity model [*Tomasko*, 1983].

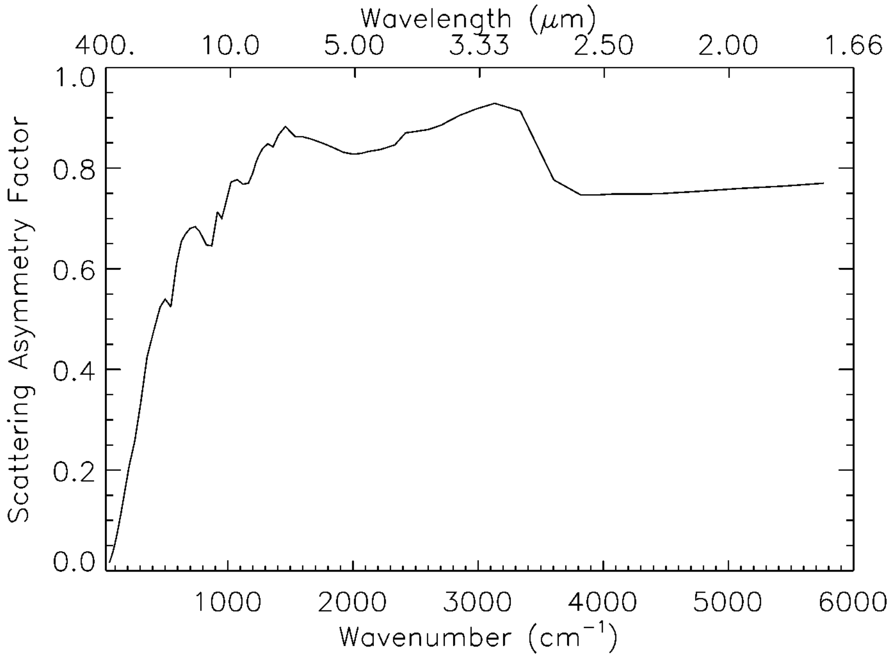

Figure 2.15 Scattering asymmetry factors averaged over particle size modes as a function of wavenumber for an atmospheric layer within the middle cloud.

The Mie scattering calculations can be summarized as supplying to the model

$$\tau_{ij}^{aer} = \tau_{ij\_ext}^{aer} \tag{2.44}$$

$$\omega_{0ij}^{aer} = \frac{\tau_{ij\_sca}^{aer}}{\tau_{ij\_ext}^{aer}} \tag{2.45}$$

$$g_{ij}^{aer} \tag{2.46}$$

where $\tau_{ij}{}^{aer}$ is the extinction optical depth due to aerosols in atmospheric layer i for the jth wavenumber interval, and $\omega_{0ij}{}^{aer}$ and $g_{ij}{}^{aer}$ are average particle single scattering albedos and scattering asymmetry factors.

Atmospheric Layer Opacity Parameters

Scattering parameters $\tau_{ij}{}^{ray}$, $\tau_{ij}{}^{aer}$, $\omega_{0ij}{}^{aer}$ and $g_{ij}{}^{aer}$ must be convolved with the other optical parameters of the atmospheric layers $\tau_{ijl}{}^{gas}$ and $\tau_{ij}{}^{con}$ to provide useful data for the infrared flux calculations. The net single-scattering albedo of an atmospheric layer is a product of the mixture of Rayleigh and Mie scatterers as well as the absorption due to continuum and permitted gaseous absorption. Recall that gaseous absorption within layer *i* for wavenumber *j* is approximated by a Gaussian quadrature of *ngauss* points with index *l*. So the single scattering albedo for atmospheric layer *i* and wavenumber interval *j* and Gaussian subinterval *l* is

$$\omega_{0ijl} = \frac{\tau_{ij}^{ray} + \omega_{0ij}^{aer}\,\tau_{ij}^{aer}}{\tau_{ijl}^{gas} + \tau_{ij}^{con} + \tau_{ij}^{ray} + \tau_{ij}^{aer}} \tag{2.47}$$

while the scattering asymmetry factor is

$$g_{ijl} = \frac{\omega_{0ij}^{aer}\,\tau_{ij}^{aer}}{\omega_{0ij}^{aer}\,\tau_{ij}^{aer} + \tau_{ij}^{ray}}\, g_{ij}^{aer} \tag{2.48}$$

for any Gaussian subinterval *l*. The total optical depth for atmospheric layer *i*, wavenumber *j* and Gaussian subinterval *l*, due to all the sources of opacity is

$$\tau_{ijl} = \tau_{ijl}^{gas} + \tau_{ij}^{con} + \tau_{ij}^{ray} + \tau_{ij}^{aer} \tag{2.49}$$

Together, (2.47), (2.48) and (2.49) along with the Gaussian weights, w_l, and level temperatures, T_i, provide all the input for calculations of the infrared flux. Plotted in Figure 2.16 is the total optical depth of the Venus atmosphere as a function of the 68 infrared wavenumber intervals, calculated from

$$\tau_j^* = \sum_{i=0}^{N-1} \sum_{l=0}^{ngauss-1} \tau_{ijl} \tag{2.50}$$

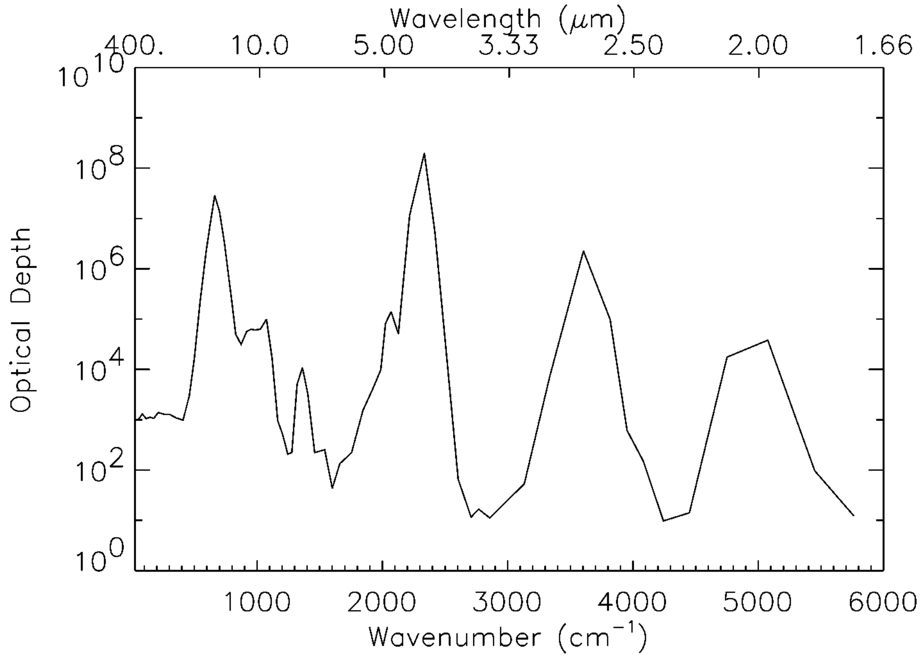

Figure 2.16. Total optical depths of the Venus atmosphere calculated from (2.50) as a function of wavenumber.

The cloud acts mostly as a grey neutral density absorber, except at small wavenumbers (wavelengths > 10 μm). Peak absorption, due to strong CO_2 bands, may be seen at 666 cm^{-1} (15 μm, the ν_2 vibrational mode), 2326 cm^{-1} (4.3 μm, the ν_3 vibrational mode), as well as at 3600 cm^{-1} (2.8 μm) and 4900 cm^{-1} (2.0 μm). The region between the two absorption bands at 666 cm^{-1} and 2326 cm^{-1} is filled in mostly with absorption due to the H_2O ν_2 transition at 1595 cm^{-1} (6.3 μm). Likewise, absorption shortward of 1100 cm^{-1} is due to H_2O pure rotational bands and H_2O continuum. Minima in the absorption occur at the atmospheric ‘windows’ between CO_2 bands, from 2600 - 3100 cm^{-1} (3.2 - 4.4 μm) and 4200 - 4600 cm^{-1} (2.2 - 2.4 μm). Optical depths are still in the range of 10 - 100 in these regions, filled in by pressure-induced absorption of the dense atmosphere and cloud opacity.

Infrared Flux Calculations

The Radiative Transfer Equations

Upward and downward infrared fluxes were calculated using a two-stream hemispheric mean approximation to the radiative transfer equation [*Toon et al.*, 1989]. A key feature of the present model is the inclusion of multiple scattering in infrared bands for flux calculations as well as the use of the Planck source function for emission in the infrared. The hemispheric mean approximates the angular dependence of the intensity so that the flux and intensity from an isotropic source are correctly related. The equation of radiative transfer for a plane-parallel emitting and scattering atmosphere is

$$\mu\frac{\partial I_\upsilon}{\partial\tau_\nu}(\tau_\nu,\mu,\phi)=I_\nu(\tau_\nu,\mu,\phi)-\frac{\omega_0}{4\pi}\int_0^{2\pi}\int_{-1}^{1}P_\nu(\mu,\phi,\mu',\phi')I_\upsilon(\tau_\nu,\mu',\phi')d\mu'd\phi'-(1-\omega_0)B_\nu(T)$$

(2.51)

where μ is the cosine of the angle between the observed monochromatic intensity I_ν and the vertical, ϕ is the azimuthal angle, τ is the vertical optical depth from the top of the atmosphere, and ω_0 is the single scattering albedo. $B_\nu(T)$ is the Planck function evaluated at wavenumber ν and the temperature T of the atmosphere at τ_ν. The monochromatic scattering phase function, P_ν, is the probability that a scattered photon with incoming angles μ, ϕ and wavenumber ν will scatter into outgoing angles μ', ϕ'. It is normalized to 1 so that

$$\frac{1}{4\pi}\int_0^{2\pi}\int_{-1}^{1}P(\mu,\phi,\mu',\phi')d\mu d\phi=1 \tag{2.52}$$

Assuming that the phase function is only dependent on the cosine of the scattering angle, it may be integrated over ϕ so that the azimuthally independent phase function is

$$P(\mu, \mu') = \frac{1}{2\pi} \int_0^{2\pi} P(\mu, \phi, \mu', \phi') d\phi \tag{2.53}$$

Hemispherical fluxes are the first moments of the intensities into each hemisphere

$$F^{\pm}(\tau) = \int_0^{2\pi} \int_0^1 I(\tau, \pm\mu, \phi) \mu d\mu d\phi \tag{2.54}$$

The azimuthally integrated intensities are

$$I^{\pm}(\tau, \mu) = \int_0^{2\pi} I(\tau, \pm\mu, \phi) d\phi \tag{2.55}$$

Using these definitions the radiative transfer equation may be integrated over upward and downward hemispheres

$$\frac{\partial F^{\pm}(\tau)}{\partial \tau} = \pm \int_0^1 I^{\pm}(\tau, \mu) d\mu \mp \frac{1}{2} \int_0^1 \int_{-1}^1 P(\mu, \mu') d\mu d\mu' \mp 2\pi(1 - \omega_0) B(\tau) \tag{2.56}$$

The hemispheric mean approximation involves a two point Gaussian quadrature for integrating over μ, with a weight of 1 and Gaussian points $\mu = \mu_1 = \pm 0.5$. Using this scheme, the upward and downward fluxes are related to the azimuthally-integrated intensities by

$$F^{\pm}(\tau) = \frac{1}{2} \int_0^1 I^{\pm}(\tau, \mu) d\mu \tag{2.57}$$

The phase function may be evaluated in a similar way, if it is expanded in terms of Legendre polynomials [*Chandrasekhar*, 1960]

$$P(\mu, \mu') = \sum_{l=0}^{N_l} g_l P_l(\mu) P_l(\mu') \tag{2.58}$$

The simplest possible expression of this expansion to two terms makes use of a scattering asymmetry factor g, where $(1 + g)/2$ is the probability that a photon will scatter into the forward hemisphere, and $(1 - g)/2$ is the probability that it will scatter into the backward hemisphere. g varies from -1 to 1. Since the quadrature demands that $\mu = 0.5$ and $\mu' = 0.5$, the normalized phase function is

$$P(\mu, \mu') = 1 + 4g\mu\mu' \tag{2.59}$$

Using (2.57) and (2.59) in the radiative transfer equation (2.56), and the two-point quadrature with $\mu = \mu_1 = 0.5$ and $\mu' = \mu_1 = 0.5$, the upward and downward flux equations become

$$\frac{\partial F^+}{\partial \tau} = 2F^+ - \omega_0(1+g)F^+ - \omega_0(1-g)F^- - 2\pi(1-\omega_0)B \tag{2.60}$$

$$\frac{\partial F^-}{\partial \tau} = -2F^- + \omega_0(1-g)F^+ + \omega_0(1+g)F^- + 2\pi(1-\omega_0)B \tag{2.61}$$

With the following definitions

$$\gamma_1 = 2 - \omega_0(1+g) \tag{2.62}$$

$$\gamma_2 = \omega_0(1-g) \tag{2.63}$$

the flux equations become

$$\frac{\partial F^+}{\partial \tau} = \gamma_1 F^+ - \gamma_2 F^- - 2\pi(1-\omega_0)B(\tau) \tag{2.64}$$

and

$$\frac{\partial F^-}{\partial \tau} = \gamma_2 F^+ - \gamma_1 F^- + 2\pi(1-\omega_0)B(\tau) \tag{2.65}$$

Equations (2.64) and (2.65) are a pair of non-homogeneous coupled first-order constant coefficient differential equations that may be decoupled by converting them to 2nd order differential equations. The resulting equations may be solved by the method of undetermined coefficients [*Powers*, 1987]. The general solutions to the two-stream flux equations for a single layer are

$$F^{+}(\tau) = Y_1\left[e^{-\lambda\left(\tau^{*}-\tau\right)} + \Gamma e^{-\lambda\tau}\right] + Y_2\left[e^{-\lambda\left(\tau^{*}-\tau\right)} - \Gamma e^{-\lambda\tau}\right] + C^{+}(\tau) \quad (2.66)$$

$$F^{-}(\tau) = Y_1\left[\Gamma e^{-\lambda\left(\tau^{*}-\tau\right)} + e^{-\lambda\tau}\right] + Y_2\left[\Gamma e^{-\lambda\left(\tau^{*}-\tau\right)} - e^{-\lambda\tau}\right] + C^{-}(\tau) \quad (2.67)$$

where

$$\lambda = \left(\gamma_1^2 - \gamma_2^2\right)^{1/2} \quad (2.68)$$

$$\Gamma = \frac{\gamma_2}{\gamma_1 + \lambda} \quad (2.69)$$

and C^{+} and C^{-} are optical-depth dependent functions of the Planck function. They are determined by representing the optical depth dependence of the Planck function in the layer as the first term of a Taylor series expansion, so that

$$B(\tau) = B_0 + B_1\tau \quad (2.70)$$

where B_0 is the Planck function evaluated at the top of the layer, and B_1 is the gradient with respect to optical depth of the Planck function across the layer

$$B_1 = \frac{B(T_b) - B_0}{\tau^{*}} \quad (2.71)$$

where T_b is the temperature at the bottom of the layer and τ^{*} is the total optical depth of the layer. With these definitions

$$C^{+}(\tau) = 2\pi\mu_1\left[B_0 + B_1\left(\tau + \frac{1}{\gamma_1 + \gamma_2}\right)\right] \quad (2.72)$$

$$C^{-}(\tau) = 2\pi\mu_1 \left[B_0 + B_1 \left(\tau - \frac{1}{\gamma_1 + \gamma_2} \right) \right] \tag{2.73}$$

Y_1 and Y_2 in (2.66) and (2.67) are determined from the top and bottom boundary conditions. For a system of N atmospheric layers with index i, where $i = 0$ is the top and $i = N$ is the bottom layer, the infrared flux boundary conditions are

$$F_0^{-}(0) = 0 \tag{2.74}$$

$$F_i^{-}(\tau_i) = F_{i+1}^{-}(0) \tag{2.75}$$

$$F_i^{+}(\tau_i) = F_{i+1}^{+}(0) \tag{2.76}$$

$$F_N^{+}(\tau_N) = (1-\varepsilon)F_N^{-}(\tau_N) + \varepsilon\pi B(T_g) \tag{2.77}$$

where T_g is the temperature of the surface and ε is its emissivity. For this model, a value of 0.9 is used for the emissivity at all wavenumbers, appropriate for a basaltic surface at high temperature [*Henderson and Jakosky*, 1997; *Kaula et al.*, 1981]. When the boundary conditions (2.74) to (2.77) are written using the flux equations (2.66) and (2.67), the result is a system of $2N$ algebraic equations with the $2N$ unknowns Y_{1i} and Y_{2i}. When these are determined, they can be inserted back into the flux equations (2.66) and (2.67) to obtain an analytic expressions for the upward and downward fluxes $F_i^{+}(\tau)$ and $F_i^{-}(\tau)$ as functions of optical depth within the layer.

Infrared Flux Equations -- Numerical Implementation

After rearranging by placing the C-functions on one side of the equations, the $2N$ flux equations may be expressed in terms of a matrix equation

$$\begin{bmatrix} \Gamma_0 e^{-\lambda_0\tau_0}+1 & \Gamma_0 e^{-\lambda_0\tau_0}-1 & 0 & 0 & 0 \\ \Gamma_0+e^{-\lambda_0\tau_0} & \Gamma_0-e^{-\lambda_0\tau_0} & -\Gamma_1 e^{-\lambda_0\tau_0}-1 & -\Gamma_1 e^{-\lambda_0\tau_0}-1 & 0 \\ 1+\Gamma_0 e^{-\lambda_0\tau_0} & 1-\Gamma_0 e^{-\lambda_0\tau_0} & -e^{-\lambda_1\tau_1}-\Gamma_1 & -e^{-\lambda_1\tau_1}+\Gamma_1 & 0 \\ \vdots & \vdots & \vdots & \vdots & \vdots \\ 0 & 0 & 0 & f1_N(\varepsilon,\Gamma,\lambda,\tau) & f2_N(\varepsilon,\Gamma,\lambda,\tau) \end{bmatrix} \begin{bmatrix} Y1_0 \\ Y2_0 \\ Y1_1 \\ \vdots \\ Y2_N \end{bmatrix} =$$

$$\begin{bmatrix} -C_0^-(0) \\ C_1^-(0)-C_0^-(\tau_0) \\ C_1^+(0)-C_0^+(\tau_0) \\ \vdots \\ C_N^-(\tau_N)-C_N^+(\tau_N)+\varepsilon\pi B(T_g) \end{bmatrix} \tag{2.78}$$

where

$$f1_N(\varepsilon,\Gamma,\lambda,\tau)=1+\Gamma_N e^{-\lambda_N\tau_N}-(1-\varepsilon)\left(\Gamma_N+e^{-\lambda_N\tau_N}\right) \tag{2.79}$$

$$f2_N(\varepsilon,\Gamma,\lambda,\tau)=1-\Gamma_N e^{-\lambda_N\tau_N}-(1-\varepsilon)\left(\Gamma_N-e^{-\lambda_N\tau_N}\right) \tag{2.80}$$

More compactly, the matrix equation can be written

$$\overleftrightarrow{\mathbf{A}}\vec{\mathbf{Y}}=\vec{\mathbf{C}} \tag{2.81}$$

The *2N* by *2N* matrix is inverted using a singular value decomposition algorithm, a robust technique that ensures that near-singular intermediate steps in the solution do not present numerical difficulties [*Press et al.*, 1988]. The $Y1_i$ and $Y2_i$ coefficients are obtained from

$$\vec{\mathbf{Y}}=\overleftrightarrow{\mathbf{A}}^{-1}\mathbf{C} \tag{2.82}$$

Inserting the $Y1_i$ and $Y2_i$ coefficients into the flux equations (2.66) and (2.67), the upward and downward fluxes as a function of optical depth within any layer are obtained. Fluxes are calculated in each layer, but they must also be calculated for each wavenumber and Gaussian subinterval. Parameters γ_1 and γ_2 from (2.62) and (2.63) are therefore

$$\gamma 1_{ijl} = 2 - \omega_{0ijl}\left(1 + g_{ijl}\right) \tag{2.83}$$

$$\gamma 2_{ijl} = \omega_{0ijl}\left(1 - g_{ijl}\right) \tag{2.84}$$

which go into

$$\lambda_{ijl} = \left(\gamma 1_{ijl}^2 - \gamma 2_{ijl}^2\right)^{1/2} \tag{2.85}$$

$$\Gamma_{ijl} = \frac{\gamma_{2ijl}}{\gamma_{1ijl} + \lambda_{ijl}} \tag{2.86}$$

The full description of the flux equations is thus

$$F_{ijl}^{+}\left(\tau_{jl}\right) = Y_{1ijl}\left[e^{-\lambda_{ijl}\left(\tau_{ijl} - \tau_{jl}\right)} + \Gamma_{ijl} e^{-\lambda_{ijl}\tau_{jl}}\right] + Y_{2_{ijl}}\left[e^{-\lambda_{ijl}\left(\tau_{ijl} - \tau_{jl}\right)} - \Gamma_{ijl} e^{-\lambda_{ijl}\tau_{jl}}\right] + C_{ijl}^{+}\left(\tau_{jl}\right) \tag{2.87}$$

$$F_{ijl}^{-}\left(\tau_{jl}\right) = Y_{1ijl}\left[\Gamma_{ijl} e^{-\lambda_{ijl}\left(\tau_{ijl} - \tau_{jl}\right)} + e^{-\lambda_{ijl}\tau_{jl}}\right] + Y_{2ijl}\left[\Gamma_{ijl} e^{-\lambda_{ijl}\left(\tau_{ijl} - \tau_{jl}\right)} - e^{-\lambda_{ijl}\tau_{jl}}\right] + C_{ijl}^{-}\left(\tau_{jl}\right) \tag{2.88}$$

The infrared fluxes are actually calculated from a 4-dimensional array, of which (2.78) is a single *2N* x *2N* slice. Matrix inversions are applied *M* x *ngaus*s times to evaluate the *2N* x *M* x *ngauss Y*-coefficients and calculate the complete set of infrared fluxes for each layer, wavenumber interval, and Gaussian subinterval. Fluxes at each layer *i* and wavenumber interval *j* are then found by Gaussian quadrature

$$F_{ij}^{+} = \sum_{l=0}^{ngauss-1} w_l F_{ijl}^{+}\left(\frac{\tau_{ijl}}{2}\right) \tag{2.89}$$

$$F_{ij}^{-} = \sum_{l=0}^{ngauss-1} w_l F_{ijl}^{-}\left(\frac{\tau_{ijl}}{2}\right) \tag{2.90}$$

Net fluxes over the infrared spectrum are

$$F_i^+ = \sum_{j=0}^{M-1} F_{ij}^+ \tag{2.91}$$

$$F_i^- = \sum_{j=0}^{M-1} F_{ij}^- \tag{2.92}$$

Radiative-Convective Equilibrium Calculations

Radiative Equilibrium

The approach to calculating equilibrium states for the Venus atmosphere involves first calculating the temperature structure for radiative equilibrium, and then making adjustments to the lapse rate to account for convection. The rate of change in temperature at a given atmospheric level must depend on the amount of energy that is deposited into it. So the local heating rate is proportional to the divergence of the net flux and inversely proportional to its heat capacity

$$\rho c_P\left(\frac{\partial T}{\partial t}\right) = -\frac{\partial}{\partial z}\left(F_S - F\right) \tag{2.93}$$

where ρ and c_P are the density and specific heat, F_S is the net solar flux and F the net infrared flux. All are functions of altitude, z. Integrating over the vertical extent of the atmosphere provides the total heating rate of the atmosphere

$$\int_0^{z_\infty} \rho c_P\left(\frac{\partial T}{\partial t}\right)dz = F(z) - F_S(z) \tag{2.94}$$

In thermodynamic equilibrium the atmosphere is neither heating up nor cooling down, so the left hand side of (2.94) must be *0*. So radiative equilibrium is defined by

$$F(z) = F_S(z) \tag{2.95}$$

In the Venus radiative transfer model, iterations of the temperature structure are made to allow the infrared flux to converge to the observed net solar flux profile. Solar flux in the Venus atmosphere was measured with the solar flux radiometer aboard the Pioneer Venus sounder probe. Upward and downward solar fluxes were obtained in a broad channel, from 0.4 to 1.0 μm, at vertical resolutions of from 100 to 500 m [*Tomasko et al.*, 1980]. These data are shown in Figure 2.17.

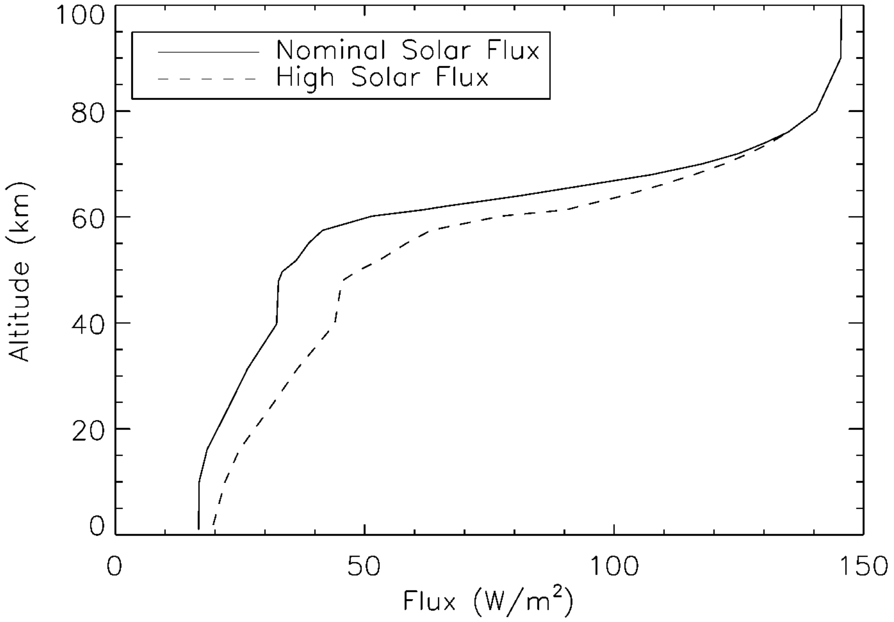

Figure 2.17 Net solar flux in the Venus atmosphere, as measured by the Pioneer Venus solar flux radiometer [*Tomasko et al.*, 1980].

For all the results reported here, the 'nominal' solar flux profile was used. Approximately 2.5% of the sunlight incident on the planet makes it to the ground, with most of what is not reflected to space being absorbed in the clouds.

Infrared fluxes were first calculated for an initial temperature structure, usually that from the Venus International Reference Atmosphere [*Kliore et al.*, 1986]. In general, these initial fluxes will not exactly balance the net solar flux as in (2.95) so that for the *i*th layer

$$F\_init_i - F_{Si} = R_i \tag{2.96}$$

where F_init_i are the net infrared fluxes calculated from the initial temperature profile and R_i represent the residual infrared fluxes. The fluxes, in addition to being dependent on the opacity of the atmosphere, also depend on the way it emits at all levels, or its temperature profile. For a given atmospheric composition, a unique temperature profile must exist in order for the fluxes to be such that (2.95) is true. We wish to calculate a new temperature profile so that all $R_i = 0$. The procedure that follows was used to calculate radiative equilibrium in the atmosphere of Titan [*McKay et al.*, 1989]. Very generally, the variation in the flux of the *i*th layer due to changes in temperatures at all levels may be approximated by the first terms in Taylor series expansions

$$dF_i = \frac{\partial F_i}{\partial T_0}\delta T_0 + \frac{\partial F_i}{\partial T_1}\delta T_1 + \ldots + \frac{\partial F_i}{\partial T_N}\delta T_N \tag{2.97}$$

The $\delta T_{i'}$ are perturbations to the temperature at each level, and the derivatives $dF_i/dT_{i'}$ represent the sensitivity of the flux at layer i to changes in temperature at level i'. Fluxes are calculated at the layer midpoints, as in (2.89) and (2.90), but their variations are determined from perturbations in temperatures at the layer boundaries (levels). The iterative procedure described below is numerically unstable if temperature perturbations are effected at the layer midpoints. This is probably due to the approximate nature of the expansion (2.97), and the propagation of 2nd order errors that do not diminish with each iteration. The sensitivity of the flux at all layers may be expressed as a matrix equation

$$\mathbf{d}\vec{\mathbf{F}} = \overleftrightarrow{\mathbf{J}}\delta\vec{\mathbf{T}} \tag{2.98}$$

where ***J*** is the Jacobian matrix defined by

$$J_{ii'} = \frac{\partial F_i}{\partial T_{i'}} \tag{2.99}$$

The objective is to calculate perturbations $\delta T_{i'}$ to the initial temperature profile that result in infrared fluxes such that all $R_i = 0$ in (2.96). This can be accomplished by identifying $-R_i$ with dF_i and inverting the matrix equation (2.98). Solving for $\delta T_{i'}$ will give the temperature corrections from the residual fluxes that are necessary to achieve fluxes for radiative equilibrium. Thus

$$\delta\vec{\mathbf{T}} = \vec{\mathbf{J}}^{-1}\left(-\vec{\mathbf{R}}\right) \tag{2.100}$$

The elements of the Jacobian matrix (2.99) were calculated using a numerical procedure. The temperature was perturbed for one level at a time, and the resulting infrared fluxes for the whole atmosphere were calculated. If the temperature at level *i'* was perturbed, and the net infrared flux at level *i* that result are designated F_i^p, then the matrix elements are

$$J_{ij} = \frac{F_i^p - F_i}{\Delta T} \tag{2.101}$$

where ΔT is the magnitude of the temperature perturbation. Typically, perturbations of 1 K provided the appropriate deviation in fluxes at all levels to accurately calculate the derivatives in (2.101). This procedure was repeated by perturbing one and only one layer at a time, and recalculating all the perturbed fluxes. So the whole procedure requires the calculation of N^2 upward and downward fluxes. The matrix equation (2.100) was solved by inverting ***J*** using LU decomposition [*Press et al.*, 1988]. The new temperatures at the levels *i* are then

$$T_{new\,i} = T_i + \delta T_i \tag{2.102}$$

Since (2.97) is only an approximation to the full sensitivity of the infrared fluxes to changes in temperature, this procedure is inexact. It is iterated until the maximum temperature difference between two subsequent temperature calculations is less than 1 K. Since the second order (error) terms are of higher order than the temperature corrections themselves, this procedure is rapidly convergent; from 3 to 7 iterations are usually required. The final level temperatures are designated T_{rei}.

Convection

Once the radiative equilibrium temperature profile has been calculated, adjustments were made to it to account for convection. The dry adiabatic lapse rate is

$$\frac{\partial T(z)}{\partial z} = -\frac{g}{c_P} \tag{2.103}$$

If in any region the atmosphere is opaque enough, the transport of energy by convection may become more efficient. For sufficiently high temperature gradients, the atmosphere becomes unstable with respect to convection. Specifically, when the lapse rate resulting from radiative equilibrium exceeds (2.103), it is assumed that convection occurs. In general, unstable regions may exist in several disconnected layers, so the following procedure is applied to the entire atmosphere, one layer at a time, starting at the top. In the model, the adiabatic lapse rate for layer *i* is calculated from

$$\Gamma_{ad_i} = \frac{gl_i}{c_{pl_i}} \tag{2.104}$$

where gl_i is the layer-averaged gravitational acceleration and c_{Pl_i} is the layer averaged specific heat at constant pressure. The radiative equilibrium lapse rate in the layers is computed from

$$\Gamma_{re_i} = \frac{T_i - T_{i+1}}{z_i - z_{i+1}} \tag{2.105}$$

and the radiative-convective equilibrium profile is calculated from

$$T_{rcon_i} = T_{re_i} + \left(\Gamma_{re_i} > \Gamma_{ad_i}\right)\left(z_{i-1} - z_i\right) \tag{2.106}$$

where > is interpreted to mean 'whichever is greater'. Since this changes the relationship between P_i, T_i and z_i in hydrostatic balance, these variables are recomputed to be consistent with hydrostatic balance via (2.8) and the process is iterated to obtain a final T_{rconi}.

Results from the Venus Radiative Transfer Model

The purpose of the Venus radiative transfer model is two-fold:

1. Accurately describe the globally-averaged temperature structure resulting from radiative-convective equilibrium.
2. Provide a flexible model for investigating changes in the state of the atmosphere that result from changes in atmospheric composition, solar flux, and cloud structure.

Results from the nominal model, whose parameters have been described above, are shown first. Following this is a discussion of the results achieved from varying sources of opacity in the Venus atmosphere, and their overall impact on the Venus greenhouse effect.

Current Venus Atmosphere

The temperature as a function of altitude, as calculated by the nominal model, is shown in Figure 2.18. Plotted along with it is the VIRA atmospheric temperature profile. They are matched extremely well everywhere except above 70 km. As noted by some workers [*Crisp*, 1986; *Tomasko et al.*, 1980], some extra source of opacity above the cloud tops is necessary in models to accurately predict the upper atmosphere temperature structure. Additionally, UV deposited in the atmosphere, mostly above 70 km, has not been accounted for, since the net solar fluxes used from Pioneer Venus have a cutoff at 0.4 μm [*Tomasko et al.*, 1980]. The addition of mode 3 particles above 65 km, with a scale height of 4 km was necessary to achieve this excellent agreement between the Venus radiative transfer model and the VIRA temperature structure.

The atmospheric stability of the calculated temperature profile, defined by

$$S_i = \Gamma_{ad_i} + \frac{\partial T_i}{\partial z_i} \tag{2.107}$$

is shown in Figure 2.19. It may be compared with the observed static stability and results from an earlier Venus radiative transfer model (that included far fewer infrared absorption bands and no scattering in the infrared) in Figure 2.20 [*Pollack et al.*, 1980]. In all cases, the atmosphere is close to adiabatic from 0 - 30 km and in the middle cloud region from 48 to 55 km. Above the middle cloud, the atmosphere becomes strongly stable. Differences in structure in the plots of Figures 2.19 and 2.20 are largely due to the fact that there were only 20 atmospheric layers used in the present model.

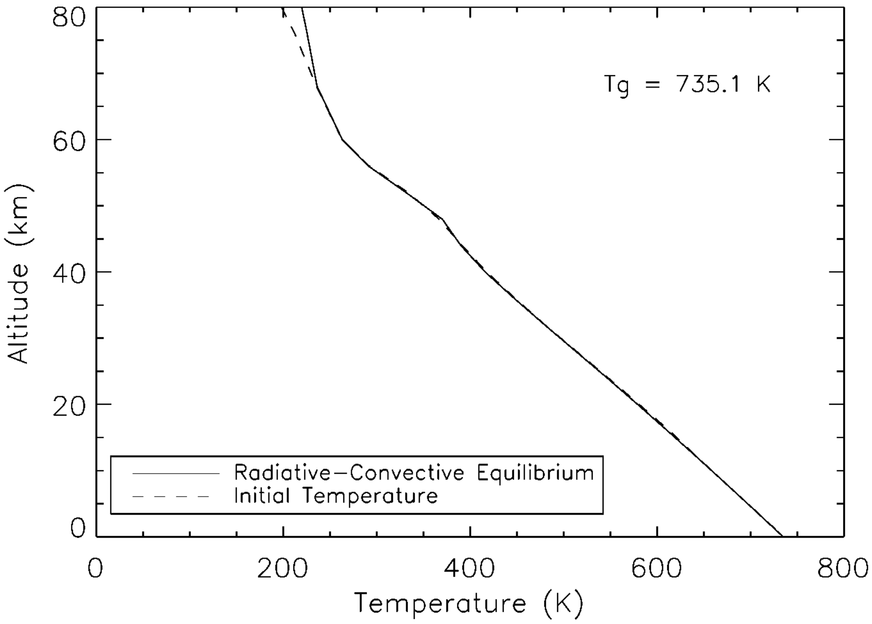

Figure 2.18 Temperature profile calculated from the Venus radiative transfer model (solid line). For comparison, the Venus International Reference Atmosphere is plotted with a dashed line [*Kliore et al.*, 1986].

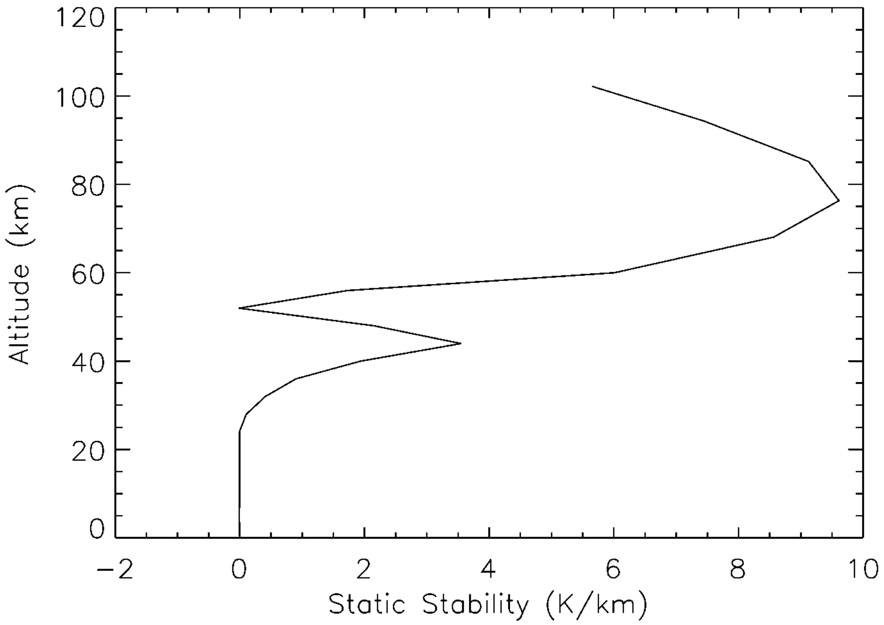

Figure 2.19 Stability structure of the atmosphere calculated from the Venus radiative transfer model. The stability parameter is the difference between the adiabatic and actual lapse rates.

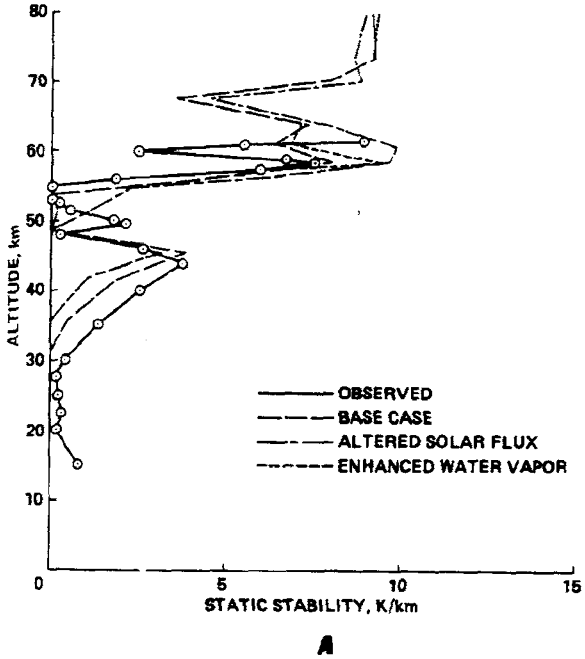

Figure 2.20 Stability structure from the *Pollack et al.* [1980] Venus radiative transfer model, and comparison with the observed static stability (solid line). The stability parameter is the difference between the adiabatic and actual lapse rates.

Calculated outgoing infrared radiation from the top of Venus' atmosphere is shown in Figure 2.21. Also plotted is the Planck function at 232 K, the approximate temperature at which the Venus atmosphere emits. Less flux is being emitted at 666 cm^{-1} due to the 15 µm CO_2 band; the atmosphere is absorbing in this band above the average level of the 232 K emission. A major fraction of the net flux is emitted in the 2.1 to 2.6 µm CO_2 window region. Although opacity due to the CO_2 continuum and 2.3 µm CO band contribute here, the peak of the Planck function near the surface is at a longer wavelength (6.8 µm in wavelength space). Raising the surface temperature would shift emission into this window, decreasing the efficiency of the greenhouse effect and limiting a further rise in surface temperature.

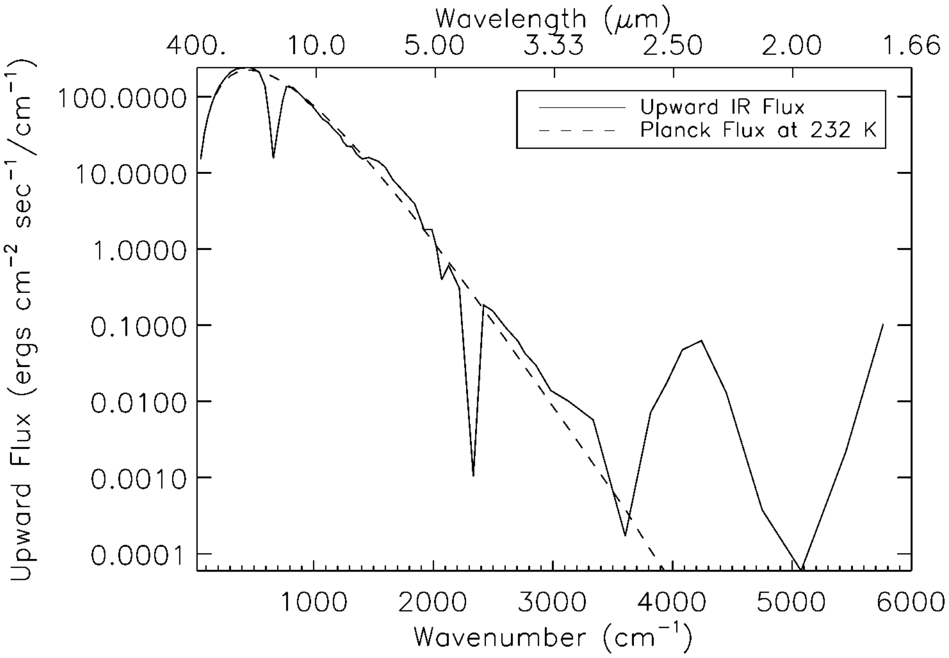

Figure 2.21 Outgoing thermal infrared fluxes in cgs units as a function of wavenumber from the Venus radiative transfer model (solid line). The dashed line is the Planck function evaluated at the effective radiating temperature of Venus, 232 K, calculated from (2.2).

The net thermal flux at the surface is shown in Figure 2.22, along with the Planck emission from the surface. The most significant window region is between 2.1 μm and 2.7 μm, between major CO_2 bands, as well as shortward of 2.0 μm where the near IR H_2O infrared windows begin. Significant flux from the surface also escapes nearer the peak of the Planck function at 3.5 and 5.8 μm. For comparison, net thermal fluxes at several levels for the models of *Pollack et al.* [1980] are shown in Figure 2.23. Major features of the spectral fluxes are similar at both the surface and top of the atmosphere, although the spectral resolutions are dissimilar.

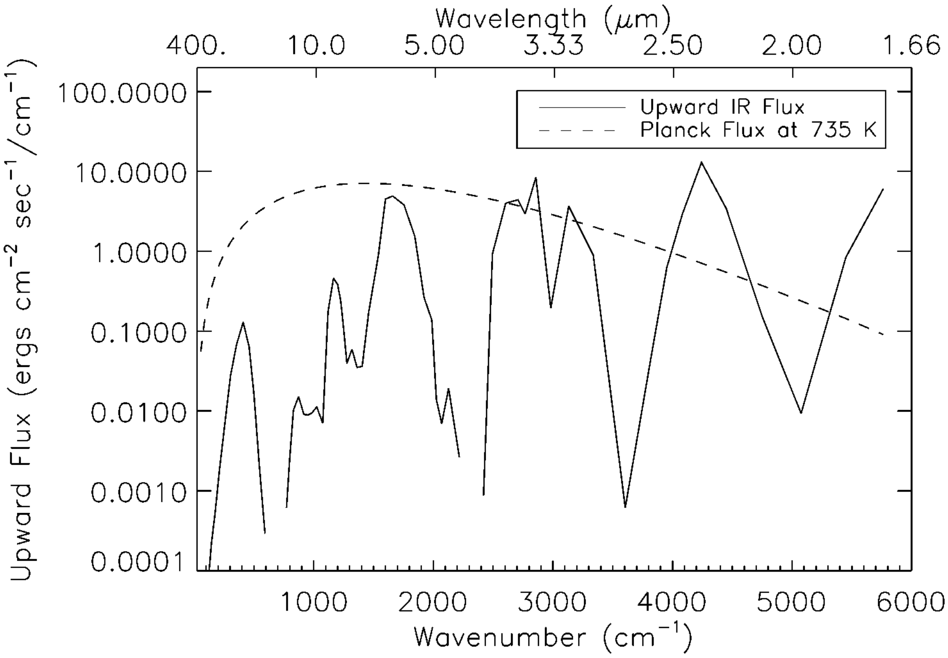

Figure 2.22 Net thermal infrared flux at the surface of Venus;in cgs units, as a function of wavenumber (solid line). The Planck emission from the surface, divided by 1000, is shown with a dashed line.

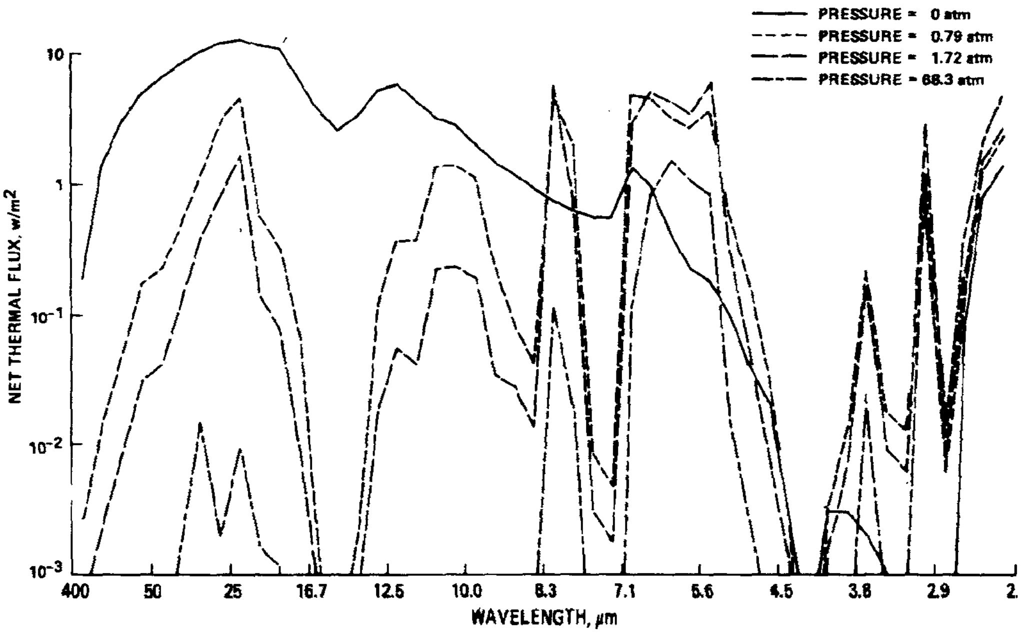

Figure 2.23 Net thermal infrared flux at several layers, from the model of *Pollack et al.* [1980].

Sensitivity of the Venus Greenhouse to Changes in Trace Species

In order to assess the sensitivity of the Venus greenhouse effect to sources of opacity in the atmosphere, various radiatively active gases were removed and the full model calculations performed. In all cases, the total pressure remained constant. This was achieved by slightly increasing the mixing ratio of N_2. Except for the case where the clouds were removed, particle mode number densities as a function of altitude and their resulting opacity remained constant. In addition, the solar net flux was not altered. These results are shown in Table 2.4, and may be compared with a similar exercise from *Pollack et al.* [1980] Venus greenhouse models, shown in Table 2.5.

Table 2.4 The Effect of the Removal of Sources of Opacity on Surface Temperature

Source Deleted	Change in Surface Temperature
HCl	1.5 K
CO	3.3 K
SO_2	2.5 K
Clouds	142.8 K
H_2O	68.8 K
OCS	12.0 K
CO_2	422.7 K

Table 2.5 Removal of Sources of Opacity in the Models of *Pollack et al.* [1980].

Source Deleted	Change in Surface Temperature
HCl	0.1
CO	13
SO_2	52
Clouds	113
H_2O	218
CO_2	463

Water

Removing H_2O in the present model results in a smaller reduction in surface temperature than in the models of *Pollack et al.* [1980]. The reason is probably due to the inclusion in the present model of a more complete spectral database for CO_2. At low abundances, H_2O is less effective at filling CO_2 windows than in the models of *Pollack et al.* [1980]. The effect on the opacity of removing H_2O is shown in Figure 2.24. The solid line is the optical depth as a function of wavenumber for the nominal Venus atmosphere, while the dashed line shows the opacity for the atmosphere without H_2O vapor.

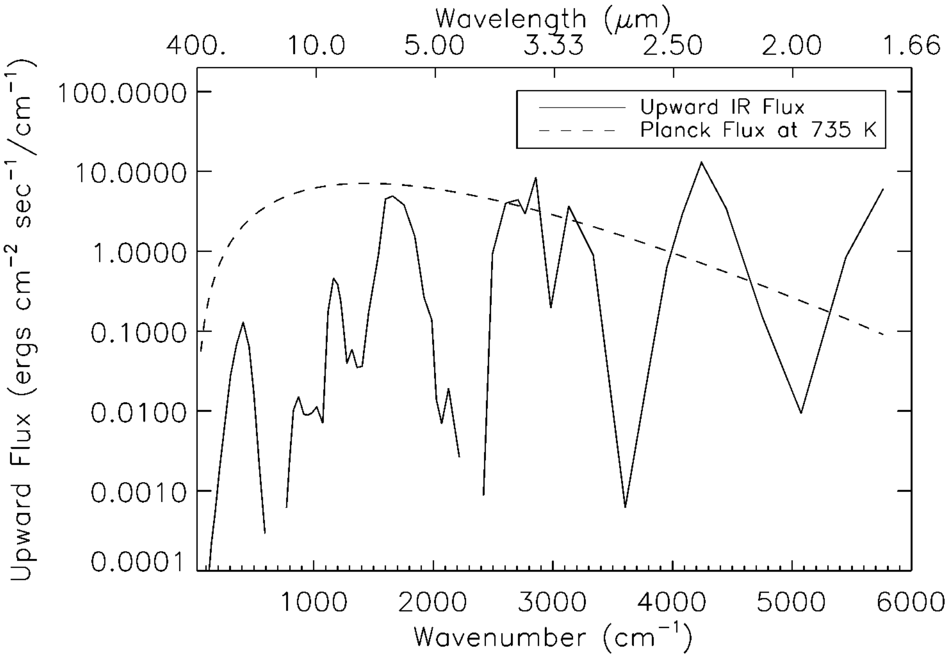

Figure 2.24 Optical depth as a function of wavenumber due to the removal of H_2O in the Venus atmosphere. The solid line is the opacity due to the nominal atmospheric mixing ratios of Figure 2.1. Optical depths due to the removal of H_2O are shown with a dashed line.

Eliminating the H_2O continuum eliminates most of the opacity shortward of 1100 cm^{-1}. The important spectral region between the 15 μm and 4.3 μm bands of CO_2 is also affected by the lack of absorption from the 6.3 μm H_2O band. The resulting temperature structure is shown in Figure 2.25. Increasing H_2O abundance results in a more effective greenhouse effect due to increased opacity between the major CO_2 bands at 15 μm, 4.3 μm, 2.8 μm and 2.0 μm. Increased continuum absorption by H_2O also contributes opacity above 100 μm. A comparison of the optical depth vs. wavenumber for the nominal Venus model and the atmosphere enhanced 100-fold in H_2O is shown in Figure 2.26. The resulting temperature structure comparison is given in Figure 2.27.

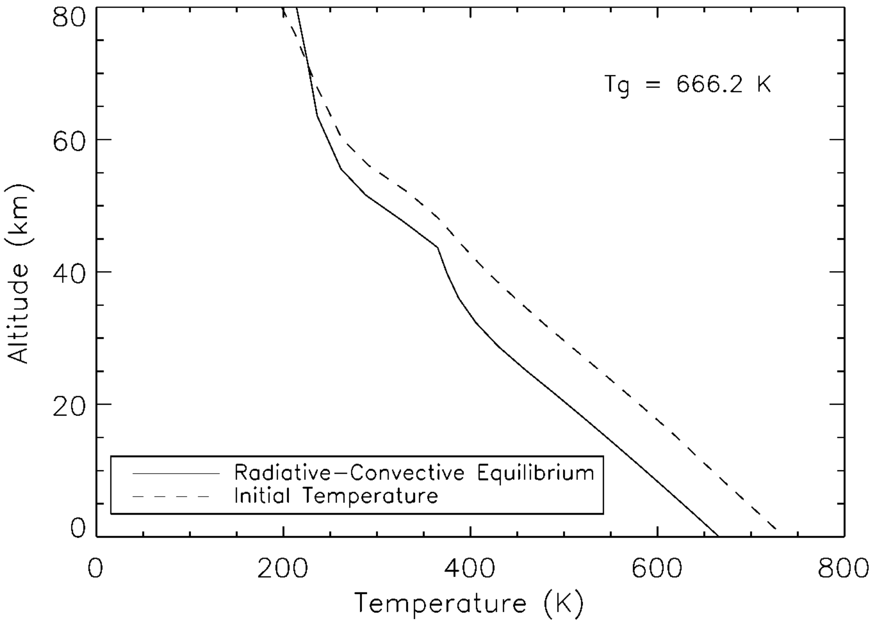

Figure 2.25 Temperature structure upon removal of H_2O in Venus' atmosphere (solid line). For comparison, the Venus International Reference Atmosphere is plotted with a dashed line [*Kliore et al.*, 1986].

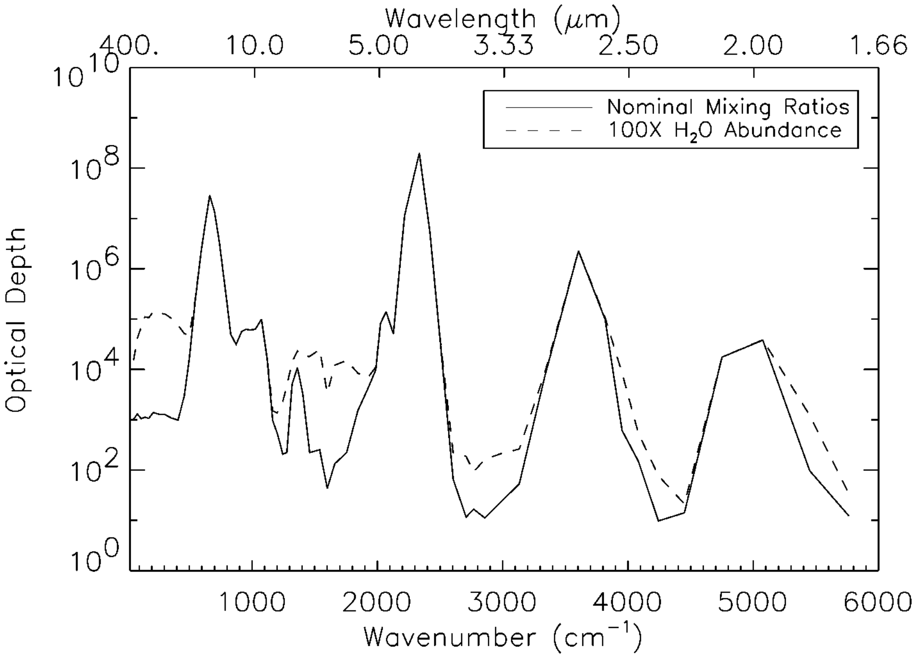

Figure 2.26 Optical depth due to a 100-fold increase in H_2O in Venus' atmosphere. The solid line is the opacity due to the nominal atmospheric mixing ratios of Figure 2.1. Optical depth due to the 100-fold increase in atmospheric H_2O is shown with a dashed line.

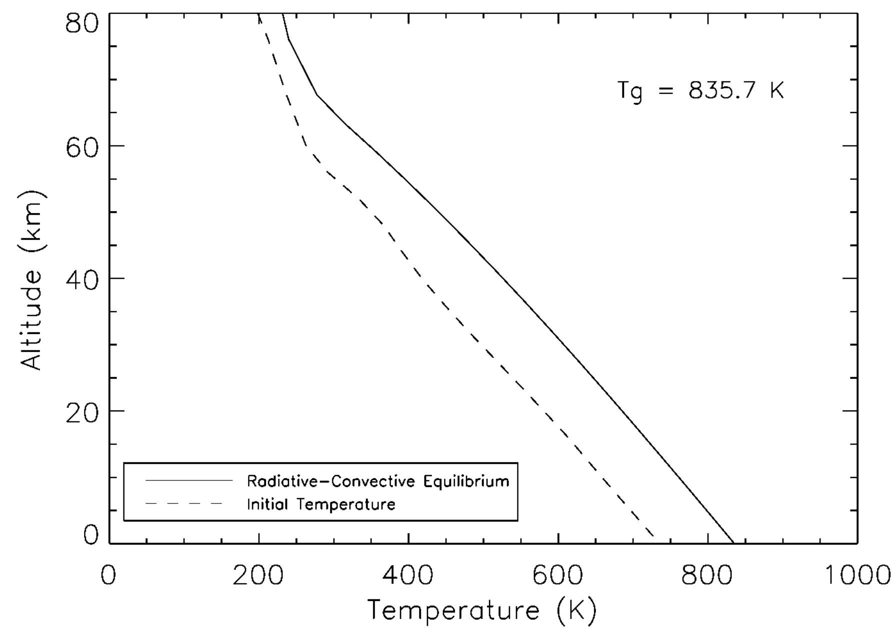

Figure 2.27 Temperature structure resulting from a 100-fold increase in H_2O in Venus' atmosphere (solid line). For comparison, the Venus International Reference Atmosphere is plotted with a dashed line [*Kliore et al.*, 1986].

The ground temperature increases to 835.7 K, an increase of 100.6 K. The outgoing infrared flux for the 100X H_2O enhanced atmosphere is shown in Figure 2.28. Comparing this with Figure 2.21, it can be seen that outgoing fluxes at 6.3 µm are increased due to increased emission. Model runs were performed for a range of H_2O vapor abundances, and the sensitivity of the surface temperature to H_2O abundance is shown in Figure 2.29. Surface temperatures vary from 666.2 K to 835.7 K as the total H_2O abundance changes from 0 to 100 times the current amount.

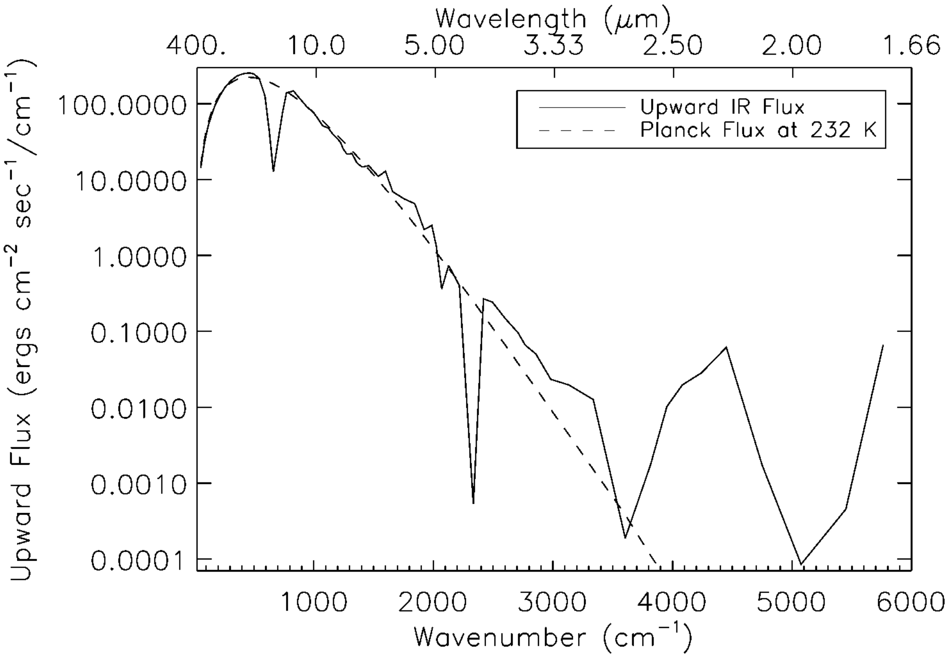

Figure 2.28 Outgoing infrared fluxes for a 100-fold increase in H_2O in the Venus atmosphere (solid line). The dashed line is the Planck function evaluated at the effective radiating temperature of Venus, 232 K, calculated from (2.2).

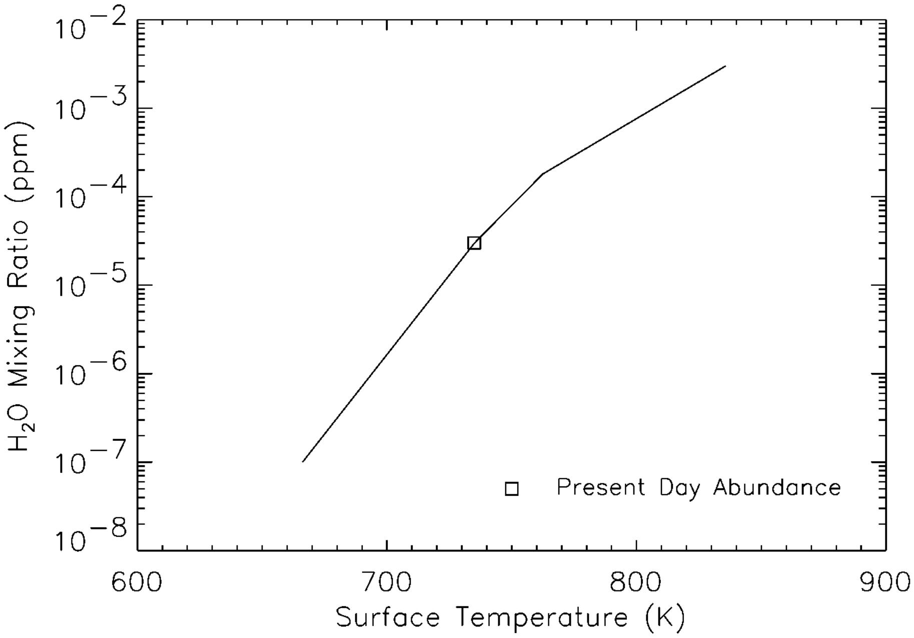

Figure 2.29 Surface temperature vs. H_2O abundance in the Venus atmosphere (solid line).

Sulfur Dioxide

Considering SO_2 abundance variation is important because it may change considerably in Venus' atmosphere over time. It is no doubt a major constituent of volcanic emissions, and it may play a major role in reactions with surface rocks [*Fegley and Treiman*, 1992]. It also is the primary source of sulfur for Venus' clouds, whose albedo controls the energy balance of the planet. Removing SO_2 results in only a 2.5 K reduction in surface temperature, again, a result that shows it is less influential on Venus' greenhouse effect than found by *Pollack et al.* [1980]. Increasing its abundance, however, can have a slightly greater effect. Figure 2.30 shows a comparison of the optical depth vs. wavenumber for the nominal Venus atmosphere and the optical depth for the atmosphere enhanced 100-fold in SO_2. Opacity is increased from a band at 7.1 μm , resulting in a surface temperature that is

11.1 K higher. The atmospheric temperature structure for an SO_2 abundance increased this much is shown in Figure 2.31. Model runs were also performed for a range of SO_2 abundances, and the sensitivity of the surface temperature is shown in Figure 2.31.

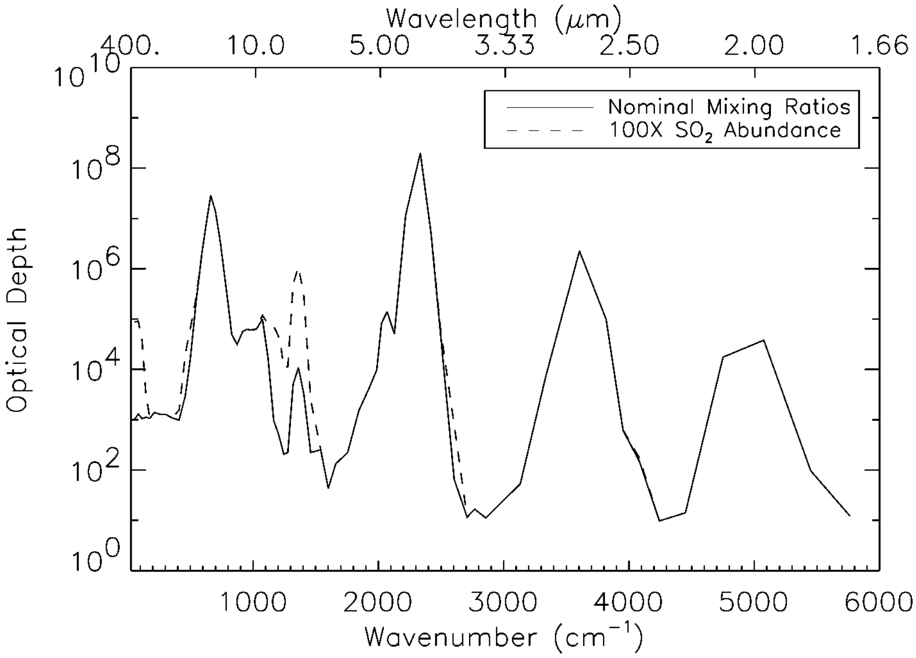

Figure 2.30 Optical depth for a 100-fold increase in SO_2 in the Venus atmosphere. The solid line is the opacity due to the nominal atmospheric mixing ratios of Figure 2.1. Optical depth due to the 100-fold increase in atmospheric SO_2 is shown with a dashed line.

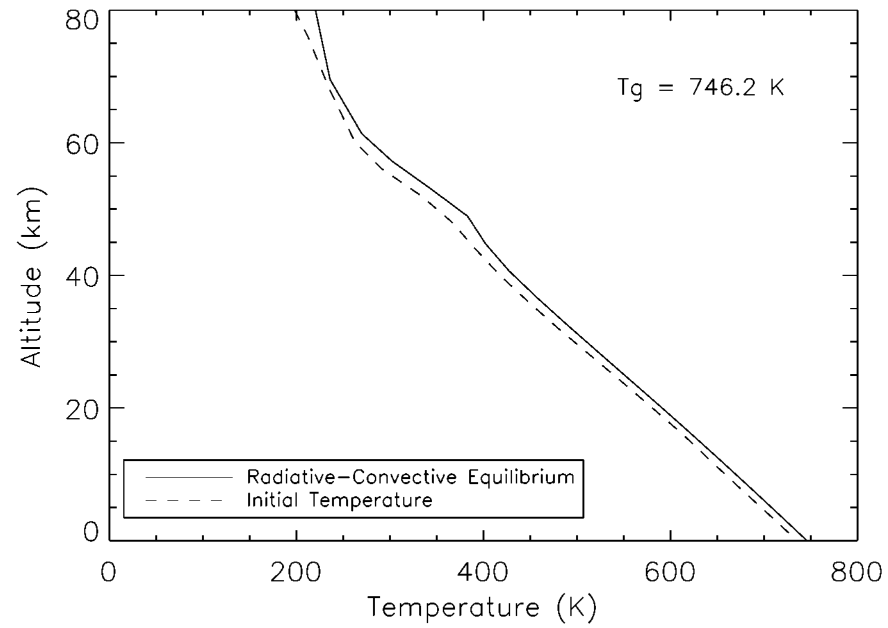

Figure 2.31 Temperature structure for a 100-fold increase in SO_2 in the Venus atmosphere (solid line). For comparison, the Venus International Reference Atmosphere is plotted with a dashed line [*Kliore et al.*, 1986].

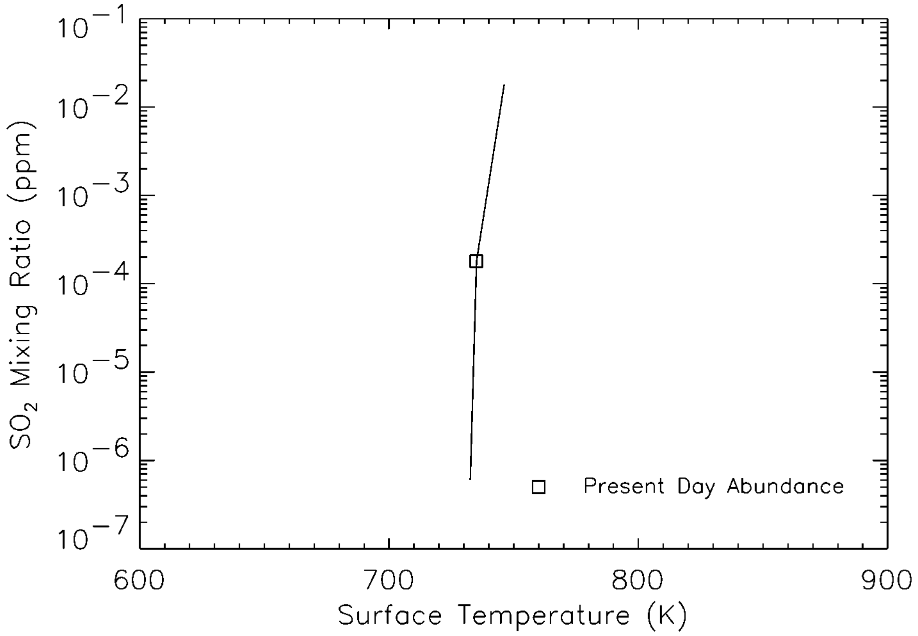

Figure 2.32 Surface temperature vs. SO_2 abundance in the Venus atmosphere.

OCS

The primary effect OCS, or carbonyl sulfide, has on the energy balance of Venus' atmosphere is in the CO_2 window region between 2.1 and 2.6 μm. A strong band at 2.4 μm accounts for sufficient opacity that the temperature cools 12 K when it is removed. Because this window region is where most of the thermal flux from the surface makes its way to space, OCS opacity in this region is important. Sulfur chemistry and the equilibrium abundance of OCS in the atmosphere can have a potentially significant effect on the surface temperature. A comparison of the optical depths in the nominal atmosphere with that of the atmosphere without OCS is shown in Figure 2.33. The decrease in opacity between 2.2 and 2.7 μm is apparent.

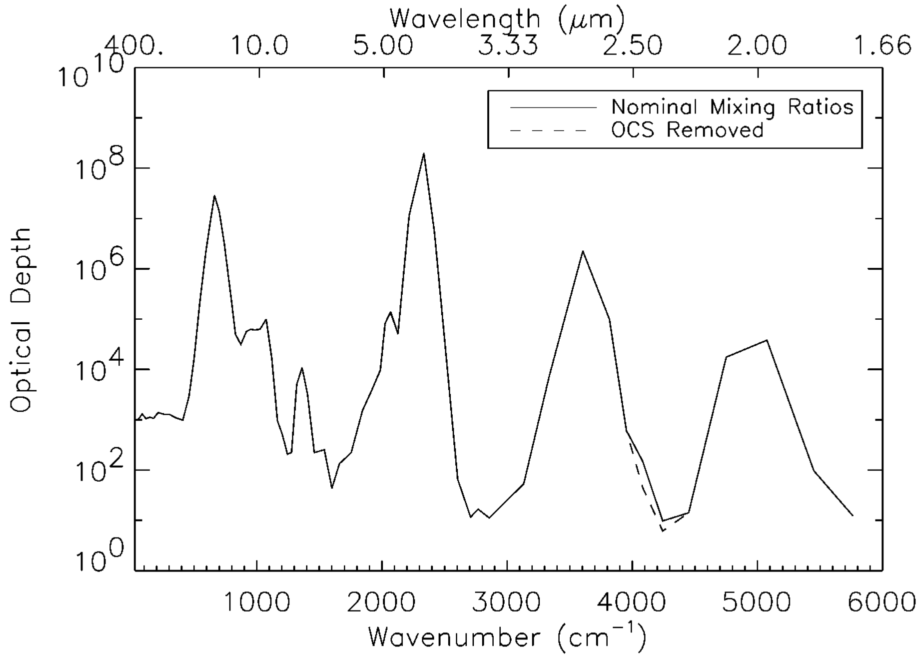

Figure 2.33 OCS: A comparison of optical depths at the surface for the nominal atmosphere (solid lines) and for the atmosphere with OCS removed (dotted line).

Clouds

The primary effect of removing clouds is on the albedo, resulting in a large increase in incoming solar radiation. Here, I consider only the thermal radiative effects of cloud opacity. If cloud opacity is removed in the Venus radiative transfer model, while keeping the solar flux profile of Figure 2.17, the surface temperature cools by 142.8 K. The temperature structure that is obtained from radiative-convective equilibrium is shown in Figure 2.34. The temperature lapse rate is adiabatic up to about 40 km. Above this, there appears a strong temperature inversion due to the absorption of sunlight that is not compensated for by the thermal radiative properties of the clouds.

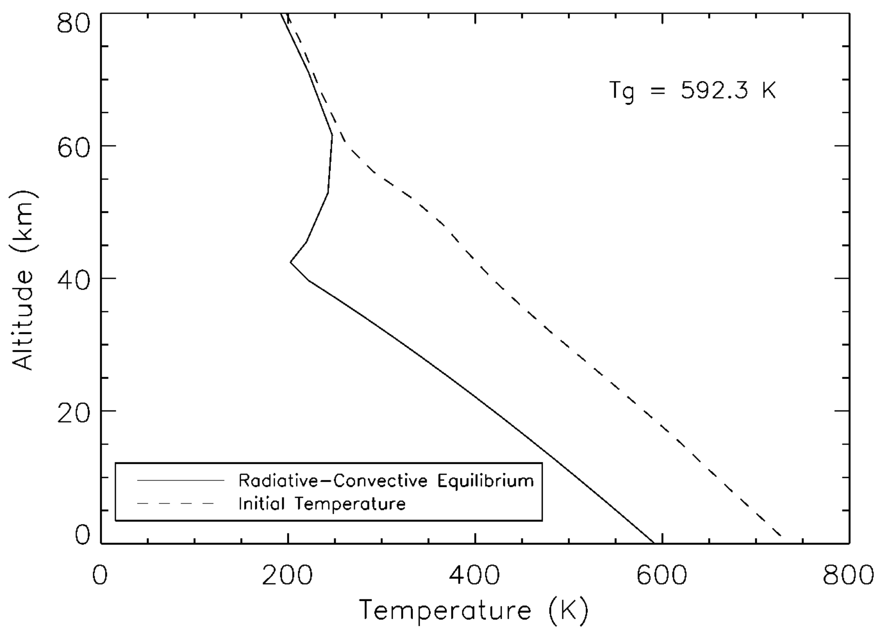

Figure 2.34 Atmospheric temperature structure resulting from removing the clouds (solid line). Only the radiative effects of the clouds in the infrared is removed; changes in solar flux absorption are not included. For comparison, the Venus International Reference Atmosphere is plotted with a dashed line [*Kliore et al.*, 1986].

The net outgoing thermal radiation is shown as a function of wavenumber in Figure 2.35. There is slightly more radiation from the surface leaking through, particularly at 3.5 μm, but some of the outgoing emission at 2 μm is missing due to a cooler atmosphere at cloud levels (compare with Figure 2.21). Since an increase in solar absorption accompanying cloud loss will increase the effective radiating temperature of the planet via (2.2), the effects will be more profound than what is found here. Modeling the structure and albedo effects of the clouds associated with changes in atmospheric abundances of SO_2 and H_2O is the subject of the next chapter.

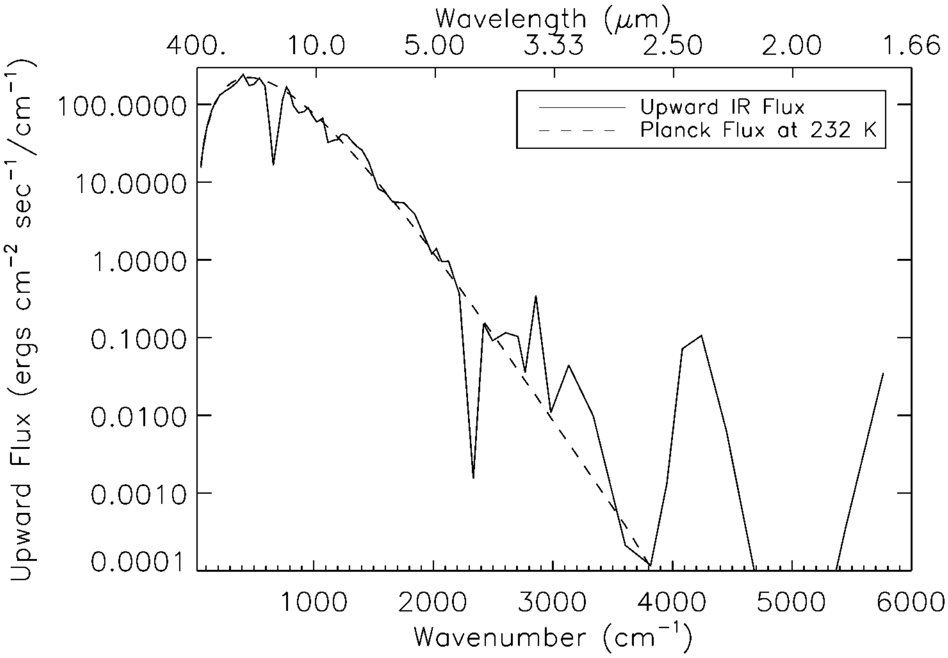

Figure 2.35 Outgoing thermal infrared flux of the Venus atmosphere with the clouds removed (solid line). The dashed line is the Planck function evaluated at the effective radiating temperature of Venus, 232 K, calculated from (2.2).

CHAPTER 3

ATMOSPHERIC CHEMISTRY AND CLOUDS

Current Knowledge of Venus clouds and Atmospheric Chemistry

The clouds of Venus occupy the atmosphere from 48 km to 70 km, with fine hazes above and below [*Esposito et al.*, 1983]. The upper layer, extending from about 57 km to 68 km, is the most tenuous and composed mostly of mode 1 particles (r_{ave} = 0.3 μm, Table 2.3). Its total optical depth at 0.63 μm is about 7. Just beneath the upper cloud is a clear region, about 1 km in depth [*Knollenberg and Hunten*, 1980], at an altitude where the atmospheric stability is rapidly increasing (Figures 2.19 and 2.20). The middle cloud, with an optical depth at 0.63 μm of about 9, extends from 51-56 km, and has contributions from all particle size modes, although the largest numbers are from modes 2 and 2' (r_{ave} = 1.0 and 1.4 μm). Another clear region of several 100 m depth separates the middle cloud from the lower, a relatively thicker condensation cloud. The lower cloud is the most compact, extending from the cloud base at 48 km to 50 km, but with an optical depth of about 10, due mostly to mode 3 (r_{ave} = 3.65 μm) aerosol opacity

Infrared images of Venus taken of its dark side at 2.3 μm by the Galileo Near Infrared Mapping Spectrometer (NIMS) show spatially varying brightness [*Carlson et al.*, 1993]. Most of the flux at 2.3 μm is generated deep in the atmosphere below the clouds and transported through the 2.1-2.6 μm CO_2/H_2O window (Figure 2.22). Bright regions in Figure 3.1 are due to IR emission from below leaking through the clouds. The lower clouds are probably thin or patchy in places [*Carlson et al.*, 1993; *Grinspoon et al.*, 1993], perhaps the result of up and down drafts at this level. Because of the importance of the 2.1-2.6 μm window region to the energy balance of

Venus' atmosphere, cloud patchiness and distribution may have a significant effect on the global energy balance. For the one-dimensional cloud and radiative transfer models, however, I employ globally averaged properties for the cloud structure, and leave an analysis of the effects of cloud variability to future work.

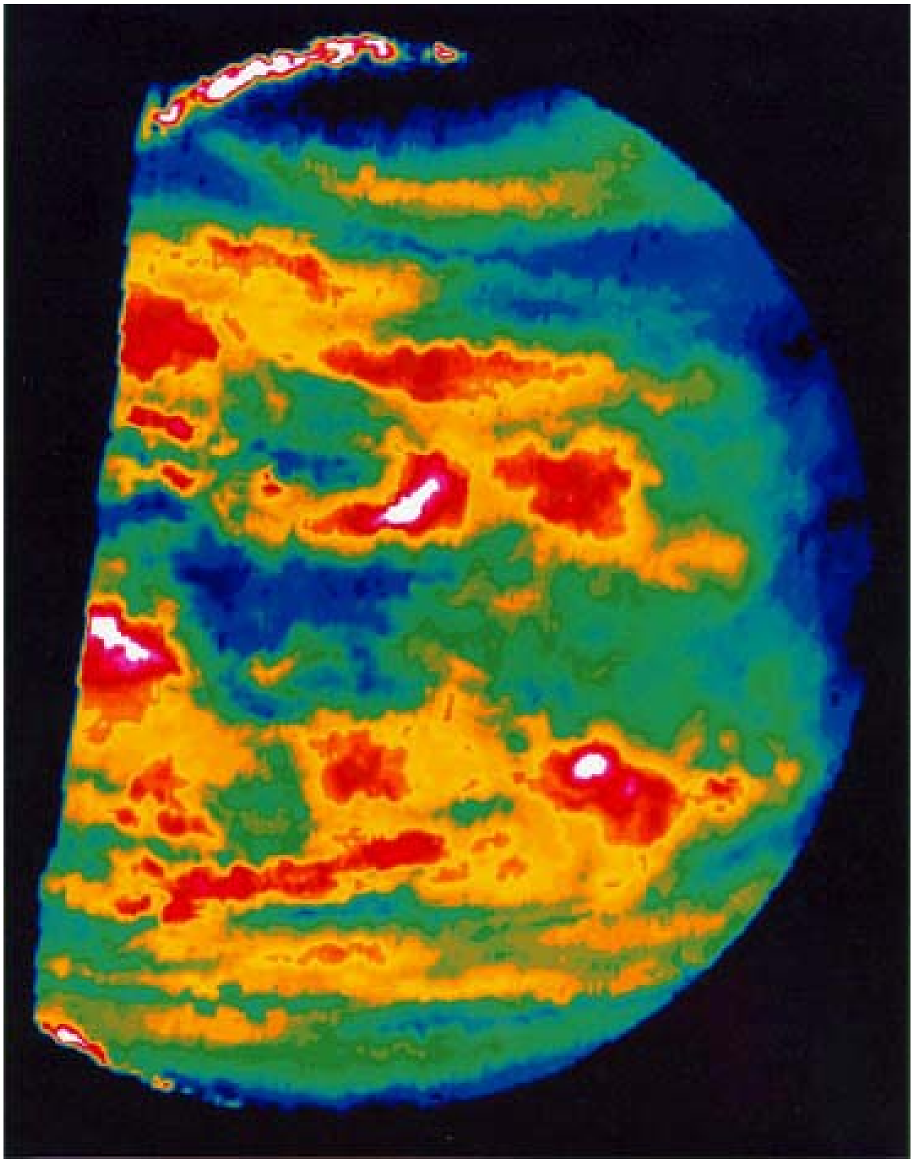

Figure 3.1 2.3 μm emission as imaged by the Galileo NIMS instrument. Bright regions are where upwelling radiation originating from below the clouds is shining through. Lower cloud patchiness is probably responsible for the variable effectiveness of the 2.1-2.6 μm IR window.

The photo-assisted reaction of atmospheric H_2O and SO_3, derived by oxidation of SO_2, produces fine aerosols of H_2SO_4. These aerosols are produced at 62-68 km, and sediment and grow into four distinct size modes at lower levels [*Krasnopolsky and Parshev*, 1983; *Yung and DeMore*, 1982]. Within the cloud, H_2O and H_2SO_4 are approximately in chemical equilibrium with their aerosols. Below, at higher temperatures, all the aerosols have evaporated, and only SO_2 vapor remains. The evaporation of H_2SO_4 occurs at about 48 km, the average cloud base. The vapor phase continues to exist down to 432 K (38 km), where it is thermally decomposed. The reservoir of H_2SO_4 vapor below the cloud base provides a source for the formation by condensation of the lower cloud particles [*Krasnopolsky and Pollack*, 1994]. At the conditions of the upper cloud, H_2O condensation is favored slightly over SO_2. Because of the steeper dependence of vapor equilibrium on temperature (via the Clausius-Clapeyron equation) of H_2O, less of it in the atmosphere is vapor at higher levels. The result is that hydrogen 'jumps ship' from H_2O vapor to H_2SO_4 vapor, and the above-cloud atmosphere is dry, at 1 ppm H_2O. H_2O vapor mixing ratio increases into the clouds as H_2SO_4 vapor decreases. The abundance of the important sulfur gases, SO_2 and OCS, vary within the cloud, in equilibrium with the changing H_2SO_4 abundance. SO_3 below the clouds, the product of H_2SO_4 thermal decomposition, is reduced by CO, causing a decline in CO abundance towards the surface [*Krasnopolsky and Pollack*, 1994]. SO_2 levels at cloud top are about 20 ppb [*Esposito*, 1984], while at the surface they are 180 ppm [*Fegley and Treiman*, 1992]. Rich in oxidized sulfur, Venus' lower atmosphere should react with surface rocks. Calcium silicates are persuaded to alter to calcium sulfates, especially at the high temperatures of Venus' surface [*Fegley and Treiman*, 1992]. A schematic drawing of the Venus cloud structure and sulfur cycle can be seen in Figure 3.2

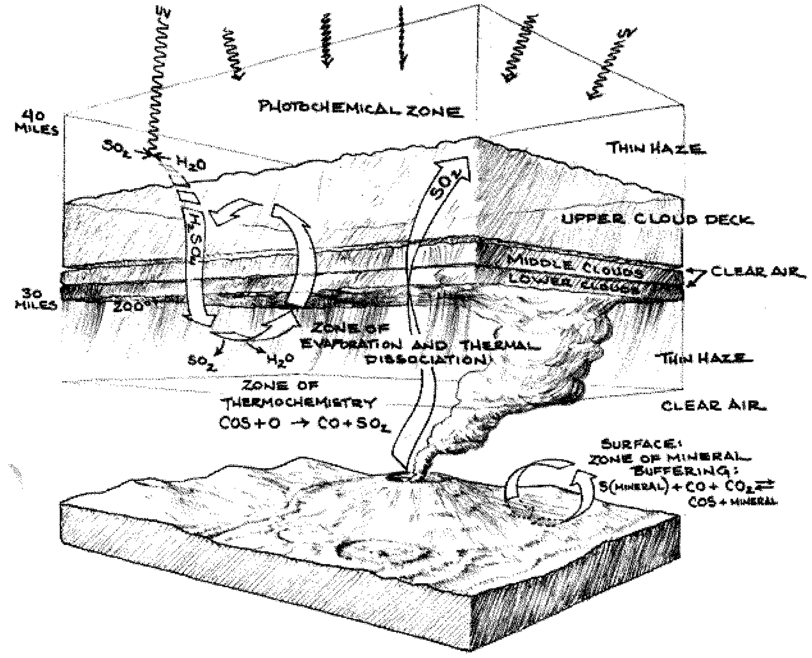

Figure 3.2 A schematic drawing of the clouds and sulfur cycle on Venus, drawn by Carter Emmart. See text above for a discussion.

Evolutionary Cloud Model

Changes in the thickness of Venus' clouds will have two effects on climate. They will

1. Alter the visual albedo, *A*, and the balance of thermal energy through (2.2)
2. Alter the thermal infrared opacity of the mid-atmosphere, affecting the temperature structure and surface temperature.

What is needed is a simple cloud model that can respond to changes in the atmospheric abundances of H_2O and SO_2, and predict changes in cloud structure, infrared opacity, and albedo. To this end, I have combined an adaptation of a thermochemical model of Venus' cloud aerosols [*Krasnopolsky and Pollack*, 1994] with a simple microphysical cloud model. Diffusion and condensation of H_2SO_4/H_2O aerosols in Venus' cloud layers is used to compute the position of the lower cloud boundary, profiles of H_2O and H_2SO_4 vapor mixing ratios, and the flux and composition of H_2SO_4/H_2O aerosols as a function of the column photochemical production rate of H_2SO_4.

H_2SO_4 vapor is produced photochemically within a narrow region of the upper cloud, at approximately 160 mbars. It diffuses downwards, being partly depleted by condensation, but ultimately being destroyed by thermal decomposition at 432 K. A strong gradient of H_2SO_4 vapor below the clouds drives a large upward flux of H_2SO_4 which condenses to form the lower cloud and produces a compensating downward flux of liquid H_2SO_4. H_2O and H_2SO_4 vapor abundances within the cloud are determined from their respective saturation vapor pressures over H_2SO_4/H_2O solution. Aerosol solution concentration is determined by including temperature-dependent chemical potentials in the relationship between the saturation vapor pressure of pure H_2O and vapor pressure of H_2O in solution. The lower cloud base is defined by the level at which the H_2SO_4 vapor pressure equals its saturation vapor pressure. The downward flux of H_2SO_4/H_2O aerosols and their composition within the cloud are used to calculate their size and number density using a simple cloud microphysical model. Assuming that particles formed within the cloud drift downwards with the Stokes velocity, and that the time scale for Brownian coagulation of aerosols is the same as the time it takes for particles to drift through the cloud, a relationship between particle size and number density is obtained. Particles are binned into four size modes by composition (or density). These size modes and their number densities form the basic cloud model input to the radiative transfer calculations described in Chapter 2. Substituting the results from this simple but versatile cloud model for the Pioneer Venus cloud number densities (Figure 2.9) allows an investigation of the role that changing SO_2 and H_2O abundances can have on the radiative balance of Venus' atmosphere. What follows is a more detailed mathematical description of the two aspects of the Venus evolutionary cloud model, the chemical and microphysical models.

Chemical Model

The abundance of H_2SO_4 vapor within the cloud, neglecting condensation, is determined by its photochemical column production rate and by eddy diffusion. The concentration gradient of H_2SO_4 vapor is set up by its production at 160 mbar and its thermal decomposition at 432 K. Even for relatively dramatic changes in atmospheric composition, I assume that the pressure at which solar UV photons are available to enable the formation of H_2SO_4 remains constant. I assume that H_2SO_4 is produced currently from an effective photochemical reaction

$$H_2O + SO_2 \Rightarrow H_2SO_4 \tag{3.1}$$

where the extra O required for (3.1) to be balanced is assumed to be readily available for oxidizing SO_2 to SO_3. Atomic O at this level is easily supplied by the photodissociation of both CO_2 and SO_2 in this region. The effective rate equation is then

$$\Phi_{H_2SO_4} = \frac{dNc_{H_2SO_4}}{dt} = k_{H_2SO_4} N_{H_2O} N_{SO_2} \tag{3.2}$$

where $Nc_{H_2SO_4}$, N_{H_2O} and N_{SO_2} are the column number density of H_2SO_4 vapor, and number densities of H_2O and SO_2 in the photochemical region. $\Phi_{H_2SO_4}$ is the column production rate of H_2SO_4. $k_{H_2SO_4}$ is the effective reaction rate constant, and assumes that the depth of the photochemistry layer is constant. From photochemical models, the current column production rate $\Phi_{H_2SO_4}$ of 2.2×10^{12} cm^{-2} s^{-1} will be used [*Krasnopolsky and Parshev*, 1983; *Yung and DeMore*, 1982]. This was also the value adopted by *Krasnopolsky and Pollack* [1994] that was found to be the most successful in their Venus cloud model. Mixing ratios of H_2O and SO_2 at 160 mbars are 3.4 and 0.6 ppm, respectively, yielding an effective rate constant (converting mixing ratios and number densities back and forth) of

$$k_{H_2SO_4} = \Phi_{H_2SO_4} \frac{1}{N_{H_2O} N_{SO_2}} = 1.03 \text{ x } 10^{-14} \ cm^4 s^{-1} \qquad (3.3)$$

This value is used for all model runs. The flux of H_2SO_4 vapor within and below the cloud base, neglecting condensation, is related to the column production rate via

$$\Phi_{H_2SO_4} = -K_k(z) \frac{dN_{H_2SO_4}(z)}{dz} \qquad (3.4)$$

where $K_k(z)$ is the eddy diffusion coefficient and N_{SO_2} is the number density of H_2SO_4 vapor (without condensation). I adopt the values of $K_k(z)$ used by [*Krasnopolsky and Pollack*, 1994], which are 2 x 10^4 cm^2/s throughout the clouds and declining logarithmically to 2.2 x 10^3 cm^2/s at 30 km. The higher static stability of the atmosphere below the clouds and large wind shears argue for these smaller values below the clouds. The abundance of H_2SO_4 within and just below the clouds is obtained by integrating (3.4)

$$N_{H_2SO_4}(z) = -\int \frac{\Phi_{H_2SO_4}}{K_k(z)} dz \qquad z > z_{bot} \qquad (3.5)$$

with boundary condition

$$N_{H_2SO_4}(z_{bot}) = 0 \qquad (3.6)$$

Below the region of thermal decomposition, z_{bot}, $N_{H_2SO_4}$ vanishes.

Because H_2SO_4 and H_2O are the primary hydrogen-bearing species in Venus' clouds, H_2O abundance is complementary to H_2SO_4. Below the depth of thermal decomposition of H_2SO_4, z_{bot}, virtually all the hydrogen is in H_2O, so the number density of H_2O within and just below the clouds is

$$N_{H_2O}(z) = Nm_{H_2O}(z_{bot}) - N_{H_2SO_4}(z) \qquad z > z_{bot} \tag{3.7}$$

where $Nm_{H_2O}(z_{bot})$ is the number mixing ratio at z_{bot} supplied by the particular atmospheric model that is being employed. Below the region of thermal decomposition of H_2SO_4

$$N_{H_2O}(z) = Nm(z) \qquad z < z_{bot} \tag{3.8}$$

The condensation of H_2O and H_2SO_4 solutions as aerosols within the cloud will perturb the vapor abundances calculated in (3.5) and (3.7). The saturation vapor pressure of H_2O in an H_2SO_4 solution is decreased due to the hygroscopic behavior of H_2SO_4. If m is the weight fraction of H_2O in theH_2SO_4/H_2O solution and $\mu_{H_2O}(m)$ the chemical potential of H_2O in solution, the saturation vapor pressure of H_2O over this solution is

$$ln\left(Ps_{H_2O}\right) = ln\left(Psp_{H_2O}\right) + \frac{\mu_{H_2O}(m) - \mu_{H_2O}(1)}{RT} \tag{3.9}$$

where Psp_{H_2O} is the vapor pressure of pure water

$$log\left(Psp_{H_2O}\right) = \frac{-2937.4}{T} - T^{4.9283} + 23.5470 \tag{3.10}$$

Chemical potentials for H_2SO_4/H_2O solutions at all concentrations, from 200 - 350 K determined in the laboratory [*Zeleznik*, 1991] are used in (3.9). The saturation vapor pressure of H_2O, Ps_{H_2O} is constrained to be consistent with atmospheric number density of H_2O calculated in (3.7). From this, $\mu_{H_2O}(m)$ may be calculated, and m derived by interpolating in temperature and abundance from the tabulated data of

Zeleznik [1991]. The saturation vapor pressure of H_2SO_4 over the H_2O/H_2SO_4 solution (with m varying with altitude) is calculated from the empirical formula

$$ln\left(Ps_{H_2SO_4}\right) = -\frac{\Delta H}{RT} + \frac{\Delta S}{R} + 7.42\left(1 + ln\frac{T_0}{T} - \frac{T_0}{T}\right) + \frac{\mu_{H_2SO_4}(m) - \mu_{H_2SO_4}(0)}{RT} \qquad (3.11)$$

Where the two profiles defined by the number density of H_2SO_4 vapor in the absence of condensation and the saturation number density intersect, condensation occurs and the lower cloud boundary is formed. The altitude of the lower cloud boundary is defined as z_{lcb}. H_2SO_4 vapor abundance follows the uncondensed profile (3.5) below the lower cloud boundary, and is determined by saturation vapor pressure (3.11) above this level. The calculated abundance of H_2SO_4 vapor within the cloud gives rise to a positive concentration gradient in H_2SO_4 and a corresponding upward eddy diffusion flux. This vapor flux is calculated from

$$\Phi v_{H_2SO_4}(z) = -K_k \frac{dNs_{H_2SO_4}(z)}{dz} \qquad z > z_{lcb} \qquad (3.12)$$

where $Ns_{H_2SO_4}(z)$ is calculated from (3.11) and the ideal gas law. This net upward flux and downward eddy diffusion from H_2SO_4 vapor production (which is smaller) must be balanced by a flux of particulate H_2SO_4

$$\Phi p_{H_2SO_4}(z) = \Phi_{H_2SO_4} + \Phi v_{H_2SO_4}(z) \qquad z > z_{lcb} \qquad (3.13)$$

Microphysical Cloud Model

The flux of particulate H_2SO_4, $\Phi p_{H_2SO_4}$, which has been determined from the photochemical production rate of vapor H_2SO_4 is used in a simple microphysical cloud model to calculate particle sizes and number densities. Particles are assumed to grow by Brownian coagulation and drift downwards through the cloud layer at the Stokes velocity. The Stokes velocity for particles of density ρ and radius r falling through the atmosphere with viscosity η and gravitational acceleration g [*Liou*, 1992], is

$$v_s = \frac{2g\rho r^2}{9\eta} \tag{3.14}$$

With this velocity, the flux of particulate H_2SO_4 is

$$\Phi p_{H_2SO_4} = \frac{v_s m_p N_p N_A}{W_{H_2SO_4}} \tag{3.15}$$

where m_p is the mass of a single particle, and N_p is the number density of particles. N_A is Avogadro's number and $W_{H_2SO_4}$ is the molar weight of H_2SO_4. For spherical particles

$$m_p = \frac{4}{3}\pi r^3 \rho \tag{3.16}$$

and the flux of particulate H_2SO_4 is

$$\Phi p_{H_2SO_4} = \frac{8\pi N_A g \rho^2 r^5 N_p}{27 W_{H_2SO_4} \eta} \tag{3.17}$$

The lifetime of particles drifting down through the cloud of thickness D with velocity v_s. is

$$\tau_s = \frac{D}{v_s} = \frac{9D\eta}{2g\rho r^2} \tag{3.18}$$

Coagulation of particles due to Brownian motion is characterized by a volume rate, K_c, determined empirically. For cloud particles a value of K_c = 3 x 10^{-10} cm^3/s is typically used [*Liou*, 1992]. If N_p is the number density of the particles, the time scale for Brownian coagulation is

$$\tau_c = \frac{1}{K_c N_p} \tag{3.19}$$

In steady state, the time for coagulation will be the same as the lifetime of particles in the cloud, so (3.18) and (3.19) may be equated, yielding a relationship between the size of the particles and their number densities

$$N_p = \frac{2}{9} \frac{g\rho r^2}{K_c D \eta} \tag{3.20}$$

(3.17) and (3.20) are two algebraic equations in the two unknowns N_p and r. They are solved simultaneously for conditions at every level z to obtain a description of the cloud in terms of number density N_p and radius r.

Cloud Model Numerical Implementation

The above model described by (3.2)-(3.20) is discretized onto the same numerical grid defined by P_i, T_i, z_i, as for the radiative transfer calculations of Chapter 2. Mixing ratios of the three molecular players in cloud production for an 80-layer atmosphere with the nominal (Figure 4.1) atmospheric mixing ratios are shown in Figure 3.3. X_{i,H_2SO_4}, the eddy diffusion-derived vapor mixing ratio for H_2SO_4 without condensation is shown by the solid line. It represents the solution to the diffusion equation (3.5), with vanishing abundance at the level of thermal decomposition, z_{bot}. The mixing ratio of saturated H_2SO_4 vapor over (the varying) H_2SO_4/H_2O solution, Xs_{i,H_2SO_4} is shown by the dot-dashed line. The weight fraction of H_2O varies for these plots from 4% at z_{bot} (38 km) to 35% at 55 km. When the vapor mixing ratio of H_2SO_4 exceeds the saturation value, here at 48.5 km, the lower cloud boundary at z_{lcb} is formed. It is interesting to note that the average of the measurements of the cloud base on Venus from the Pioneer Venus nephelometer measurements of the four entry probes is 48.4 ± 0.75 km [*Ragent and Blamont*, 1980].

The H_2O vapor mixing ratio, X_{i,H_2O}, is depicted with the dashed line. Its value is defined by (3.7) to be consistent with the conservation of hydrogen throughout the cloud.

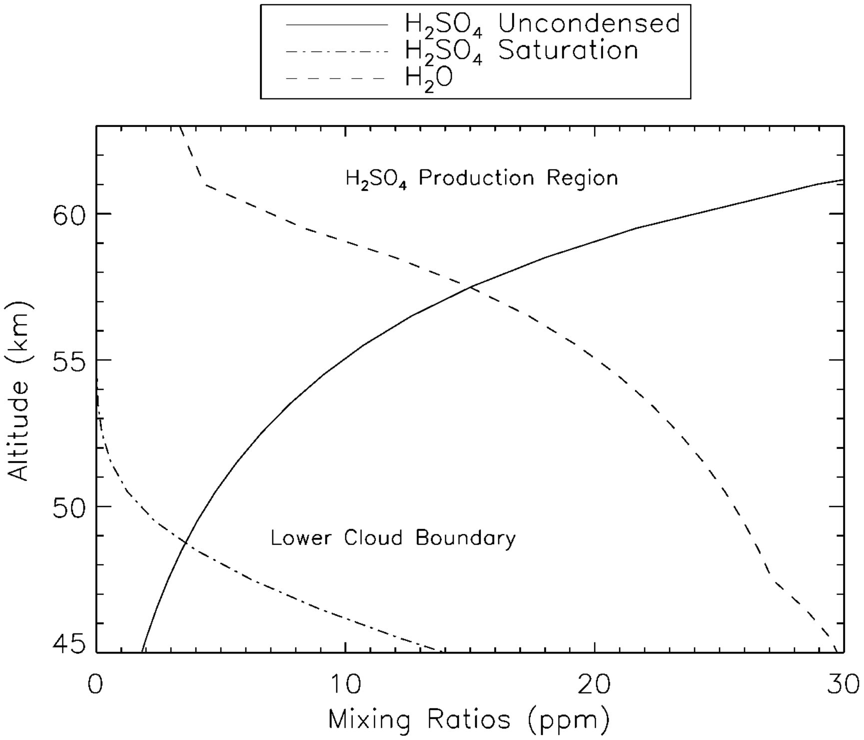

Figure 3.3 H_2O and H_2SO_4 abundances within the nominal cloud model. The mixing ratio of H_2SO_4 in the absence of condensation is shown by the solid line. The saturation mixing ratio of H_2SO_4 over H_2SO_4/H_2O solution for the calculated weight fractions is shown with the dot-dashed line. The lower cloud boundary, z_{lcb}, is where these two curves intersect. The H_2O mixing ratio within the cloud, calculated from the conservation of hydrogen, is shown with the dashed curve.

Notice that the concentration gradient of Xs_{i,H_2SO_4}, which is negative, drives an upward flux of vapor H_2SO_4. It is this flux of gaseous H_2SO_4 that is compensated for (accounting for the variation of m with height) by the downward flux of liquid

SO_2/H_2O aerosols. The net downward flux of particulate H_2SO_4, $Np_{iH_2SO_4}$, for the nominal cloud model is shown in Figure 3.4. The cloud production region is at 64 km, and the downward flux disappears at the lower cloud boundary, where evaporation of particulates takes place.

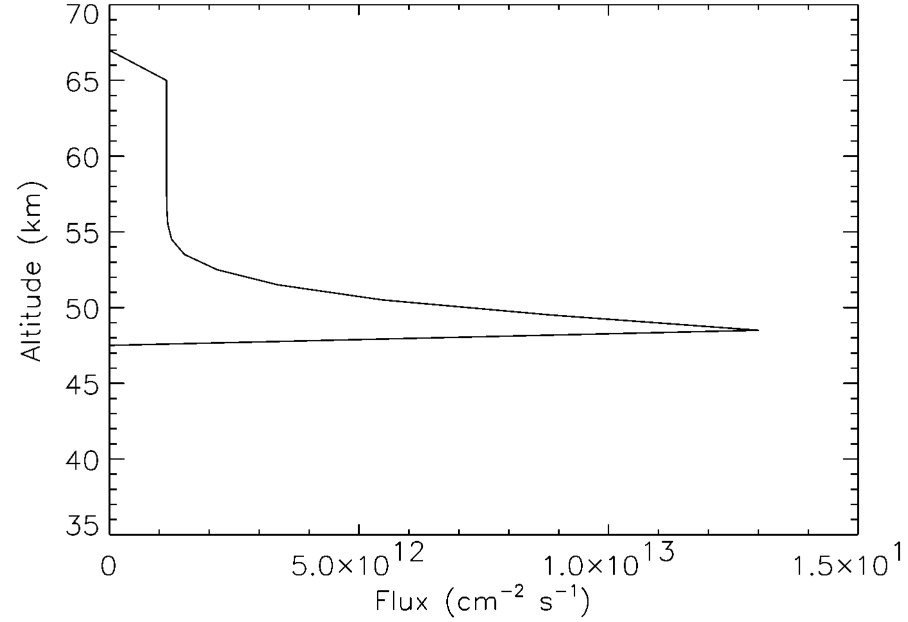

Figure 3.4 The net downward flux of particulate H_2SO_4 as a function of altitude. The lower cloud boundary can be seen where the flux abruptly stops at the level of evaporation It is largest in the lower cloud, and declines monotonically throughout the cloud layer.

Cloud particle modes for this model are somewhat arbitrarily defined by aerosol composition. Particles are grouped into four bins depending upon their weight fraction of H_2O. The average weight fraction $m_{j'}$ of bin j', where j' goes from 0 to 3 is calculated for each level i. Particle modes did not differ much in their modal radius, which was about 2 μm, because the small changes in density had little effect on their evolution. The number densities $N_{ij'}$ at each layer and for each mode j' and the particle sizes $r_{j'}$ are determined by employing (3.17) and (3.20) $i \times j'$ times. The total cloud particle number densities as a function of altitude are shown in Figure 3.5 with the solid line.

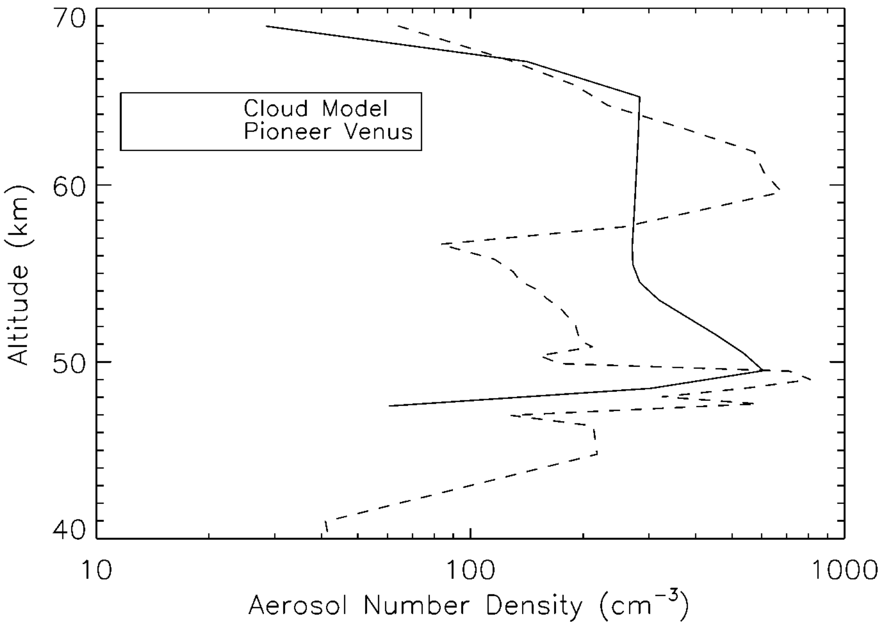

Figure 3.5 Nominal cloud number densities as a function of altitude (solid line). Results for the real Venus cloud from the Pioneer Venus nephelometer are shown with the dashed line.

Comparison with the Pioneer Venus nephelometer results for the real Venus clouds (dashed line) shows the model cloud structure to be fairly crude, but the essential features are similar. Although the model does not account for the production and transport of distinct particle populations, the altitude of the cloud base, tops, and approximate total number densities are similar to the PV measurements. Due to the simple physics used in the model, size modes are not distinguished much by radius and their spatial segregation in the cloud did not occur. However, the proper altitudes and pronounced lower cloud, as well as the results of Mie calculations suggest that such a model is adequate for studying the coupled effects of greenhouse warming and albedo feedback.

The particle mass loading of the nominal model cloud, in g/cm^3, is plotted as a function of altitude as the solid line in Figure 3.6. The total column mass of the cloud created in this simulation was about 0.027 g/cm^2, compared with 0.015 g/cm^2 from the Pioneer Venus nephelometer results for Venus clouds.

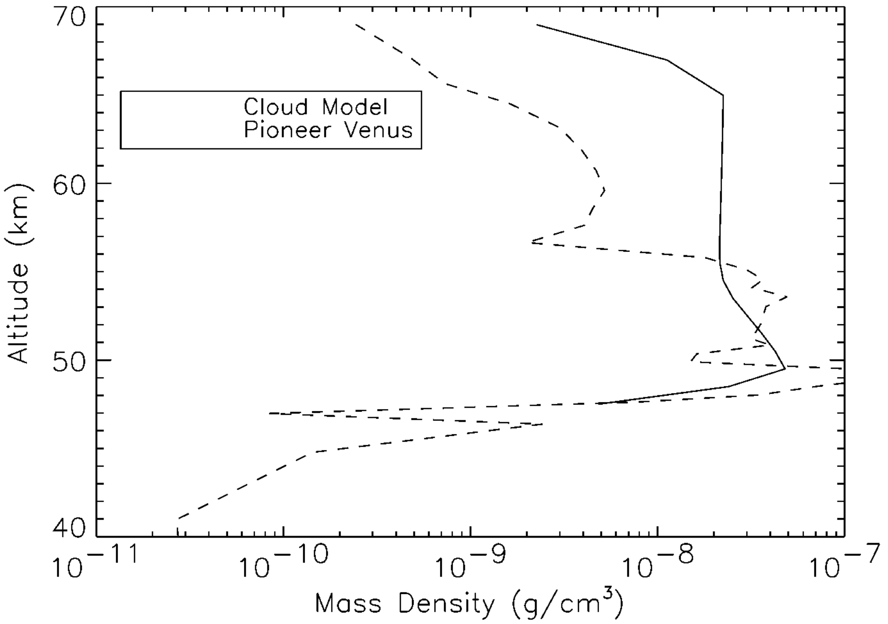

Figure 3.6 Nominal cloud mass loading in g/cm^3 (solid line). The dashed line is for the real Venus cloud from the Pioneer Venus nephelometer. Total column mass of the model cloud is 0.027 g/cm^2.

Mie calculations of the cloud particles over all wavenumber intervals j and levels i yield the extinction optical depths, $\tau^{aer}{}_{ij}$ single scattering albedos ω_{oij} and scattering asymmetry factors g_{ij}. The extinction optical depths at 0.63 μm for an 80 layer atmospheric model (with cloud in about 37 of them) is shown in Figure 3.7. The total optical depth of the cloud is 26, compared with the value of 20 computed from Mie calculations of the Pioneer Venus measured cloud of [*Knollenberg and Hunten*, 1980] (Figure 2.12). The single scattering albedos of the nominal and real clouds may be compared by looking at Figure 3.8 and Figure 2.13.

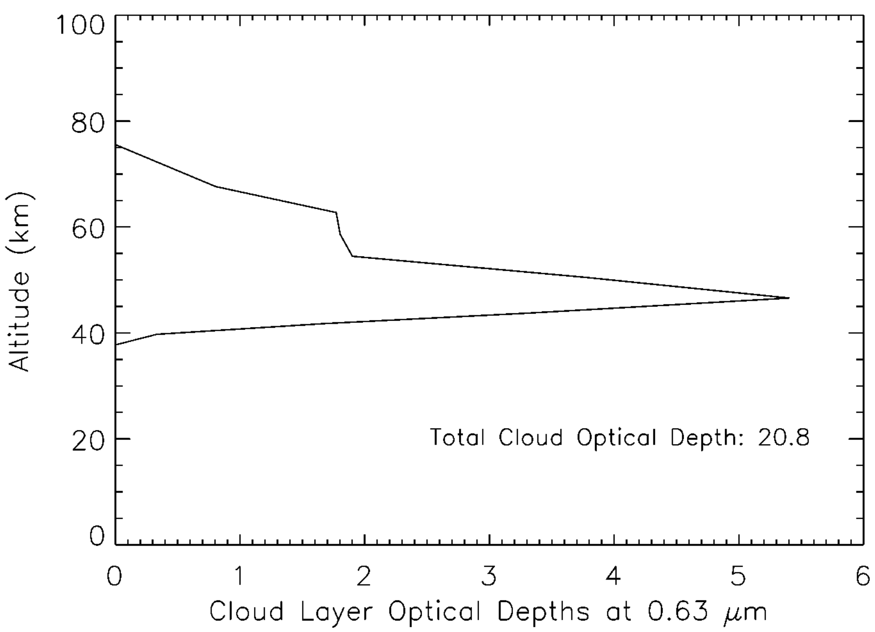

Figure 3.7 Nominal cloud extinction optical depth for each layer of a 24-layer atmosphere, at 0.63 μm. Total cloud optical depth is 20.8.

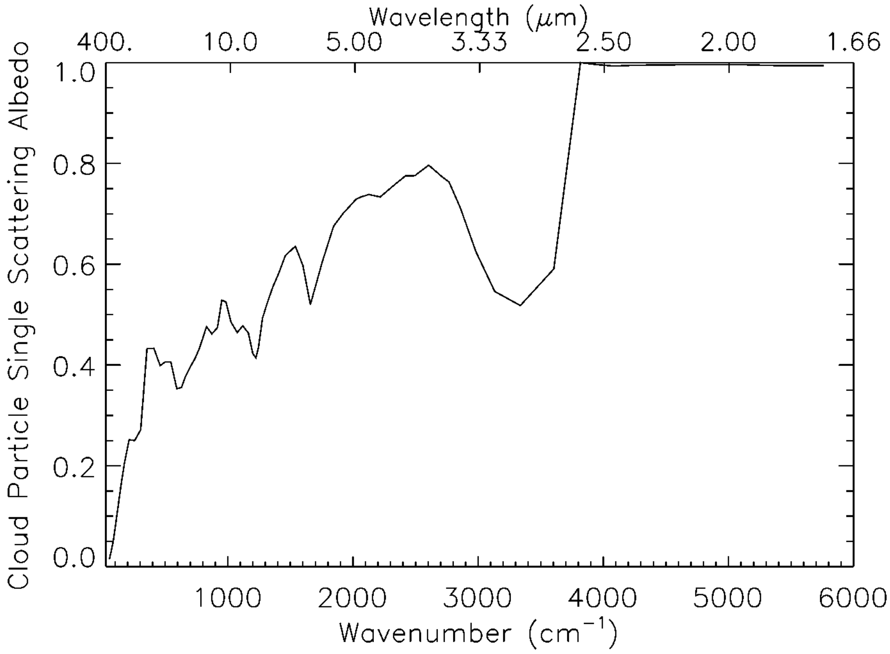

Figure 3.8 Single scattering albedo as a function of wavenumber for a typical layer within the middle cloud, for the nominal cloud model.

The Effects on Cloud Properties of Varying Atmospheric Abundances

The response of the cloud with respect to changes in SO_2 and H_2O abundance, but independent of atmospheric temperature and pressure changes was investigated first. That is, the temperature structure was rendered independent of changes in infrared flux forcing or changes in net solar flux due to albedo variation. The visual albedo of the clouds was calculated using a simple grey two-stream approximation for the transfer of incident solar radiation [*Lenoble*, 1985]. I used the total value of the extinction optical depth at solar wavelengths, τ^*_{vis}, and cloud averaged values for single scattering albedo $\omega_{o_{vis}}$ and scattering asymmetry factor g_{vis} (typically 0.998 and 0.7, respectively) and treated the cloud as a single layer. The cloud albedo is then

$$a = \frac{G\left(1 - e^{-2k\tau_{vis}^{*}}\right)}{1 - G^{2}e^{-2k\tau_{vis}^{*}}} \tag{3.21}$$

where

$$G = \frac{r - s}{r + s} \tag{3.22}$$

$$r = 1 - \omega_0^{vis} g^{vis} \tag{3.23}$$

$$s = 1 - \omega_0^{vis}\left(1 + g^{vis}\right) - \left(\omega_0^{vis}\right)^2 + \frac{\left(\omega_0^{vis}\right)^2\left(1 - g^{vis}\right)^2}{2} \tag{3.24}$$

$$k = \frac{s}{\mu_0} \tag{3.25}$$

where μ_0 is the cosine of the solar incidence angle, set to an average value of √3/2.

Clouds were grown in model runs for a range of H_2O and SO_2 abundances, from 0.001 to 100 times their current values. The effects of these changes in abundance on the cloud albedo *a* is shown in Figure 3.9. The nominal cloud albedo from the model (indicated by the diamonds) for present day abundances of SO_2 and H_2O is 0.84, close to the spacecraft derived value of 0.85. Increased H_2O and/or SO_2 lead to higher number densities and more opaque clouds, and hence higher visual albedos. Since the present cloud is so optically thick, however, it cannot get much brighter, and maximum albedos are achieved at about 0.90. However, reducing the abundance of SO_2 to 0.2 ppm (one thousandth of its present value) renders the clouds almost nonexistent, with total visual optical depths of less than 1. If H_2O is reduced to one thousandth of its present value, or 0.03 ppm, the cloud also becomes highly attenuated. In both cases, the albedo of Venus is dominated by Rayleigh scattering if its massive atmosphere, and has a value of about 0.4. These cloud responses do not include changes to atmospheric temperatures that they engender through altering radiative-convective equilibrium, an important feedback that will be treated next.

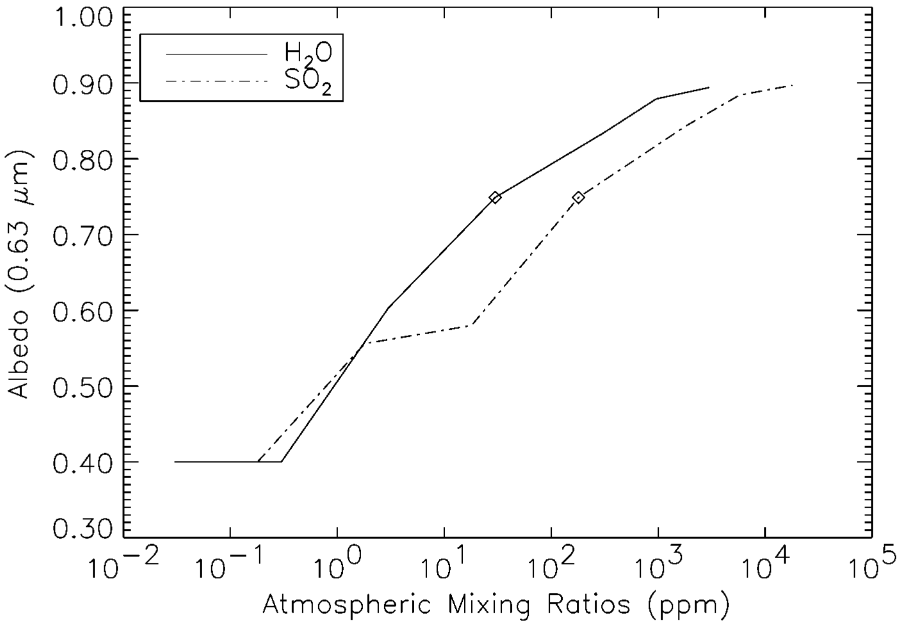

Figure 3.9 Cloud albedo as a function of the abundance of SO_2 and H_2O;, without adjusting atmospheric temperatures. The solid line is for H_2O, the dot-dashed line is SO_2. Diamonds indicate their current atmospheric abundances and albedo. Thicker clouds are formed when the abundance of these species is increased, although the albedo changes little. Albedo rapidly decreases, however, with lowered abundances.

Coupling the Cloud Model to Radiative Equilibrium Calculations

Numerical Implementation

The most interesting effects that changing clouds would have on Venus' climate are on its albedo and subsequent solar flux forcing. In addition, thermal infrared forcing changes with cloud opacity. The coupling between radiative effects in the atmosphere and changes in cloud structure engendered by varying SO_2 and H_2O atmospheric abundances on Venus may now be studied. Coupling the cloud model with the radiative-convective calculations of Chapter 2 involves inserting the cloud number densities and particle mode properties into the radiative transfer code. Since the properties of the cloud depend on the temperature and pressure structures of the atmosphere, an iterative procedure is used with the following features:

1. Solar flux deposition in the atmosphere is scaled by the cloud albedo via

$$F_s' = \frac{1-a}{1-A} F_s \tag{3.26}$$

   where a is the calculated albedo from (3.21), A is the current albedo (0.85), F_S is the solar flux profile from the Pioneer Venus solar flux radiometer [*Tomasko et al.*, 1980] (Figure 2.17).

2. The entire calculation to radiative-convective equilibrium is iterated to allow the cloud to adjust to the new temperature and pressure structure. Usually, 4-6 iterations of the radiative transfer/cloud model assembly is required for the atmosphere to converge on steady cloud albedo, infrared fluxes, and surface temperatures.

The Greenhouse Effect with Cloud Albedo Feedback

The response of cloud albedo to changes in atmospheric SO_2 and H_2O including changes to radiative forcing are shown in Figure 3.10. The solid line is for H_2O and the dashed line is for SO_2; current abundances and albedo are plotted as diamonds.

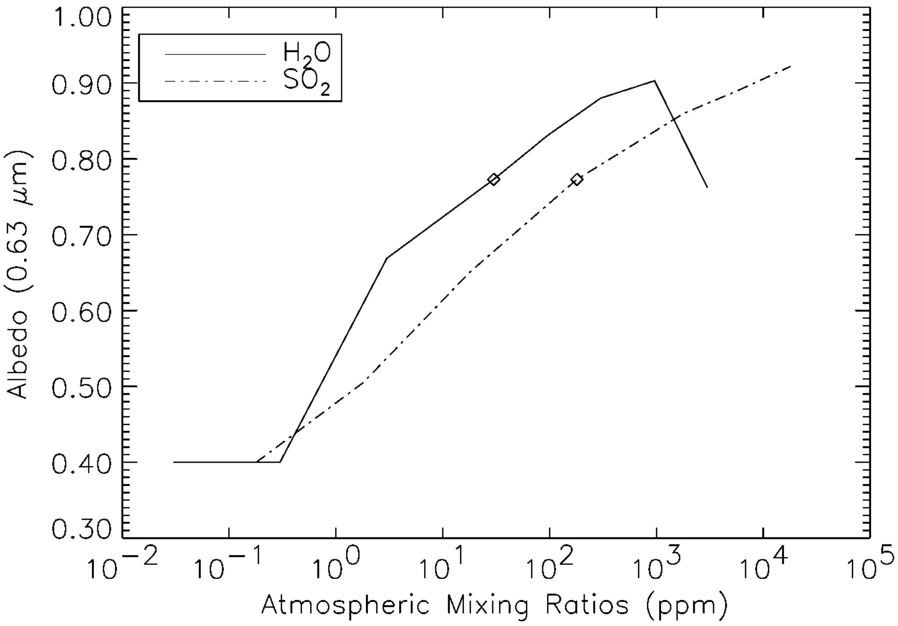

Figure 3.10 Cloud albedo as a function of the abundance of SO_2 and H_2O; for the coupled cloud/radiative transfer model. The solid line is for H_2O, the dot-dashed line is SO_2. Diamonds indicate their current atmospheric abundances and albedo. Thicker clouds are formed when the abundance of these species is increased, although a transition to high, thin clouds can be seen for H_2O abundances above 150 ppm..

As these abundances drop the clouds become thinner, increasing the available solar flux. However, infrared opacity is reduced due to less absorption by these gases deep in the atmosphere and by less infrared opacity in the cloud regions. Lowering cloud albedo dominates, and the atmosphere becomes hotter. Because it becomes hotter, the cloud base is shifted upwards, and the clouds become thinner still. This is why the slopes for abundances less than present values are greater in Figure 3.10 than in Figure 3.9. Clouds disappear entirely when the deep H_2O abundance drops below 0.3 ppm or the SO_2 abundance drops below 1 ppm. An interesting transition occurs when atmospheric H_2O is increased to more than about 50 times its current value. Because the Venus greenhouse effect is so sensitive to H_2O abundance, the atmosphere heats up sufficiently to overcome the effects of increased cloud albedo. The result is a rapid decrease in cloud thickness and albedo, as the rising atmospheric temperatures erode the cloud base from below, leaving a high, thin cloud. Cloud optical depths at 0.63 μm are plotted as a function of H_2O and SO_2 abundances in Figure 3.11. Although cloud opacity increases steadily with increasing SO_2 abundance, the aforementioned transition to lower cloud optical depths as H_2O abundance increases is apparent. The climatic effects of varying atmospheric H_2O and SO_2 on the combined radiative transfer/cloud model is illustrated by plotting the surface temperature as a function of these abundances in Figure 3.12. For very low abundances H_2O and SO_2 (0.3 and 0.2 ppm, respectively), no clouds exist but the surface temperature is about 725 K, slightly cooler than present conditions. The reason for this is three-fold: There is a lower infrared gaseous opacity, there is no cloud infrared opacity, and the cloud-free albedo is relatively high, at 0.4. As abundances increase, however, the surface temperature rises due to the dominance of extra gaseous and cloud opacity over cloud albedo effects. Surface temperatures can rise as high as 800 K due to variations in SO_2 below current values, but they can only drop when SO_2 is increased beyond its present abundance. Below current H_2O abundances, the surface temperature never rises much above current values. For SO_2 abundances greater than 2 ppm (one hundredth current values) or H_2O abundances greater than 5 ppm (one sixth current values) increasing cloud albedo dominates, and surface temperatures drop. This continues to be the case as SO_2 abundance increases. However, as H_2O is increased, the enhanced greenhouse dominates, and the surface temperature rises rapidly to 900 K as the clouds thin.

The important result here is that there is the potential for the surface temperature of Venus to become very high when atmospheric H_2O is abundant, but this is not true for SO_2. Furthermore, dissipation of clouds due to lowered H_2O and SO_2 abundances does not increase the surface temperature above about 800 K, and with the clouds gone altogether, the surface is just slightly cooler than it is today.

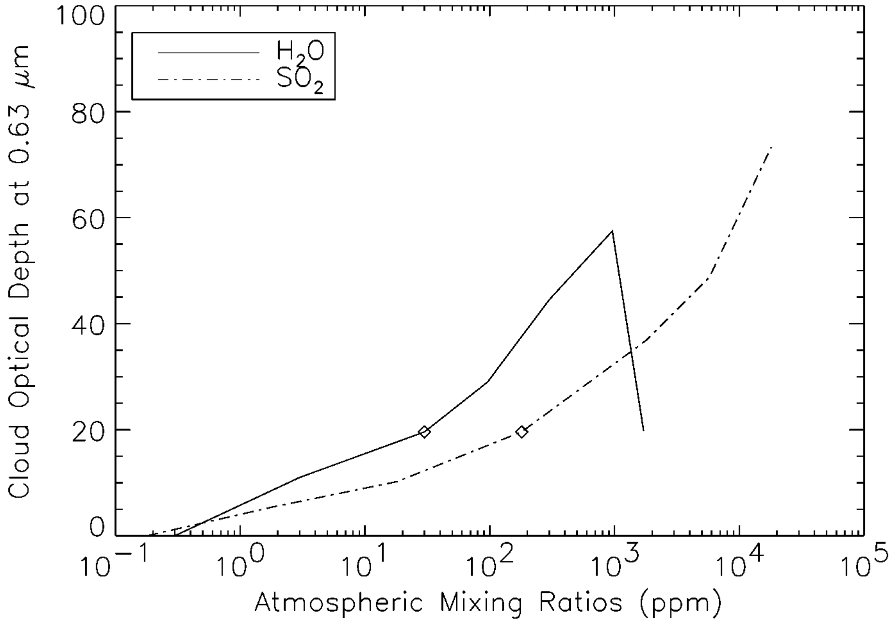

Figure 3.11 Cloud visual optical depth (0.63 μm) as a function of the abundance of SO_2 and H_2O. The solid line is for H_2O, the dot-dashed line is SO_2. Diamonds indicate the current atmospheric abundances and cloud optical depth. Thicker clouds are formed when the abundance of these species is increased, although a transition to high, thin clouds can be seen for H_2O abundances above 1000 ppm. Clouds disappear when H_2O abundance goes below 0.3 ppm or SO_2 abundance goes below 0.2 ppm.

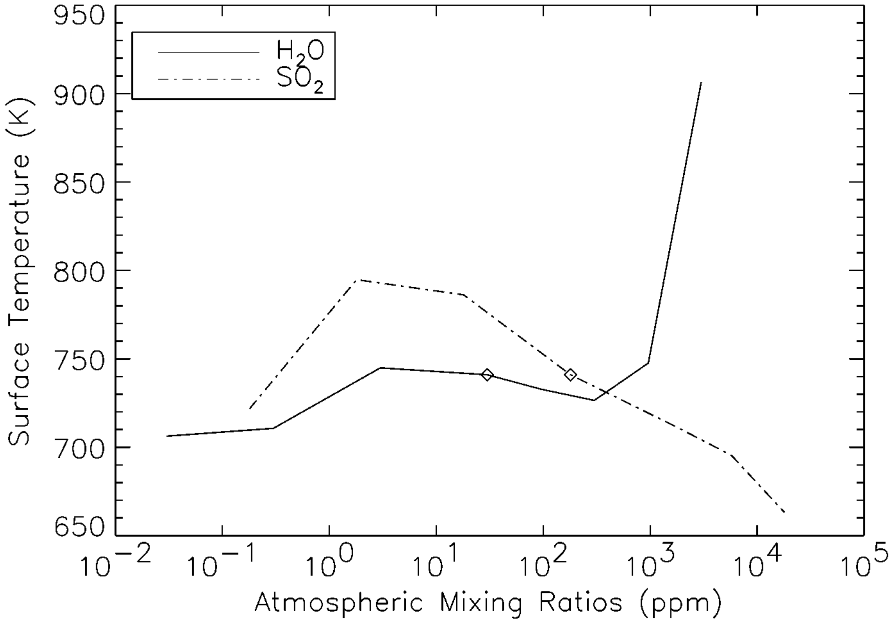

Figure 3.12 Surface temperature as a function of the abundance of atmospheric SO_2 and H_2O for the coupled Venus radiative transfer/cloud model. The solid line is for H_2O, the dot-dashed line is SO_2. Diamonds indicate the current atmospheric abundances and surface temperature. Surface temperatures stay between 700 and 800 K until abundances are greater than about 1000 ppm. As H_2O increased beyond that, the surface temperature reaches 900 K. As SO_2 is increased beyond this amount, surface temperatures cool below 700 K.

The surface temperature of Venus can be affected by changes in atmospheric abundance of key radiatively active species such as H_2O and SO_2, as demonstrated in Chapter 2. These same volatiles, however, are involved in the construction of Venus' clouds, which wield a powerful influence on the energy balance of the planet through their albedo. Atmospheric temperature and pressure structure influence cloud physics and hence optical properties of the clouds. Atmospheric and surface temperatures are therefore influenced by a fairly complex feedback between the greenhouse and cloud albedo, when variations of H_2O and SO_2 are considered. In addition to having all these effects on the energy balance of the atmosphere, SO_2 and H_2O (along with CO_2) are the major volatiles outgassed by volcanoes over the course of geologic time on the terrestrial planets. Defining the possible time history of these volatiles from surface sources is the subject of the next chapter. Together with the climate sensitivity studies of this chapter, the basis for discussing the magnitude, rate, and time-scales of possible climate evolution will then be available.

CHAPTER 4

GEOLOGICAL SOURCES OF VOLATILES

Geological Processes on Venus and the Impact Cratering Record

Geological History

The formation of atmospheres on the terrestrial planets most likely occurred contemporaneously with accretion or shortly thereafter by impact degassing of volatiles. At the same time, vigorous overturning and outgassing of the mantle, heated by accretion and core formation, shaped the early terrestrial atmospheres. Subsequent to their formation, terrestrial planet atmospheres were also the products of ongoing communication between the crust, mantle, surface reservoirs, and space. On the terrestrial planets geological processes shape the atmosphere as well as the surface. The essential driver of geology, geothermal energy, is also a force in determining the evolution of planetary atmospheres by enabling the transport of volatiles. Recent geological events, interpreted from the surface record, must have left their mark in the atmosphere as well.

The Earth and Venus are nearly the same size and probably have roughly the same bulk compositions [*Phillips and Malin*, 1983]. One would expect similar thermal histories if their concentrations of radioactive heat generating elements are similar. On the Earth, the global system of plate tectonics is linked to the recycling of CO_2 from the atmosphere. Transport from the atmosphere to subduction at trenches is temperature dependent, resulting in a negative feedback that stabilizes CO_2 in the atmosphere [*Holland*, 1978]. As far as we know, little such recycling has occurred on Venus in the recent geological past. Plate tectonics, except possibly on a limited scale, are not in evidence [*Schubert and Sandwell*, 1995]. Massive volcanic edifices do exist, however, perched on volcanic plains that cover 80% of the planet [*Head et al.*, 1992]. The remaining 20% has experienced severe tectonic disruption, possibly as a prelude to plains emplacement [*Basilevsky and Head*, 1995].

Volcanoes provide a time-dependent source of volatiles to the atmosphere, a process shared by the Earth and Venus. Although variations in the volcanic flux do exist, heat transport by the creation and subduction of lithosphere on the Earth provides a steady and reliable means to transport heat from the interior [*Turcotte and Schubert*, 1982]. The formation of immense volcanic provinces on the Earth, possibly associated with enormous buoyant plumes of magma within the mantle, may also be associated with larger impulses of volatiles to the atmosphere [*Coffin*, 1994]. On Venus, it appears that transport of heat from the interior has been accomplished in the recent geologic past by the formation of the basaltic plains, and later by the large volcanoes that grew on top of them.

Much of the geological history of Venus remained speculative before the Magellan mission, relegated to comparisons with the Earth and predictions based on presumed similarities in composition and geothermal heat fluxes. With Magellan, a global picture of the history of Venus' surface is emerging. Surprisingly, it has become obvious that in spite of their similarities, the crusts of the Earth and Venus have had distinctly different histories. The Magellan spacecraft accomplished a global reconnaissance of Venus using 12.6 cm radio waves to image the planet with synthetic aperture radar. The surface of Venus was mapped almost in its entirety to a resolution of 200 m [*Saunders et al.*, 1992].

On the Earth, we understand the impact cratering record to some extent. Craters forming on the land are degraded by wind and water erosion at rates that are interpretable from the sedimentary record. Because the resurfacing of land is a roughly constant process, impact craters are seen in a wide range of degradational states, depending on their age and therefore on the age of the surface on which they lie. The astonishing thing about Venus' impact craters is that not only do they appear to be randomly placed about the planet, but they almost all appear to be pristine [*Phillips et al.*, 1992; *Schaber et al.*, 1992]. An equal area sinusoidal projection of the surface of Venus, with all impact craters depicted in red is shown in Figure 4.1. The shading represents the local crater density, averaged over a 1400 km circle at each point.

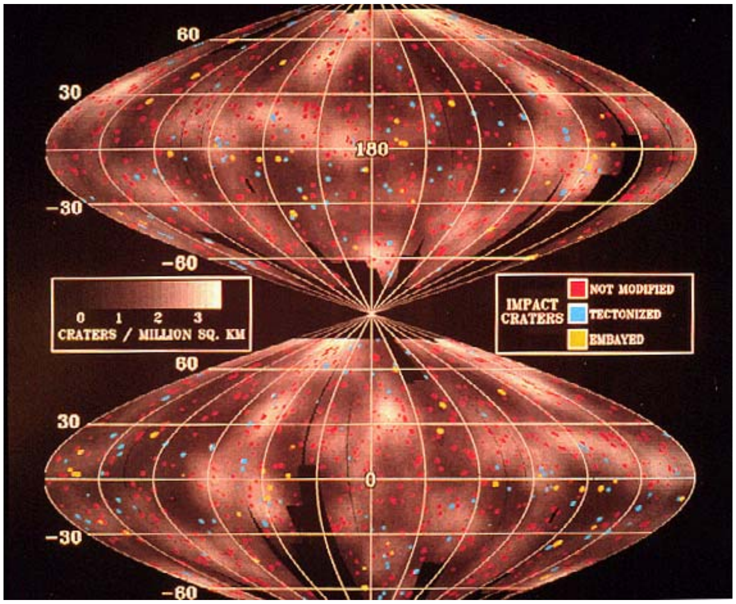

Figure 4.1 The global distribution of impact craters on Venus, indicated by red circles. Blue circles are impact craters disrupted by tectonism, and yellow circles are craters that have been altered by volcanism. Shading depicts the local impact crater density averaged over 1400 km circles. From [*Phillips et al.*, 1992].

The average crater density on Venus, as revealed by detailed radar images from the Magellan spacecraft, implies that the surface of the planet is 600-1100 million years old [*McKinnon et al.*, 1997; *Phillips et al.*, 1992; *Schaber et al.*, 1992]. The nature and rates of the planetary resurfacing processes are recorded in the styles and distribution of modified craters. A distinctive feature of Venus' crater population is that only a small number of them are apparently modified by volcanism [*Phillips et al.*, 1991; *Schaber et al.*, 1992]. *Schaber et al.* [1992] report that out of a total of 912 identified impact craters, only 4-7% are partially embayed by volcanic lavas, while 33% are tectonically modified. These facts alone suggest that the surface is young and has undergone little geological processing since it was emplaced. The implication is that an older surface may have been entirely wiped out by some event followed by a quiescent period and the collection of random impacts from space ever since.

Models of the Resurfacing of Venus

Any process that was removing craters gradually such as chemical or physical weathering, aeolian erosion or burial, viscous relaxation or volcanic flooding would be expected to leave a suite of craters in various states of degradation. Two hypotheses have been put forth to explain this conundrum. Each involves a unique combination of resurfacing spatial scales and time dependence. The extensive basaltic plains and subsequent large volcanic edifices depict a vigorously active planet, but the impact cratering record does not.

The first hypothesis, the single production age or 'catastrophic resurfacing' model, is that resurfacing rates on Venus were sufficiently high to effectively destroy all craters in the past, and then rapidly declined, allowing subsequent crater preservation in pristine form [*Head et al.*, 1992; *Phillips et al.*, 1992; *Schaber et al.*, 1992]. The age of this change in surface activity may be approximately constrained by crater densities, and the subsequent resurfacing rate may be quantified by the small but nonzero number of partially embayed craters. A schematic drawing of this process is depicted in Figure 4.2. If a catastrophic volcanic and tectonic event did take place 500 million years ago, the implications for the evolution of the atmosphere are potentially enormous. Global stratigraphic analyses of the Magellan data have determined that a catastrophic resurfacing must have occurred within 10-100 million years in order to preserve the present cratering record [*Head et al.*, 1994; *Strom et al.*, 1994]. A complete disruption of the crust in such a short interval would have released vast amounts of volatiles into the atmosphere.

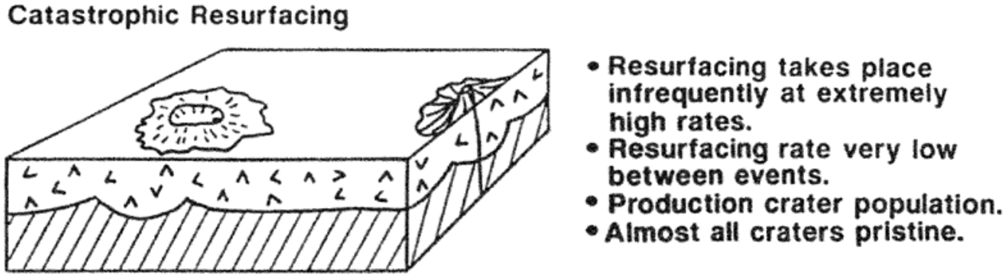

Figure 4.2 Schematic representation of the Catastrophic Resurfacing Model. Widespread geological activity, with perhaps a global foundering of the crust, is followed by quiescence and the collection of impact craters. Graphic courtesy of Jim Head, Brown University.

Given the sensitivity of the Venus greenhouse effect to small changes in H_2O and SO_2 (Figures 2.28 and 2.31), it is likely that if such an event occurred, Venus' climate would have undergone significant change. The clouds themselves may be an ancient remnant, a signature of the catastrophic event that reworked the crust with subsequent outgassing of large amounts of SO_2 and H_2O.

The second hypothesis is that there has been a relatively constant rate of 'regional resurfacing' [*Head et al.*, 1992; *Phillips et al.*, 1991]. Statistical analyses of the spatial distribution of observed craters reveals that they are consistent with complete spatial randomness, ruling out extensive resurfacing events over large areas in the last 5 - 10 x 10^8 years. This hypothesis suggests that the characteristic scale of the resurfacing events which dominates the steady state evolution of the surface is smaller than the scale of randomness of the craters. The absence of any small craters due to the thick atmosphere means that this scale of randomness is large enough to allow a significant, perhaps the dominant, portion of the volcanic resurfacing activity to occur on a scale that is less than the average inter-crater separation (about 700 km).

The regional resurfacing model [*Phillips et al.*, 1992] was developed by considering a characteristic regional patch size of fractional area *a*, and a characteristic resurfacing rate *w*. They found that impact crater spatial randomness was preserved, and crater densities accounted for, with patch sizes less than 0.0003 (140,000 km^2), and frequencies greater than once per 150,000 years. Additionally, the statistics of the observed crater population could be accounted for by considering resurfacing patch sizes greater than 0.1 (4.6×10^7 km^2), and frequencies of less than once per 50 million years. These two solution branches were considered in their model to represent a steady state between impact cratering and resurfacing events. To some extent, this hypothesis is supported by the apparent younger age of the large shield volcanoes, determined by regional crater counting. Atmospheric evolution in this case would be less dramatic, but driven to some extent by a constant flux from the outgassing of volatiles through volcanic activity. The features of the equilibrium resurfacing end-member resurfacing model are shown schematically in Figure 4.3.

These two simple resurfacing schemes describe the opposing ends of a continuum of possible resurfacing histories. They are constrained by the observed crater population in a number of ways. First, there is the important observation by *Phillips et al.* [1992] that the observed impact crater population cannot be distinguished from a spatially random one. This is partly due to the poor Poisson statistics of Venus' crater population. However, a concentration of heavily fractured and lava embayed craters are found along major fracture belts and the rifted uplands of Aphrodite, Atla, Beta, Themis and Pheobe Regiones. These areas are undoubtedly younger than surrounding plains areas, but quantifying the relative ages of these areas is difficult due to the small number of craters.

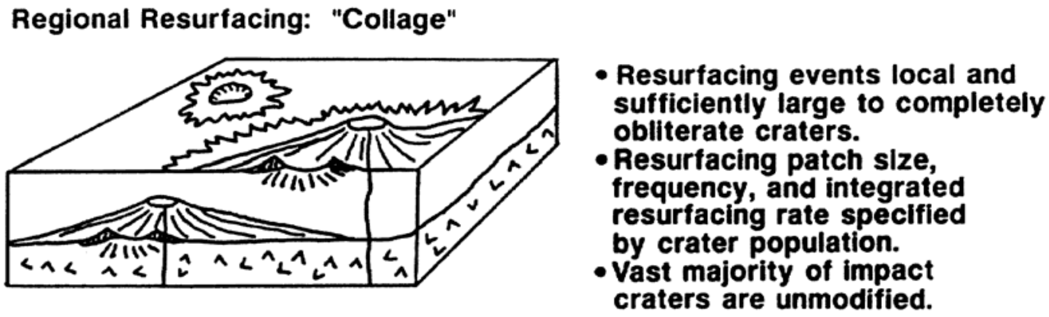

Figure 4.3 Schematic representation of the Equilibrium Resurfacing Model. Geological activity occurs at a constant rate on scales small enough to leave the impact crater population intact. Graphic courtesy of Jim Head, Brown University.

For the purpose of determining an average volcanic resurfacing rate, the limitations of the cratering statistics force us to use the apparent randomness of the distribution of impact craters as a constraint in modeling efforts, and to be content at present with predicting only globally averaged rates. The second important feature of Venus' cratering record is the small number of observed partially embayed craters. Any quantitative model of resurfacing processes must correctly account for this, and it can provide an important constraint on both spatial and temporal scales of resurfacing.

Two dimensional models that consider patches of planetary surface that are reworked by impact cratering and volcanic resurfacing can only be constrained by the areal and size frequency distributions of the observed crater population. For this reason, they are unable to distinguish between the two end member models discussed above. In order to choose between the widely differing predictions of Venus' surface age, a more complete picture of the way impact craters are removed and modified on Venus must be incorporated into a resurfacing model. I have implemented a 3-dimensional Monte Carlo resurfacing model, simulating the evolving surface of Venus under the influence of a flux of impacting objects and a variety of styles of volcanic resurfacing [*Bullock et al.*, 1993]. Simulated surfaces with a wide range of constant volcanic resurfacing rates have been generated. The evolution of partially embayed craters is tracked during each run, and the resulting crater populations may be compared with observations. By incorporating constant resurfacing rates and a power law distribution of flow sizes I predict the volcanic fluxes necessary for achieving a steady state between impact crater production and annihilation. Similarly, I show the resurfacing rates that are necessary to produce surfaces that are in crater production with predicted percentages of partially embayed impact craters.

By exploring the parametric space and analyzing the resulting size-frequency distributions of impact craters, I show which combinations of parameters lead to the emergence of surfaces statistically similar to Venus'. In particular, the question of whether Venus' crater population represents a surface that is in equilibrium or production is addressed. The simulations are also shown to place constraints on the amount of time since the last large scale resurfacing event, and upon the globally averaged resurfacing rate.

A 3-Dimensional Monte Carlo Model of the Resurfacing of Venus

Model Description

The computer simulation of the planetary surface is represented on a 3-D grid, with a surface resolution of 5 km and a vertical resolution of 100 m. The total grid represents an area of 4 x 10^8 km^2, the approximate surface area of Venus. The surface is initially flat, with volcanism and impact cratering being the only forces shaping subsequent topography. Monte Carlo methods are used to randomly place impact craters, at rates and diameters derived from the observed mass distribution of Earth and Venus crossing asteroids and comets [*Shoemaker et al.*, 1991]. The impact crater diameters are chosen from

$$N(D) = C_1 D^{-b} \tag{4.1}$$

Figure 4.4 is the cumulative size-frequency distribution of all Venus impact craters, with each size bin chosen so that craters with diameters from D to $D + 2^{1/2}D$ are included. The solid line shows the statistics for the real Venus surface, while the dotted line shows the size-frequency distribution from integrating (4.1). Rim heights are calculated from the diameter/height relationships for lunar impact craters [*Pike*, 1977],

$$R_H = C_2 D^{-c} \tag{4.2}$$

A wide range of volcanic features are represented on the planet. The observed size-frequency distribution for volcanic features on Venus [*Head et al.*, 1992] is used to randomly select volcanic forms and to place them on the planet. Again, the observed distribution is fit to a power law for the Monte Carlo simulation,

$$N(V) = C_3 V^{-a} \tag{4.3}$$

A histogram summarizing the size-frequency distribution of volcanic features on Venus is shown in Figure 4.5. The areal extent of shield fields, large volcanoes, and lava flows is determined in the simulations by sampling the appropriate distributions for the feature type from Magellan data [*Head et al.*, 1992].

Lava flow features are modeled using an energy minimization technique to simulate the effects of local topography on the shape and extent of flows.

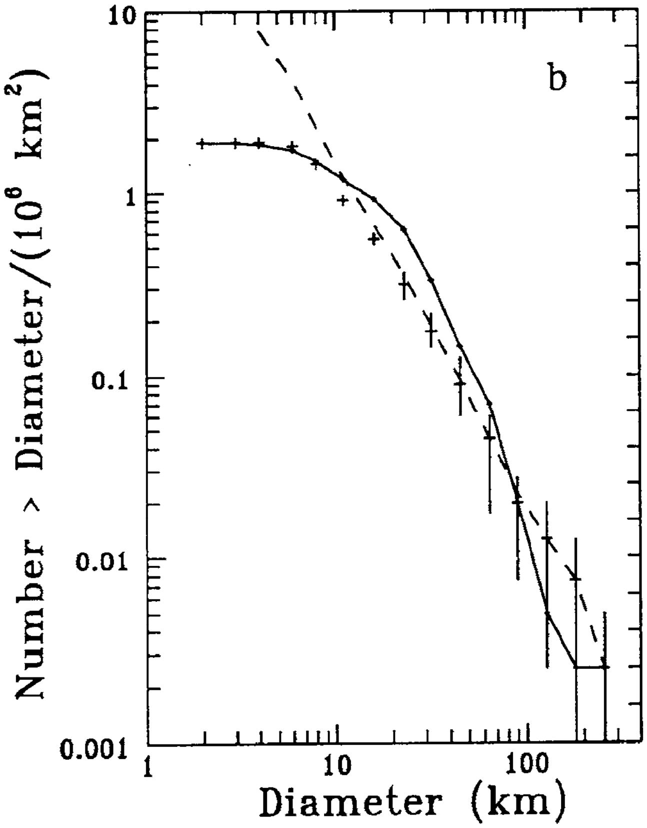

Figure 4.4 Cumulative size-frequency distribution for impact craters on Venus (solid line). The dashed line shows the size-frequency distribution that is sampled for use in the Monte Carlo model. Bins are for craters with diameters between *D* and *D* + $2^{1/2}D$. See text below for a discussion of the choice of size-frequency distribution used for the model.

Time steps of approximately 1 million years are chosen; the model selects craters at a given cratering rate and volcanic features at a specified volume rate. Superimposed craters and volcanic features are analyzed by their relative placement and topographies. Volcanic features may completely obscure old impact craters, partially cover old crater floor, or simply flow around crater rims. The surviving craters are counted and binned at each time step. Special attention is paid to the number of partially embayed craters. Their production is monitored and plotted as a function of time.

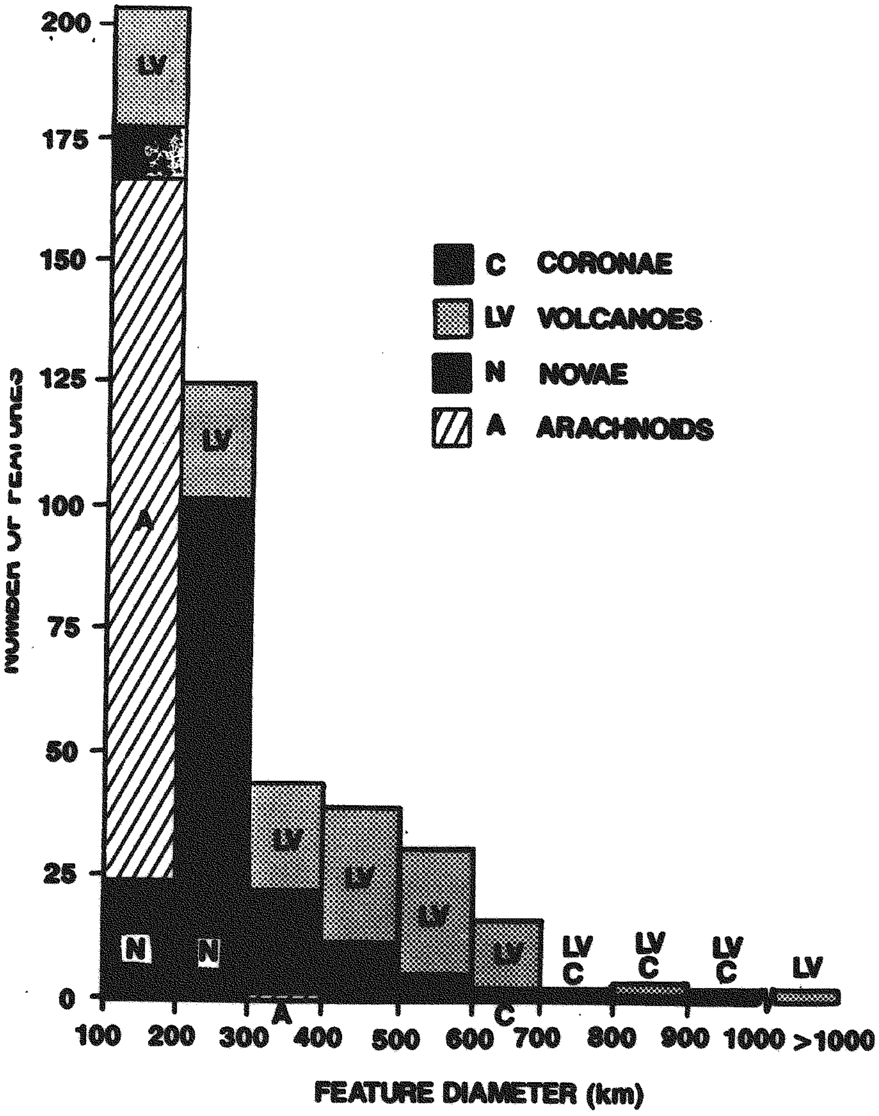

Figure 4.5 Size-frequency distribution of volcanic land forms on Venus. A power law is fit to the histogram for use in the Monte Carlo resurfacing model. Graphic courtesy of Jim Head, Brown University.

The size frequency distribution is calculated at the end of each run, which varies in total duration from 1 to 3 billion years. By varying the ratio of cratering rates to volcanic fluxes, surfaces of different crater populations, and therefore ages, can be produced. Depending upon the distribution of volcanic feature size and rates, surfaces with varying densities of partially modified craters may also be produced. The severe roll off of the crater size-frequency distribution due to atmospheric filtering is approximated by introducing a low diameter cutoff at a crater diameter of 16 km. Although this ignores the preferential removal of small craters, the cutoff has been selected to compensate for craters less than 16 km by overestimating the number with diameters between 16 and 32 km, such that the total number of craters will be close to that which would be produced by a more sophisticated treatment of the small-end distribution. The effects of atmospheric filtering of small impactors and the consequences for the size-frequency distribution of impact craters on Venus has been recently modeled [*McKinnon et al.*, 1997; *Zahnle*, 1992], but are not included here.

Another potential source of error in the model is the way in which the 3-dimensional simulation produces partially embayed craters. An accurate representation of the large numbers and volumes of flows on a planetary surface over geologic time is beyond the computational scope of the present model. Although surface topography partly influences the construction of simulated flows in the model, impact craters become embayed when adjacent flows exceed the crater rim height. *Schaber et al.* [1992], in their assessment of the number of partially embayed craters, use the criterion that some part of the rim material be embayed by adjacent flows. Since the present model requires that the crater rim is actually breached, to some extent the number of partially embayed craters is underestimated. Additionally, recent work on the rim height/diameter relation of Venusian impact craters [*Schaber et al.*, 1992; *Sharpton*, 1992] reveal that crater rim heights on Venus are slightly greater than those on the moon. Our use of lunar rim height/diameter ratios therefore results in a slight underestimate of the number of lava-breached impact craters. Future enhancements to the model will address the question of the embayment of crater ejecta deposits and the observed 'dark splotches' as well as incorporate time-dependent volcanic fluxes and improved data on impact crater rim height/diameter ratios.

If enough volcanic flow material is present in the vicinity of the impact crater, the crater may become obliterated during a resurfacing event. In this way, craters are removed or modified in the simulations by the action of volcanic flows. Since actual crater removal and modification processes are vastly more complex than this, there are obvious uncertainties in the numerical estimate of partially embayed craters.

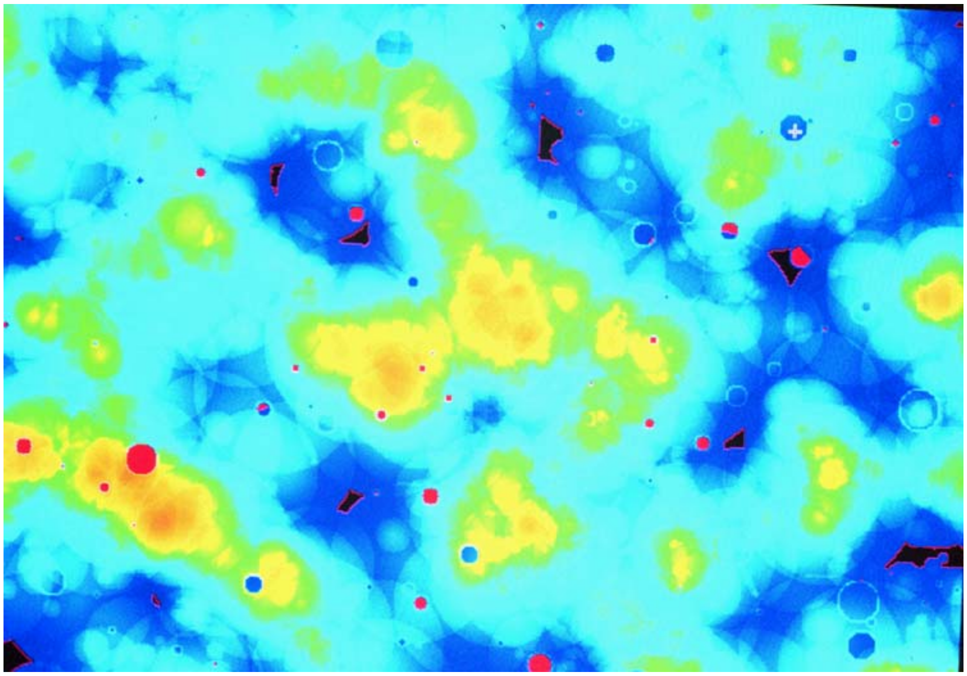

Figure 4.6 Color coded contour map of a 500 km x 500 km section of modeled surface from the 3-D Monte Carlo model. Computer generated volcanic topography is represented from blue to orange. Blue areas are lowlands, grading up the spectrum to orange mountain tops. Black is surface that has not been modified at all in the model, while craters are depicted in red. Partially embayed craters can be seen as semicircles or arcs.

Figure 4.6 is a color coded contour map of a 500 km x 500 km section of modeled surface from the 3-D Monte Carlo model. Computer generated volcanic topography is represented from blue to orange. Blue areas are lowlands, grading up the spectrum to orange mountain tops. Black is surface that has not been modified at all in the model, while craters are depicted in red. Partially embayed craters can be seen as semicircles or arcs. The numerical results from the 3-D simulation are remarkably landscape-like. Vast lava plains and fields of volcanoes were juxtaposed with impact craters resulting in sometimes startling synthetic stratigraphies. An example of a tiny piece of this landscape is shown in Figure 4.7. Here, a 25 km impact crater can be seen emplaced on an existing volcanic plain, but with a recent lava flow breaching part of the rim.

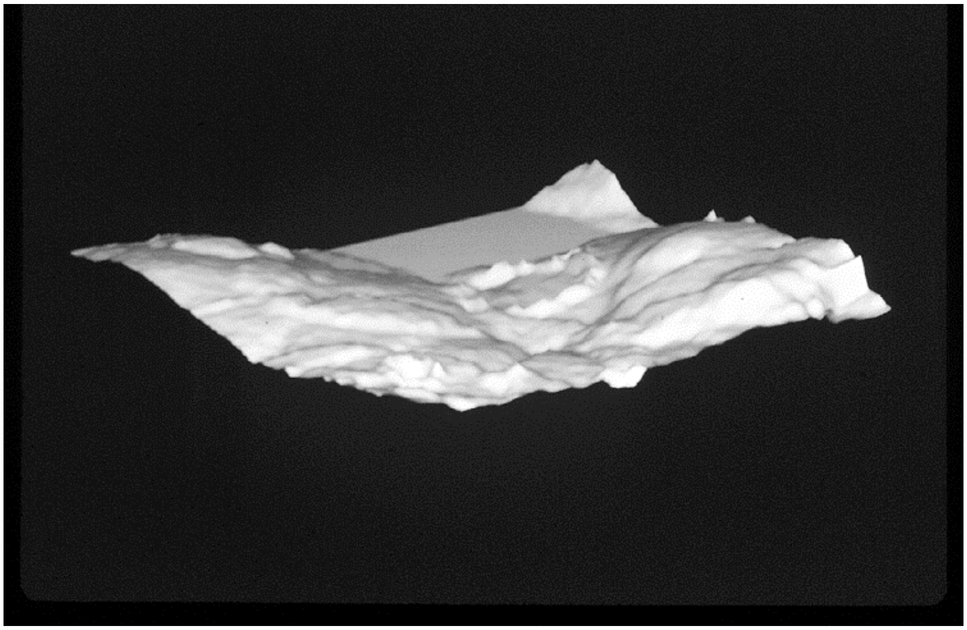

Figure 4.7 A small section of the synthetic planetary surface calculated from the 3-D Monte Carlo model. A partially embayed crater may be seen, surrounded by a volcanically-produced landscape.

Results from the Monte Carlo Model

Results for several runs are shown in Figures 4.8 and 4.9. In these simulations, surfaces were allowed to evolve for a billion years, reflecting the competing processes of constant-rate impact cratering and volcanism. Figure 1 shows the time evolution of surviving impact craters when the resurfacing rate is high enough for equilibrium between production and destruction processes to be evident after less than 1 billion years.

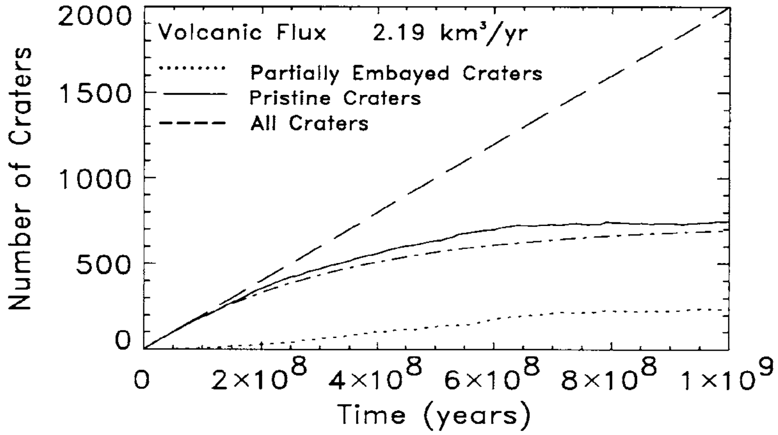

Figure 4.8 Model results for a volcanic flux of 2.19 km^3/year. The dashed line represents the production of impact craters without resurfacing. The solid line shows the evolution of surviving craters, and the dotted line shows the evolution of partially embayed craters. A steady state with 750 craters is achieved, with about 30% of them partially embayed. The dot-dashed line shows the result from the analytic model for the same parameters as the 3-D Monte Carlo model.

The equilibrium number of craters is significantly less than the number of observed craters on Venus, when the surface is subjected to a constant volcanic flux of 2.19 km^3/yr. More importantly, as can be seen by the dotted line trace, the fraction of surviving craters that are partially embayed by lava is quite high, at about 30%. By performing simulations with a wide range of resurfacing rates, it is apparent that this is a general feature of model runs which have a sufficiently high resurfacing rate to reach an equilibrium number of craters in 1 to 2 billion years. These resurfacing rates always produce a fraction of partially embayed craters substantially greater than that observed.

As a check on the numerical algorithms used in the Monte Carlo model, a simple 2-D analytic resurfacing model which predicts only the number of surviving impact craters as a function of time was also developed. The results of the analytic model, for a volcanic flux of 2.19 km^3/yr are also shown in Figure 4.8. With the assumptions of a constant resurfacing rate, and an initially crater free surface, the age of the surface and the subsequent resurfacing rate are uniquely determined by the number of observed surviving and partially embayed craters. This result is shown in Figure 4.9, where a constant flux of 0.37 km^3/yr results in approximately 950 surviving craters after 550 m.y., with 5% being partially embayed by flows.

For the purpose of comparing the results of this 3-dimensional model to those of the 2-dimensional models by *Phillips et al.* [1992], I have performed several runs with parameters that simulate the 2-dimensional parameters of these models. The results of model runs for the two solution branches of the Phillips *et al.* model are shown in Figures 4.10 and 4.11. For the ‘small patch’ solution branch, where the resurfacing patch size is 0.0003 or less, with a period of 150,000 years or more, it is found that the essential feature of the randomness of the surviving impact craters is preserved (Figure 4.10). However, for the 3-dimensional runs reported here, a large percentage of the surviving craters (15%) are partially embayed by the lava flows. Since resurfacing in the 2-dimensional model occurs in constant patches with a uniform thickness of 2 km, the number of partially embayed craters for these runs is greatly underestimated, and may be taken as a lower limit.

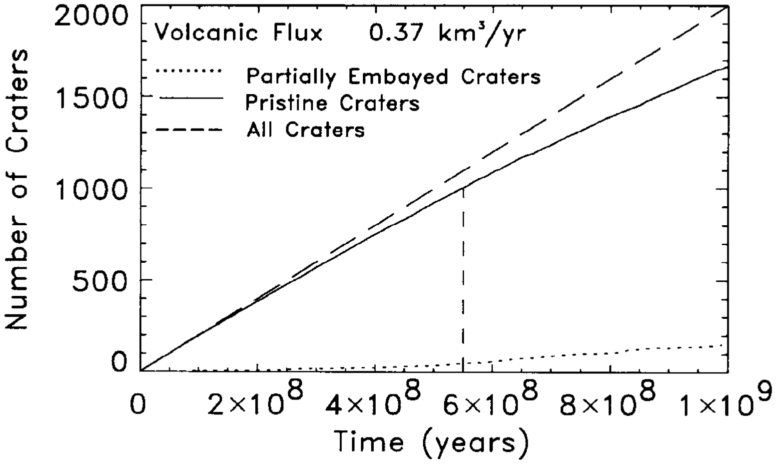

Figure 4.9 Monte Carlo model results for a volcanic flux of 0.37 km^3/year. 550 million years is required to obtain approximately 950 craters, with 5% of them partially embayed, as shown by the vertical dashed line.

For the ‘large patch’ solution branch, where the patch size is 0.1 with a period of 50 million years, the resulting crater population is manifestly not random (Figure 4.11). By modeling the resurfacing process in three dimensions, it can be seen that the equilibrium resurfacing model by *Phillips et al.* [1992] that is consistent with the observation of crater spatial randomness cannot also be consistent with the requirement of a small number of partially embayed craters. For this reason, it appears that a model that favors vigorous resurfacing in the past, followed by a low level of volcanic resurfacing, is far more consistent with the observed crater population.

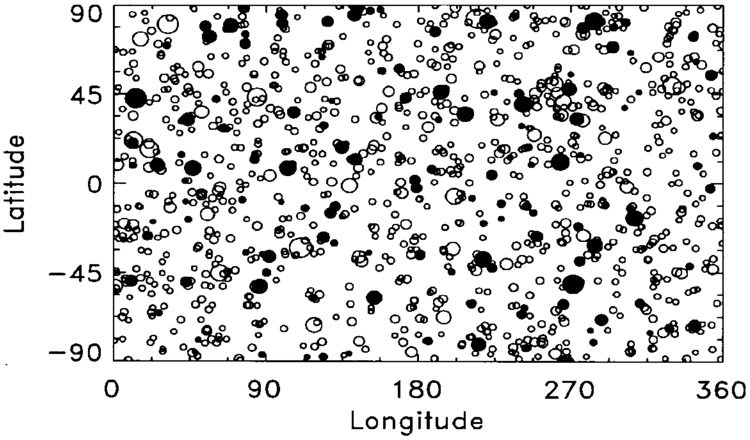

Figure 4.10 Model results using parameters from the 2-D model of *Phillips et al.* [1992] 'small patch' solution branch. The size of the area resurfaced per event is 0.0003 of the total area, and the period of periodic resurfacing is 150,000 years. Pristine craters are open circles, embayed craters (which represent 15% of the total population) are shaded.

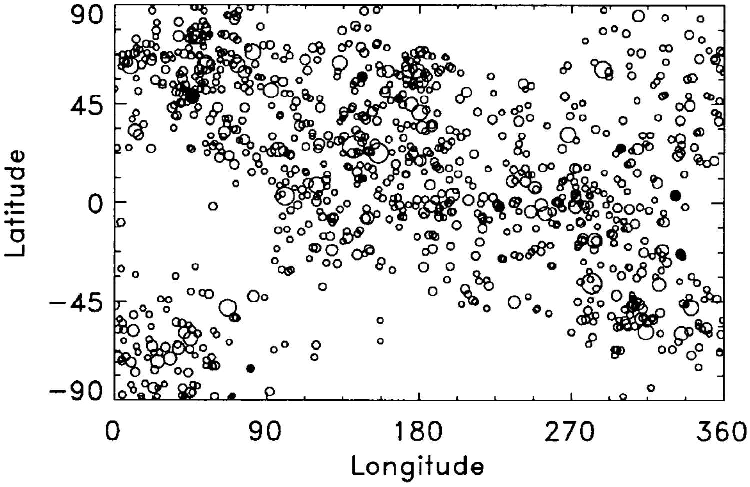

Figure 4.11 Model results using parameters from the 2-D model of *Phillips et al.* [1992], 'large patch' solution branch. The size of the area resurfaced per event is 0.1 of the total area, and the period of periodic resurfacing is 50 m.y. Crater coding is the same as in Figure 4.10.

Analytic Resurfacing Model

As a guide for exploring the relationships between impact cratering rate, volcanic resurfacing rate, and crater and volcanic size distributions, I have developed a simple 2-D analytic resurfacing model. Since the simulation of a 3-D surface evolving in time is necessarily a complex numerical problem, it was decided that demonstrating a correspondence between the Monte Carlo results and a simpler, probabilistic analysis would serve as a check on the numerical algorithms. The analytic model describes the number of surviving craters as a function of time by multiplying the probability that an area is cratered by the probability that it is not resurfaced by volcanic processes.

If A is the fraction of area that is cratered per time step, and x is the fraction of area not resurfaced in that time step, then the total surviving cratered area in N time steps can be shown to be T_N, where

$$T_N = A\sum_{i=1}^{N} x^i \tag{4.4}$$

In this model, an equilibrium value for the total area is eventually achieved by taking the limit as N goes to infinity, so that the total equilibrium cratered area is

$$T_{eq} = \lim_{N\to\infty} A\sum_{i=1}^{N} x^i = A\left(\frac{x}{1-x}\right) \tag{4.5}$$

It is instructive to use ensemble averages from the power law distributions of the Monte Carlo model to analytically predict the time evolution of surviving impact craters. Although such a simple 2-D treatment ignores a great deal of the details of planetary resurfacing processes, it is a useful check against the numerical model. Figure 4.8 shows the comparisons between the Monte Carlo and analytic models in describing the time evolution of surviving craters. The excellent agreement demonstrates that the algorithms used in the numerical model are working correctly. The 3-dimensional aspect of the model, crucial for modeling the statistics of important surface features such as partially embayed craters are not amenable to this simple analytic approach.

Discussion

The Monte Carlo model presented here simulates the evolving surface of a planet by considering impact cratering and volcanic resurfacing. Impact cratering and volcanism are assumed to be spatially random, and occur uniformly in time. The initial conditions are simple: the planet is at first assumed to be free of impact craters and topography. Given these assumptions and a consistent scheme for calculating the number of surviving pristine and modified craters, the constraints provided by the total observed crater population yield unique solutions to both the average resurfacing rate and the globally averaged surface age. I have shown (Figure 4.9) that the 3-D Monte Carlo model best simulates the total number of both surviving and partially embayed craters observed on Venus with a volcanic flux of about 0.37 km^3/yr. The resulting globally averaged surface age in this case is about 550 million years. This estimate is consistent with an earlier estimate for the upper bound of the volcanic flux (2 km^3/yr) based on the surface density of craters from Venera 15 and 16 [*Grimm and Solomon*, 1987].

Due to the constraint provided by the dearth of partially embayed craters, an equilibrium regional resurfacing scenario, with the impact crater population in a steady state with resurfacing, is implausible. Resurfacing rates of approximately 2 km^3/yr or greater produce surfaces with the required number of craters that reach equilibrium in less than 1 billion years, but with far too large a proportion of volcanically modified craters. On the other hand, the model results presented here support the conclusion that a catastrophic resurfacing event that removed nearly all craters occurred on Venus and was followed by a low level of regional resurfacing for approximately 550 million years.

Estimates of Volcanic Outgassing Rates

Volatile Content of Venus Magmas

The degree to which the geologic history of Venus has affected its atmospheric evolution is dependent upon the volatile content of its magmas. By assuming an atmospheric steady state between present-day outgassing and escape to space, [*Grinspoon*, 1993] estimates an upper bound for the H_2O content of erupting lavas of about 50 ppm. This is consistent with more detailed geochemical modeling of crustal reservoirs [*Namiki and Solomon*, 1997], who found an average mantle abundance of 5 ppm, and concluded that crustal magmas are probably enhanced about 10-fold. For lack of better data, I will assume 50 ppm of H_2O in erupting lavas, far lower than the 1% or so found on the wetter Earth.

SO_2 abundances are harder to constrain, but typical values for the Earth are about 0.2% [*Coffin*, 1994]. This value will be used to estimate atmospheric source functions for the present model of Venus. Given these assumptions, two scenarios for the recent outgassing of Venus' crust are entertained. The first is the outgassing that accompanied catastrophic resurfacing, in the form of crustal foundering, with the result that the planet was covered in magma to a globally averaged depth of from 1-10 km in 10-100 million years [*Head et al.*, 1994; *Strom et al.*, 1994]. Following this is a lack of volcanic activity, which is unrealistic, but provides an impulsive input to investigate the effect it may have on the evolution of Venus' climate. The other case I will consider is that of the low level constant volcanic flux, derived from the Monte Carlo model, that is consistent with the random impact crater population and the number of partially embayed craters.

If the density of erupting basaltic magmas is taken to be $\rho_b = 3.3\ g/cm^3$, then the mass density of outgassed H_2O is

$$\rho_{H_2O} = 50 \text{ x } 10^{-6} \rho_b = 1.65 \text{ x } 10^{11} \text{ g / km}^3 \tag{4.6}$$

and the mass density of outgassed SO_2 is

$$\rho_{SO_2} = 0.002 \rho_b = 6.60 \text{ x } 10^{12} \text{ g / km}^3 \tag{4.7}$$

Outgassing Associated with the Catastrophic Resurfacing Event

If the globally averaged depth of lava deposited during catastrophic resurfacing is *d*, and the surface area of Venus is *S* (4.6 X 10^8 km^2), then for an exponentially decreasing volcanic flux with *e*-folding time of τ_r, the initial rate of outgassing for molecular species *j* is

$$F_{Ij} = \frac{S d \rho_j}{\int_0^\infty e^{-\tau/t} dt} \tag{4.8}$$

The rate of outgassing of molecular species *j* to the atmosphere is

$$F_{R_j}(t) = F_{Ij} e^{-\frac{t}{\tau_R}} \tag{4.9}$$

These estimated time-histories for the volcanic outgassing during a catastrophic resurfacing on Venus are plotted in Figures 4.12 and 4.13. Four possible histories are depicted: A global layer *d* 1 km thick with a time constant τ_r of 10 My, a global layer 10 km thick with a time constant of 10 My, 1 km thick with a time constant of 100 My and a 10 km layer with time constant 100 My.

Outgassing Associated with Recent Constant-Rate Volcanism

Results from the 3-D Monte Carlo model are used to estimate a constant rate of volcanic outgassing following a catastrophic resurfacing event, an estimate relevant to the more recent past of Venus. If the volcanic flux of lava in km^3/yr is F_V, then the rate of outgassing of molecular species j to the atmosphere is

$$F_{C_j} = F_V \rho_j \tag{4.10}$$

This outgassing history, for H_2O and SO_2, is shown in Figure 4.14. Possible outgassing histories of H_2O and SO_2 following a catastrophic resurfacing event on Venus are represented by (4.9) and (4.10). They are used as time-dependent inputs to the Venus climate model to investigate the response of the atmosphere to plausible evolutionary changes induced by the unique geological history of the planet.

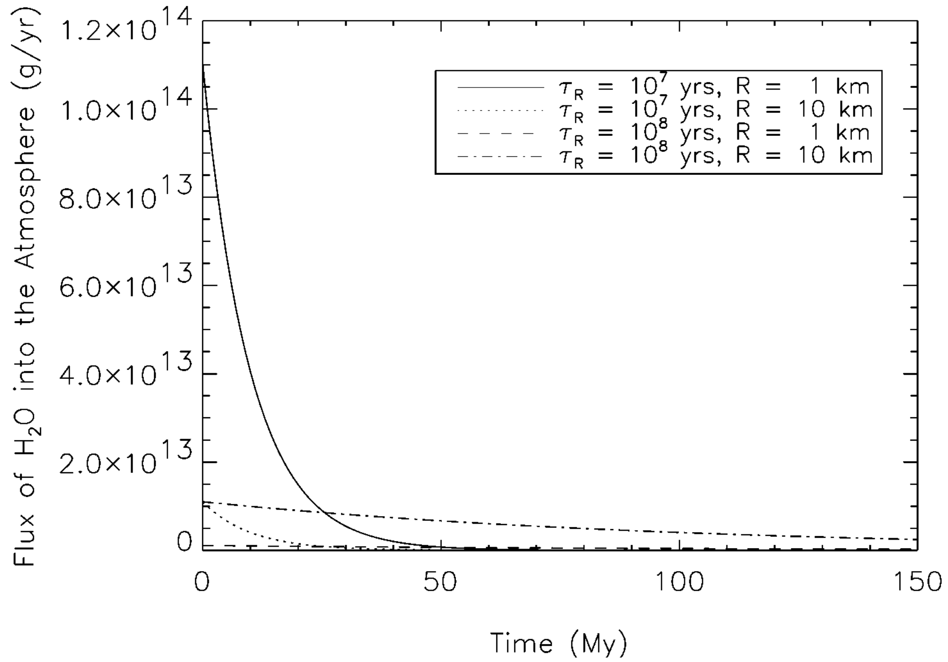

Figure 4.12 The time history of H_2O outgassing following a catastrophic resurfacing event. The traces show the expected outgassing of H_2O assuming an abundance in the lavas of 50 ppm, a globally averaged quantity of lava 1-10 km deep, and a 10-100 My duration for the event.

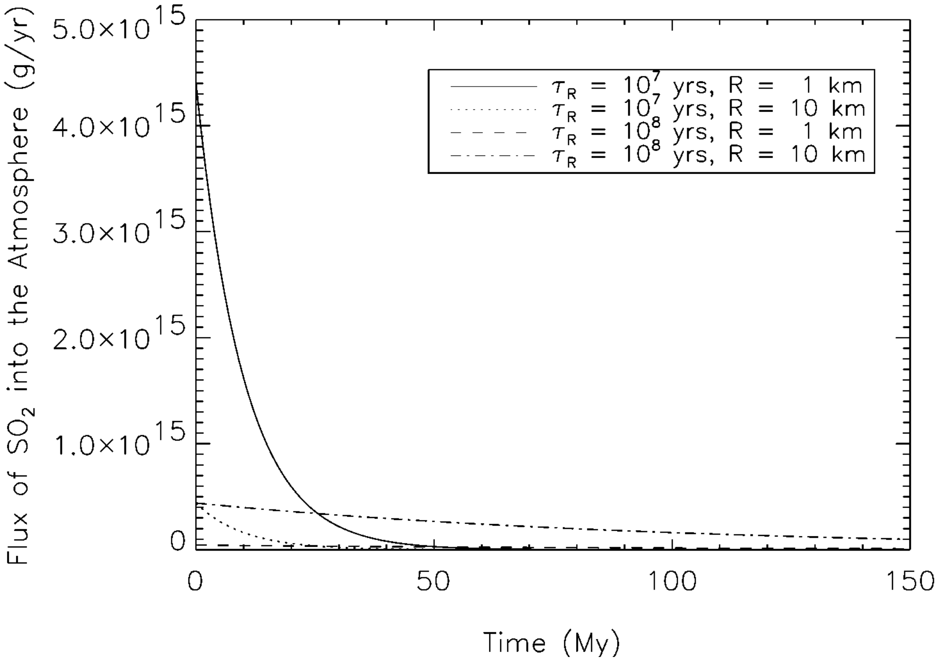

Figure 4.13 The time history of SO_2 outgassing following a catastrophic resurfacing event. The traces show the expected outgassing of SO_2 assuming an abundance in the lavas of 0.2%, a globally averaged quantity of lava 1-10 km deep, and a 10-100 My duration for the event.

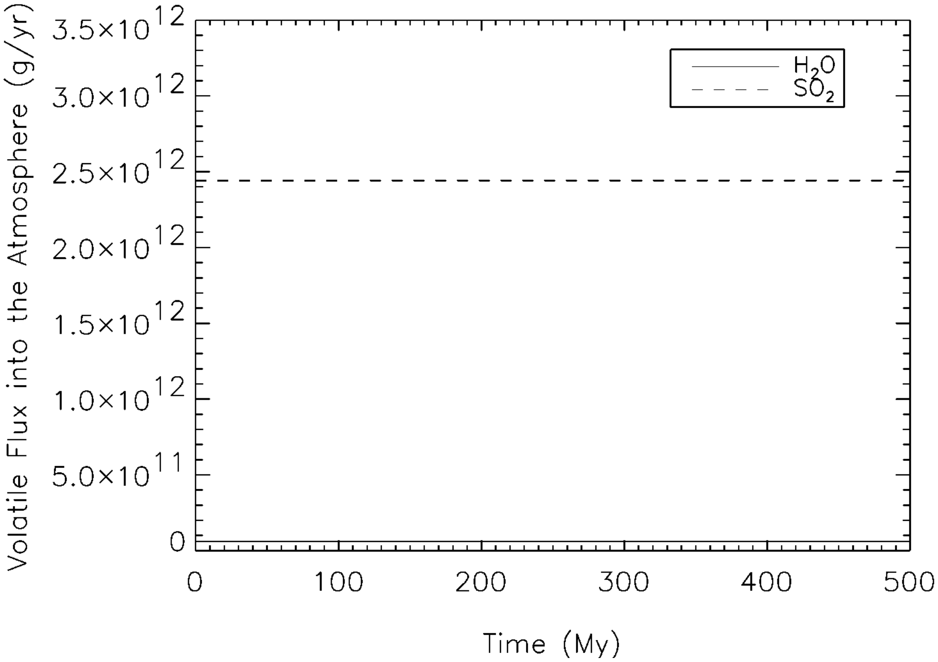

Figure 4.14 The outgassing history of H_2O (solid line) and SO_2 for a constant volcanic flux of 0.37 km^3/yr, assuming 50 ppm H_2O and 0.2% SO_2 abundance in the erupting lavas.

CHAPTER 5

GEOCHEMICAL PROCESSES ON VENUS

The History of Volatiles on Venus

The history of volatiles on Venus, the key to understanding the evolution of climate, remains in the realm of theoretical knowledge. It has been inferred from the photogeological record that little crustal and hence volatile recycling has occurred in the last 300 million to one billion years [*Phillips et al.*, 1992]. On Venus, plate tectonics may or may not have operated vigorously before this, but there is scant evidence. Lithospheric plate subduction is an important sink on Earth, establishing the return cycle of CO_2 and H_2O to the interior. The radiogenic ^{40}Ar abundance in the atmosphere, the product of radioactive decay of ^{40}K ($\tau_{1/2}$ = 1.3 Gy) is only one fourth as abundant on Venus as on the Earth. This implies less efficient outgassing on Venus over the age of the planet. Nevertheless, some means of transferring geothermal heat out of the planet must have prevailed; on the Earth, plate tectonics accounts for about 70% of the geothermal heat transport [*Turcotte*, 1995].

Geophysical Models

Three categories of models exist for the fate of Venus' lithosphere and with them, three pictures of volatile outgassing history.

1. *Turcotte* [1995] has proposed that episodically, Venus' lithosphere experiences a global-wide foundering, the result of instability due to a build up of heat in the mantle. Turcotte's conceptual model is the overturning of solidified crust on lava lakes, and subsequent lake-wide submersion and destruction of the crust. Following the global subduction of the lithosphere, a new one would form and cool,

thickening to the point where conductive heat transport is once again inhibited. Heat builds up in the mantle, followed every 300-700 My by another global lithospheric destruction episode.

Similar episodic behavior for the lithosphere has been predicted from geophysical models that consider other mechanisms. Models of temperature-dependent mantle convection [*Arkani-Hamed et al.*, 1993; *Arkani-Hamed and Toksoz*, 1984] indicate that it may undergo pronounced changes in style from vigorous and oscillatory, involving the lithosphere, to steady and slow, essentially decoupled from the lithosphere. Episodic mantle convection, induced by chemical differentiation of a two-layer mantle [*Herrick and Parmentier*, 1994; *Parmentier and Hess*, 1992] has been proposed as a means to explain large variations in lithospheric activity. All these 'catastrophic' models of the coupled history of the mantle and lithosphere are associated with large episodic injections of radiatively important volatiles to the Venus atmosphere.

2. In keeping with the 'uniformitarian' concept of geological activity (close to the Equilibrium Resurfacing end-member model of *Phillips et al.* [1992]), models have been proposed that seek to explain a steady-state transport of heat that results in something looking much like the present surface. Two mechanisms can make this work in the absence of plate subduction. One is hot spot volcanism; there is clear evidence for this currently in the massive shield edifices apparent in the Magellan radar images. However, with 37 major hot spot regions on the Earth (Hawaii being the largest by far), this mechanism accounts for only 26% of the terrestrial heat flux. Estimates for Venus require about 80 Hawaii-sized hot spots to transport the necessary heat. There is insufficient evidence in Venus' surface record for this much activity in the current era.

The second mechanism involves delamination of the lower crust, where the weaker but cooler lithospheric crust peels off to be subducted into the mantle. Crustal delamination is thought to occur on the Earth [*Turcotte and Schubert*, 1982] beneath the continents, but the magnitude of the phenomenon and its mechanism are obscure. *Turcotte*, [1995] has calculated that the entire lower crust of Venus must delaminate every 20 million years to account for the global heat transfer from the interior. Such a mechanism would probably greatly retard outgassing, a fact that is at least consistent with the reduced ^{40}Ar (relative to Earth) found in the atmosphere. Some combination of hot spot activity and delamination for long periods (2 billion years) up to the present cannot be ruled out.

3. Efficient differentiation of the radioactive heat-producing isotopes (^{40}K, ^{232}Th, ^{235}U, ^{238}U) into the crust, which then cools the planet conductively, is one possible explanation for Venus thermal history [*Kaula*, 1995]. The concentrations required to adequately account for planetary heat loss are not inconsistent with *in situ* γ and XRF spectroscopy measurements made by the Venera and Vega landers. A picture of relatively steady surface geological activity is envisioned, close to the Equilibrium Resurfacing end-member resurfacing model of *Phillips et al.* [1992].

Geochemical Cycles

Geochemical cycles involving the reactions of atmospheric gases with surface rocks are probably important on Venus, as they are on Earth. Although CO_2 is a greenhouse gas on Earth, its low abundance in the atmosphere is controlled by life and the CO_2 geochemical cycle. In addition, there is clear evidence that the terrestrial abundance of atmospheric CO_2 is currently being affected by anthropogenic sources [*Houghton et al.*, 1990]. A comparison of the total inventories of CO_2 [*Fegley and Lodders*, 1992; *Wildt*, 1940] shows that the atmosphere of Venus contains approximately the same amount of CO_2 as the Earth's, including terrestrial carbonates formed by sedimentation and biological processes, as well as the CO_2 in the atmosphere. At the temperatures and pressures found at Venus' surface, it is likely that much of the planet's total carbon inventory resides in the atmosphere. However, just as on the Earth and Mars, a CO_2 geochemical cycle probably exists or did exist on Venus. On the Earth, reactions between the surface and atmosphere are mediated by liquid water, providing the kinetic advantages of aqueous chemistry. On Venus, no such mediator exists that we know of, but heterogeneous surface/atmosphere reactions are probably important. Simple chemical rules of thumb lead us to expect that the higher temperatures and pressures will lead to surface reactions that operate 5000 times faster than they do on Earth.

The high temperatures and pressures (~92 bars) at the surface of Venus have led to the suggestion that surface/atmosphere interactions may play an important role in buffering CO_2 and other volatiles. *Urey* [1952] first proposed that atmospheric CO_2 on Venus could be buffered through reactions with surface minerals and *Rasool and de Bergh* [1970] proposed that heterogeneous reactions may have important implications for the evolution of climate on Venus. They showed that the surface temperature and pressure on Venus coincide approximately with the pressure-temperature equilibrium of the calcite-wollastonite-CO_2 mineral reaction. Recent laboratory data on the equilibria and kinetics of possible surface/atmosphere reactions under Venus-like conditions provide important insights into the role that they may play in moderating Venus' climate [*Fegley et al.*, 1995; *Fegley and Treiman*, 1992].

Small changes in radiatively active atmospheric species can change the magnitude of the Venus greenhouse effect and shift the equilibrium points of key mineral buffers, resulting in an important climate feedback mechanism. If this is the case, perturbations to the atmospheric inventory of radiatively active species, caused by volcanic eruptions, may have a significant impact on the climate of Venus, and upon the stability of the greenhouse effect.

Heterogeneous reactions between SO_2 and the surface are seen to proceed rapidly in chemical kinetics experiments performed under Venus-like conditions [*Fegley and*

Prinn, 1989; *Fegley and Treiman*, 1992]. Since the deep atmosphere abundances are one to two orders of magnitude higher than can be accounted for by equilibrium with surface minerals [*Fegley and Treiman*, 1992], this implies active sources and sinks of sulfur. If surface reactions are indeed active in altering atmospheric SO_2 and CO_2, and if reaction rates are significant on geologic timescales, it is of interest to assess the impact they may have on the climate of Venus.

The Fate of Hydrogen and Deuterium

Much of the theoretical work on the early climate evolution of Venus has focused on the fate of its water. With a largely anhydrous crust (most hydrated minerals are unstable [*Fegley and Treiman*, 1992]), and an atmospheric mixing ratio of 30 ppm, Venus has about 100,000 times less water than the Earth. Either Venus formed with a far smaller endowment of water, it is sequestered in the mantle, or the H has escaped to space, leaving O to equilibrate with the surface. Simulations of the late stages of solar system formation indicate that icy planetesimals from various outer regions were scattered somewhat uniformly into the inner solar system [*Ip and Fernandez*, 1988]. This conclusion has led to models of volatile inventories among the terrestrial planets that are dominated by comparable rates of impacts of icy planetesimals [*Owen et al.*, 1992]. In addition, the bulk density and apparent similarities in the CO_2 and N_2 inventories lend credibility to the notion that the Earth and Venus received approximately equal amounts of water early on.

The ratio of D/H in the water within Venus cloud particles was measured *in situ* by the Pioneer Venus neutral mass spectrometer, and was found to be an astonishing 120 times the D/H of terrestrial water [*Donahue et al.*, 1982]. Massive fractionating loss by exospheric escape from a large primordial reservoir is a likely mechanism for the D/H signature seen in the Venus atmosphere today [*Donahue and Hodges*, 1992; *Kasting*, 1988; *Pepin*, 1991; *Zahnle and Kasting*, 1986]. With a very moist troposphere resulting in no cold trapping at the tropopause, stratospheric water would have been susceptible to photodissociation by the early intense solar ultraviolet flux.

Modeling of hydrodynamic water loss on early Venus provides estimates that a terrestrial ocean's worth could have been lost in 300-600 million years [*Donahue and Pollack*, 1983; *Kasting et al.*, 1984]. Lower limits for the amount of water originally on Venus, based on the current D/H ratio, vary from 0.12 to 1.1% of a terrestrial ocean [*Donahue et al.*, 1997]. *Grinspoon* [1993], however, has argued that the current D/H ratio in Venus' atmosphere can also be explained as the product of continuous outgassing from a highly fractionated mantle source, or Rayleigh fractionation after massive outgassing associated with a catastrophic resurfacing event 0.5 to 1 billion years ago. In the latter case, atmospheric water abundance would have been 150 times as high in the relatively recent past as it is today.

With the majority of the planet's inventory of water leaving Venus at some time in the past, the timing of these processes is important for understanding the geochemistry of other volatiles on Venus. Abundant water early on would have greatly aided the formation of vast beds of carbonates and sulfates, sequestering carbon and sulfur in the possibly recycling crust. The removal of these gases would in turn have affected climate through altering the greenhouse effect. This processing must have slowed immensely as atmospheric water dispersed to space. Additionally, the cessation of plate tectonics would have led to the build-up of atmospheric volatiles through volcanic and tectonic outgassing.

The timing of these events, if they occurred, is unclear. Nevertheless, it is possible to calculate the effects that changing abundances may have on climate through the use of the radiative transfer and cloud models presented in Chapters 2 and 3. In addition, the equilibria and reaction rates derived from laboratory experiments may be harnessed to derive time rates of change of key atmospheric volatiles due to reactions with the surface. The following section describes how this is done, and how these data are scaled to the global regime, where diffusion of atmospheric species to new reaction sites within the crust is critical. Coupling the time history of volatile transport due to surface/atmosphere interactions with the radiative transfer and cloud models provides a unique way to explore the stability of Venus' climate. Similarly, the continued escape of H and D from Venus' exosphere is modeled so that their effects can be simulated in the Venus climate model.

Surface-Atmosphere Interactions

For the purpose of modeling the effects of surface/atmosphere interactions on the climate of Venus, heterogeneous reactions were selected by employing the following criteria:

1) Surface minerals involved in reactions with the atmosphere should have a high probability of being present under current Venus conditions. Venera 13/14 and Vega 2 X-ray fluorescence measurements provided compositional data for elements heavier than Mg. Ca is present and can be in the form of oxides, carbonates, and silicates. Abundant Fe assures that some oxidized Fe exists in surface rocks, probably in large amounts [*Barsukov et al.*, 1986; *Surkov et al.*, 1984; *Surkov et al.*, 1986].
2) Equilibrium values for proposed reactions should be close to those found at Venus' surface. The extensive study of possible surface/atmosphere reactions by [*Fegley and Treiman*, 1992] discusses a large number of such reactions, and predicts the stability of many possible mineral assemblages at Venus' surface.
3) Only reactions for which laboratory kinetic data was available were considered. Although this severely restricts the number of reactions under consideration, surface/atmospheric reactions can only be effective if they are kinetically favored. A number of potential buffering mechanisms for such important volatiles as H_2O, HCl, and HF have been proposed [*Fegley and Treiman*, 1992; *Lewis*, 1970;

Volkov et al., 1986], but must await laboratory determinations of reaction rates before their impact on Venus' climate can be ascertained.

Of the hundred or so surface/atmosphere reactions considered in the literature, only three meet the above three criteria. They are:

$$\underset{(\text{calcite})}{CaCO_3} + \underset{(\text{quartz})}{Si0_2} \Leftrightarrow \underset{(\text{wollastonite})}{CaSiO_3} + CO_2 \tag{5.1}$$

$$SO_2 + \underset{(\text{calcite})}{CaCO_3} \Leftrightarrow \underset{(\text{anhydrite})}{CaSO_4} + CO \tag{5.2}$$

$$\underset{(\text{pyrite})}{3FeS_2} + 2CO + 4CO_2 \Leftrightarrow 6COS + \underset{(\text{magnetite})}{Fe_3O_4} \tag{5.3}$$

Reaction Thermochemical Equilibria

Reaction (1), the calcite-wollastonite-CO_2 reaction, was originally proposed [*Urey*, 1952] as a key mechanism for the buffering of CO_2 on Venus. Subsequent laboratory investigations of equilibrium values of this and other possible CO_2 buffering mechanisms [*Fegley and Treiman*, 1992] as well as improved determinations of Venus' surface conditions, have confirmed that this reaction may indeed be a very important geochemical mechanism for the regulation of CO_2 on Venus. The calcite/wollastonite reaction involving CO_2 is an important metamorphic process in the Earth's crust, and is a key part of the carbonate-silicate geochemical cycle. CO_2 is liberated by this reaction as it is dissolved in magmas which eventually find their way to the surface through volcanism. On Venus, it is remarkable that the equilibrium point for this reaction coincides nearly exactly with the surface temperature and pressure. The laboratory-derived phase diagram for this reaction is shown in Figure 5.1 by the solid line. The dashed line shows the partial pressure of

CO_2 vs. temperature for the Venus atmosphere. The two curves intersect at the approximately the conditions of the Venus surface.

However, the uncertainty in the equilibrium data is large. The majority of Venus' surface may reside well away from the CO_2-mineral equilibrium line. If all the available CO_2 were in the atmosphere and the surface temperature is higher than the CO_2-mineral equilibrium point, there we be no carbonate on most of the planet's surface. Reaction (1) would not proceed and would not affect the climate in this case.

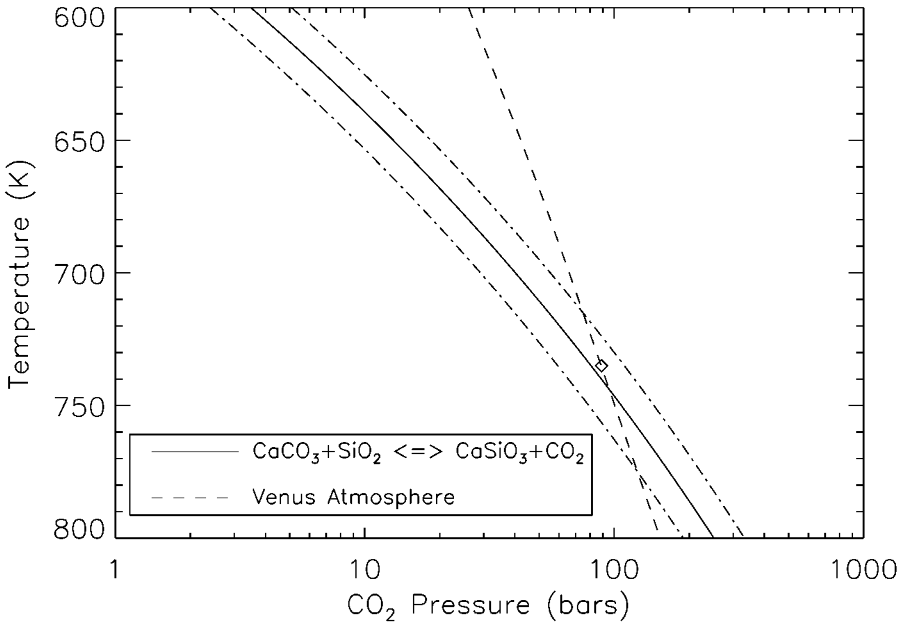

Figure 5.1 The laboratory-derived equilibrium phase diagram for the Urey reaction (1), shown by the solid line. The dashed line shows the partial pressure of CO_2 vs. temperature for the Venus atmosphere. The two curves intersect at the approximately the conditions of the Venus surface. The dot-dashed lines show the range in uncertainty in the laboratory equilibrium data.

Reaction (2), the conversion of calcite to anhydrite, involves the exchange of sulfur between the atmosphere and surface. The current abundance of SO_2 in Venus' atmosphere is about two orders of magnitude greater than that predicted by equilibrium with surface rocks at Venus surface temperatures. The equilibrium values for this reaction are shown in Figure 5.2 with a solid line. The dashed line depicts the partial pressure of SO_2 currently in the Venus atmosphere.

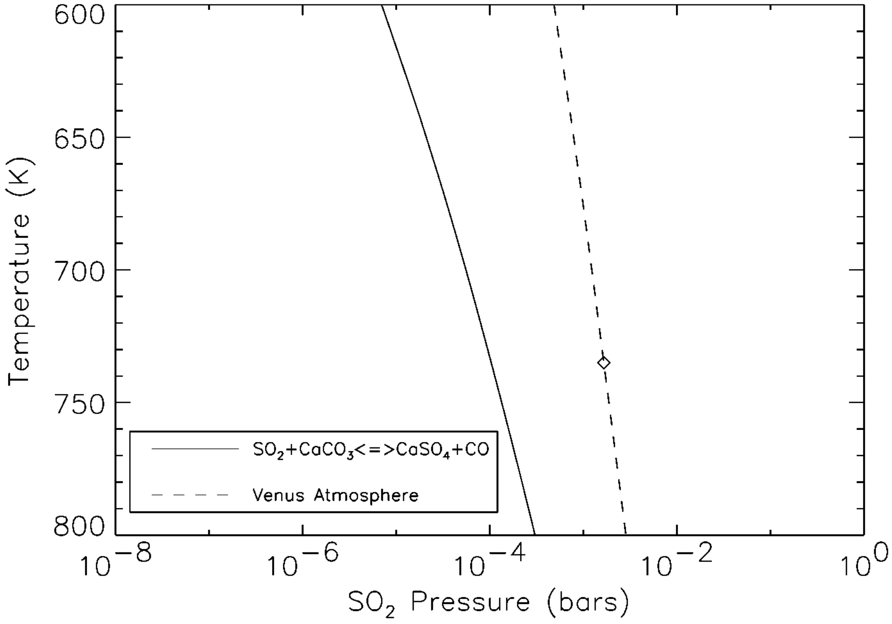

Figure 5.2 The laboratory-derived equilibrium phase diagram for the reaction of atmospheric SO_2 with carbonate to form anhydrite (reaction 2), shown with the solid line. The dashed line shows the partial pressure of SO_2 vs. temperature for the Venus atmosphere. Current SO_2 abundance in the atmosphere of Venus is about two orders of magnitude higher than the equilibrium value for this reaction.

One of the striking results from the Magellan spacecraft mission to Venus was the observation of areas of extremely low microwave emissivity in the highlands. It has been proposed [*Pettengill et al.*, 1982] that this is due to minerals consisting of inclusions of conducting material dispersed in a more insulating matrix. Pyrite is an abundant product of poorly oxidized magmas and an excellent candidate for explaining this phenomenon. However, *Fegley et al.* [1995] have shown with laboratory kinetic experiments that it oxidizes swiftly under Venus conditions. This reaction (3) involves the conversion of pyrite to magnetite. In the process, COS is evolved. The equilibrium phase diagram, in terms of COS partial pressure, is shown in Figure 5.3 with a solid line. The dashed line depicts the partial pressure of COS currently in the atmosphere.

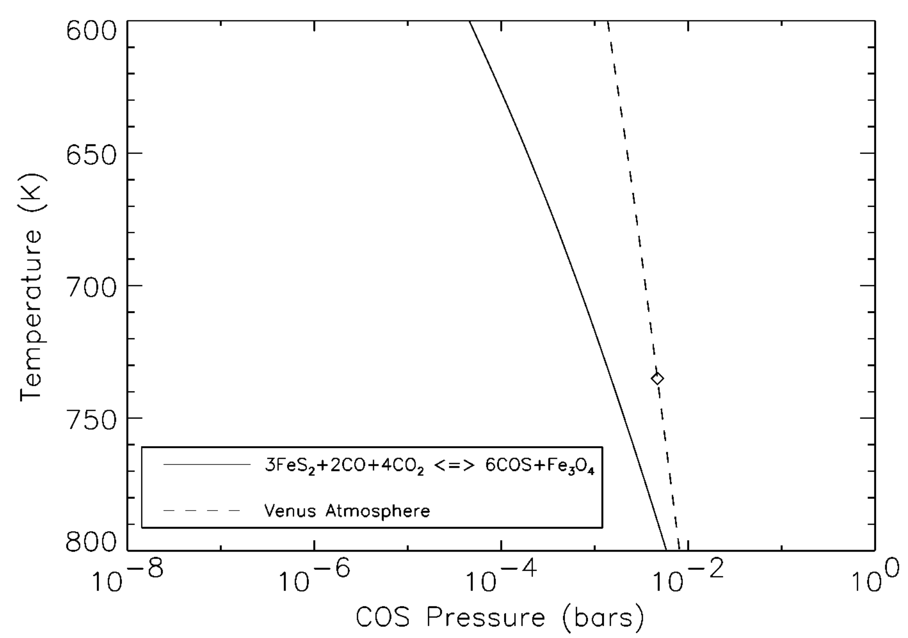

Figure 5.3 The laboratory-derived equilibrium phase diagram for oxidation of pyrite to magnetite (reaction 3), and subsequent evolution of atmospheric COS, shown with the solid line. The dashed line shows the partial pressure of COS vs. temperature for the current Venus atmosphere. COS abundance in the atmosphere of Venus is about 5 times higher than the equilibrium value for this reaction.

Diffusion-Reaction Kinetics

Mueller and Kridelbaugh [1973] attempted to determine the rate of reaction (1) under Venus-like conditions. Although their work has been criticized by *Fegley and Treiman* [1992] as being inapplicable to Venus due to faulty analysis of the laboratory data, it will be shown here that with the proper formalism, the results are roughly scalable to Venus.

Mueller and Kridelbaugh proposed a rate constant for the decarbonation of calcite by directly measuring its rate of decomposition. Their data is in the form of an Arrhenius plot, which yields the activation energy ΔE_a, and therefore a rate constant in sec^{-1}, from

$$R_{CO_2} = Ae^{-\frac{\Delta E_a}{RT}} \tag{5.4}$$

Fegley and Treiman have asserted that this cannot be applicable to a planetary problem, since only a small fraction of available grain surface was covered in carbonate. However, given the conditions at which the experiments took place, it is possible to derive a simple reaction-diffusion equation to deduce a plausible surface reaction rate. Laboratory rate measurements provide surface reaction rates that are in general not limited by the time it takes for gases to diffuse long distances to reaction sites.

If n is the atmospheric number density of CO_2, z is the depth into the soil, and D is the molecular diffusion coefficient for CO_2 in the soil pore space, the atmospheric number density of CO_2 at the surface due to this reaction may be described by

$$\frac{\partial n}{\partial t} = D\frac{\partial^2 n}{\partial z^2} + \frac{n}{\tau} \tag{5.5}$$

Here, the rate constant R_{CO_2}, derived in the laboratory, is simply $1/\tau$. Solving the reaction-diffusion equation, the effective instantaneous surface reaction rate is simply the net flux of CO_2 into the soil, or

$$F = n\left(\frac{D}{\tau}\right)^{\frac{1}{2}} \tag{5.6}$$

and depends on the atmospheric number density, the lifetime, τ, and on the diffusion coefficient [*Bullock et al.*, 1994]. Diffusion of CO_2 into or out of the soil proceeds due to the concentration gradient set up by its reaction with mineral surfaces. The determination of the coefficient for the diffusion of gases into the soil is critical for understanding time scales for significant change in atmospheric species due to reactions with the surface. It is assumed that the atmosphere is in pressure equilibrium with gases in the interstitial spaces of the soil. Without an external concentration gradient, the flux of molecules impinging upon the plane of the Venus surface would be equal to the flux of molecules reentering the atmosphere. A concentration gradient is set up in the soil, however, by diffusion of the vapor phase downwards and subsequent reaction of the gas with soil grain surfaces.

Diffusion of a gas through porous media may be modeled by two different mechanisms depending on whether the mean free path of the gas is greater or less than the average pore diameter. If pores are mostly larger than the mean free path, diffusion is dominated by molecular collisions. In this case, the diffusion coefficient is the gas diffusion coefficient of CO_2 multiplied by a constant that depends upon the geometry of the soil pore spaces. This transport mechanism is referred to as molecular diffusion. An analytic expression for the diffusion coefficient is obtained by modeling the pores in the soil as randomly twisted and distributed tubes embedded in a cross section of the soil [*Ball*, 1981]

Porosity is defined as the ratio of the pore space volume to total volume. The porosity of the Venus soil is quite unknown, but estimates of soil porosity on planetary surfaces range from 0.2 to 0.8 [*Smoluchowski*, 1967], with 0.5 the value usually assumed for martian weathered basalts [*Fanale et al.*, 1986]. Tortuosity is the ratio of total path length to length projected onto a preferred axis (the direction of the flux). An average over an appropriate ensemble of tortuous tubes is used to characterize a given soil. The value used for most soils with porosities between 0.2 and 0.8 and thus assumed for the Venus surface is 5 [*Satterfield*, 1970; *Smoluchowski*, 1967]. The molecular diffusion coefficient is given analytically as

$$D_m = \left(\frac{\varepsilon}{q}\right) D_o \tag{5.7}$$

where D_O is the gas-gas diffusion coefficient, ε is the soil porosity, and q is the soil tortuosity [*Flood*, 1967]. The gas-gas diffusion coefficient is derived from statistical mechanics [*Reif*, 1965] to be

$$D_o = \frac{2}{3\sqrt{\pi}} \frac{1}{P\sigma_o} \sqrt{\frac{(k_B T)^3}{m}} \tag{5.8}$$

where P is the pressure, σ_O is the cross-section of the molecule, k_B is Boltzmann's constant, T is temperature, and m is the mass of the molecule. The value of the molecular diffusion coefficient D_m for CO_2 at Venus surface conditions is 5.5 x 10^{-3} cm^2 s^{-1}. If pores are mostly smaller than the mean free path, molecular collisions with the pore walls dominate the transport of CO_2, a process known as Knudsen diffusion. The average pore size of the Venus surface is again unconstrained, but a value of at least 1 μm is appropriate for weathered basalts, such as found on Mars [*Fanale et al.*, 1986]

The mean free path l of CO_2 diffusing through pore spaces in the Venus surface is obtained from the statistical mechanics of gases [*Reif*, 1965], and depends on the temperature and pressure,

$$l = \frac{1}{\sqrt{2}} \frac{k_B T}{\sigma_o P} \tag{5.9}$$

Under Venus surface conditions, the mean free path of CO_2 is about 0.2 μm. Therefore, diffusion of CO_2 into the soil proceeds by molecular diffusion, adjusted for soil porosity and tortuosity, as in (5.7). The direct application of laboratory kinetic data yields the interpretation of a reaction rate that is temperature but not concentration dependent. Over geological timescales, the progress of a given geochemical sink will obviously be dependent upon the atmospheric column abundance. Using the above flux, derived by considering both the diffusion and reaction of atmospheric species in the soil, a more accurate analysis of the effect of heterogeneous surface/atmosphere interactions on climate is made possible.

By using this formalism to adapt the Mueller and Kridelbaugh laboratory data for the decarbonation rate of calcite under Venus surface conditions, it is found that the calcite-wollastonite-CO_2 buffer reaction proceeds with surface reaction rate of

$$R_1 = 10^{15.91} e^{-\frac{11356}{T}} \text{ molecules / cm}^2 \text{ sec} \tag{5.10}$$

The effect of this reaction on present day Venus is shown in Figure 5.4. Because there is a slight offset between the average Venus surface temperature (the diamond in Figure 5.1) and the equilibrium line of reaction (1), CO_2 leaves the atmosphere to produce carbonate at the surface. At 735 K, this proceeds quickly, and approximately 8 bars is lost from the atmosphere in 20 million years. These kinetics assume that wollastonite or some other suitable silicate is available for reaction to form carbonate.

Fegley and Prinn [1989] directly measured the surface reaction rate of the SO_2 anhydrite buffer, reaction (2). Their results were derived for current Venus surface conditions (T = 735 K, P_{SO_2} = 12 mbar), and the reaction rate as a function of temperature was found to be

$$R_2 = 10^{19.64} e^{-\frac{15248}{T}} \text{ molecules / cm}^2 \text{ sec} \tag{5.11}$$

In order to scale these laboratory data to other climate regimes (i.e., other temperatures and partial pressures), a formalism similar to that employed for reaction (1) was used. Thus the net effect of the proposed SO_2-anydrite buffering mechanism on Venus' climate is dependent upon temperature through both the reaction rate and the diffusion coefficient.

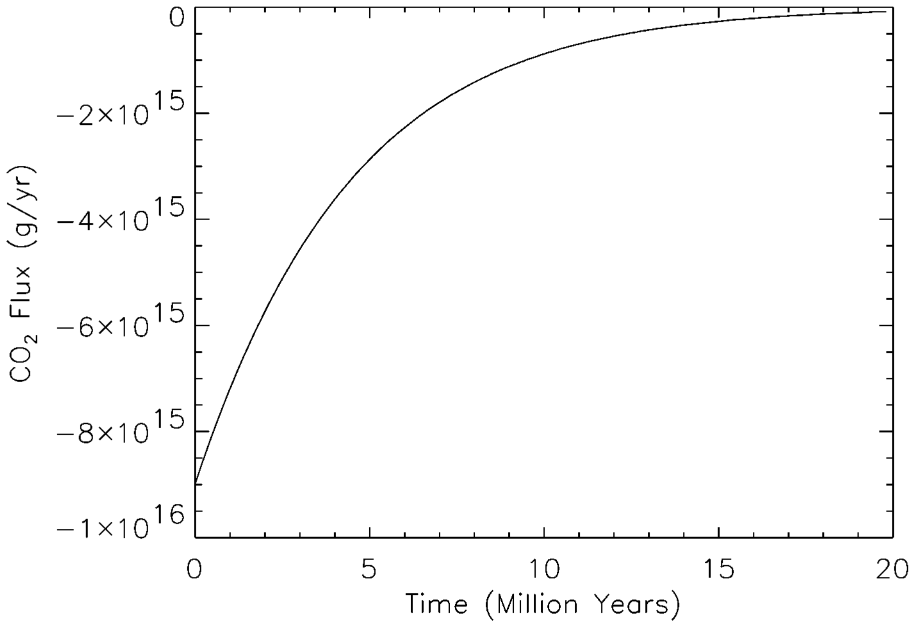

Figure 5.4 The flux of CO_2 into the Venus surface as a result of the atmosphere achieving equilibrium with silicates through the Urey reaction (1). Equilibrium is achieved in approximately 20 million years, removing a total of about 8 bars from the atmosphere.

Furthermore, through the flux equation, the surface reaction rate is also dependent directly upon the atmospheric concentration found at the surface. The evolution of the atmospheric mixing ratio of SO_2 as a result of reaction-diffusion kinetics of reaction (2) is shown in Figure 5.5. Atmospheric SO_2 abundance drops two orders of magnitude in 10 million years as it equilibrates with surface carbonate. The kinetics of pyrite weathering under Venus conditions has been determined in the laboratory [*Fegley et al.*, 1995]. They report activation energies and rate constants for the decomposition of pyrite under a variety of temperatures and CO_2-dominated atmospheric compositions. These data may easily be converted to a temperature-dependent surface reaction rate under Venus conditions.

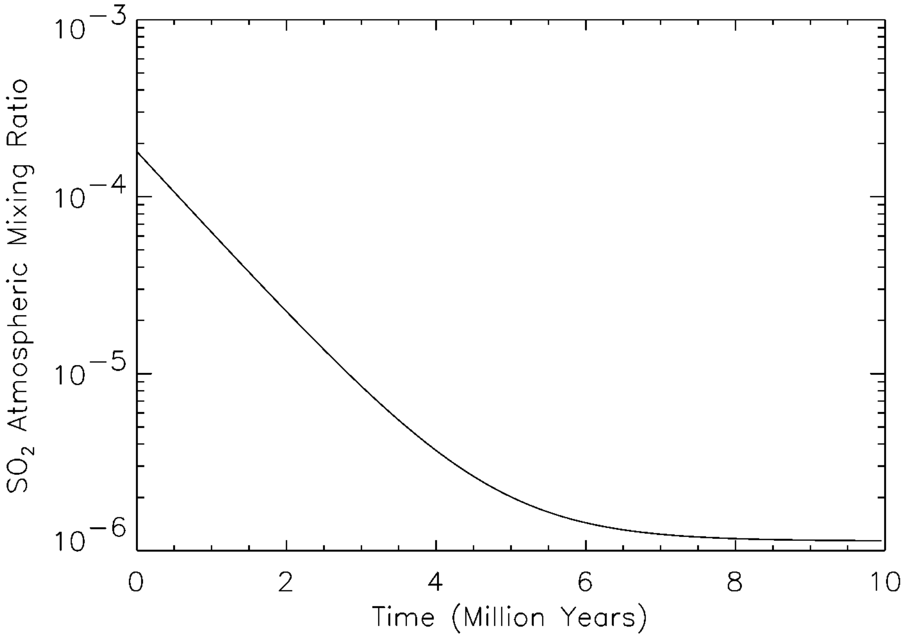

Figure 5.5 The evolution of the atmospheric mixing ratio of SO_2 as a result of reaction-diffusion kinetics of reaction (2). Atmospheric SO_2 abundance drops two orders of magnitude in 10 million years as it equilibrates with surface carbonate.

Using an activation energy of 1.5 x 10^6 joule/mole, and a reaction rate of 4 x 10^{-4} cm/hour, the reaction rate in terms of the number of sulfur atoms is:

$$R_3 = 10^{25.81} e^{-\frac{18050}{T}} \text{ molecules / cm}^2 \text{ sec} \tag{5.12}$$

This reaction may have important consequences for the atmospheric abundances of COS, and therefore on tropospheric chemistry. The reaction may therefore present important feedbacks on atmospheric chemistry, volatile abundances, and climate, so it is included in the present model. The evolution of atmospheric COS under the effects of reaction (3) are shown in Figure 5.6.

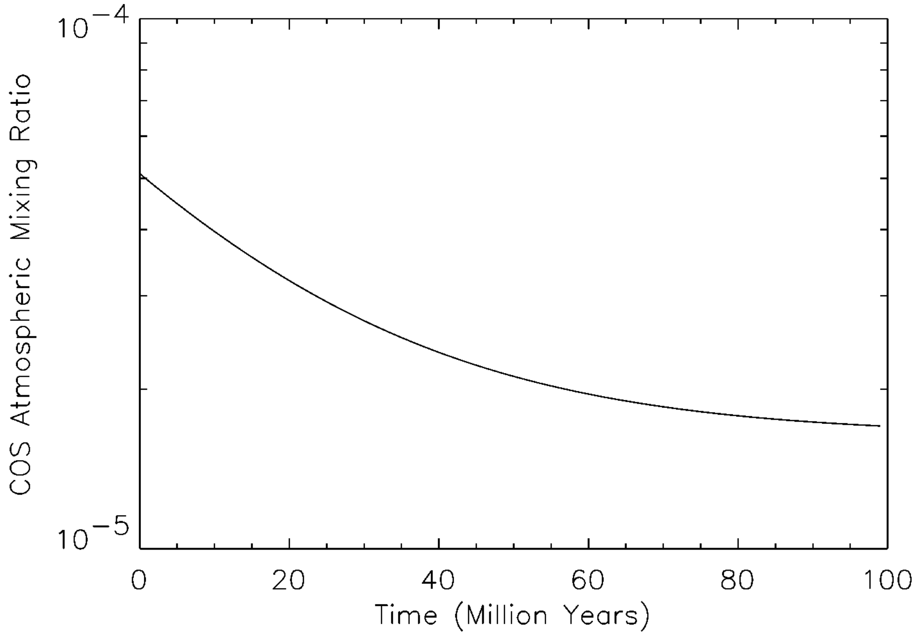

Figure 5.6 The evolution of atmospheric COS mixing ratio due to equilibrium of reaction (3), driven by reaction-diffusion kinetics.

Surface-Atmosphere Reactions Plus Outgassing

On Venus, the evolution of CO_2 and SO_2 may involve outgassing due to volcanism, as described in Chapter 4, as well as the effects of surface/atmosphere interactions. Using the reaction-diffusion scheme presented in this chapter, it is possible to contrive plausible scenarios for the evolution of these volatiles in the atmosphere under varying surface conditions.

Possible volatile histories incorporating both these effects, but ignoring changes in surface temperature due to climate feedback, are shown in Figures 5.7-5.9. Figure 5.7 shows the time evolution of SO_2 atmospheric mixing ratio for the case where SO_2 is outgassed quickly during a major geological event (Figure 4.13, 10 km global layer of lava in 10 My), while simultaneously reacting with surface rocks. After a 20-fold spike in atmospheric abundance, SO_2 equilibrates with the surface in 100 million years. For more leisurely outgassing associated with a milder global resurfacing event (Figure 4.13, 1 km in 100 My), and reaction of SO_2 with surface rocks, Figure 5.8 depicts the evolution of atmospheric SO_2. SO_2 abundance never increases, but has not yet equilibrated after 200 million years. For the case representative of a small rate of constant outgassing (Figure 4.14), along with the reaction of SO_2 with the surface, the evolution of atmospheric SO_2 is shown in Figure 5.9. Note that a steady-state abundance of atmospheric SO_2 is achieved after only 10 million years, at an abundance 5 times that of equilibrium.

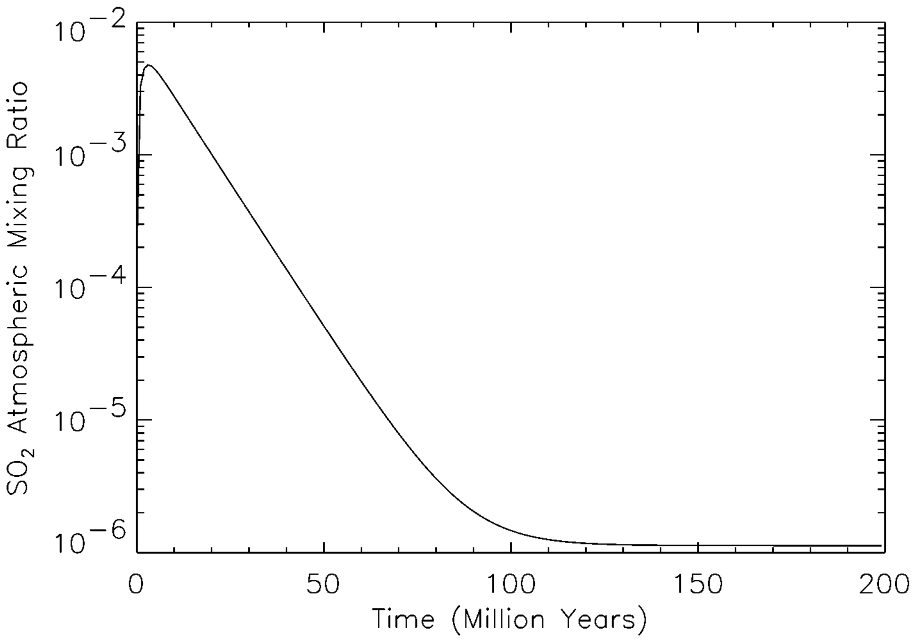

Figure 5.7 The time evolution of atmospheric SO_2 mixing ratio under the influence of massive outgassing associated with global resurfacing, and reaction of SO_2 with surface minerals. Outgassing is described as an exponentially decaying flux from lavas covering the planet in a global layer 10 km thick with a decay time constant of 10 My (see Chapter 4 for details).

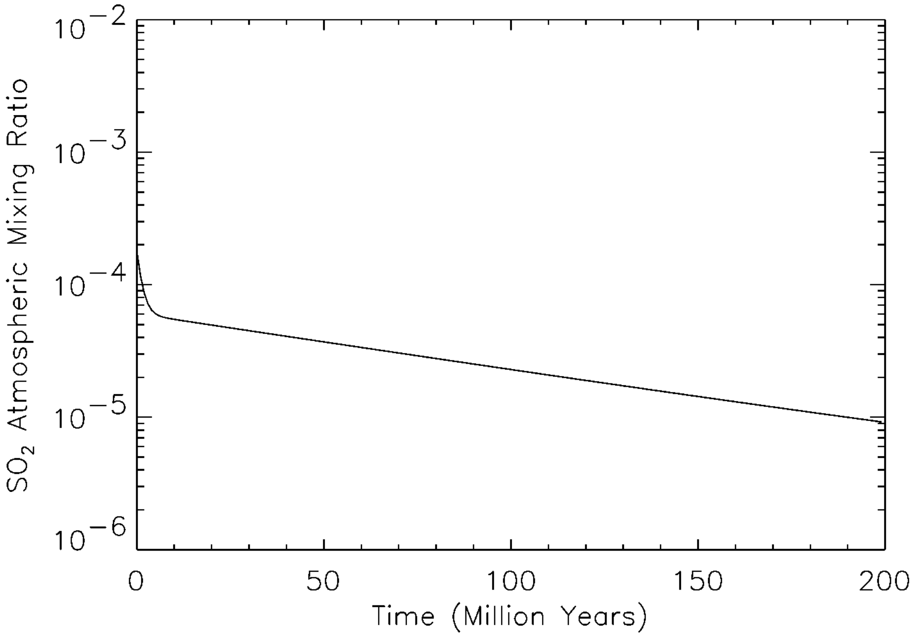

Figure 5.8 The time evolution of atmospheric SO_2 mixing ratio under the influence of massive outgassing associated with global resurfacing, and reaction of SO_2 with surface minerals. Outgassing is described as an exponentially decaying flux from lavas covering the planet in a global layer 1 km thick with a decay time constant of 100 My (see Chapter 4 for details).

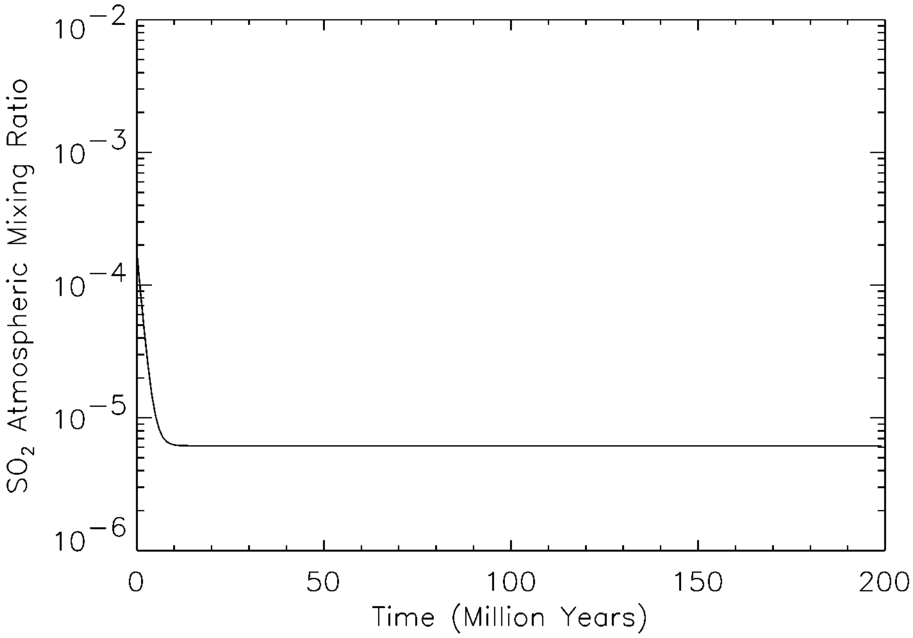

Figure 5.9 The time evolution of atmospheric SO_2 mixing ratio under the influence of constant low-level volcanic outgassing, and the reaction of SO_2 with surface minerals. Derivation of the constant volcanic outgassing source function is described in Chapter 4.

Exospheric Escape Processes

The current escape flux of H from Venus is due to two mechanisms: an electric field driven flow of ions in the night-side hydrogen bulge, and charge exchange. Each of these processes have different solar cycle average loss rates, but combined, they amount to an average flux of 1.6×10^7 cm^{-2} s^{-1} [*Donahue et al.*, 1997]. D, inhibited from escape by its larger mass, leaves Venus at a rate of about a tenth of this. For diffusion-limited escape, where the loss rate is limited by the ability of H and D to diffuse to the exobase, these amount to H and D lifetimes in the atmosphere of 170 million years and 1.7 billion years, respectively. The diffusion limit approximation is utilized to calculate the loss of H and D from the top of the atmosphere in the Venus climate model, although it a crude representation of the actual loss physics. In this case, if n_k is the number density and τ_k the lifetime against escape of species k,

$$\frac{\partial n_k}{\partial t} = -\frac{1}{\tau_k} n_k \tag{5.13}$$

Then the number density as a function of time is

$$n_k(t) = n_k(0) e^{-\frac{t}{\tau_k}} \tag{5.14}$$

The incorporation of H and D escape into the Venus climate model is straightforward. At timestep t_e the number of H_2O molecules removed from the atmosphere is

$$\Delta n_{e,H_2O} = \frac{1}{2}\left(\frac{t_e - t_{e-1}}{\tau_{H_2O}}\right) n_{e-1,H_2O} \tag{5.15}$$

and likewise for D

$$\Delta n_{e,HDO} = \left(\frac{t_e - t_{e-1}}{\tau_{HDO}}\right) n_{e-1,HDO} \tag{5.16}$$

The atmospheric mixing ratio of H_2O as a function of time, due to exospheric escape alone is shown in Figure 5.10. The initial conditions for this plot are atmospheric H_2O abundances of 100 times the current value. The initial D/H ratio is approximately the same as terrestrial, evolving to current ratio and abundances in 720 million years. When atmospheric escape of H and D is combined with the three possible outgassing histories, the evolution of atmospheric H_2O is shown in Figures 5.11-5.13. Rapid, extensive outgassing in conjunction with fractionating exospheric escape is depicted in Figure 5.11. A terrestrial D/H ratio for Venus' mantle has been assumed, and the atmosphere evolved to the current ratio and abundances about 800 million years. H_2O abundance peaks during the global outgassing event to a value of about 100 times the current one. This scenario is consistent with the hypothesis of Rayleigh fractionation after massive outgassing associated with a catastrophic resurfacing event [*Grinspoon*, 1993]. For a longer duration, milder outgassing event along with fractionating exospheric escape, the evolution of H_2O and HDO is shown in Figure 5.12. Again, a mantle source with terrestrial D/H is assumed. The atmospheric H_2O abundance peaks at about 3 times the current value, and achieves the current abundances and D/H ratio in 450 million years. Finally, the effects of low-level outgassing, consistent with the present surface record, in conjunction with fractionating exospheric escape are shown in Figure 5.13. Both H_2O and HDO remain in roughly steady-state at their current abundances.

The description of volatile sources and sinks on Venus presented in this chapter represents the best that can currently be done within constraints imposed by the available data. Combined with the outgassing scenarios of Chapter 4 and the atmospheric radiative transfer and cloud models of Chapters 2 and 3, it is possible now to investigate the effects of changing volatile abundances on the climate of Venus. In particular, I explore the kinds of climate feedbacks that develop from the interaction of these processes, climate stability on Venus, and likely time scales for climate change. This is the culmination of the work presented so far, and is the subject of the next chapter.

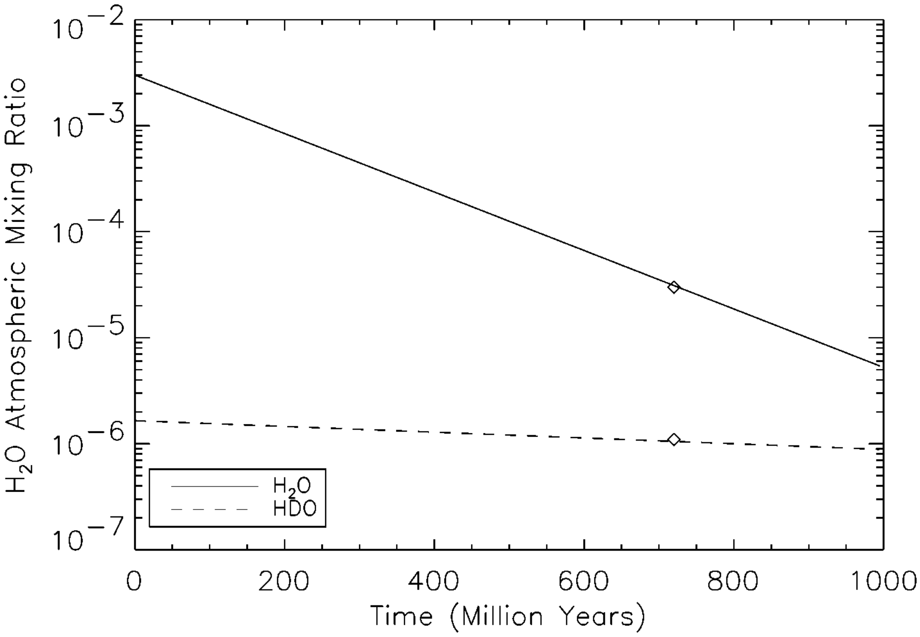

Figure 5.10 The evolution of atmospheric H_2O mixing ratio due to diffusion-limited exospheric escape (solid line). Initial abundance is 100 times the current value. Evolution of HDO is shown with the dashed line. Current abundances are marked with diamonds.

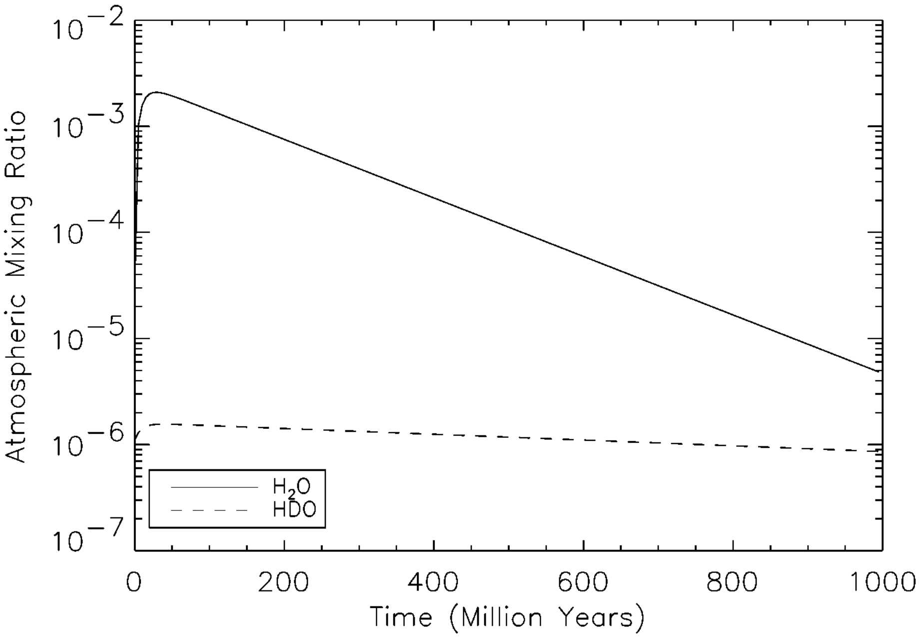

Figure 5.11 The evolution of atmospheric H_2O and HDO mixing ratio due to exospheric escape and volcanic outgassing. Outgassing is described as an exponentially decaying flux from lavas covering the planet in a global layer 10 km thick with a decay time constant of 10 My (see Chapter 4 for details). Outgassing source assumes terrestrial D/H values. Evolution of HDO is shown with the dashed line.

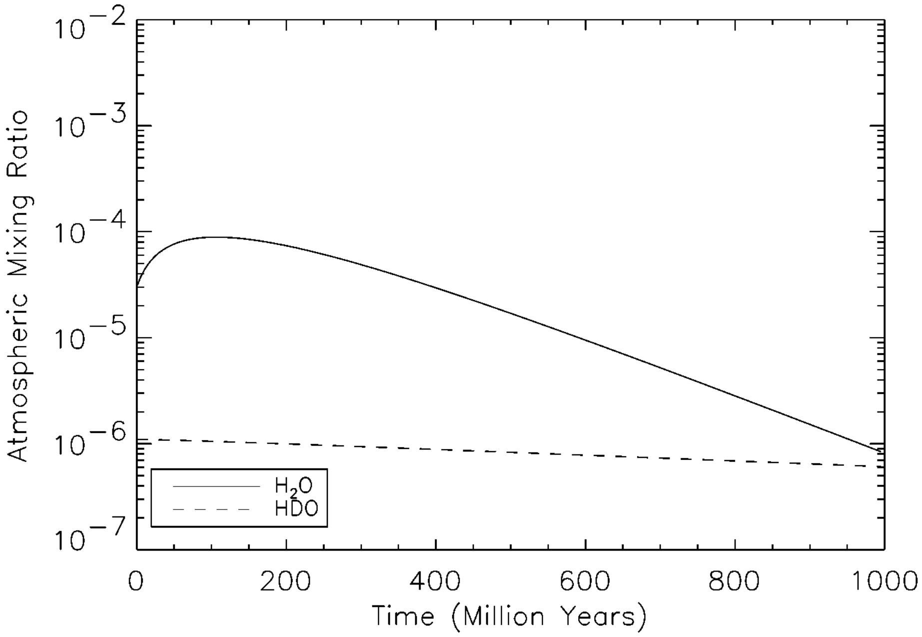

Figure 5.12 The evolution of atmospheric H_2O mixing ratio due to exospheric escape and volcanic outgassing. Outgassing is described as an exponentially decaying flux from lavas covering the planet in a global layer 1 km thick with a decay time constant of 100 My (see Chapter 4 for details). Outgassing source assumes terrestrial D/H values. Evolution of HDO is shown with the dashed line.

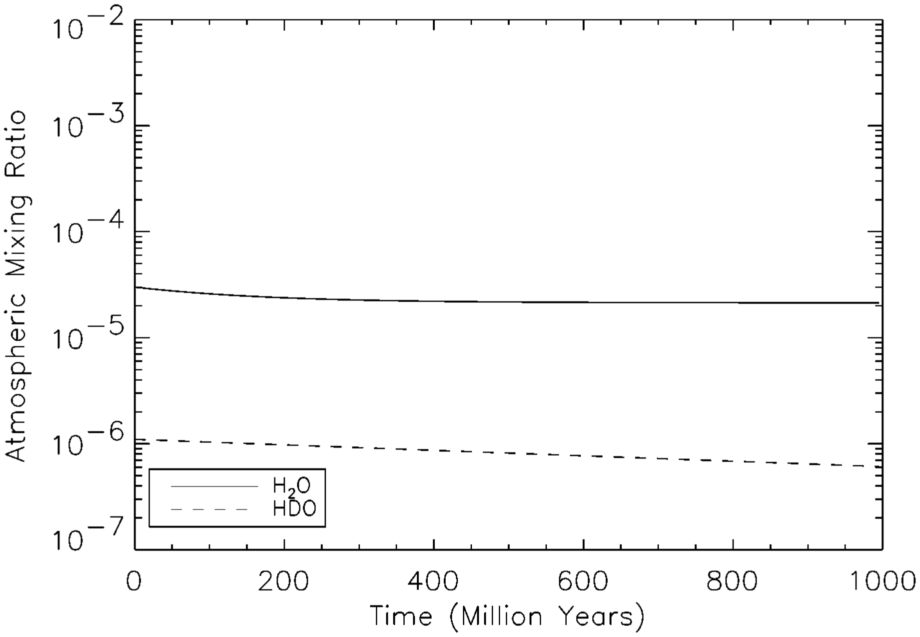

Figure 5.13 The evolution of atmospheric H_2O mixing ratio due to exospheric escape and low-level constant volcanic outgassing. Derivation of the constant volcanic outgassing source function is described in Chapter 4. Outgassing source assumes terrestrial D/H values. Evolution of HDO is shown with the dashed line.

CHAPTER 6

THE VENUS CLIMATE EVOLUTION MODEL

Conceptual Description

The previous chapters presented mathematical models of five planetary-scale processes that affect the climate of Venus. They were:

1) A nongrey, one-dimensional two stream model of atmospheric radiative-convective equilibrium.
2) A cloud chemical and microphysical model of the distribution and transport of H_2SO_4/H_2O aerosols in the atmosphere.
3) Models of geologically recent crustal outgassing on Venus due to:
    i) Intense volcanism associated with rapid global plains emplacement.
    ii) A constant volcanic flux consistent with the impact cratering record.
4) Modeling of the loss of atmospheric water due to exospheric escape of hydrogen.
5) Equilibrium and kinetic modeling of the reaction of atmospheric carbon dioxide, sulfur dioxide, and carbonyl sulfide with surface minerals.

These five mathematical models have been fashioned into numerical algorithms which are executed as five distinct computer programs. The Venus climate is simulated by linking these programs into a time-marching, evolutionary model. Radiative-convective equilibrium is first calculated for an initial model atmosphere. Changes to atmospheric abundances due to processes 2-5 are then calculated for subsequent time steps. These are used as new atmosphere model inputs for the calculation of radiative-convective equilibrium. The flow chart in Figure 6.1 depicts how these programs are linked, the input files involved, output files, and variables that are passed between them. A detailed description of their implementation is described in the next section.

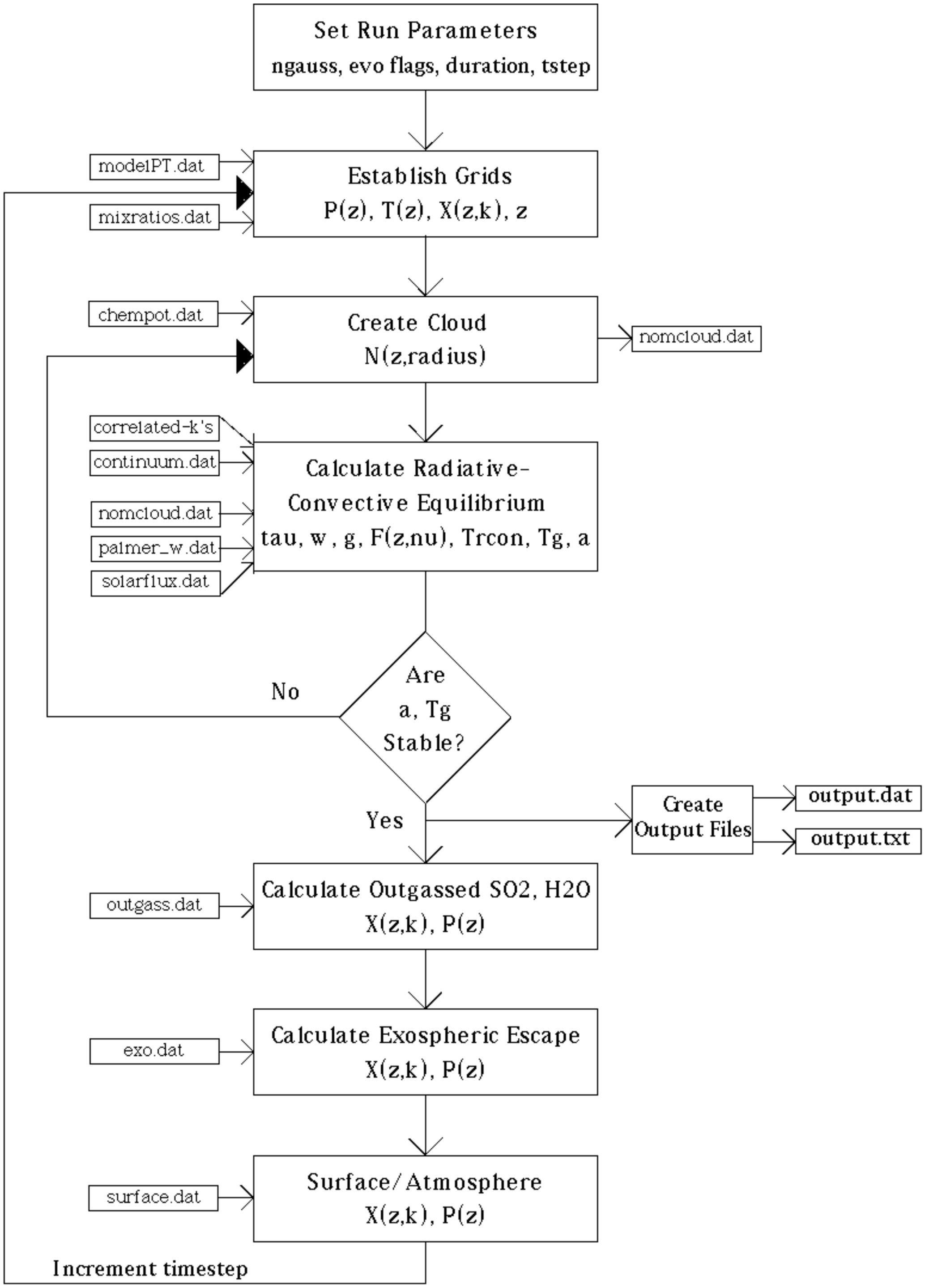

Figure 6.1 Flow chart for the Venus climate evolution model. Input files are depicted as small rectangles at the left, output files on the right. In the center column are the main program modules for the Venus climate model.

The Computer Code

All the numerical models described in previous chapters were written in Research System Incorporated's IDL language, version 4.01. The one exception was the Mie scattering code, which is a Fortran 77 program taken directly from *Hansen and Travis* [1974]. IDL is the Interactive Data Language, an interpreted Fortran-like computational and image processing computer language. IDL is optimized, both syntactically and computationally, for manipulating arrays. Therefore, all input and output data were cast as large multidimensional arrays, and computations were typically performed on relevant lower dimensional subsections of these arrays. For example, all atmospheric parameters, including pressures, temperatures, specific heats, optical depths as functions of wavenumber, fluxes, etc., where contained in one large multidimensional array, sections of which were operated upon at various stages in the calculations.

Input files for the atmosphere, clouds, volcanic outgassing rates, surface/atmosphere reaction parameters and exospheric escape are either selected or created before each model run. Upon start-up, model run parameters are selected from a dialog box (Figure 6.2). The method for calculating infrared opacities is selected here: Rosseland mean opacities, reading pre-calculated opacities from a file, or calculating full non-grey opacities from tabulated correlated-k absorption coefficients are the choices. Rosseland mean opacities are useful for quick checks of variations to a full non-grey solution, being about 20 times faster than a full non-grey calculation. Also determined at this time are the number of Gauss points, *ngauss*, used in calculating flux quadratures. Aerosols may be chosen to be included at this time, and the choice of calculating pure radiative or radiative-convective equilibrium is made.

Flags are set to include the various processes involved in climate evolution. Cloud evolution is actually a time-independent iterative adjustment with the radiative-convective atmospheric temperature profile. Evolutionary processes that may be included are volcanic outgassing, surface/atmosphere reactions, and exospheric escape. Finally, the duration and number of timesteps are entered, output file names are assigned, and the calculations begin.

The initial model atmosphere is read from two files: *modelPT.dat* which has level pressures and temperatures, and *mixratios.dat* which contains the mixing ratios for each molecule at all levels. The first calculational step is to determine a number of atmospheric parameters such as altitude (calculated from hydrostatic equilibrium), lapse rate, adiabatic lapse rate and path lengths for each level. The model grid is then used along with the atmospheric mixing ratios to calculate cloud parameters. These are the cloud particle number densities and sizes, written to the file *nomcloud.dat*. Compositional data (H_2SO_4/H_2O ratio) for the cloud particles is also calculated as a function of altitude and included in this file. The cloud model has as an input a database of chemical potentials for H_2SO_4/H_2O solutions as functions of concentration and temperature, *chempot.dat*.

The calculation of radiative-convective equilibrium follows the cloud calculations. If full non-grey opacities are desired, the correlated-k absorption coefficients for each molecule are convolved for the mixing ratios at each atmospheric level and interpolated logarithmically in temperature and pressure to obtain absorption coefficients for all wavenumber intervals and altitudes. Gaseous optical depths within each layer and wavenumber interval are calculated from these. Continuum opacities for CO_2 and H_2O are interpolated in wavenumber, temperature and pressure from data in the files *co2continuum.dat* and *h2ocontinuum.dat*. Similarly, Rayleigh scattering optical depths are obtained from data in the files *rayco2.dat* and *rayn2.dat*. The Mie code uses optical data for H_2SO_4/H_2O particles (*palmer_w.dat*) and the cloud particle number densities, sizes and composition in *nomcloud.dat*. Output from the Mie code gives cloud extinction optical depths, single scattering albedos and scattering asymmetry factors for each layer and wavenumber interval.

All these sources of infrared opacity are combined for the calculation of thermal infrared fluxes at each level and wavenumber interval using Gaussian quadrature. The fluxes and ultimately, the radiative-convective solution, are found via the techniques described in Chapter 2 and using a data file of net solar fluxes, *solarflux.dat.* The visual albedo is calculated using a grey-Eddington approximation. Changes to the initial model atmosphere temperatures affect the clouds, so the cloud is recalculated using the radiative-convective equilibrium solution. A new solution to radiative-convective equilibrium is found, and again the cloud is recalculated. This process is iterated until a stable cloud and atmosphere prevails.

Once the solution for the equilibrium state of the atmosphere is obtained, all input and output parameters are written to output files of two types: *output.dat,* which records the state of the model in IDL format, and *output.txt*, which contains most of the interesting atmospheric inputs and results. In addition, a third file may be written, *output.ps*, which contains user-selected output plots in PostScript format.

If evolution flags are set, the model proceeds to calculate changes in atmospheric abundances and total pressure that may result over the specified time interval. The outgassing calculation reads parameters for lava volatile abundances and the time evolution of outgassing from the file *outgas.dat.* If surface/atmosphere reactions are enabled, reaction kinetic and thermodynamic parameters are read from the file *surface.dat*. This file also contains flags that have been set before run-time for selecting which reactions are to be active.

The evolutionary processes alter atmospheric abundances of CO_2, H_2O, SO_2 and COS, as well as the total pressure of the atmosphere. These new parameters are used for the subsequent time step, where atmospheric radiative-convective equilibrium and cloud structure are once again calculated. The new state of the atmosphere is once again written to output files, and the entire sequence is repeated until the duration of the run is reached.

The SimVenus Interface

All the numerical models described in previous chapters were orchestrated by the main controlling computer program, dubbed 'SimVenus'. SimVenus and all its subsidiary data handling, computational, and input and output modules were also written in IDL. SimVenus provides a graphical, windows-based user interface for adjusting all input and model run parameters, as well as for graphically displaying a wide range of model input and output. A typical computer screen display is shown and explained in Figure 6.2. The major functions provided by the SimVenus interface are shown in Figure 6.3. They are grouped into seven categories:

1. File: Opening and closing output data files and program editing, display, compilation and execution. Upon issuing the 'run' command, a dialog box appears for setting run parameters (Figure 6.2).
2. Atmosphere: Displays of all input files, including correlated-k absorption coefficients. For illustrating gaseous opacity calculations, transmissivities for a layer of atmosphere of any path length, comprised of any mixture of species may also be calculated and displayed. Model input files may be selected, altered or created. Upon run completion, this menu also provides interactive access to nine graphical output displays of atmospheric results as well as the output text file. Figure 6.4 illustrates two of these output displays for a model run that has calculated the radiative-convective equilibrium state for the present Venus atmosphere.

3. Clouds: Provides access to graphical displays of cloud particle densities, cloud mass loading, and the optical data input files from *Palmer and Williams* [1975]. The cloud may be defined here as either taken from a file, or calculated from the model discussed in Chapter 3. Interactive displays of cloud opacity and optical properties as functions of wavenumber and layer are also provided.
4. Surface: Provides graphical displays of surface/atmosphere reaction equilibria (phase diagrams) and kinetics. Also gives plots of outgassing rates for whatever outgassing model has been selected. This menu also enables or disables each of the surface/atmosphere reactions and provides the ability to select an outgassing model.
5. Escape: Provides a graphical display of the evolution of H_2O with time due to the exospheric escape of H, and allows the adjustment of the H escape rate.
6. Evolution: Displays the results from an evolutionary calculation. This menu is used to open all of the output files associated with an evolutionary run, and displays the evolution of atmospheric and surface temperatures, atmospheric abundances, and pressures as functions of time.
7. Help: Provides access to an extensive set of help files on SimVenus, description of the models, and links to relevant published papers.

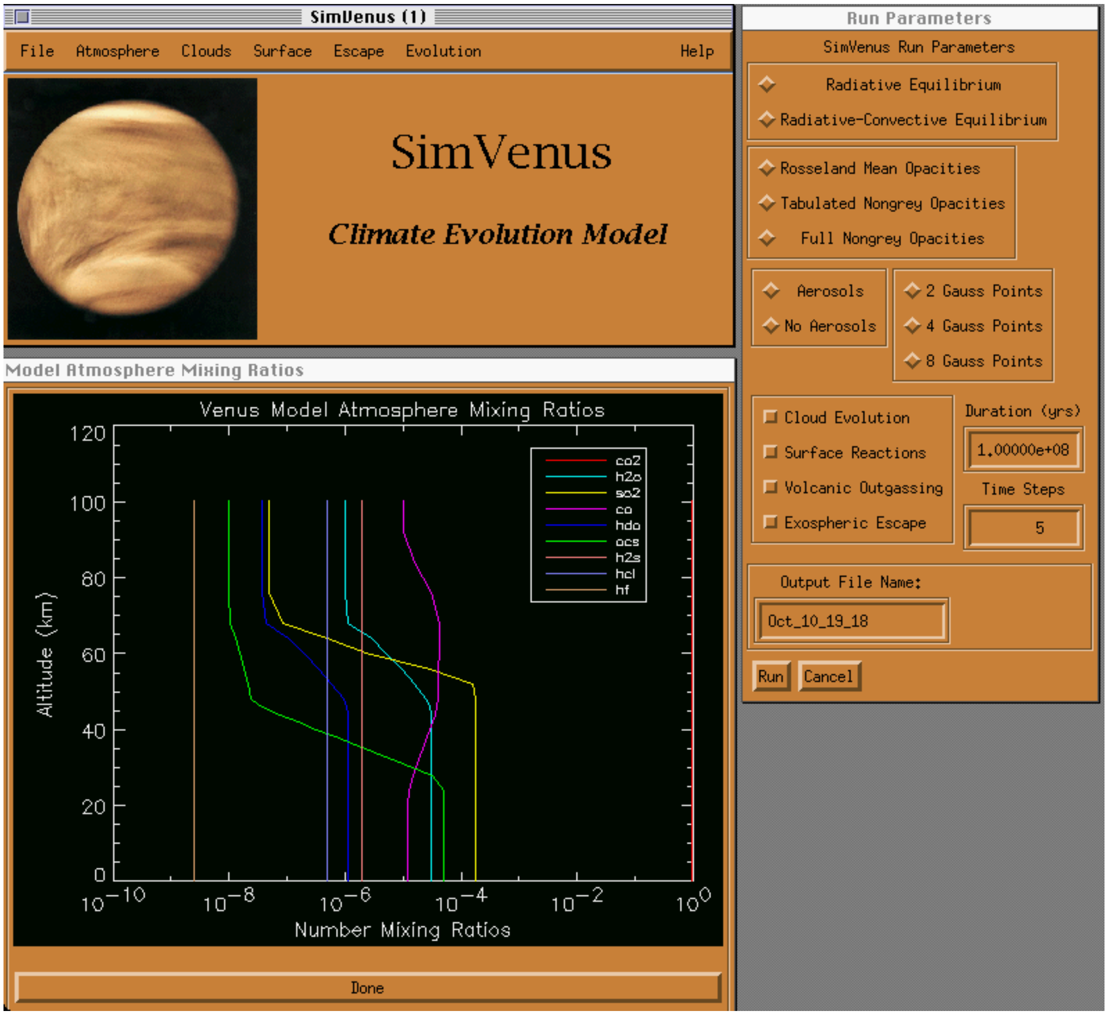

Duration (yrs) 1.00000e+08

Time Steps 5

Output File Name: Oct_10_19_18

Figure 6.2 SimVenus computer program interface. The rectangle at the upper left is the main control window, providing access and modifications to input parameters, visual and textual display of model run output, help files and file utilities. The long vertical rectangle at the upper right is used to determine run parameters such as methods of calculating opacity, duration and time interval of the evolutionary calculations, and the inclusion of cloud evolution, surface atmosphere reactions, volcanic outgassing and exospheric escape in the calculations. The square window at the lower left is a graphical display of one of the input files for starting atmospheric mixing ratios, on a logarithmic axis as a function of altitude.

Figure 6.3 Schematic showing the major functions provided by the SimVenus climate model interface.

Figure 6.3 Schematic showing the major functions provided by the SimVenus climate model interface.

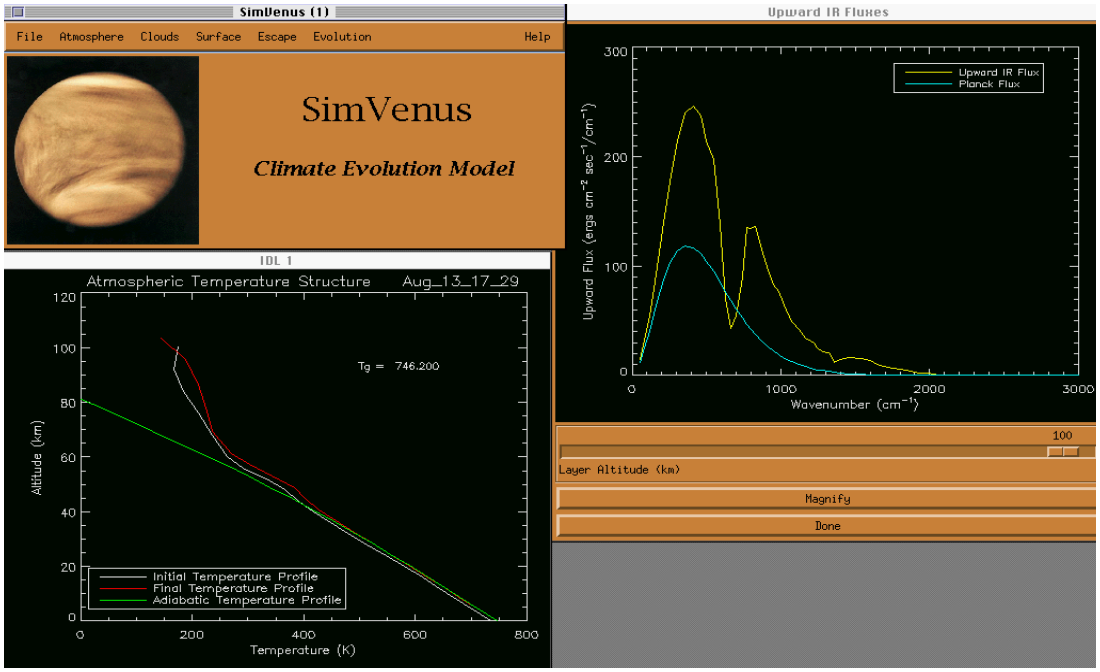

Figure 6.4 SimVenus computer program interface showing two of many possible displays of output from a model that has calculated the radiative-equilibrium for the present Venus atmospheric conditions. The rectangle at the upper left is the SimVenus control module, with a plot of the atmospheric temperature profile at the lower left. Also on this plot is the adiabatic temperature (intersecting the vertical axis at 80 km), and the initial atmospheric temperature (the one that is cooler at 95 km) used in the calculation. At the upper right is an example of one of the many possible output displays. The outgoing infrared flux as a function of wavenumber for any layer can be displayed with this module; in this case, at the top of the atmosphere.

Description of the Model Runs

I employed the Venus climate model to investigate eight evolutionary scenarios designed to address the five questions on Venus climate evolution presented in Chapter 1. They are:

Case 1: Investigates the climatic effects of steadily decreasing atmospheric H_2O due to the exospheric escape of H over 1.84 billion years. The initial H_2O abundance is set to 100 times the current value, approximately the amount that may be expected from outgassing due to rapid, global plains emplacement [*Grinspoon*, 1993]. The residence time for atmospheric H_2O is assumed to be 160 My [*Grinspoon*, 1993]. H escape is limited by the its ability to diffuse to the exobase. Atmospheric SO_2 abundance is set to the current value.

Case 2: Looks at how the Venus climate changes with the rapid injection of H_2O and SO_2 due to an exponentially decaying pulse of volcanic outgassing. The outgassing associated with an epoch of rapid global plains emplacement is assumed to have an e-folding lifetime of 100 My, with a total amount of lava sufficient to cover the planet in a global layer 1 km thick. Atmospheric loss of H_2O due to exospheric escape of H (H_2O residence time of 160 My) is also included, but there is no sink for SO_2. The initial abundance of atmospheric SO_2 is set to approximately 0.01 times the current abundance, or that which would exist if it were equilibrated with surface minerals at the current surface temperature. The initial abundance of H_2O is set to the current value.

Case 3: Investigates how Venus' climate changes with the rapid injection of H_2O and SO_2 and exospheric escape of H (H_2O residence time of 160 My), but also includes the kinetics of atmospheric SO_2 equilibration with surface minerals. The outgassing associated with an epoch of rapid global plains emplacement is assumed to have an e-folding lifetime of 100 My, with a total amount of lava sufficient to cover the planet in a global layer 10 km thick. The initial abundance of atmospheric SO_2 is set to approximately 0.01 times the current abundance, or that which would exist if it were equilibrated with surface minerals at the current surface temperature. The initial abundance of H_2O is set to the current value.

Case 4: Simulates the evolution of Venus' climate under the influence of constant outgassing of SO_2 and H_2O, exospheric escape of H (H_2O residence time of 160 My), and the equilibration of atmospheric SO_2 with the surface. The constant outgassing rate corresponds to a lava production rate of 0.4 km3/yr, a value shown in Chapter 4 to be consistent with the impact cratering record. All initial atmospheric abundances are set to the current values.

Case 5: Looks at how the Venus climate changes when only sinks for atmospheric volatiles are considered. Starting with current atmospheric abundances, H_2O is lost to exospheric escape of H (H_2O residence time of 160 My) and SO_2 is lost by its equilibration with surface minerals.

Cases 1-5 model the evolution of Venus' climate with respect to changes in atmospheric abundances of H_2O and SO_2 due to exospheric escape of H, outgassing associated with volcanism, and the equilibration of SO_2 with the surface. The remaining three cases deal with the evolution of Venus climate due to these processes as well as the equilibration of CO_2 with the surface. They are qualitatively different in that large changes in atmospheric mass are possible if surface minerals are capable of exchanging large quantities of CO_2 with the atmosphere.

The amount of CO_2 in Venus' atmosphere may represent all the available carbon in the crust and atmosphere. If all the CO_2 is already in Venus' atmosphere, the surface temperature may be above the equilibrium point for the CO_2-mineral equilibrium. There would be no carbonate on the majority of Venus' surface and the reaction would not proceed. Within the uncertainties in the available thermodynamic data, the surface temperature of Venus may be 20 K above the CO_2-mineral equilibrium (Figure 5.1).

From Cases 1-5, however, we can see that the surface temperature of Venus may easily stray to a value coincident with CO_2-surface mineral equilibrium. This interaction may or may not be operating today, but it probably did in the past, especially following a global outgassing epoch. Because of this, wider excursions in climate are possible, and these runs were designed to investigate the stability of Venus' climate with respect to perturbations in atmospheric SO_2 and H_2O. For Cases 6-8 I take the approach of assuming that the CO_2-mineral equilibrium is active. An analysis of the behavior of the climate model may be used to test the hypothesis that the Urey buffer is active today.

Case 6: Investigates the climatic effects due to a rapid injection of SO_2 and H_2O associated with an epoch of global plains emplacement, the loss of H_2O due to exospheric escape of H, and the equilibration of SO_2 and CO_2 with surface minerals. The outgassing associated with an epoch of rapid global plains emplacement is assumed to have an e-folding lifetime of 100 My, with a total amount of lava sufficient to cover the planet in a global layer 1 km thick. Initial atmospheric abundances equal to current abundances are assumed.

Case 7: Simulates the evolution of Venus' climate when only atmospheric sinks, including that for CO_2, are included. Equilibration of CO_2 and SO_2 proceed as in previous cases by diffusion-limited reactions with surface minerals, and atmospheric H_2O decreases due to the exospheric escape of H with an H_2O residence time of 160 My. Initial atmospheric abundances equal to current abundances are assumed.

Case 8: Simulates the evolution of Venus' climate when the volcanic outgassing rate is constant in time, atmospheric H_2O is lost due the exospheric escape of H, and the equilibration of CO_2 and SO_2 with surface minerals is enabled. Again, initial atmospheric abundances equal to current abundances are assumed.

Results

Case 1

Results from Case 1 are displayed in the four plots of figure 6.5. Figure 6.5a shows the exponential loss of atmospheric H_2O over 1.84 billion years as a plot of atmospheric mixing ratio vs. time. At 740 million years atmospheric H_2O abundance has decreased to the presently-observed value of 30 ppm, marked with an asterisk. By 1.84 billion years, it has decreased to 0.03 ppm, or one thousandth of its current value.

Figures 6.5b and 6.5c depict the evolution of the clouds as atmospheric H_2O decreases over this range. Figure 6.5b plots planetary albedo as a function of time, while 6.5c shows the time-evolution of cloud opacity with altitude. The shading in Figure 6.5c represents the visual opacity of the cloud (at 0.63 μm); brighter shading is higher opacity, while black is transparent. The opacity in atmospheric layers is shaded as a function of altitude, so the figure shows how a vertical cross section of cloud evolves in time. Figure 6.5d shows how the surface temperature changes with time as atmospheric H_2O declines in abundance. The present surface temperature is marked with an asterisk.

Exospheric escape of H leading to atmospheric H_2O loss is only one of several planetary-scale processes that may affect the climate of Venus. This model run allows us to calculate the effects of this process alone, thereby facilitating a comparison of the magnitude of it to other planetary processes. Also, some general conclusions about the sensitivity of the clouds and climate to changes in atmospheric H_2O may be derived.

Conclusions from Case 1 Results

There are four important features of this model run that bear on the recent evolution of climate on Venus:

1. With 100 times the present abundance of H_2O (and no change in SO_2), the atmosphere is too hot (due to an enhanced greenhouse) to support a massive H_2SO_4/H_2O cloud. Instead, a thin, high H_2O cloud exists with a visual optical depth of about 4 between 72 and 85 km. The surface temperature is slightly above 900 K due the increased greenhouse and lower planetary albedo.

2. As H_2O abundance decreases the atmosphere cools, allowing H_2SO_4/H_2O aerosols to condense and creating a thicker cloud. The thicker cloud has a higher albedo which cools the atmosphere further, lowering the cloud base and thickening the cloud further. This results in the runaway growth of the cloud to about 4 times the present optical depth when atmospheric H_2O abundance is about 50 times its current value. The runaway growth of the cloud is limited by the availability of H_2O to form cloud aerosols. The surface temperature drops dramatically in 50 million years from 900 K to about 720 K as the greenhouse becomes less efficient and cloud albedo increases rapidly.

3. With atmospheric H_2O abundances between about 50 and 1/100 times the current abundance, the surface temperature is relatively stable. It varies from 720 K to 750 K. Decreasing albedo of the clouds as H_2O abundance declines is partially offset by the decreasing effectiveness of the greenhouse. The net result is a slight increase in surface temperature over this range.

4. The clouds go away as atmospheric abundance of H_2O falls below 0.3 ppm, or 1/100 times the current value. This is true for this case, where SO_2 abundance

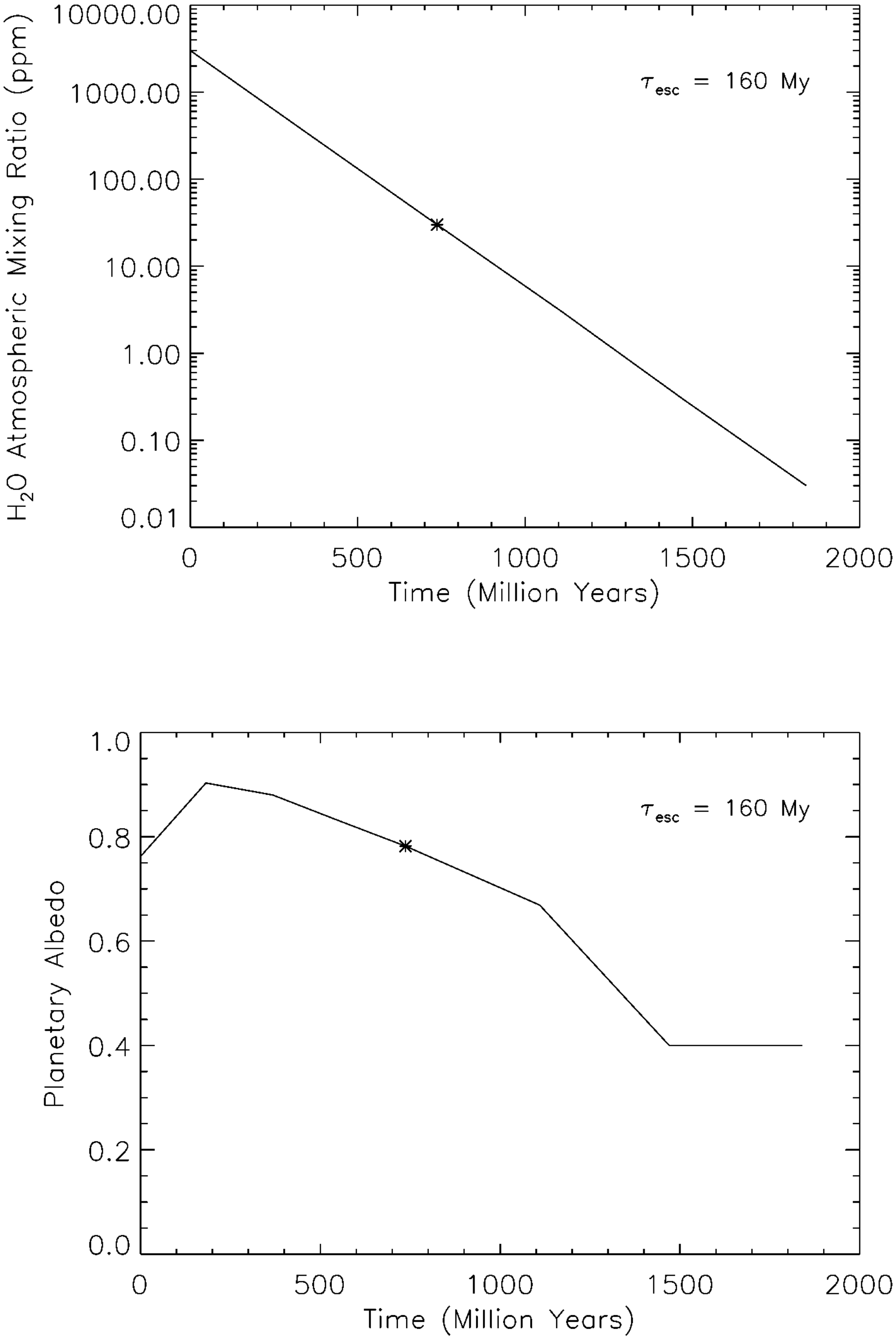

Figure 6.5a and 6.5b Case 1: Exospheric escape of H with τ_{esc} = 160 My. Top figure is the evolution of H_2O atmospheric mixing ratio; bottom figure is the evolution of Venus' albedo.

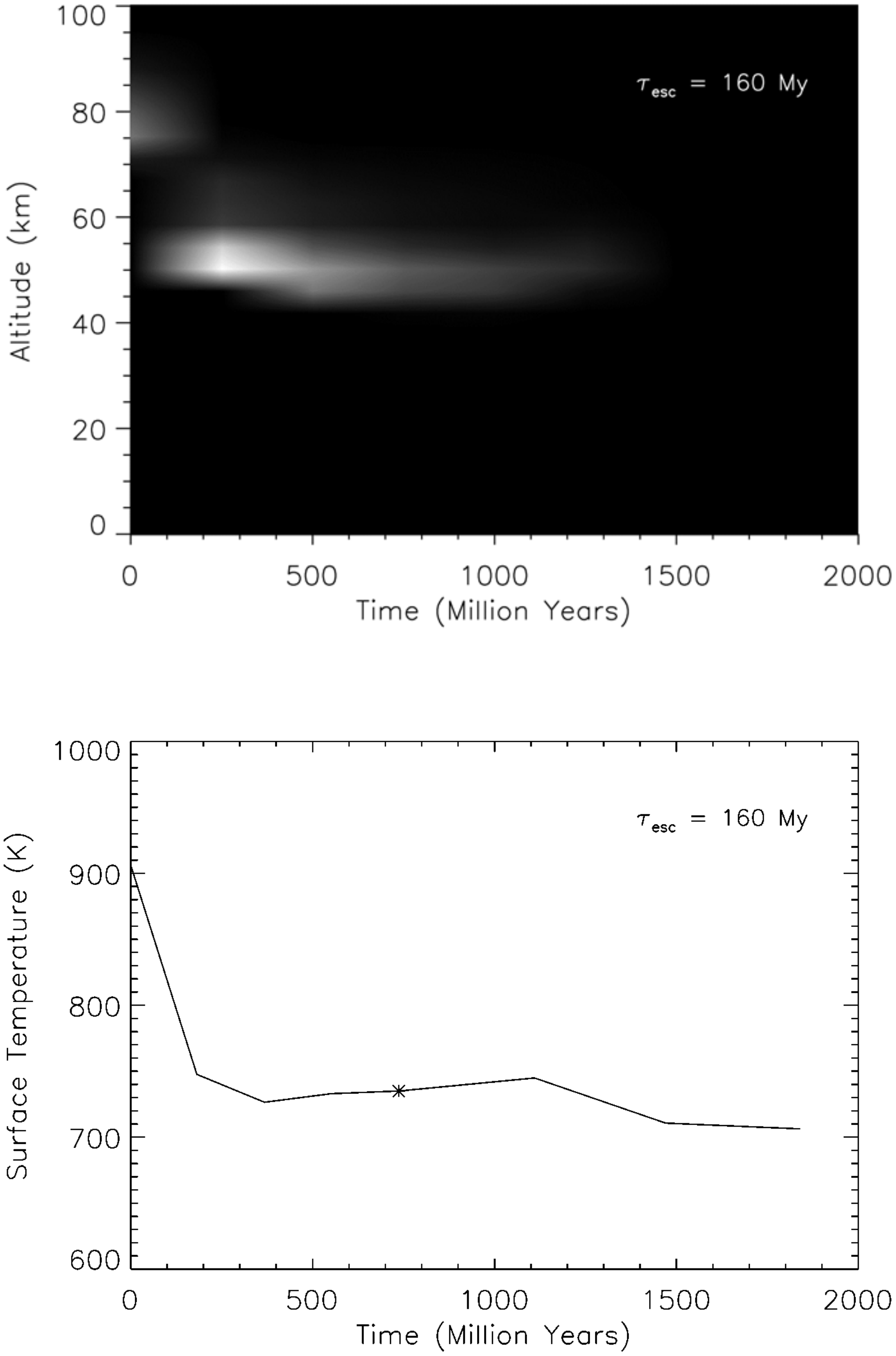

Figure 6.5c and 6.5d Case 1: Exospheric escape of H with τ_{esc} = 160 My. Top figure is the evolution of cloud optical depths as a function of altitude; bottom figure is the evolution of Venus' surface temperature.

remains at its current level. The surface temperature actually declines as the clouds go away due to losses in atmospheric infrared opacity of the gas and clouds. Reduced atmospheric opacity dominates over albedo effects because of the already high atmospheric albedo (0.4) due to Rayleigh scattering in the dense CO_2 atmosphere.

Case 2

Results from Case 2 are shown in the four plots of Figure 6.6. Figure 6.6a plots the atmospheric mixing ratios of H_2O and SO_2 as functions of time. Rapid outgassing with an exponential decay causes SO_2 abundances to rise almost four orders of magnitude in 100 My since there is no sink for SO_2 in this case. SO_2 atmospheric mixing ratios reach 0.01 by 500 My. H_2O is also outgassed into the atmosphere but its increase in abundance is compensated by loss due to exospheric escape of H. Its abundance peaks at three times the current value, or 90 ppm, in 100 My. It steadily declines after that, reaching present-day abundances in 600 My.

The rapid injection of atmospheric SO_2 results in the creation of a massive cloud in Venus' atmosphere within the first 50 My. It persists for the 600 My duration of the model run. The planetary albedo remains high, at 0.9, with minor fluctuations due to albedo/greenhouse feedback as atmospheric H_2O declines (Figure 6.6b). During this time, the cloud has a total optical depth in the visual of about 60 and inhabits the atmosphere from 40-70 km (Figure 6.6c).

The initial conditions for this case assume that SO_2 is equilibrated with surface minerals, and that all other atmospheric abundances are equal to the present-day values. Under these conditions, a very thin cloud exists, and the surface temperature is about 780 K. Surface temperatures drop to below 700 K in 100 My and remain in the range of 670 - 720 K under the massive cloud. The climate in this case is stable, although the clouds will eventually go away as H_2O is lost due to the exospheric escape of H. In this scenario, it would take another 700 My for the clouds to

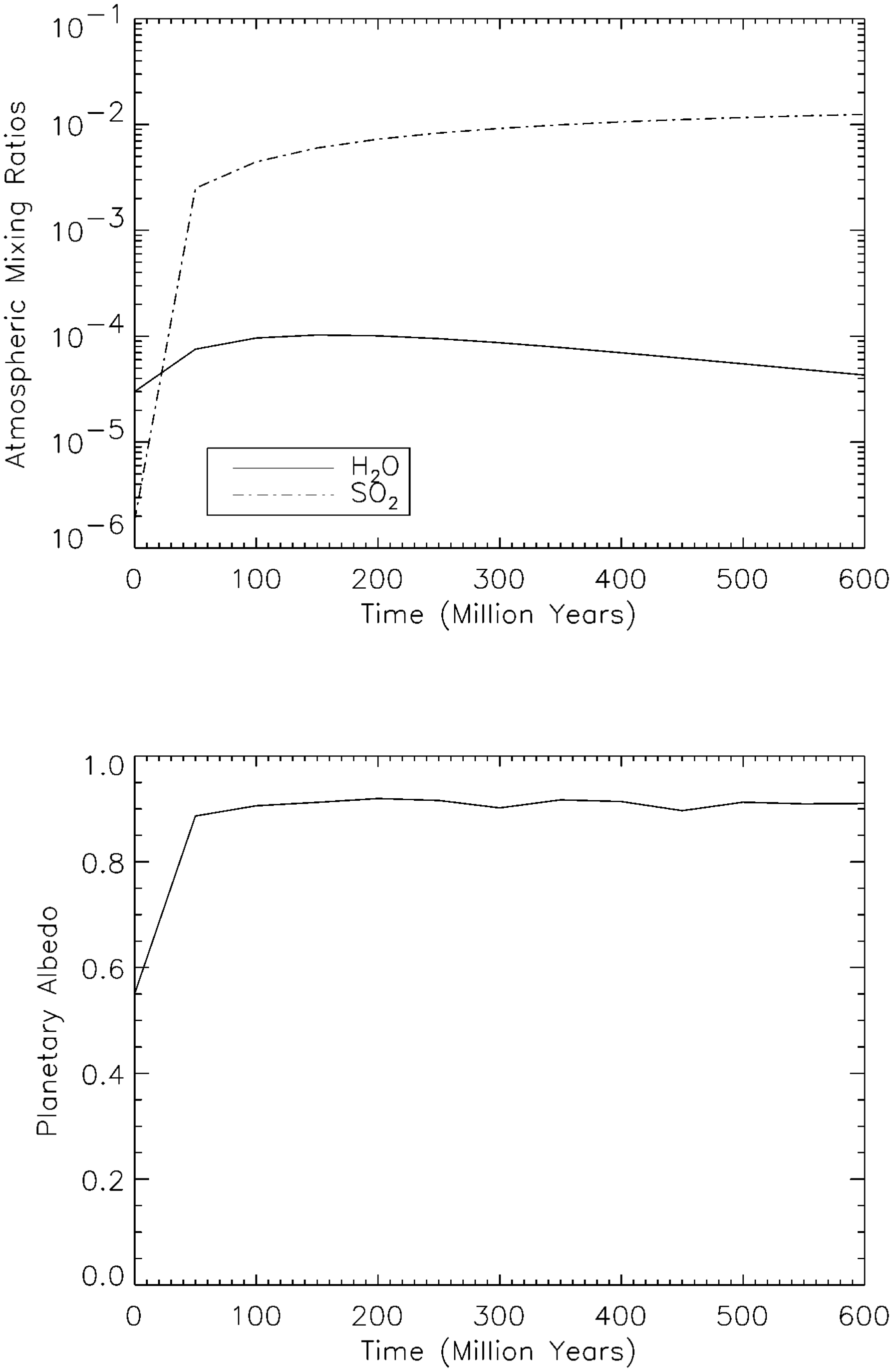

Figure 6.6a and 6.6b Case 2: Rapid outgassing with exponential decay (τ = 100 My) sufficient to cover the planet with a global 1 km layer of lava. Top is the evolution of atmospheric mixing ratios, bottom is albedo. H escape included.

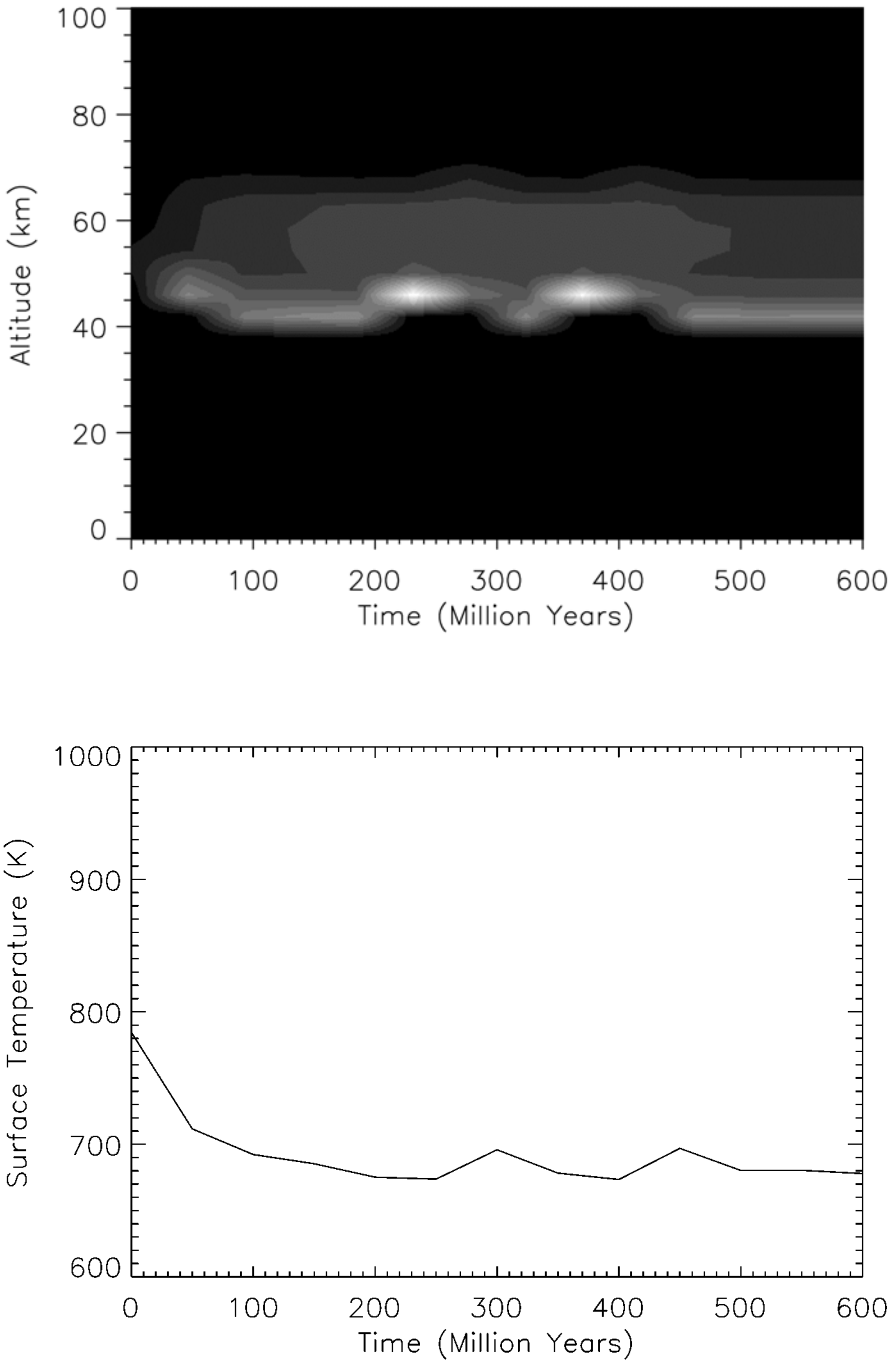

Figure 6.6c and 6.6d Case 2: Rapid outgassing with exponential decay ($\tau = 100$ My) sufficient to cover the planet with a global 1 km layer of lava. Top is the evolution of cloud optical depth, bottom is surface temperature. H escape included.

disappear, or 1.3 Gy after the start of the outgassing event. Although not shown, it may be inferred from the cloud response results of Chapter 3 that the surface temperature would increase to about 780 K as the clouds thin, and then decrease to around 720 K as they disappear altogether (the latter due to the loss of infrared opacity of the clouds).

Case 3

Results for Case 3 are shown in Figure 6.7. Here, rapidly outgassed H_2O and SO_2 are subject to loss due to exospheric escape of H and reactions with surface minerals, respectively. For this case, a more extensive outgassing event is simulated, one that is 10 times the magnitude considered in Case 2. Atmospheric mixing ratios of SO_2, however, peak at 0.002 due to the effectiveness of SO_2 reactions with the surface (Figure 6.7a). The outgassing event has an exponential decay of 100 My, while the SO_2-mineral reaction has a time constant of 20 My at 735 K. Atmospheric H_2O abundances increase 90 fold in 100 My, and ultimately decay with the lifetime against H escape, 160 My. Again due to the large injection of SO_2 and H_2O, a massive cloud forms in the first 50 My, increasing the planetary albedo to 0.94 (Figure 6.7b). Due to the loss of atmospheric SO_2, however, the cloud begins to dissipate steadily over the next 500 My (Figure 6.7c) and the planetary albedo begins to decrease. This scenario has an important difference with Case 2 in that atmospheric H_2O abundances may remain high while SO_2 abundances decline rapidly due to surface reactions. Depending upon the H_2O concentrations of erupting lavas, and the amount erupted, it is possible for the atmosphere to enter a regime such as that encountered at the beginning of Case 1, namely, high thin H_2O clouds and surface temperatures approaching 900 K. Surface temperatures decline to 650 K in the first 100 My and then increase steadily for 400 My as the clouds thin (Figure 6.7d). Temperatures peak at about 870 K and remain that way for at least 150 My. A

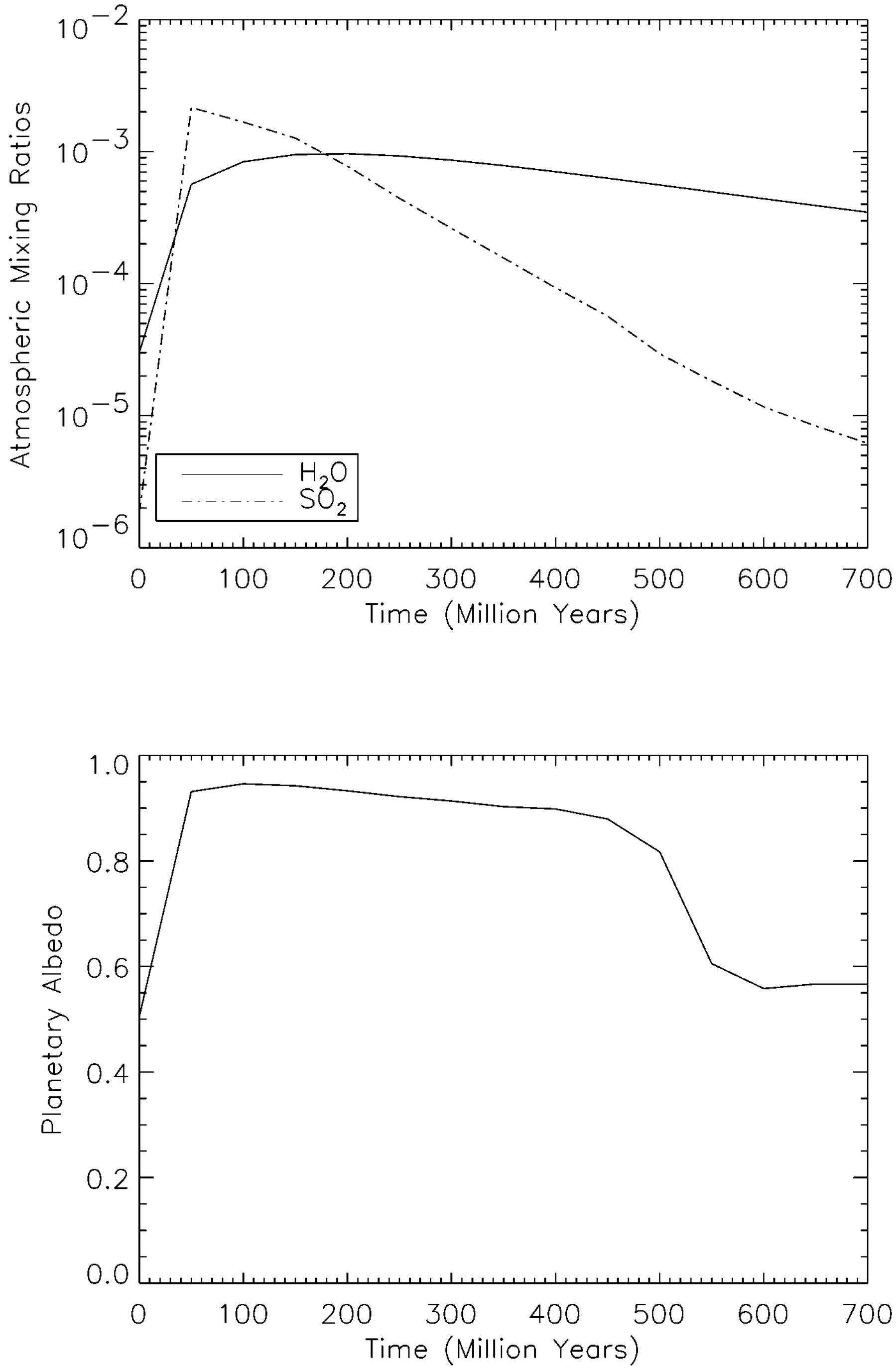

Figure 6.7a and 6.7b Case 3: Rapid outgassing (100 My, 10 km), with exospheric escape (160 My) and SO_2 reactions with the surface. Top is the evolution of atmospheric mixing ratios, bottom is albedo.

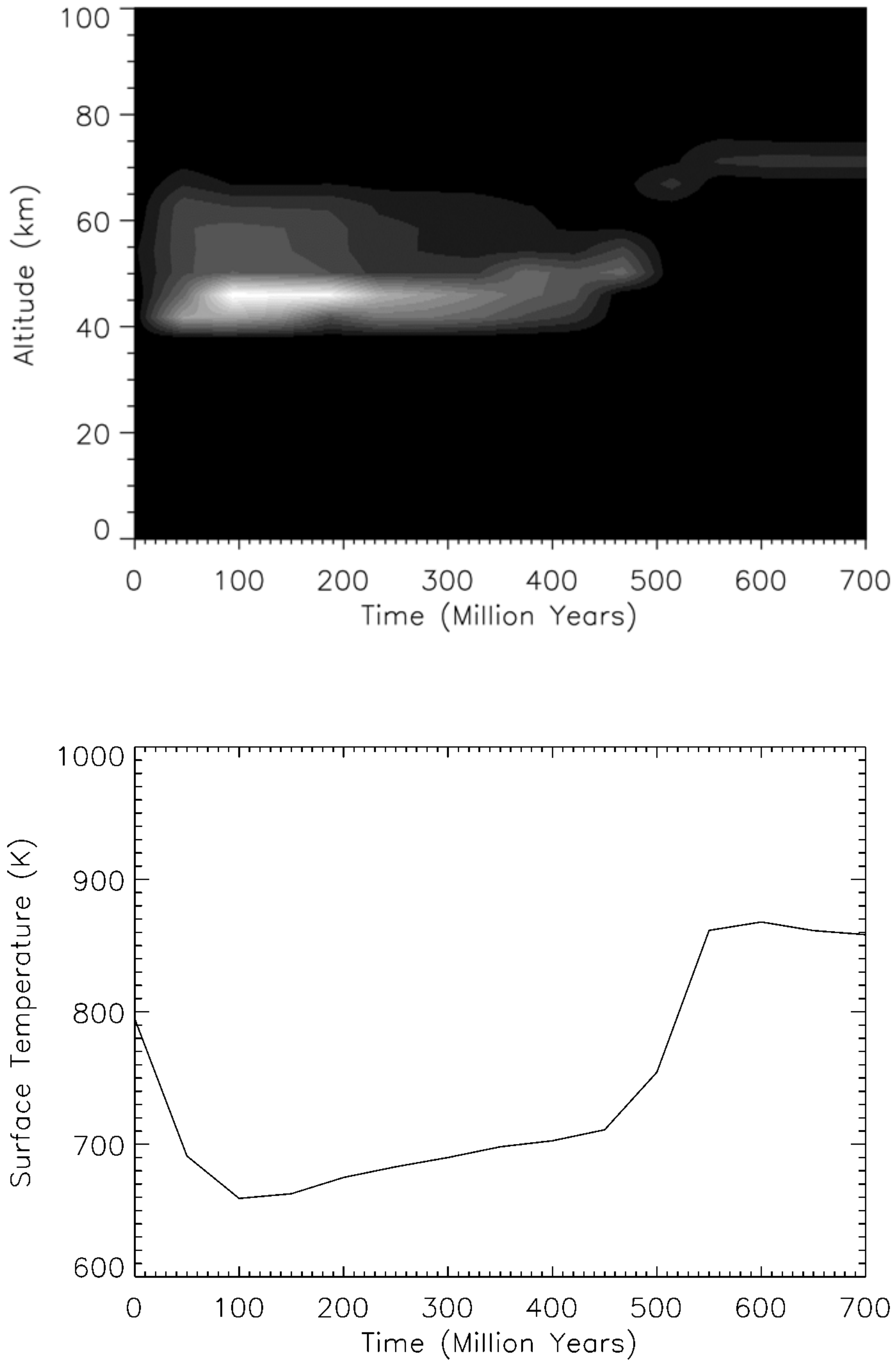

Figure 6.7c and 6.7d Case 3: Rapid outgassing (100 My, 10 km), with exospheric escape (160 My) and SO_2 reactions with the surface. Top is the evolution of cloud optical depth, bottom is surface temperature.

discussion of the conclusions from the results of Cases 2,3,4 and 5 is deferred until after a description of Case 5 results.

Case 4

Case 4 results are shown in the four plots of Figure 6.8. Constant outgassing of SO_2 and H_2O is balanced against the uptake of SO_2 by surface minerals and loss of H_2O by the exospheric escape of H. The SO_2 source is not as strong as its sink, resulting in almost an order of magnitude decrease in atmospheric SO_2 from current abundances (Figure 6.8a). H_2O abundances remain approximately constant. A stronger volcanic source of volatiles, or one that was more sulfur-rich would have resulted in a higher steady state atmospheric abundance of SO_2. In this scenario, steady state climate conditions prevail with a planetary albedo slightly below the current value (Figure 6.8b) and a slightly thinner cloud (Figure 6.8c). As a result, surface temperatures rise slightly to 775 K, and remain there. A greater volcanic source of SO_2 would have resulted in stable conditions much like present day Venus. A weaker source, or one that was less sulfur-rich than assumed, would have resulted in a thinner cloud and a stable but higher surface temperature than at present.

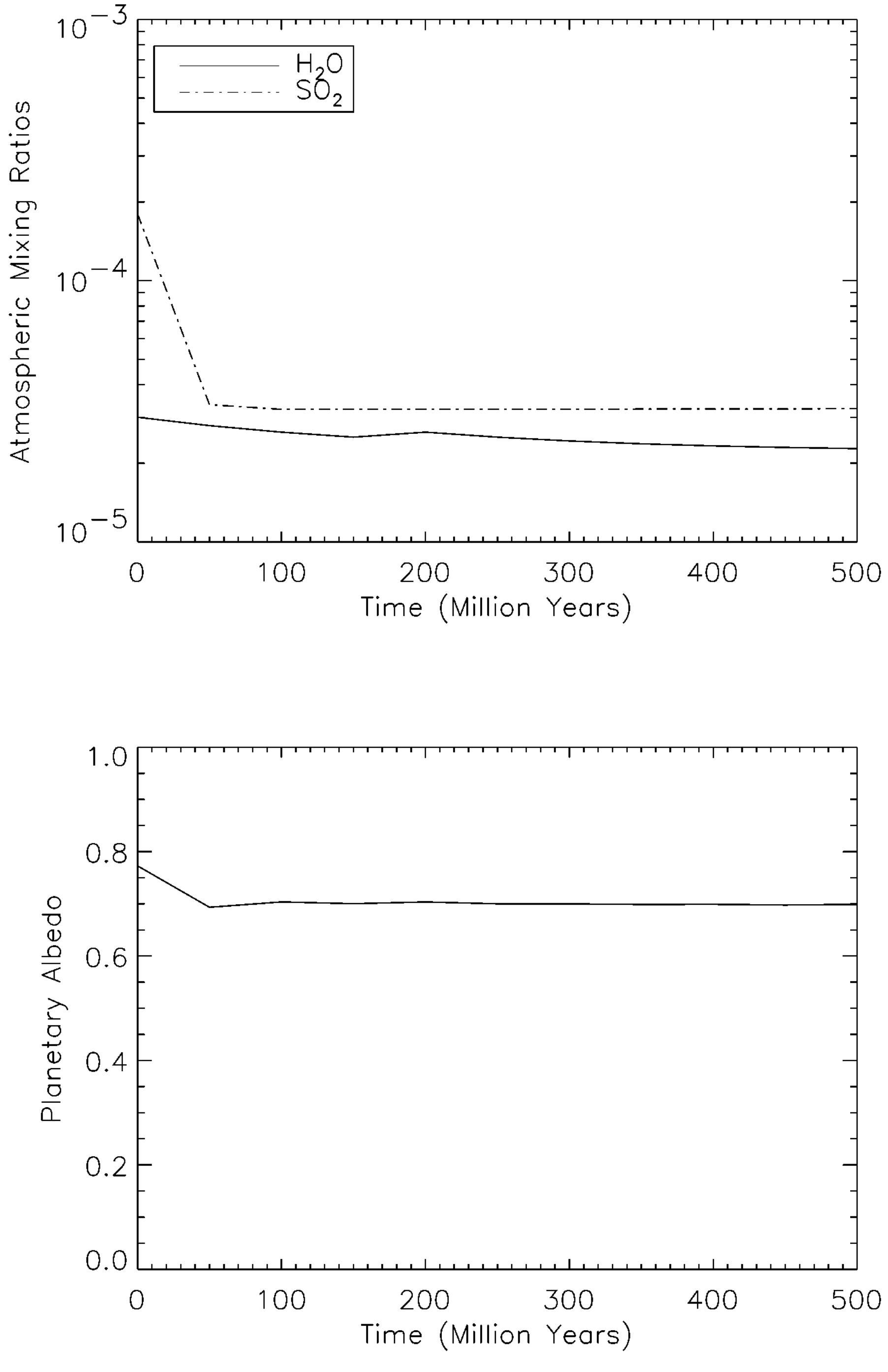

Figure 6.8a and 6.8b Case 4: Constant outgassing (0.37 km^3 lava/yr), with exospheric escape (160 My) and SO_2 reactions with the surface. Top is the evolution of atmospheric mixing ratios, bottom is albedo.

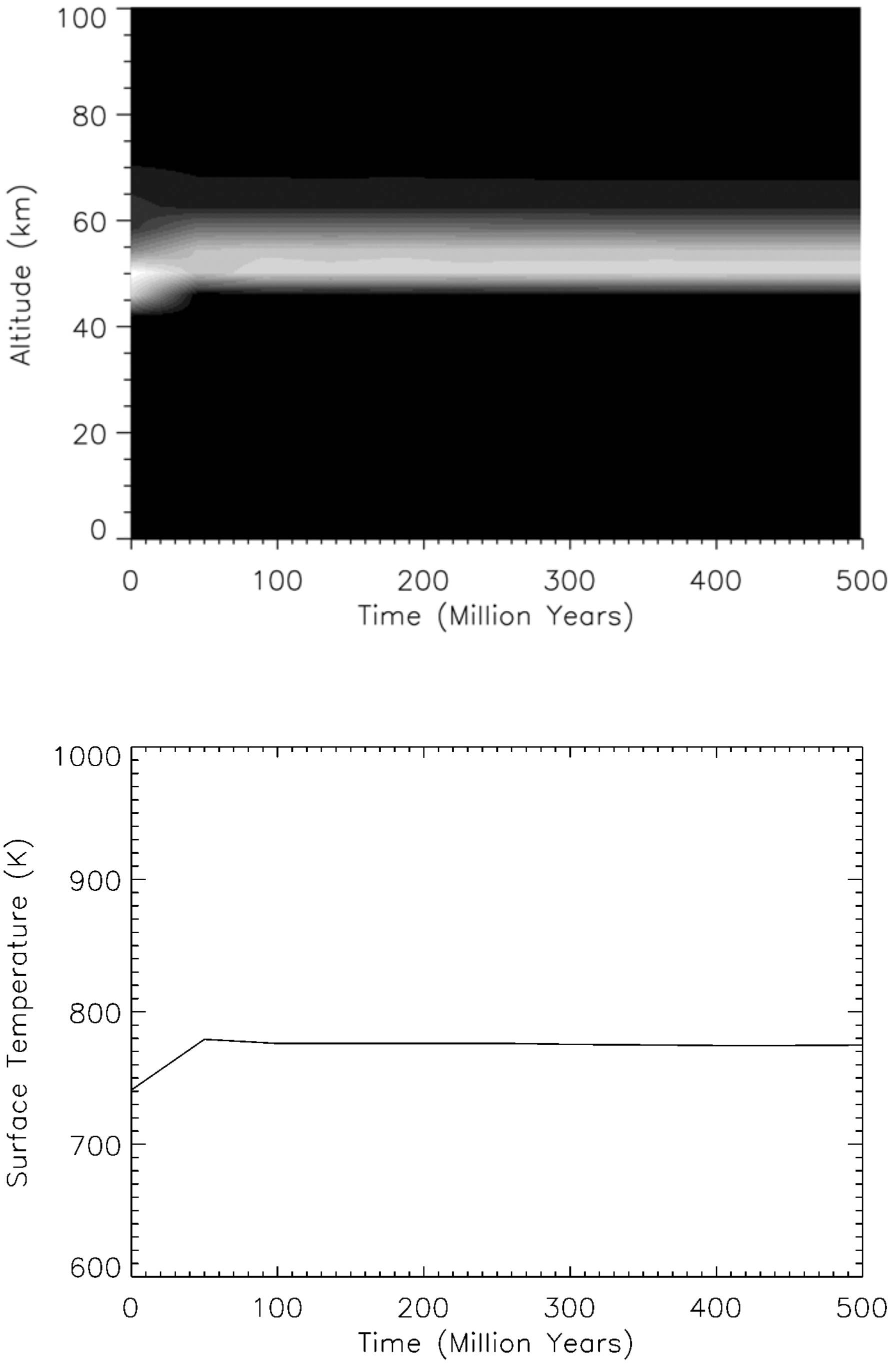

Figure 6.8c and 6.8d Case 4: Constant outgassing (0.47 km^3 lava/yr), with exospheric escape (160 My) and SO_2 reactions with the surface. Top is the evolution of cloud optical depth, bottom is surface temperature.

Case 5

In order to facilitate comparisons between the effects of various sources and sinks of volatiles in the Venus climate system, I also included a model run that incorporates the loss of SO_2 and H_2O without any resupply. The results for Case 5 are shown in the four plots of Figure 6.9. Figure 6.9a shows the evolution of SO_2 and H_2O atmospheric mixing ratio due to reaction with surface minerals and exospheric escape, respectively. Atmospheric H_2O abundance declines exponentially with a lifetime of 160 My, while SO_2 declines 2 orders of magnitude in about 50 My to an equilibrium abundance of about 1 ppm. The clouds disappear in this time frame, as shown by the rapid reduction in planetary albedo in Figure 6.9b. Venus' albedo remains at 0.4 due to Rayleigh scattering by the thick CO_2 atmosphere. The vertical cloud structure, as shown by its optical depth as a function of altitude over time is shown in Figure 6.9c. Surface temperatures decline slightly to about 710 K as the clouds go away, and decrease very slightly as the greenhouse effect lessens due to decreasing atmospheric and H_2O and SO_2 abundance (Figure 6.9d). The total duration of this run was 500 My.

Conclusions from Case 2,3, 4 and 5

1. Intense volcanic outgassing of volatiles accompanying a global epoch of rapid plains emplacement would have cooled the surface of Venus for at least 300 million years. The formation of massive clouds would have raised the albedo of Venus, dominating over an enhanced greenhouse effect resulting from increased abundance of atmospheric H_2O and SO_2. Surface temperatures as low as 650 K may have prevailed after 100 My if the outgassing event was large enough.
2. If atmospheric SO_2 was able to react with surface minerals following a global outgassing event, present-day surface temperatures would have developed in about

500 My. As SO_2 declined further while atmospheric H_2O remained high, however, surface temperatures would have risen rapidly after this. The formation of high, thin clouds would have raised surface temperatures to close to 900 K.

3. As atmospheric H_2O declined due to the exospheric escape of H, the SO_2/H_2O ratio in the atmosphere would have increased, producing the H_2SO_4/H_2O clouds and surface temperatures that we see today.

4. Without a surface sink for atmospheric SO_2, or with a large continuous volcanic source following a global outgassing event, clouds remain very think with a global albedo of 0.9 for about 500 My. The clouds thin very slowly over 1.3-1.6 Gy due to loss of H_2O from exospheric escape of H, but atmospheric SO_2 abundance remains very high.

5. A constant source of volcanic volatiles along with sinks for atmospheric SO_2 and H_2O due to reactions with the surface and exospheric escape of H, respectively, results in stable clouds and climate on Venus close to presently observed conditions. A stronger or more sulfur rich source than I consider results in a thicker cloud and cooler surface temperatures. A weaker or less sulfur rich source results in thinner clouds and slightly hotter surface conditions.

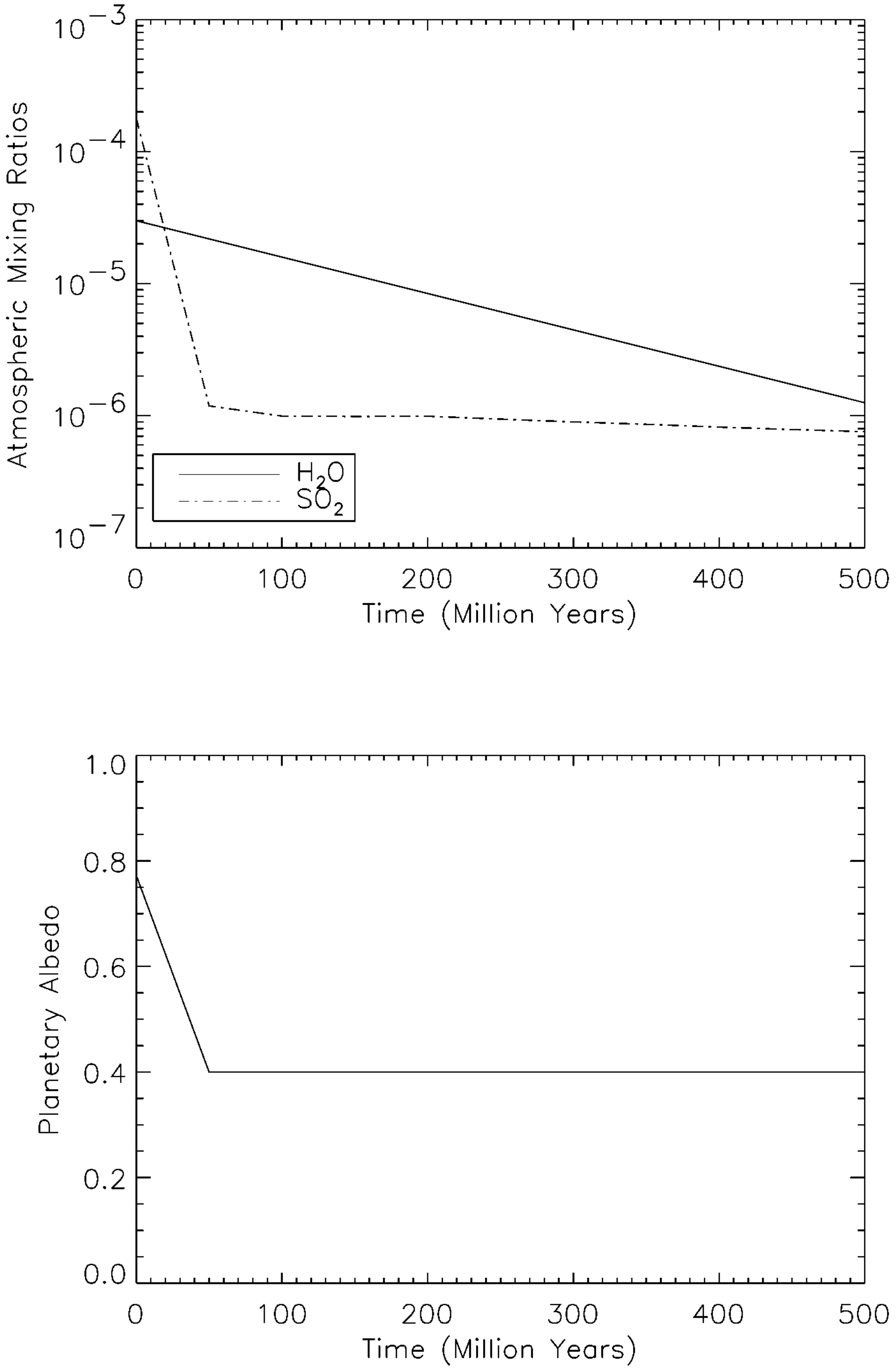

Figure 6.9a and 6.9b Case 5: SO_2 reactions with the surface and exospheric escape (160 My). Top is the evolution of atmospheric mixing ratios, bottom is albedo.

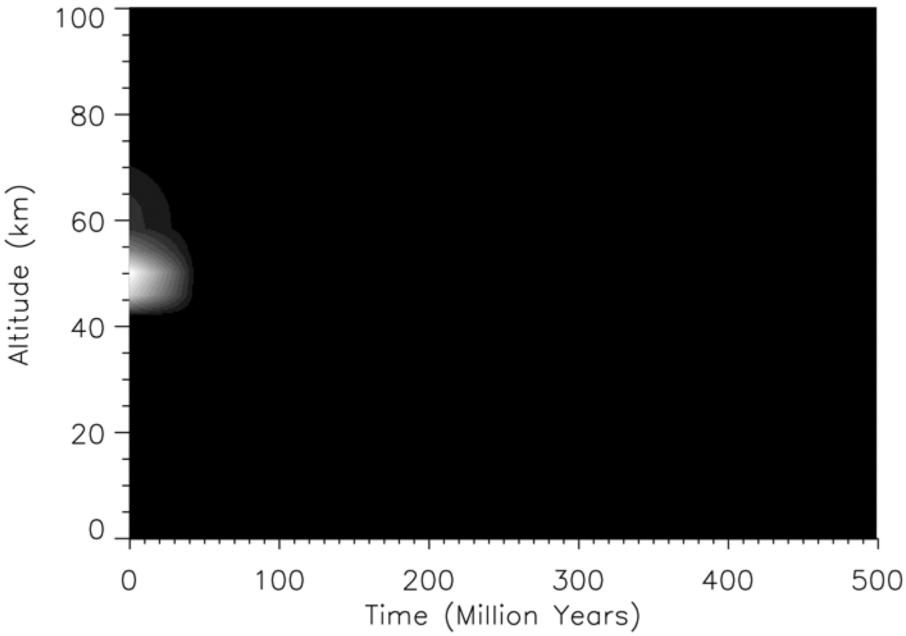

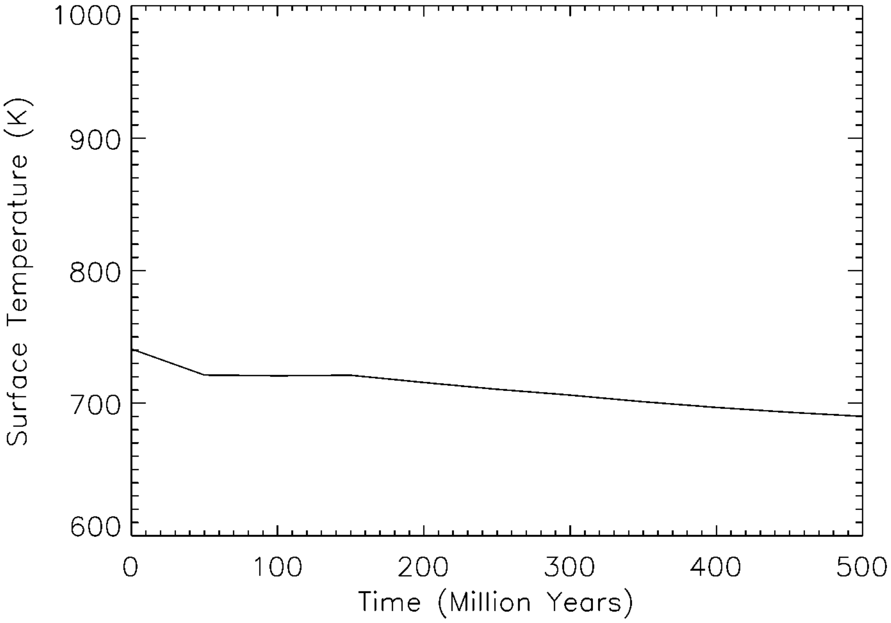

Figure 6.9c and 6.9d Case 5: SO_2 reactions with the surface and exospheric escape (160 My). Top is the evolution of cloud optical depth, bottom is surface temperature.

The Climatic Effects of the CO_2-Calcite-Wollastonite (Urey) Equilibrium

A potentially interesting class of evolutionary models involves an investigation of the CO_2-calcite-wollastonite equilibrium on the stability of Venus' climate. The nature of this stability can be made apparent by plotting the equilibrium of this reaction in pressure-temperature space (a phase diagram) along with the associated surface temperature and pressure that results from atmospheric radiative-convective equilibrium. This kind of a plot first appeared for a grey model of Venus' atmosphere without considering cloud albedo feedback effects [*Bullock and Grinspoon*, 1996].

Results for the fully coupled non-grey radiative-convective/cloud model of this thesis appear in Figure 6.10. The solid line shows the CO_2-calcite-wollastonite equilibrium in pressure-temperature space. The dotted line shows the Venus surface temperature calculated from radiative-convective equilibrium as a function of atmospheric pressure with present-day abundances of H2O and SO2. The stability of Venus' climate is related to the angle these two curves make in the temperature-pressure diagram. Current Venus conditions are close to the right-hand intersection of the curves and are indicated by the diamond in Figure 6.10.

Since the slope of the radiative-convective equilibrium line is greater than the mineral equilibrium line, Venus' climate is currently near an unstable equilibrium point. That is, perturbations to the current conditions are unstable with respect to the CO_2-calcite-wollastonite equilibrium. A small increase in surface temperature, for example, would shift the mineral equilibrium to one of a higher CO_2 pressure. This in turn enhances the greenhouse effect and thus surface temperature, evoking further decarbonation of minerals and still higher surface temperatures. The step seen in the (dotted) radiative-convective equilibrium curve is caused by transition to a cloud-free regime. This kind of behavior can only be sustained if there is sufficient calcite in the surface to increase atmospheric CO_2.

On the other hand, a small decrease in surface temperature leads to atmospheric CO_2 being taken up by surface minerals, reducing the greenhouse effect and further decreasing surface temperature. Carbonate formation proceeds kinetically until a stable state is reached, represented by the intersection of the two curves on the left hand side of the diagram. Very massive clouds form as the surface cools. At a surface temperature of 240 K, the atmosphere is almost all N_2, with a minuscule amount of atmospheric CO_2 in equilibrium with carbonate at the surface. The step seen in the radiative-convective equilibrium curve at low temperatures is due to the fact that clouds have reached the ground and no longer increase the albedo as the temperature decreases.

The stability plot of Figure 6.10 does not tell the whole story, however, because SO_2 and H_2O probably evolve over time by the processes modeled previously. Runaway climate to hotter regimes are probably limited by available carbon, and runaway states to cooler regimes may be inhibited by the effect of volatile sources combined with the relatively small angle seen between the two curves in Figure 6.10. An investigation of the dynamics of the climate of Venus with respect to volatile sources and sinks and considering the CO_2-calcite-wollastonite equilibrium is the subject of Case 6-8.

Case 6

The behavior of the Venus climate system in response to an epoch of rapid volcanic outgassing, CO_2 and SO_2 reactions with the surface, and exospheric escape is depicted in the five plots of Figure 6.11. Figure 6.11a plots the partial pressures of CO_2, H_2O and SO_2 as functions of time. Atmospheric SO_2 decreases for 40 My due to rapid (compared with outgassing) equilibration with surface rocks. It sharply increases after this due to a shutting off of the kinetics of the SO_2 equilibration reaction and build up of outgassed SO_2.

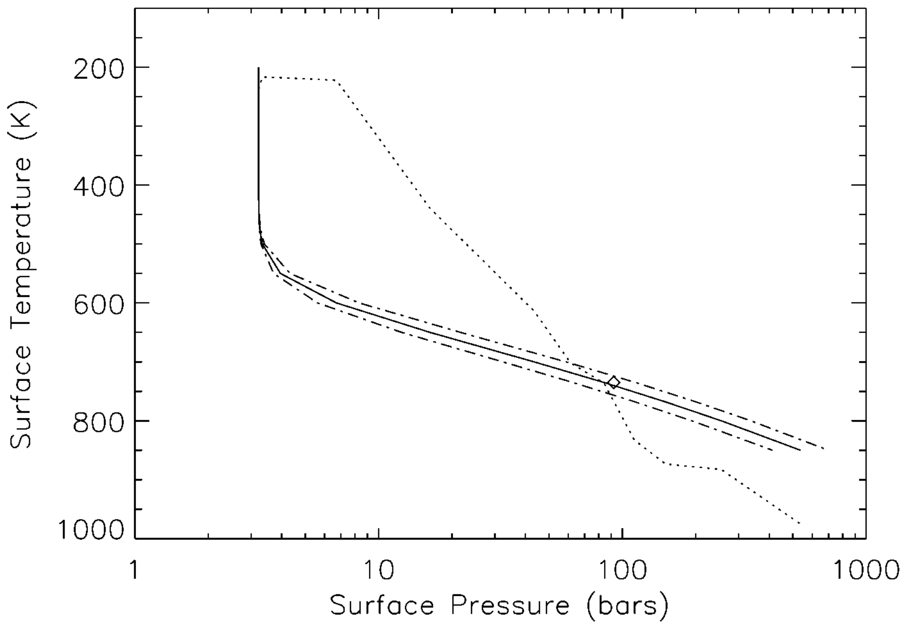

Figure 6.10 Radiative-convective equilibrium (dotted line) compared with atmospheric pressure corresponding to the Urey atmosphere/mineral equilibrium. The diamond represents the current state of the Venus atmosphere. Radiative-convective equilibrium is calculated for varying abundances of atmospheric CO_2, with current abundances of H_2O and SO_2. The dot-dashed line shows the uncertainty in the laboratory thermodynamic data.

The surface is cooling as a result of a reduced greenhouse from lowering CO_2 abundances. A runaway cooling surface is underway, but SO_2 and H_2O abundances are increasing. As a result, a massive cloud forms, dramatically raising the albedo and cooling the surface (Figures 6.11c and 6.11d). Figure 6.11e shows how the surface temperature and pressure evolve (dot-dashed line) on the stability plot of 6.10. Runaway cooling is even more dramatic than when atmospheric SO_2 and H_2O remain the same (dotted line). The thick global cloud layer produces lower surface

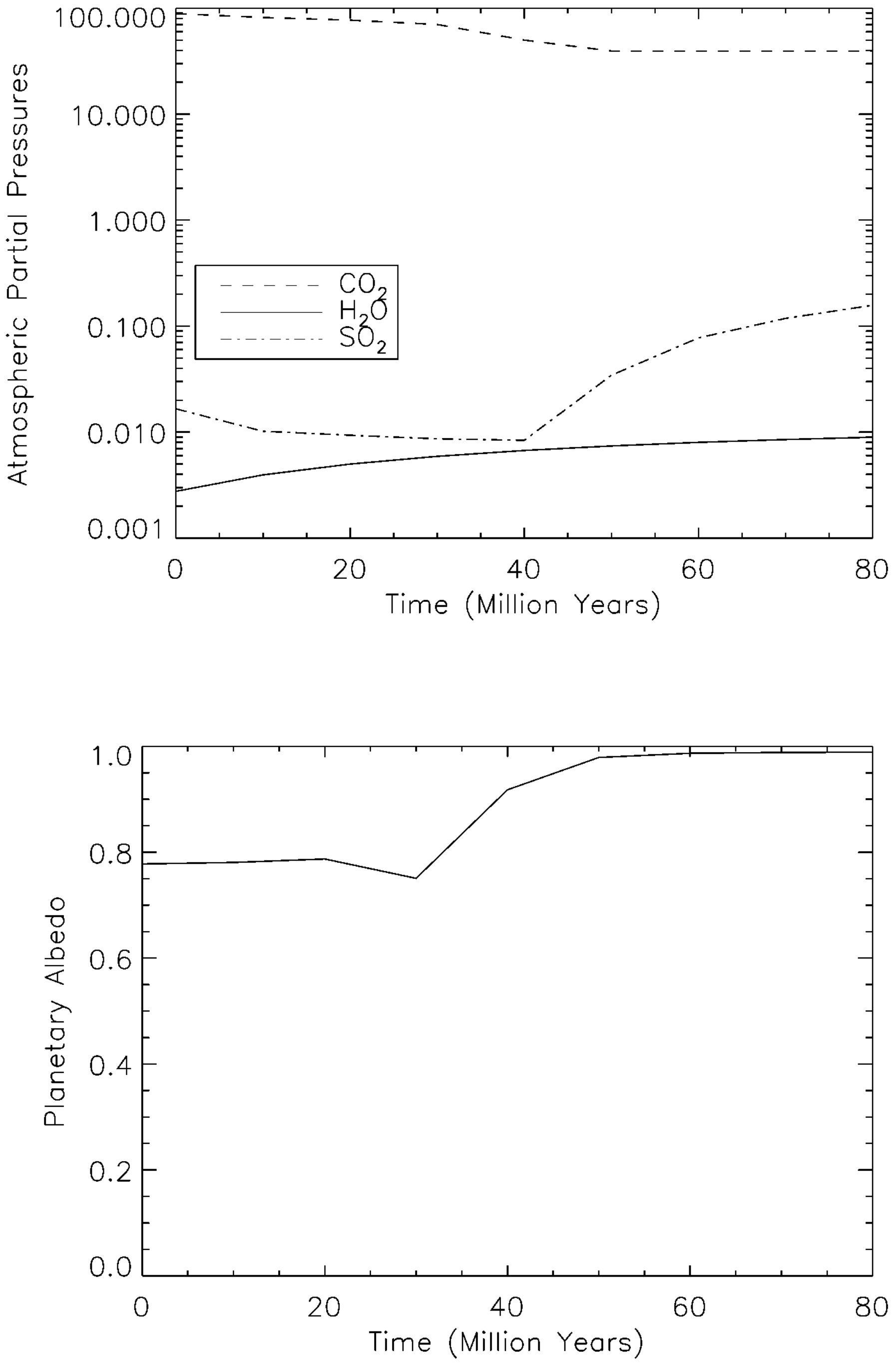

Figure 6.11a and 6.11b Case 6: CO_2 and SO_2 reactions with the surface, rapid outgassing, and exospheric escape of H. Top is the evolution of atmospheric partial pressures, bottom is albedo.

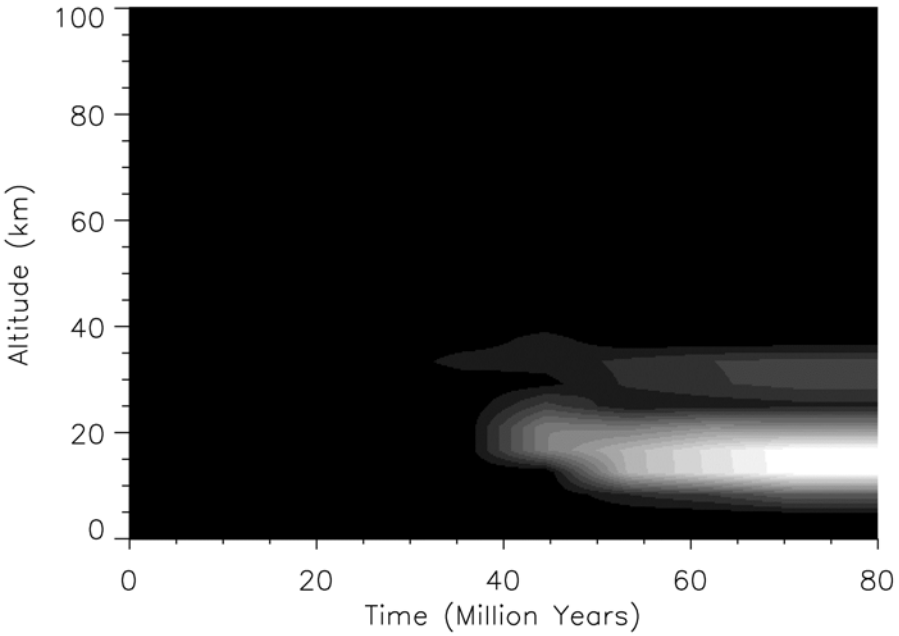

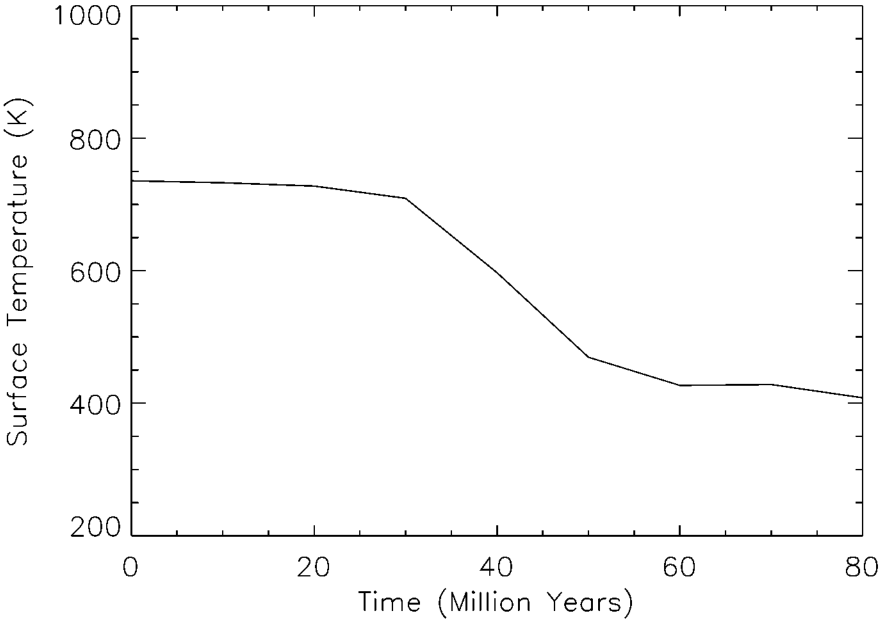

Figure 6.11c and 6.11d Case 6: CO_2 and SO_2 reactions with the surface, rapid outgassing, and exospheric escape of H. Top is the evolution of cloud optical depth, bottom is surface temperature.

temperatures, hastening the climate to a stable, low-CO_2 state in 60 My. The stable configuration for the climate in this case is 400 K and 43 bars.

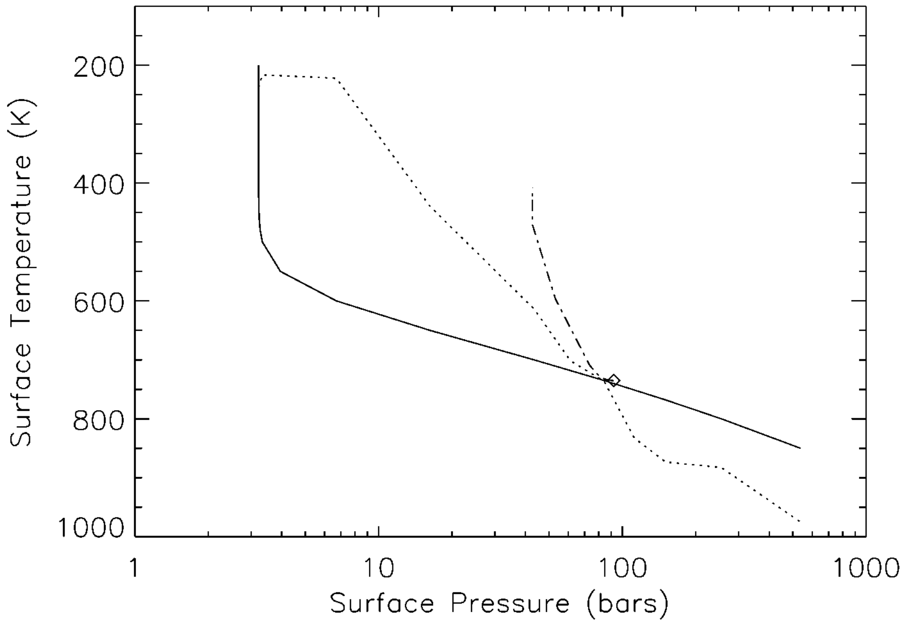

Figure 6.11e Case 6: Stability plot of Figure 6.10 with the evolution of surface pressure and temperature in time (dot-dashed line). For CO_2 and SO_2 reactions with the surface, rapid outgassing, and exospheric escape of H. Evolution is upward along the line, beginning with present conditions (diamond).

Case 7

The evolution of Venus' climate without an outgassing impulse of volatiles but with surface reactions and exospheric escape is shown in the five plots of Figure 6.12. Figure 6.12a shows how the partial pressures of CO_2, SO_2 and H_2O evolve over time. Atmospheric SO_2 declines as it equilibrates with the surface, removing the clouds. The planet also gets cooler, perturbing the CO_2-mineral equilibrium and inducing a cooling runaway. In 30 My, however, clouds appear whose infrared radiative effects dominate over the slightly increased albedo. The surface becomes warmer, and the CO_2-mineral equilibrium shifts to one with more atmospheric CO_2. The clouds go away again and the process repeats. This can be seen in Figures 6.12b and Figure 6.12c, where the existence of the clouds oscillates on a 30-40 My timescale. The amplitude of the corresponding surface temperature is small, about 30 K (Figure 6.12d). Venus' climate executes a limit cycle, visible in the plot of surface temperature vs. pressure in Figure 6.12e. The climate evolution is described by progressing counter-clockwise around the dot-dashed line. Total surface pressure oscillates from 92 to about 53 bars on this timescale, surface minerals breathing CO_2 in and out.

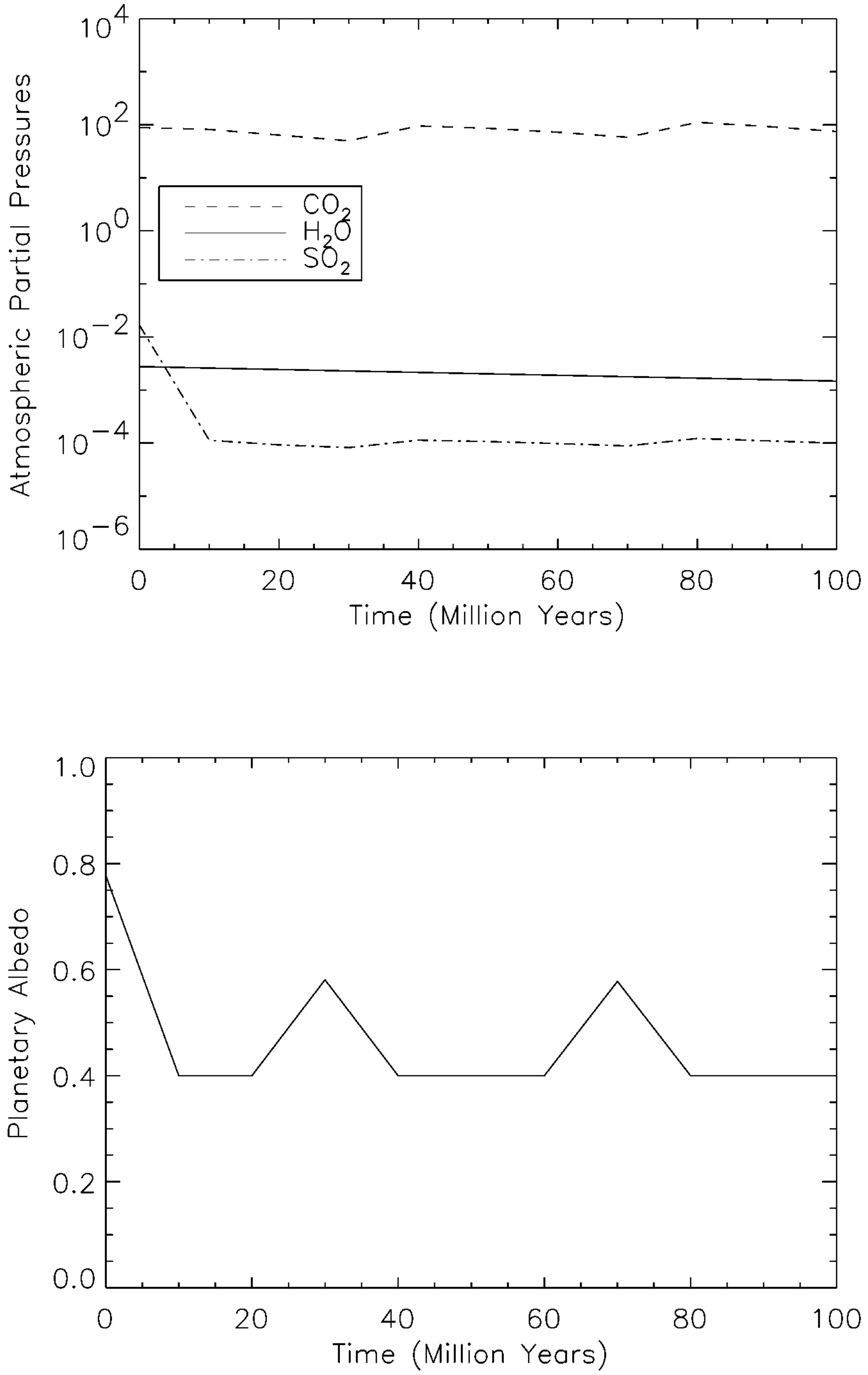

Figure 6.12a and 6.12b Case 7: CO_2 and SO_2 reactions with the surface and exospheric escape of H only. Top is the evolution of atmospheric partial pressures, bottom is albedo.

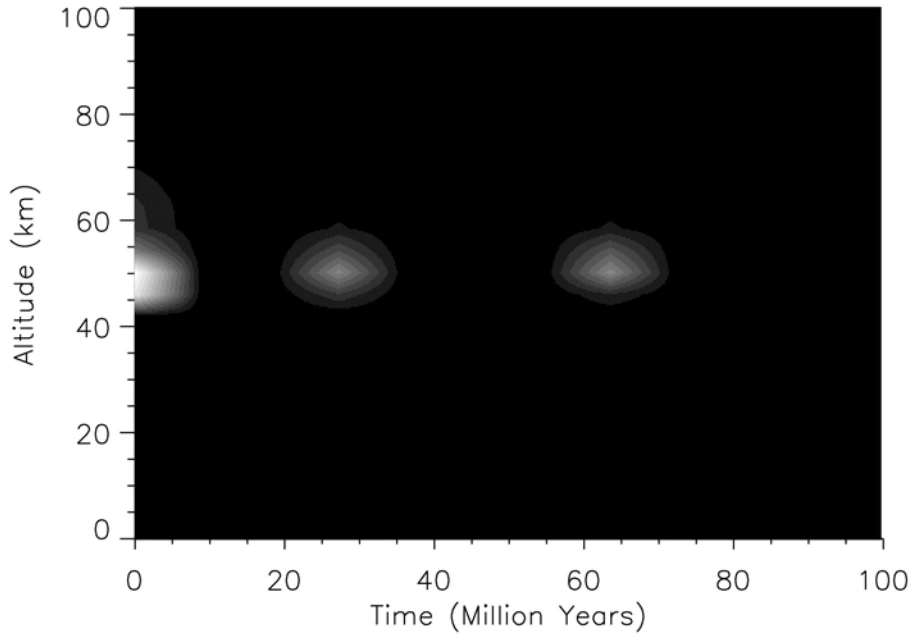

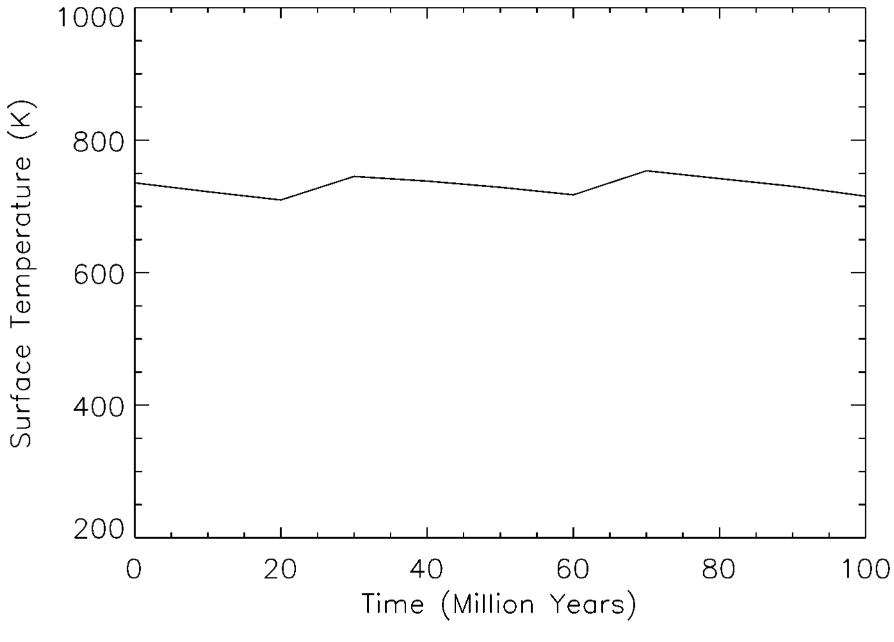

Figure 6.12c and 6.12d Case 7: CO_2 and SO_2 reactions with the surface and exospheric escape of H only. Top is the evolution of cloud optical depth, bottom is surface temperature.

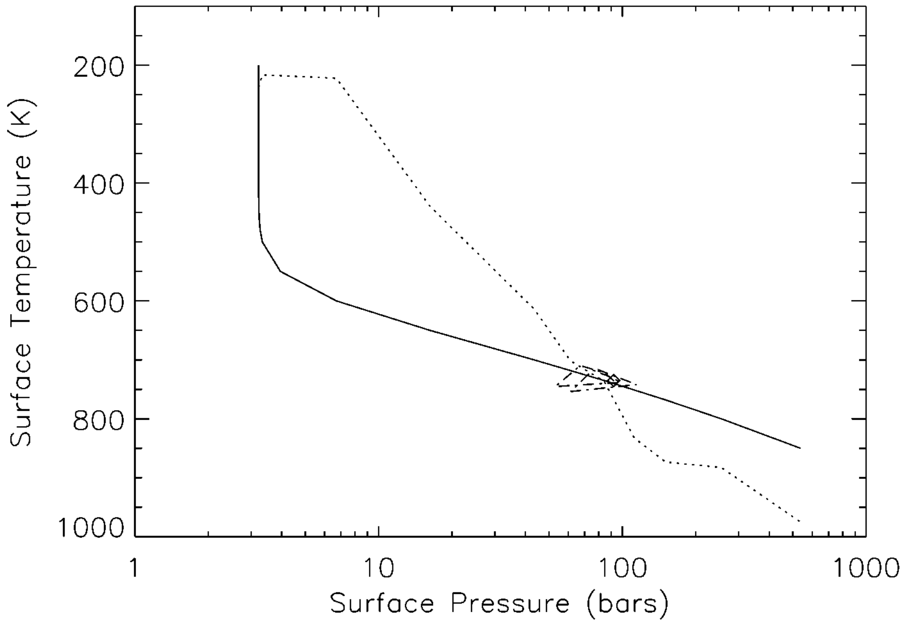

Figure 6.12e Case 7: Stability plot of Figure 6.10 with the evolution of surface pressure and temperature in time (dot-dashed line). For CO_2 and SO_2 reactions with the surface and exospheric escape of H only. Venus' climate is exhibiting an oscillation, beginning with present conditions (diamond) and going counter clockwise around the loop.

Case 8

The final case describes the evolution of Venus' climate with a constant volcanic source of H_2O and SO_2, CO_2 and SO_2 reactions with the surface, and exospheric escape. The results of this evolution are shown in the five plots of Figure 6.13. The injection of SO_2 is compensated for by surface reactions, resulting in more atmospheric H_2O than SO_2 (Figure 6.13a). As seen before in Cases 1 and 3, this leads to higher surface temperatures due to a higher, thinner cloud. The CO_2-mineral reaction runs away when the SO_2 abundance falls significantly below the H_2O abundance, in about 10 My. The atmospheric pressure reaches 1000 bars in 30 My if there is sufficient CO_2 in the rocks to provide it. The planetary albedo drops as the clouds thin, but increases again as Rayleigh scattering becomes more efficient in the 1000 bar atmosphere (figure 6.13b). The evolution of the cloud may be seen in Figure 6.13c, a plot of visual opacity as a function of altitude and time. Surface temperature increase steadily to 975 K 30 My (Figure 6.13d). Beyond this, the spectral databases are unreliable, but clearly the runaway to a hot climate state persists.

A plot of the evolution of the surface pressure and temperature for this case on the stability diagram of Figure 6.10 is shown in Figure 6.13e. Conditions are described by moving down and to the right along the dot-dashed line. Temperatures initially increase as the clouds thin, and the CO_2-mineral equilibrium responds by forcing the atmosphere to a higher temperature and pressure state in 40 My.

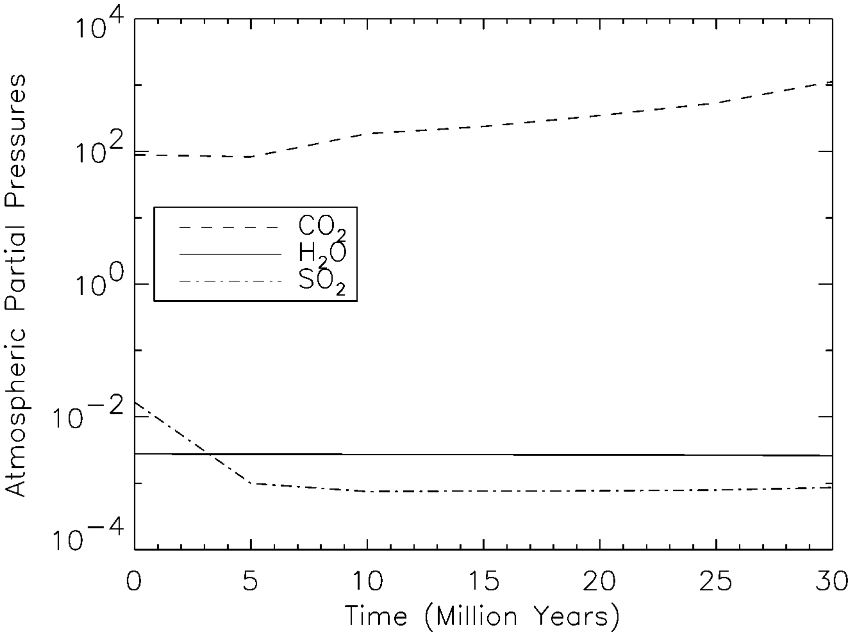

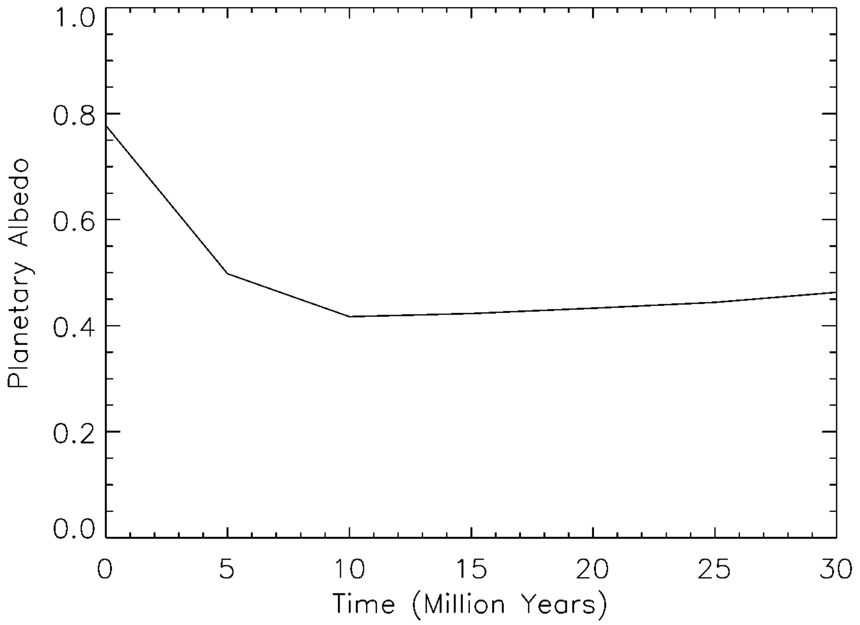

Figure 6.13a and 6.13b Case 8: CO_2 and SO_2 reactions with the surface, constant outgassing, and exospheric escape of H. Top is the evolution of atmospheric partial pressures, bottom is albedo.

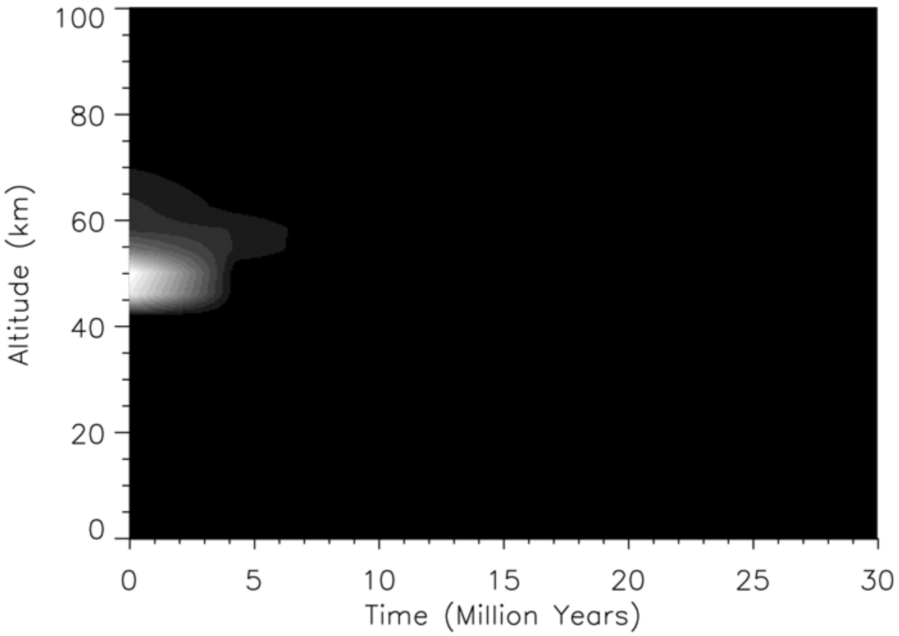

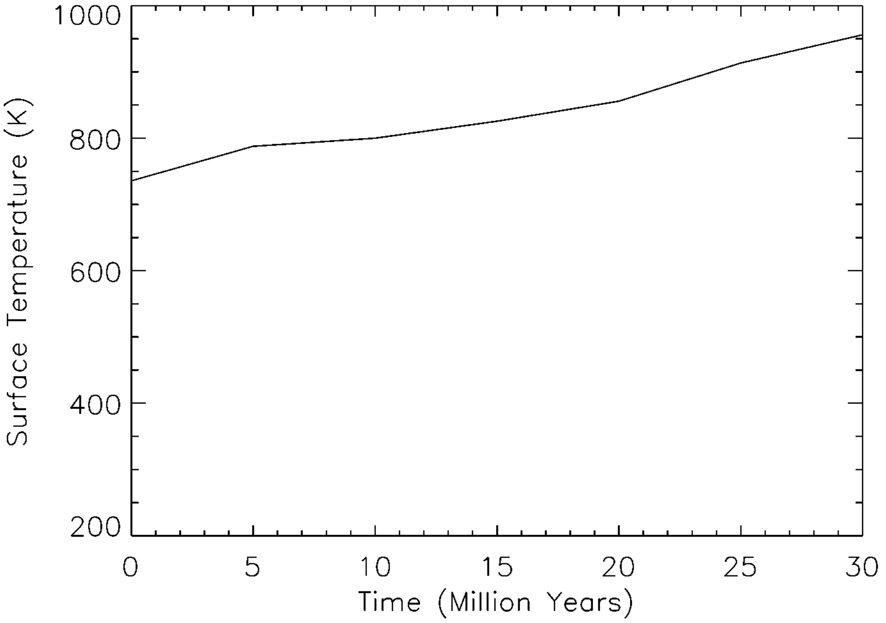

Figure 6.13c and 6.13d Case 8: CO_2 and SO_2 reactions with the surface, constant outgassing, and exospheric escape of H. Top is the evolution of cloud optical depth, bottom is surface temperature.

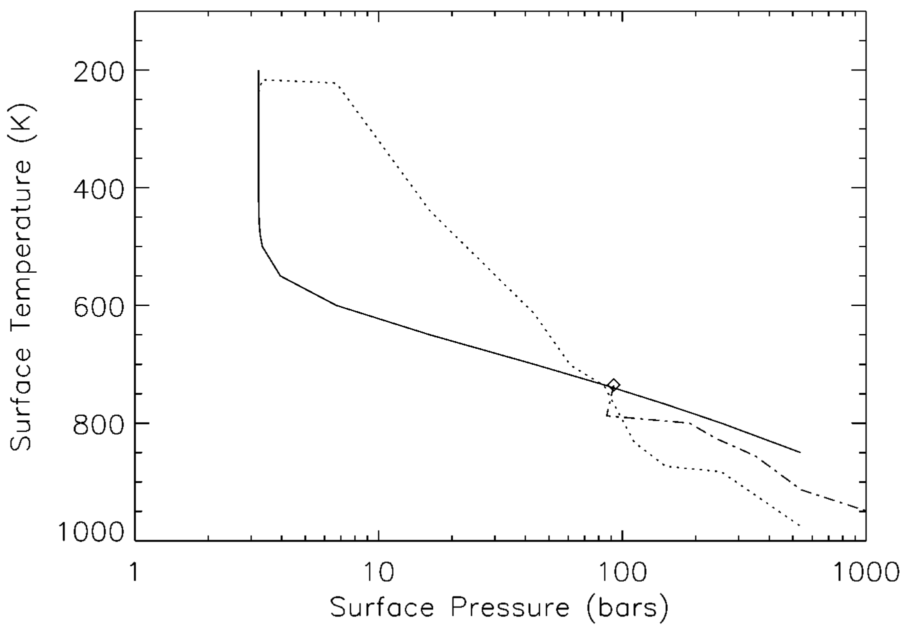

Figure 6.13e Case 8: Stability plot of Figure 6.10 with the evolution of surface pressure and temperature in time (dot-dashed line). For CO_2 and SO_2 reactions with the surface, constant outgassing, and exospheric escape of H. Venus' climate runs away rapidly to higher surface temperatures and pressures.

Conclusions from Cases 6,7 and 8 Results

Under the influence of outgassing associated with volcanic activity, exospheric escape, and CO_2 and SO_2 reactions with the surface, the climate of Venus exhibits three distinctive responses:

1. When outgassing is rapid and intense, thick clouds form due to the increased H_2O and SO_2, and the surface cools. This favors the runaway uptake of CO_2 by surface minerals, resulting in surface temperatures approaching 400 K in 60 million years.
2. When outgassing is shut off, but reactions between atmospheric SO_2 and H_2O and the surface continue along with exospheric escape of H, Venus' climate oscillates. The oscillation is due to the periodic appearance of clouds which control the surface temperature and thus the CO_2-mineral reaction. Clouds disappear at first, but reappear as the surface cools due to the uptake of CO_2. The clouds have a net heating effect on the surface, pushing the CO_2-mineral reaction the other way and decarbonating minerals. Atmospheric temperatures rise again and the clouds disappear. This climate 'limit cycle' has a period of 30 My as surface temperatures vary 30 K and surface pressure varies by 40 bars. The oscillation eventually disappears as lowering H_2O abundances inhibit cloud production. The climate then runs away to a cooler, low pressure state as in (1). This may describe the ultimate fate of Venus as volcanism slows and outgassing eventually ceases.
3. When outgassing is constant, atmospheric H_2O becomes more abundant than SO_2 due to the rapid loss of SO_2 to the surface. Thin, high H_2O clouds form, providing more heating by infrared radiating effects than cooling by increased albedo. CO_2-mineral equilibrium responds by increasing CO_2 abundance, and runway heating occurs due to feedback between this and radiative-convective equilibrium.

4. The CO_2-mineral reaction is probably not active on Venus today. If it were, small perturbations in SO_2 or H_2O would precipitate runaways to stable hot or cold regimes.

5. The CO_2-mineral reaction probably was active following a global outgassing event. Surface temperatures in time can easily span the entire range of uncertainty in the thermodynamic data. The primary effect would be to drive surface temperatures even lower than the 650 K observed in Case 3, as a runaway to cooler temperatures began.

6. The most likely mode of recovery from a large scale outgassing event and drastic cooling was a reduction in atmospheric SO_2 due to reactions with the surface. The high H_2O/SO_2 ratio and high H_2O abundance would have created a hot H_2O greenhouse with high, thin clouds. A CO_2-mineral runaway would have then proceeded until most of the CO_2 had evolved out of the crust. Exospheric escape of H would then have lowered the H_2O/SO_2 ratio and the H_2SO_4/H_2O clouds that we see today would have appeared.

CHAPTER 7

SUMMARY AND CONCLUSIONS

The Venus Climate Evolution Model -- Summary

I have developed a model of the evolution of climate on Venus that calculates the one-dimensional radiative-convective equilibrium state of the atmosphere as it changes in time. Atmospheric infrared fluxes are calculated using a two-stream non-gray method that treats thermal absorption, emission, and scattering in the atmosphere and clouds. Gaseous opacities are calculated using high temperature spectral databases for nine atmospheric constituents and the correlated-k absorption coefficients. The clouds are treated by using a chemical/microphysical model coupled to radiative-convective equilibrium, and cloud opacities are calculated using standard Mie theory for atmospheric aerosols.

I consider three planetary-scale processes that can affect the climate of Venus. They are the loss of H_2O due to exospheric escape of H, the injection of SO_2 and H_2O into the atmosphere from volcanic outgassing, and the reactions of CO_2 and SO_2 with surface minerals. The exospheric escape of H is modeled as a diffusion limited process, where the loss rate depends only upon the global atmospheric abundance of H_2O. Three scenarios for volcanic outgassing are treated: A massive outgassing event declining exponentially in time, a constant source of volatiles, and no outgassing at all. Reactions of CO_2 and SO_2 are modeled using laboratory equilibrium and kinetic data and a reaction/diffusion formalism to scale these data to Venus.

The Venus climate evolution model couples all these processes in a self-consistent, time-marching model that calculates the state of the atmosphere as it evolves in time. Eight evolutionary cases have been presented to show how these processes interact to alter the climate under varying assumptions. Feedback among them is complex, stabilizing the climate in some regimes, and destabilizing it in others. The Venus climate model was designed to provide answers to the following questions:

1. How do variations in atmospheric water and sulfur dioxide affect cloud structure and planetary albedo? How do these, in turn, affect the temperature at the surface?

2. How does the equilibration of atmospheric sulfur dioxide with surface minerals affect cloud structure and surface temperature, and over what timescales?

3. How have changes in atmospheric water abundance due to exospheric escape of hydrogen and volcanic outgassing affected cloud structure and surface temperature, and over what timescales?

4. What was the effect on Venus' cloud structure and surface temperature of an epoch of rapid plains emplacement and consequent widespread, global volcanism?

5. What is the stability of Venus' climate (as described by its surface temperature and pressure) with respect to the equilibration of carbon dioxide with surface minerals? Over what timescales can the climate of Venus change due to this process?

I sought answers to these questions by designing eight numerical climate experiments. The conditions of these experiments were chosen to isolate the effects of individual evolutionary processes in some cases and to investigate their combined effects in others. A complete description of the physical processes and initial conditions used in each of the eight cases may be found in Chapter 6. In summary, the eight evolutionary cases were.

1. The evolution of Venus' climate due to the exospheric escape of H and subsequent loss of atmospheric H_2O over time, with no other evolutionary processes acting. The starting conditions for this run assumed 100 times the current atmospheric H_2O abundance, and present day values for everything else.

2. The evolution of Venus' climate due to the rapid injection of atmospheric SO_2 and H_2O with an exponentially declining outgassing flux, and the loss of H_2O to exospheric escape of H. The initial SO_2 abundance assumed was 0.01 times the current value, while H_2O abundance was 30 ppm, the current value. This case started with thin H_2SO_4/H_2O clouds.

3. Evolution with a rapid injection of atmospheric SO_2 and H_2O, an exponentially declining outgassing flux, and the loss of H_2O to exospheric escape of H. In addition, the effects of SO_2 reactions with surface minerals were included. The initial SO_2 abundance assumed was 0.01 times the current value, while H_2O abundance was 30 ppm, the current value.

4. The evolution of Venus' climate due to the a constant volcanic source of SO_2 and H_2O, the loss of H_2O to exospheric escape of H, and SO_2 reactions with the surface. Present-day abundances were assumed as initial conditions.

5. Evolution of climate with no sources of either SO_2 or H_2O, but with the loss of H_2O to exospheric escape of H and SO_2 reactions with the surface. Present-day abundances were assumed as initial conditions.

6. The evolution of Venus' climate due to the rapid injection of atmospheric SO_2 and H_2O with an exponentially declining outgassing flux, and the loss of H_2O to

exospheric escape of H. In addition, the effects of SO_2 and CO_2 reactions with surface minerals were included. Present-day abundances were assumed as initial conditions.

7. Evolution with no sources of either SO_2 or H_2O, but with the loss of H_2O to exospheric escape of H, and SO_2 and CO_2 reactions with the surface. Present-day abundances were assumed as initial conditions.

8. The evolution of Venus' climate due to the a constant volcanic source of SO_2 and H_2O, the loss of H_2O to exospheric escape of H, and SO_2 and CO_2 reactions with the surface. Present-day abundances were assumed as initial conditions.

Conclusions drawn from the results of each of these eight evolutionary calculations may be found in Chapter 6. The discussion in that chapter includes detailed references to the results, presented in Figures 6.5 - 6.13. Together, these evolutionary calculations provide insight into the evolution and stability of Venus' climate. They illustrate how cloud albedo and radiative-convective equilibrium foster climate feedbacks with surface/atmosphere interactions and other sources and sinks for atmospheric SO_2 and H_2O. What follows are the general conclusions I have drawn about the climate of Venus that bear on the five questions posed in the Introduction and at the beginning of this chapter.

Sensitivity of the Clouds to Changes in Atmospheric Abundances

The response of the clouds and surface temperature to changes in atmospheric SO_2 and H_2O is shown in Figures 3.10, 3.11 and 3.12. As these abundances decrease the clouds become thinner, increasing the available solar flux. However, infrared opacity is reduced due to less absorption by these gases deep in the atmosphere and by less infrared opacity in the cloud regions. Lowering cloud albedo dominates over the decreased greenhouse, and the atmosphere becomes hotter. Because it becomes hotter, the cloud base is shifted upwards, and the clouds become thinner still. Clouds disappear entirely when the deep H_2O abundance drops below 0.3 ppm or the SO_2 abundance drops below 1 ppm. Surface temperatures decline to 720 K as the clouds go away due to the decrease in gaseous and aerosol infrared opacity and the high Rayleigh scattering albedo of the atmosphere.

An interesting transition occurs when atmospheric H_2O is increased to more than about 50 times its current value. Because the Venus greenhouse effect is so sensitive to H_2O abundance, the atmosphere heats up sufficiently to overcome the effects of increased cloud albedo. The result is a rapid decrease in cloud thickness and albedo, as the rising atmospheric temperatures erode the cloud base from below, leaving a high, thin cloud H_2O cloud. Surface temperatures when this happens are slightly in excess of 900 K if there is sufficient atmospheric H_2O for an enhanced greenhouse. From 0.1 to 10 times the current atmospheric H_2O abundance, cloud albedo is roughly compensated for by changes in the greenhouse effect, and temperatures close to current values prevail.

Cloud opacity increases steadily with increasing SO_2 abundance, resulting in decreasing surface temperatures. With ten times the current SO_2 abundance, but no change to atmospheric H_2O, the surface is 700 K. Surface temperatures remain close to present values for only a narrow range around present-day abundances of atmospheric SO_2.

The Effects of SO_2-Surface Reactions on Venus' Climate

Atmospheric SO_2 reacts rapidly with surface carbonate under present Venus conditions. The time scale for the chemical equilibration of atmospheric SO_2 with the surface is approximately 20 My at 735 K. The atmosphere currently has 100 times more SO_2 than it would if it were equilibrated, indicating a source active within the last 20 My. Reactions with the surface have probably buffered large amounts of outgassed SO_2, playing a crucial role in controlling the abundance of atmospheric SO_2. The timescale for the removal of atmospheric SO_2 is short compared to the timescale for the loss of atmospheric H_2O due to the exospheric escape of H. If H_2O becomes much more abundant than SO_2 because of this, thick H_2SO_4/H_2O clouds are replaced by high, thin H_2O clouds. The reduced albedo of these clouds can increase surface temperatures to 900 K. However, the kinetics of the SO_2-surface reaction are highly temperature dependent. If surface temperatures go below about 575 K, SO_2 uptake by the surface is insufficient to prevent the buildup of atmospheric SO_2 from volcanic outgassing. Large amounts of atmospheric SO_2 result in thick H_2SO_4/H_2O clouds and cooler temperatures. If the CO_2-mineral reaction is considered, large amounts of atmospheric SO_2 cause Venus' climate to run away to a cool, lower pressure state with surface temperature and pressures of 400 K and 43 bars, respectively. In this case, a thick H_2SO_4/H_2O would exist near the surface, and the albedo of Venus would be very near 0.95.

The Effects of a Global Geological Resurfacing on Venus' Climate

A massive outgassing event such as one associated with an epoch of rapid global plains emplacement would have first cooled Venus' surface due to the buildup of thick clouds and an increased albedo. This can most clearly be seen in the first 300 My of Case 3 (Figure 6.7) when CO_2 reactions with surface minerals are not included and in 60 My in Case 6 (Figure 6.11) for when they are.

If atmospheric CO_2 cannot react with minerals, surface temperatures as low as 650 K can be reached and remain below 700 K for about 300 million years. The magnitude and duration of such a cooling episode are dependent upon the volume of outgassed volatiles, the ratio of H_2O/SO_2 in erupting magmas, and the initial atmospheric abundances of H_2O and SO_2. The ratio of atmospheric H_2O to SO_2

rises over time due reactions of SO_2 with surface minerals. Loss of atmospheric H_2O due to exospheric escape of H is slower than SO_2 reactions with the surface, and a critical abundance ratio (H_2O/SO_2) of about 15 is reached in 500 My. At this point, the thick H_2SO_4/H_2O clouds give way to high, thin H_2O clouds, and the surface becomes very hot. How hot and for how long depend on exactly how much H_2O there was in the atmosphere to begin with and how wet erupting magmas were. Surface temperatures would have remained in the range of 800-930 K for 200-600 My. Ultimately, the atmosphere and surface would have achieved something like their current states 700 to 1100 My after an outgassing event and after traversing these cold and hot regimes.

If the surface cooled enough to enable atmospheric CO_2 reactions with minerals, very massive clouds would have formed, and the surface temperature would have dropped. Carbonation of minerals would result in a reduction in the greenhouse effect and a runaway to a stable, much cooler state in only 60 My (Figure 6.11). This state is characterized by a surface pressure of 43 bars and a surface temperature of about 400 K. A thick H_2SO_4/H_2O fog exists from near the surface to about 40 km. The climate is stable in this regime because low surface temperatures effectively shut off SO_2 reactions with the surface, allowing SO_2 to build up in the atmosphere. This happens in only 40 My, as atmospheric CO_2 is lost to surface minerals and surface temperatures go below 575 K due to the decreased greenhouse effect. Such a fate for Venus could only have been avoided if either CO_2 reactions with the surface are much slower than I have assumed or if atmospheric H_2O was significantly higher. A 100-fold increase in atmospheric H_2O, for example, due either to initial conditions or wetter magmas would have kept surface temperatures high enough to avoid such a cold runaway scenario. If either of these conditions prevailed, the first 200 My after the onset of resurfacing would be cool, followed by a hot period, as in Case 3. The duration of elevated surface temperatures to 800-920 K depends upon the ratio of H_2O to SO_2 in the source, and is between 200 and 800 My.

The Stability of Venus' Present Climate

We have seen in the last discussion that a rapid injection of SO_2 and H_2O into the atmosphere causes the climate to run away to a cold, lower pressure regime. Case 4 (Figure 6.8) shows that with a constant source of SO_2 and H_2O, SO_2 reactions with the surface and loss of H_2O due to exospheric escape, Venus' climate is stable. This steady state may represent the situation on Venus today, but the conclusion is only valid if CO_2 cannot react with surface minerals. If they can, the picture changes dramatically, as shown in Figure 6.13 for Case 8. A constant source of volatiles, along with a rapid crustal sink for SO_2 keeps atmospheric H_2O abundances high enough to precipitate a CO_2-mineral runaway to a hot, high-pressure state. In Case 8, surface temperature and pressure rapidly increase to 950 K and 1000 bars, respectively, in only 30 My. Clouds disappear quickly (in 10 My) in such a scenario, since the atmosphere becomes too hot to support them.

Atmospheric SO2 abundances are 100 times higher than they would be if they were in equilibrium with surface rocks. These reactions are rapid, implying a volcanic source of volatiles active in the last 20 My.

Neither of the runaway climate scenarios are plausible since they evolve quickly to stable states that are vastly different from what we see today. More likely, most of the surface is devoid of carbonate and the Urey equilibrium has no effect on the current climate of Venus. However, an injection of 3-10 times the current total abundance of atmospheric SO_2 (depending on the exact thermodynamic properties of the Urey equilibrium) would dramatically cool the surface due to the increase in cloud albedo. It would be enough to engage the Urey equilibrium, resulting in a rapid runaway to the cool stable state at 400 K and 43 bars. Such a fate for Venus is not out of the question, and it may have cycled between that state and present conditions one or more times in the past. Increased atmospheric abundance of H_2O, due either to a large comet or outgassing by wet magmas, would have been required to return the climate to presently observed conditions.

Comets

It is conceivable that comets could have played a decisive role in the evolution of Venus' climate to its current state. Venus' atmosphere currently contains 7 x 10^{18} g of H_2O, about as much as in a 25 km comet. It has been suggested that the current H_2O abundance in Venus' atmosphere is the result of a steady state between delivery by comets, volcanic outgassing, and exospheric hydrogen escape [*Grinspoon*, 1987; *Grinspoon and Lewis*, 1988]. Using fluxes and mass exponents for long-period comets [*Shoemaker et al.*, 1990] and short period comets [*Shoemaker et al.*, 1991], the total integrated mass of comets delivered to Venus in one billion years is about 2 x 10^{19} g. If these comets are on average one half H_2O ice, comets could be delivering a substantial amount of the H_2O required for it to be in steady state with exospheric escape at currently observed atmospheric abundances.

However, a billion-year comet that was 100 km in diameter could deliver as much as 40 times the current atmospheric abundance of H_2O in an instant. Such an impact today would precipitate a positive feedback between the clouds and greenhouse effect, resulting in surface temperatures rapidly rising to 900 K. This phenomenon was observed in Case 3 at 500 million years and its reverse was observed at the beginning of Case 1.

The impact of a large comet during the cooler temperatures following a global outgassing epoch could have raised the atmospheric H_2O/SO_2 ratio significantly. As we have seen, this is just the condition that could have prevented a runaway to a cooler state. In addition, an impact of this magnitude would have been able to nudge

Venus' climate out of the cooler regime produced by massive clouds, and put it on the path to the conditions we see today.

The Future Climate of Venus

The eventual fate of Venus will be sealed when volcanism wanes and outgassing shuts off. Case 7 (Figure 6.12) best illustrates the beginning of the end for climate change on Venus.

Here, all volcanic sources have been shut off, but surface/atmosphere reactions and exospheric escape are allowed to continue. Venus' climate begins to oscillate between warm, cloudy conditions and a cooler, cloud-free regime. This periodicity in Venus' climate is due to a complex interaction between cloud albedo, the greenhouse effect, and CO_2 and SO_2 reactions with the surface. Atmospheric SO_2 declines as it equilibrates with the surface, removing the clouds. The planet also gets cooler due to the loss of cloud thermal infrared opacity, perturbing the CO_2-mineral equilibrium and inducing a cooling runaway. In 30 My, however, clouds appear whose infrared radiative effects dominate over the slightly increased albedo. The surface becomes warmer, and the CO_2-mineral equilibrium shifts to one with more atmospheric CO_2. The clouds go away again and the process repeats.

The amplitude of these surface temperature variations is about 30 K. Venus' climate becomes quasi-periodic around the unstable Urey/radiative-convective equilibrium point. Ultimately, as atmospheric H_2O is lost due to the exospheric escape of H, the oscillation would dampen and the climate would runaway to a cool, low pressure state. It finally settles with a thick H_2SO_4/H_2O fog close to the ground and surface temperature and pressure of 400 K and 43 bars. . Such a scenario is likely because as the clouds initially go away surface temperatures drop sufficiently to enable CO2 reactions with the surface.

Hypothesis: The Stability and Recent Evolution of Venus

The conclusions that I have drawn so far from the model results apply to the range of assumptions I have used regarding the magnitude and timing of planetary processes. In addition, the initial conditions affect the outcome of all the model runs. It is compelling, however, to attempt to reconstruct the recent evolution of Venus based on an understanding of the complex climate interactions that I have explored. The exercise is speculative, but important for informing future, more sophisticated studies of the climate of Venus. I suggest the following scenario for the recent evolution and present stability of climate on Venus:

Venus experienced a global epoch of rapid plains emplacement 600-1100 My ago. During this time, which lasted 10-100 My, large quantities of SO_2 and H_2O were injected into the atmosphere. This caused the surface to cool for 300 My due to a massive build-up of clouds. A climate runaway to a cool, lower pressure state due to mineral/radiative-convective instability was probably averted by sufficient initial atmospheric H_2O. As atmospheric SO_2 equilibrated with surface minerals, the ratio of H_2O to SO_2 in the atmosphere rose. Thick H_2SO_4/H_2O clouds gave way to thin, high H_2O clouds 400 - 800 My following the onset of global resurfacing. The reduced albedo of Venus combined with an enhanced greenhouse effect drove surface temperatures to 800 - 930 K, where they stayed for 100 - 500 My. These conditions could also have been induced by H_2O brought in with a 100 km comet, an event expected for Venus in one billion years.

Evolution to current conditions on Venus occurred as atmospheric H_2O was lost due the exospheric escape of H. As the atmospheric SO_2/H_2O ratio rose, the thicker H_2SO_4/H_2O clouds we see today developed. Current conditions are maintained by the continued low-level outgassing of SO_2 and H_2O from volcanoes active in the last

20 My. CO2-mineral reactions (Urey equilibrium) are probably not actively involved in the stability of the present climate of Venus.

An episode of increased outgassing, especially if it is sulfur-rich, has the potential to destabilize Venus' current climate and precipitate a runaway to a cool, low-pressure state. A thick fog would exist close to the ground, and sulfur reactions with surface reactions would be shut off. Alternatively, if atmospheric H_2O continues to decrease due to exospheric loss of H and outgassing ceases, the climate of Venus may oscillate and then runaway to the same stable state at 400 K and with a surface pressure of 43 bars.

Climate Change on Venus -- Future Missions and Data

The study of climate change on Venus provides us with the means to investigate a fascinating interplay between global-scale processes and planetary climate. The true story of Venus' past can only be told when sufficient data has been collected from the planet. Venus is a difficult place to explore, especially with tight fiscal constraints on planetary space exploration. However, there are a number of mission possibilities that are both practical and capable of illuminating the issue of Venus' recent climate evolution.

The signature of atmospheric and surface evolution is to some degree written in its rare gas and isotopic abundances. Significant gaps in these data exist, leaving us unable to distinguish the relative importance of volatile outgassing, atmospheric erosion due to impacts, escape history, and the role of solar wind implantation and grain accretion in the formation of the initial atmosphere. In particular, Xe isotope abundances are almost completely unconstrained. An upper atmosphere sample and return mission could be simple, spectacular, and vast in scientific value. Such a spacecraft would be inexpensive, having no instruments and minimal downlink requirements.

A mission to Venus that involved a Magellan-like spacecraft, but with the ability to do radar interferometry, would be a valuable tool for looking at dynamic surface processes. With orbital tracks within kilometers of each other, the motion of the ground can be sensed through the construction of synthetic aperture radar fringes. A high resolution altimeter could accompany such a mission, improving topographic information on Venus by at least an order of magnitude over Magellan.

The best evidence for climate change on Venus is probably contained in its surface record. A photovisual reconnaissance of Venus is essential for making valid comparisons between Venus geology and geology on the other terrestrial planets. High resolution images of recently exposed cliff faces may show the sedimentary history that radar cannot. Diagenetic layers, indicative of eras of altered atmospheric chemistry have been proposed to explain layering observed in the wall of Valles Marineris on Mars, for example [*Treiman et al.*, 1995]. Visual observations of the surface are possible from either balloon-borne or aerobot cameras, or from gliders that could take advantage of Venus' atmospheric superrotation to map the planet. These missions would obviously be more expensive and demand the development of new and risky technologies.

Finally, the conclusions I have presented regarding the stability of climate on Venus depend upon the effectiveness of CO_2 reactions with surface minerals. The best available kinetic data on heterogeneous carbonate formation under Venus-like conditions is poor. Experiments to determine the rate of these reactions are necessary to comment on the viability of this mechanism for inducing changes in climate on Venus.

REFERENCES

Abramowitz, M., and I.A. Stegun, Handbook of Mathematical Functions, Dover, New York, 1965.

Anderson, H.L., *A Physicist's Desk Reference*, American Institute of Physics, New York, 1989.

Arfken, G., *Mathematical Methods for Physicists*, Academic Press, San Diego, 1985.

Arkani-Hamed, J., G.G. Schaber, and R.G. Strom, Constraints on the thermal evolution of Venus inferred from Magellan data, *J. Geophys. Res.*, *98*, 5309-5315, 1993.

Arkani-Hamed, J., and M.N. Toksoz, Thermal evolution of Venus, *Physics of The Earth and Planetary Interiors*, *34*, 232-250, 1984.

Ball, B.C., Modelling of soil pores as tubes using gas permeabilities, gas diffusivities and water release, *Journal of Soil Science*, *32*, 465 - 481, 1981.

Barath, F.T., A.H. Barrett, J. Copeland, D.C. Jones, and A.E. Lilley, Microwave radiometers, part of Mariner II: Preliminary reports on measurements of Venus, *Science*, *139*, 908 - 909, 1963.

Barsukov, V.L., Y.A. Surkov, L.V. Dimitriyev, and I.L. Khodakovsky, Geochemical studies on Venus with the landers from the Vega 1 and Vega 2 probes, *Geochemistry International*, *23*, 53 - 65, 1986.

Basilevsky, A.T., and J.W. Head, Global stratigraphy of Venus: Analysis of a random sample of thirty-six test areas, *Earth, Moon and Planets*, *66*, 285-336, 1995.

Bertaux, J.-L., T. Widemann, A. Hauchecorne, V.I. Moroz, and A.P. Ekonomov, Vega-1 and Vega-2 entry probes: An investigation of UV absorption (220-400 nm) in the atmosphere of Venus, *J. Geophys. Res.*, *101*, 12,709-12,745, 1996.

Bezard, B., C. de Bergh, D. Crisp, and J.P. Maillard, The deep atmosphere of Venus revealed by high-resolution nightside spectra, *Nature*, *345*, 508 - 511, 1990.

Bezard, B., C. de Bergh, B. Fegley, J.P. Maillard, D. Crisp, T. Owen, J.B. Pollack, and D.H. Grinspoon, The abundance of sulfur dioxide below the clouds of Venus, *Geophys. Res. Lett.*, *20*, 1587-1590, 1993.

Bullock, M.A., and D.H. Grinspoon, The stability of climate on Venus, *J. Geophys. Res.*, *101*, 7521-7529, 1996.

Bullock, M.A., D.H. Grinspoon, and J.W. Head, Venus resurfacing rates: Constraints provided by 3-D Monte Carlo simulations, *Geophys. Res. Lett.*, *20*, 2147-2150, 1993.

Bullock, M.A., C.R. Stoker, C.P. McKay, and A.P. Zent, A coupled soil-atmosphere model of H_2O_2 on Mars, *Icarus*, *107*, 142-154, 1994.

Carlson, R.W., L.W. Kamp, K.H. Baines, J.B. Pollack, D.H. Grinspoon, T. Encrenaz, P. Drossart, E. Lellouch, and B. Bezard, Variations in Venus cloud particle properties: A new view of Venus's cloud morphology as observed by the Galileo near-infrared mapping spectrometer, *Planet Space Sci.*, *41*, 477-486, 1993.

Chandrasekhar, S., *Radiative Transfer*, Dover, New York, 1960.

Clough, S.A., F.X. Kneizys, R. Davis, R. Gamache, and R. Tipping, Theoretical line shape for H_2O vapor: Application to the continuum, in *Atmospheric Water Vapor*, edited by A. Deepak, T.D. Wilkerson, and L.H. Ruhnke, pp. 25-46, Academic Press, New York, 1980.

Coffin, M.F., Large igneous provinces: Crustal structure, dimensions, and external consequences, *Rev. Geophys.*, *32*, 1-36, 1994.

Crisp, D., Radiative forcing of the Venus mesosphere, *Icarus*, *67*, 484-514, 1986.

Crisp, D., D.A. Allen, D.H. Grinspoon, and J.B. Pollack, The dark side of Venus: Near-infrared images and spectra from the Anglo-Australian Observatory, *Science*, *253*, 1263 - 1266, 1991.

de Bergh, C., B. Bezard, D. Crisp, J.P. Maillard, T. Owen, J.B. Pollack, and D.H. Grinspoon, Water in the deep atmosphere of Venus from high-resolution spectra of the night Side, *Adv. Space Res.*, *15*, (4)79-(4)88, 1995.

de Bergh, C., B. Bezard, T. Owen, D. Crisp, J.P. Maillard, and B.L. Lutz, Deuterium on Venus: Observations from Earth, *Science*, *251*, 547-549, 1991.

Donahue, T.M., D.H. Grinspoon, R.E. Hartle, and R.R. Hodges, Ion/neutral escape of hydrogen and deuterium: Evolution of water, in *Venus II*, edited by D.M. Hunten, University of Arizona Press, Tucson, Arizona, 1997.

Donahue, T.M., and R.R. Hodges, Past and present water budget of Venus, *J. Geophys. Res.*, *97*, 6083 - 6091, 1992.

Donahue, T.M., J.H. Hoffman, R.R. Hodges, and A.J. Watson, Venus was wet: A measurement of the ratio of D to H, *Science*, *216*, 630-633, 1982.

Donahue, T.M., and J.B. Pollack, Origin and evolution of the atmosphere of Venus, in *Venus*, edited by D.M. Hunten, L. Colin, T.M. Donahue, and V.I. Moroz, pp. 1003-1036, University of Arizona Press, Tucson, 1983.

Esposito, L.W., Sulfur dioxide: Episodic injection shows evidence for active Venus volcanism, *Science*, *223*, 1072-1074, 1984.

Esposito, L.W., R.G. Knollenberg, M.Y. Marov, O.B. Toon, and R.P. Turco, The clouds and hazes of Venus, in *Venus*, edited by D.M. Hunten, L. Colin, T.M. Donahue, and V.I. Moroz, pp. 484-564, University of Arizona Press, Tucson, 1983.

Fanale, F.P., J.R. Salvail, A.P. Zent, and S.E. Postawko, Global distribution and migration of subsurface ice on Mars, *Icarus*, *67*, 1 - 18, 1986.

Fegley, B., and K. Lodders, The Rate of Chemical Weathering of Pyrite on the Surface of Venus, in *Abstracts of the 24th Lunar and Planetary Science Conference*, pp. 467-468, 1992.

Fegley, B., K. Lodders, A.H. Treiman, and G. Klingelhofer, The rate of pyrite decomposition on the surface of Venus, *Icarus*, *115*, 159-180, 1995.

Fegley, B., and R.G. Prinn, Estimation of the rate of Volcanism on Venus from reaction rate measurements, *Nature*, *337*, 55-58, 1989.

Fegley, B., and A.H. Treiman, Chemistry of atmosphere-surface interactions on Venus and Mars, in *Venus and Mars: Atmospheres, Ionospheres and Solar Wind Interactions*, edited by J.G. Luhmann, M. Tatrallyay, and R.O. Pepin, pp. 7-71, American Geophysical Union, Washington, DC, 1992.

Flood, E.A., The Solid Gas Interface, Dekker, New York, 1967.

Giver, L.P., and C. Chackerian, Intensity and position measurements of carbon dioxide lines in the 4370 to 4640 cm^{-1} region., 46th International Symposium on Molecular Spectroscopy, Columbus, OH, 1991.

Goody, R.M., R.A. West, L. Chen, and D. Crisp, The correlated-k method for radiation calculations in nonhomogeneous atmospheres, *J. Quant. Spectrosc. Rad. Transfer*, *42*, 539-550, 1989.

Goody, R.M., and Y.L. Yung, *Atmospheric Radiation: Theoretical Basis*, Oxford University Press, Oxford, 1989.

Grimm, R.E., and S.C. Solomon, Limits on the modes of lithospheric heat transport on Venus from impact crater density, *Geophysics Research Letters*, *14*, 538-541, 1987.

Grinspoon, D.H., Was Venus Wet? Deuterium Reconsidered, *Science*, *238*, 1702 - 1704, 1987.

Grinspoon, D.H., Implications of the high D/H ratio for the sources of water in Venus' atmosphere, *Nature*, *363*, 428-431, 1993.

Grinspoon, D.H., and J.S. Lewis, Cometary water on Venus: Implications of stochastic impacts, *Icarus*, *74*, 21-35, 1988.

Grinspoon, D.H., J.B. Pollack, B.R. Sitton, R.W. Carlson, L.W. Kamp, K.H. Baines, T. Encrenaz, and F.W. Taylor, Probing Venus' cloud structure with Galileo NIMS, *Planet Space Sci.*, *41* (July 1993), 515-542, 1993.

Hansen, J.E., and J.W. Houvenier, Interpretation of the polarization of Venus, *J. Atmos. Sci.*, *31*, 1137-1160, 1974.

Hansen, J.E., and L.D. Travis, Light scattering in planetary atmospheres, *Space Sci. Rev.*, *16*, 527-610, 1974.

Head, J.W., L.S. Crumpler, J.C. Aubele, J.E. Guest, and R.S. Saunders, Venus volcanism: Classification of volcanic features and structures, associations, and global distribution from Magellan data, *J. Geophys. Res.*, *97*, 13153-13198, 1992.

Head, J.W., E.M. Parmentier, and P.C. Hess, Venus: Vertical accretion of crust and depleted mantle and implications for geological history and processes, *Planet Space Sci.*, *42*, 803-833, 1994.

Henderson, B.G., and B.M. Jakosky, Near-surface thermal gradients and mid-IR emission spectra: A new model including scattering and application to real data, *J. Geophys. Res.*, *102*, 6567-6580, 1997.

Herrick, D.L., and E.M. Parmentier, Episodic large-scale overturn of two layer mantles in terrestrial planets, *J. Geophys. Res.*, *99*, 2053-2062, 1994.

Holland, H.D., *The Chemistry of the Atmospheres and Oceans*, Wiley, New York, 1978.

Houghton, J.T., G.J. Jenkins, and J.J. Ephraums, Climate Change: The IPCC Scientific Assessment, Cambridge University Press, Cambridge, 1990.

Ingersoll, A.P., The runaway greenhouse: A history of water on Venus, *J. Atmos. Sci.*, *26*, 1191-1198, 1969.

Ip, W.-H., and J.A. Fernandez, Exchange of condensed matter among the outer and terrestrial proto-planets and the effect on surface impact and atmospheric accretion, *Icarus*, *74*, 47-61, 1988.

Kargel, J.S., R.L. Kirk, B. Fegley, and A.H. Treiman, Carbonate-sulfate volcanism on Venus?, *Icarus*, *112*, 219-252, 1994.

Kasting, J.F., Runaway and moist greenhouse atmospheres and the evolution of Earth and Venus, *Icarus*, *74*, 472-494, 1988.

Kasting, J.F., J.B. Pollack, and T.P. Ackerman, Response of Earth's atmosphere to increases in solar flux and implications for loss of water from Venus, *Icarus*, *57*, 335-355, 1984.

Kaula, W.M., Venus reconsidered, *Science*, *270*, 1460 - 1464, 1995.

Kaula, W.M., J.W. Head, R.B. Merrill, R.O. Pepin, S.C. Solomon, D. Walker, and C.A. Wood, Basaltic Volcanism on the Terrestrial Planets, Pergamon Press, New York, 1981.

Kliore, A., V.I. Moroz, and G.M. Keating, The Venus International Reference Atmosphere, in *COSPAR*, Pergamon Press, Oxford, 1986.

Kneizys, F., J. Chetwynd, R. Fenn, E. Shettle, L. Abreu, R. McClatchey, W. Gallery, and J. Selby, Atmospheric transmittance/radiance computer code LOWTRAN 5, Air Force Geophysical Laboratory, 1980.

Knollenberg, and Hunten, The microphysics of the clouds of Venus: Results of the Pioneer Venus particle size spectrometer experiment, *J. Geophys. Res.*, *85*, 8039-8058, 1980.

Krasnopolsky, V.A., and V.A. Parshev, Photochemistry of the Venus atmosphere, in *Venus*, edited by D.M. Hunten, L. Colin, T.M. Donahue, and V.I. Moroz, pp. 431-458, University of Arizona Press, Tucson, 1983.

Krasnopolsky, V.A., and J.B. Pollack, H_2O-H_2SO_4 system in Venus' clouds and OCS, CO and H_2SO_4 profiles in Venus' troposphere, *Icarus*, *109*, 58-78, 1994.

Lacis, A.A., and V. Oinas, A description of the correlated k method for modeling nongray gaseous absorption, thermal emission and multiple scattering in vertically inhomogeneous atmospheres, *J. Geophys. Res.*, *96*, 9027 - 9063, 1991.

Lenoble, J., Radiative Transfer in Scattering and Absorbing Atmospheres: Standard Computational Procedures, Deepak Publishing, Hampton, 1985.

Lewis, J.S., Venus: Atmospheric and lithospheric composition, *Earth and Planetary Science Letters*, *10*, 73-80, 1970.

Liou, K.N., *Radiation and Cloud Processes in the Atmosphere*, 487 pp., Oxford University Press, New York, 1992.

Mayer, C.H., T.P. McCullough, and R.M. Sloanaker, Observations of Venus at 3.15 cm wavelength, *Astrophys. J.*, *127*, 1, 1958.

McKay, C.P., J.B. Pollack, and R. Courtin, The thermal structure of Titan's atmosphere, *Icarus*, *80*, 23-53, 1989.

McKinnon, W.B., K.J. Zahnle, B.A. Ivanov, and H.J. Melosh, Cratering on Venus: Models and observations, in *Venus II, in preparation*, edited by S.W. Bougher, D.M. Hunten, and R.J. Phillips, University of Arizona Press, Tucson, 1997.

Meadows, V.S., and D. Crisp, Ground-based near-infrared observations of the Venus night side: The thermal structure and water abundance near the surface, *J. Geophys. Res.*, *101*, 4595-4622, 1996.

Moroz, V.I., B.E. Moshkin, A.P. Ekonomov, N.F. San'ko, N.A. Parfent'ev, and Y.M. Golovin, Spectrophotometric experiment on board the Venera-11, -12 descenders: Some results of the analysis of the Venus day-sky spectrum., in *Space Research Institute Acadamy Science Leningrad Publication*, 1978.

Moskalenko, N.I., Y.A. Il'in, S.N. Parzhin, and L.V. Rodinovon, Pressure-induced IR radiation absorption in atmospheres, *Bulletin of the Academy of Science USSR, Atmospheric and Oceanic Physics*, *15*, 632-637, 1979.

Mueller, R.F., and S.J. Kridelbaugh, Kinetics of CO_2 production on Venus, *Icarus*, *19*, 531-541, 1973.

Namiki, N., Argon degassing and crustal production rates on Venus, in *Abstracts of the 25th Lunar and Planetary Science Conference*, pp. 971-972, 1994.

Namiki, N., and S.C. Solomon, Volcanic degassing of argon and helium and the history of crustal production on Venus, *submitted to Journal of Geophysical Research*, *in press*, 1997.

Nature, More news from Venus, *Nature*, *216*, 427-428, 1967.

Owen, T., A. Bar-Nun, and I. Kleinfeld, Possible cometary origin of heavy noble gases in the atmospheres of Venus, Earth and Mars, *Nature*, *358*, 43 - 46, 1992.

Oyama, V.I., G.C. Carle, F. Woeller, and J.B. Pollack, Venus lower atmosphere composition: Analysis by gas chromatography, *Science*, *203*, 802-804, 1979.

Oyama, V.I., G.C. Carle, F. Woeller, J.B. Pollack, R.T. Reynolds, and R.A. Craig, Pioneer Venus gas chromatography of the lower atmosphere of Venus, *J. Geophys. Res.*, *85*, 7891-7902, 1980.

Palmer, K.F., and D. Williams, Optical constants of sulfuric acid: Application to the clouds of Venus?, *Appl. Opt.*, *14*, 208-219, 1975.

Parmentier, E.M., and P.C. Hess, Chemical differentiation of a convecting planetary interior: Consequences for a one plate planet such as Venus, *Geophys. Res. Lett.*, *19*, 2015-2018, 1992.

Pepin, R.O., On the origin and early evolution of terrestrial planet atmospheres and meteoritic volatiles, *Icarus*, *92*, 2-79, 1991.

Pettengill, G.H., P.G. Ford, and S. Nozette, Venus: Global surface radar reflectivity, *Science*, *217*, 640-642, 1982.

Phillips, R.J., R.E. Arvidson, J.M. Boyce, D.B. Campbell, J.E. Guest, G.G. Schaber, and L.A. Soderblom, Impact craters on Venus: Initial analysis from Magellan, *Science*, *252*, 288 - 297, 1991.

Phillips, R.J., and V.L. Hansen, Venus now and then: Rises, plains, plumes and plateaus, *submitted to Science*, 1997.

Phillips, R.J., and M.C. Malin, The interior of Venus and tectonic implications, in *Venus*, edited by D.M. Hunten, L. Colin, T.M. Donahue, and V.I. Moroz, pp. 159-214, University of Arizona Press, Tucson, 1983.

Phillips, R.J., R.F. Raubertas, R.E. Arvidson, I.C. Sarker, R.R. Herrick, N.R. Izenberg, and R.E. Grimm, Impact craters and Venus resurfacing history, *J. Geophys. Res.*, *97*, 15923-15948, 1992.

Pike, R.J., Size dependence in the shape of fresh impact craters on the moon, in *Impact and Explosion Cratering*, Pergamon Press, New York, 1977.

Pollack, J.B., A nongray CO_2-H_2O greenhouse model of Venus, *Icarus*, *10*, 314-341, 1969a.

Pollack, J.B., Temperature structure of nongray planetary atmospheres, *Icarus*, *10*, 301-313, 1969b.

Pollack, J.B., Climate change on the terrestrial planets, *Icarus*, *37*, 479-553, 1979.

Pollack, J.B., J.B. Dalton, D.H. Grinspoon, R.B. Wattson, R. Freedman, D. Crisp, D.A. Allen, B. Bezard, C. de Bergh, L.P. Giver, Q. Ma, and R.H. Tipping, Near infrared light from Venus' nightside: A spectroscopic analysis, *Icarus*, *103*, 1-42, 1993.

Pollack, J.B., D.W. Strecker, F.C. Witteborn, E.F. Erickson, and B.J. Baldwin, Properties of the clouds of Venus, as inferred from airborne observations of its near infrared reflectivity spectrum, *Icarus*, *34*, 28-45, 1978.

Pollack, J.B., O.B. Toon, and R. Boese, Greenhouse models of Venus' high surface temperature, as constrained by Pioneer Venus measurements, *J. Geophys. Res.*, *85*, 8223-8231, 1980.

Powers, D.L., *Boundary Value Problems*, Harcourt Brace Jovanovish, San Diego, 1987.

Press, W.H., B.P. Flannery, S.A. Teukolsky, and W.T. Vetterling, *Numerical Recipes in C*, Cambridge University Press, Cambridge, 1988.

Ragent, B., and J.E. Blamont, The structure of the clouds of Venus: Results of the Pioneer Venus nephelometric experiment, *J. Geophys. Res.*, *85*, 8089-8105, 1980.

Rasool, S.I., and C. de Bergh, The runaway greenhouse and accumulation of CO_2 in the Venus atmosphere, *Nature*, *226*, 1037-1039, 1970.

Reif, F., *Fundamentals of Statistical and Thermal Physics*, McGraw-Hill, New York, 1965.

Roberts, E., J. Selby, and L. Biberman, Infrared continuum absorption by atmospheric water vapor in the 8-12 um window, *Appl. Opt.*, *15*, 2085-2090, 1976.

Rothman, L.S., R.R. Gamache, R.H. Tipping, C.P. Rinsland, and M.A.H. Smith, The HITRAN molecular database: editions of 1991 and 1992, *J. Quant. Spectrosc. Rad. Transfer*, *48*, 469, 1992.

Rothman, L.S., R.B. Wattson, R.R. Gamache, D. Goorvith, R.L. Hawkins, J.E.A. Selby, C. Camy-Peyret, J.M. Flaud, J. Schroeder, and A. McCann, HITEMP, the high-temperature molecular spectroscopic database, *J. Quant. Spectrosc. Rad. Transfer*, *in press*, 1997.

Sagan, C., The radiation balance of Venus, JPL, Pasadena, California, 1960.

Sagan, C., and G. Mullen, Earth and Mars: Evolution of atmospheres and surface temperatures, *Science*, *177*, 52-56, 1972.

Satterfield, C.N., *Mass Transfer in Heterogeneous Catalysis*, M.I.T. Press, Cambridge, 1970.

Saunders, R.S., A.J. Spear, P.C. Allin, R.S. Austin, A.L. Berman, R.C. Chandler, J. Clark, A.V. Decharon, E.M. DeJong, D.G. Griffith, J.M. Gunn, S. Hensley, W.T.K. Johnson, C.E. Kirby, K.S. Leung, D.T. Lyons, G.A. Michaels, J. Miller, R.B. Morris, R.G. Pierson, J.F. Scott, S.J. Schaffer, J.P. Slonski, E.R. Stofan, R.W. Thompson, and S.D. Wall, Magellan mission summary, *J. Geophys. Res.*, *97*, 13067-13090, 1992.

Schaber, G.G., R.G. Strom, H.J. Moore, L.A. Soderblom, R.L. Kirk, D.J. Chadwick, D.D. Dawson, L.R. Gaddis, J.M. Boyce, and J. Russel, Geology and distribution of impact craters on Venus: What are they telling us?, *J. Geophys. Res.*, *97*, 13257-13302, 1992.

Schidlowski, M., A 3,800 million-year isotopic record of life from carbon in sedimentary rocks, *Nature*, *333*, 313-318, 1988.

Schubert, G., and D.T. Sandwell, A Global Survey of Possible Subduction Sites on Venus, *Icarus*, *117*, 173 - 196, 1995.

Seiff, A., The thermal structure of the atmosphere, in *Venus*, edited by D.M. Hunten, L. Colin, T.M. Donahue, and V.I. Moroz, pp. 215-279, University of Arizona Press, Tucson, 1983.

Sharpton, V.L., Paradigm Lost: Venus Crater Depths and the Role of Gravity in Crater Modification, in *International Conference on Large Impact Structures and Planetary Evolution*, pp. 65 - 66, 1992.

Shoemaker, E.M., R.F. Wolfe, and C.S. Shoemaker, Asteroid and Comet Flux in the Neighborhood of Earth, in *Global Catastrophes in Earth History: An Interdisciplinary Conference on Impacts, Volcanism, and Mass Mortality*, edited by V.L. Sharpton, and P.D. Ward, pp. 155 - 170, Geological Society of America, 1990.

Shoemaker, E.M., R.F. Wolfe, and C.S. Shoemaker, Asteroid Flux and Impact Cratering Rate on Venus, in *Abstracts of the 22nd Lunar and Planetary Science Conference*, pp. 1253 - 1254, 1991.

Smoluchowski, R., Mars: Retention of ice, *Science*, *159*, 1348 - 1350, 1967.

Strom, R.G., G.G. Schaber, and D.D. Dawson, The global resurfacing of Venus, *J. Geophys. Res.*, *99*, 10899-10926, 1994.

Surkov, Y.A., V.L. Barsukov, L.P. Moskalyeva, V.P. Kharyukova, and A.L. Kemurdzhian, New data on the composition, structure and properties of Venus rock obtained by Venera 13 and Venera 14, in *Proceedings of the 14th Lunar and Planetary Science Conference*, pp. B393-B402, Journal of Geophysical Research, 1984.

Surkov, Y.A., L.P. Moskalyeva, V.P. Kharyukova, A.D. Dudin, G.G. Smirnov, and S.Y. Zaitseva, Venus rock composition at the Vega 2 landing site, in *Proceedings of the 17th Lunar and Planetary Science Conference*, pp. E215-E218, Journal of Geophysical Research, 1986.

Tomasko, M.G., The thermal balance of the lower atmosphere of Venus, in *Venus*, edited by D.M. Hunten, L. Colin, T.M. Donahue, and V.I. Moroz, pp. 604-631, University of Arizona Press, Tucson, 1983.

Tomasko, M.G., L.R. Doose, P.H. Smith, and A.P. Odell, Measurements of the flux of sunlight in the atmosphere of Venus, *J. Geophys. Res.*, *85*, 8167-8186, 1980.

Toon, O.B., C.P. McKay, and T.P. Ackerman, Rapid calculation of radiative heating rates and photodissociation rates in inhomogeneous multiple scattering atmospheres, *J. Geophys. Res.*, *94*, 16287, 1989.

Treiman, A.H., K.H. Fuks, and S. Murchie, Diagenetic Layers in the Upper Walls of Valles Marineris, Mars: Evidence for Drastic Climate Change Since the mid-Hesperian, *J. Geophys. Res.*, *100*, 26,339-26,344, 1995.

Turcotte, D.L., How did Venus lose heat?, *J. Geophys. Res.*, *100*, 16,931 - 16,940, 1995.

Turcotte, D.L., and G. Schubert, *Geodynamics*, Wiley, New York, 1982.

Urey, H.C., *The Planets*, Yale University Press, New Haven, 1952.

van de Hulst, H.C., *Light Scattering by Small Particles*, Dover, New York, 1981.

Volkov, V.P., M.Y. Zolotov, and I.L. Khodakovsky, Lithospheric-atmospheric interaction on Venus, in *Chemistry and Physics of the Terrestrial Planets*, edited by S.K. Saxena, pp. 136-190, Springer-Verlag, New York, 1986.

Washburn, E.W., C.J. West, and N.E. Dorsey, International Critical Tables of Numerical Data, Physics, Chemistry and Technology, McGraw Hill, National Research Council, New York, 1930.

Wattson, R.B., and L.S. Rothman, Direct numerical diagonalization: Wave of the future, *J. Quant. Spectrosc. Rad. Transfer*, *48*, 763-780, 1992.

Wildt, R., Note on the surface temperature of Venus, *Astrophys. J.*, *91*, 266-268, 1940.

Young, A.T., and L.D. Young, Comments on the composition of the Venus cloud tops in light of recent spectroscopic data, *The Astrophysical Journal*, *179*, 39-43, 1973.

Yung, Y.L., and W.B. DeMore, Photochemistry of the stratosphere of Venus: Implications for atmospheric evolution, *Icarus*, *51*, 199-248, 1982.

Zahnle, K.J., Airburst origin of dark shadows on Venus, *J. Geophys. Res.*, *97*, 10,243 - 10,255, 1992.

Zahnle, K.J., Planetary noble gases, in *Protostars and Planets III*, edited by E.H. Levy, and J.I. Lunine, pp. 1305-1338, University of Arizona Press, Tucson, 1993.

Zahnle, K.J., and J.F. Kasting, Mass fractionation during transonic escape and implications for loss of water from Mars and Venus, *Icarus*, *68*, 462-480, 1986.

Zeleznik, F.J., Thermodynamic properties of the aqueous sulfuric acid system to 350 K, *J. Phys. Chem. Ref. Data*, *20*, 1157-1200, 1991.